

# **Microstructure and Engineering Properties of Alkali Activated Fly Ash**

**-as an environment friendly alternative to  
Portland cement**

**Yuwei Ma**



# **Microstructure and Engineering Properties of Alkali Activated Fly Ash**

**-as an environment friendly alternative to Portland cement**

Proefschrift

ter verkrijging van de graad van doctor  
aan de Technische Universiteit Delft,  
op gezag van de Rector Magnificus prof. ir. K.C.A.M. Luyben,  
voorzitter van het College voor Promoties,  
in het openbaar te verdedigen  
op donderdag 17 oktober 2013 om 10.00 uur

door

Yuwei Ma

Master of Science aan de Wuhan University, China  
geboren te Wuhan, Hubei Province, China

Dit proefschrift is goedgekeurd door de promotor:  
Prof.dr.ir. K. van Breugel

Copromotor:  
Dr. G. Ye

Samenstelling promotiecommissie:

Rector Magnificus,	voorzitter
Prof.dr.ir. K. van Breugel,	Technische Universiteit Delft, promotor
Dr. G. Ye,	Technische Universiteit Delft, copromotor
Prof.dr. P. Yan,	Tsinghua University, China
Prof.dr. A. Palomo,	Eduardo Torroja Institute, Spain
Prof.dr. J.L. Provis,	The University of Sheffield, UK
Prof.dr. R.B. Polder,	Technische Universiteit Delft/TNO
Dr. S. Valcke,	TNO
Prof.dr.ir. H.E.J.G. Schlangen,	Technische Universiteit Delft, reservelid

ISBN: 978-94-6186226-6

Keywords: alkali activated fly ash, geopolymer, microstructure, transport properties, shrinkage.

Printed by Haveka B.V., the Netherlands

Copyright © 2013 by Yuwei Ma

All right reserved. No part of the material protected by this copyright notice may be reproduced or utilized in any form or by any means, electronic or mechanical, including photocopying, recording or by any information storage and retrieval system, without written permission from the author.

*The way ahead is long; I see no ending; yet high and low I'll search with my will  
unbending*

*- Qu Yuan (343-278 BCE)*

*“路漫漫其修远兮，吾将上下而求索”*

*-屈原 (公元前 343-278)*



# Summary

---

Alkali activated fly ash (AAFA), also named “geopolymer”, has emerged as a novel engineering material in the construction industry. This material is normally formed by the reaction between fly ash and aqueous hydroxide or alkali silicate solution. The reaction product is an alkali aluminosilicate gel, which is different from the calcium silicate hydrate (C-S-H) gel in Portland cement, but has also cementitious properties. With proper mix design, AAFA can present comparable or superior engineering properties to Portland cement. Moreover, this material shows great potential for sustainable development since its production has a significantly lower CO<sub>2</sub> emission than the production of Portland cement. Despite these environmental and technological features of AAFA, challenges still exist in the evaluation of the long-term stability of this material, which is related to the mix proportion of the activator content and the evolution of its underlying microstructure.

This study aims at a better understanding of the microstructure and engineering properties (including mechanical properties, permeability and shrinkage) of AAFA with different activator content, i.e. SiO<sub>2</sub> and Na<sub>2</sub>O. The evaluation of the mix proportion of the activator is not only based on the early age properties of AAFA, e.g. setting time, workability, heat release, mechanical properties (Chapter 3), but also taking into account the durability related issues, such as permeability (Chapter 6) and shrinkage (Chapter 7). The measurements results of AAFA were compared with those of Portland cement, for instance, the results of pore structure, permeability, water content and shrinkage. These comparisons and further discussions reveal how the differences in microstructure affect the macro-properties of these two systems. In addition, the different performance of AAFA and Portland cement should be carefully evaluated when AAFA is used as an alternative to Portland cement.

In Chapter 3, a series of activating solutions with different SiO<sub>2</sub> and Na<sub>2</sub>O content were prepared to produce AAFA. Before synthesis, the chemical composition, particle size distribution, chemical reactivity of the raw material, i.e. fly ash, was evaluated to see if it is suitable for alkali activation. The performance of AAFA mixtures was evaluated with respect to the workability, setting time, heat release and mechanical strength. Based on the experimental results, a group of AAFA mixtures with 7 and 28 days strength similar or superior to those of cement pastes (w/c=0.4) were chosen for further study.

The effect of SiO<sub>2</sub> and Na<sub>2</sub>O on the microstructure of AAFA pastes was experimentally studied in Chapter 4 and Chapter 5. The experimental results showed that a higher amount of sodium (between 1.0 mol/kg fly ash and 1.5 mol/kg fly ash) enhanced the dissolution of fly ash particles, leading to a higher degree of reaction and a denser microstructure both at 7 and 28 days. Thus AAFA mixtures with a higher sodium content showed a higher mechanical strength and a lower water permeability (Chapter 6) both at 7 days and 28 days.

The effect of the silica content on AAFA is twofold: On the one hand, the addition of a higher amount of silica (e.g. 1.5 mol/kg fly ash compared to 1.0 mol/kg fly ash) retarded the dissolution of fly ash particles, leading to a lower degree of reaction both at 7 and 28 days. On the other hand, the added silica was incorporated in the gel, which resulted in a more homogeneous and denser matrix of AAFA pastes, and a high elastic modulus of the gel phase. Due to these two conflicting effects, AAFA mixture with a higher silica content (e.g. 1.5 mol/kg fly ash compared to 1.0 mol/kg fly ash) showed a denser microstructure, higher compressive strength and lower water permeability at 7 days. At 28 days, however, for AAFA mixtures with less silica content, i.e. a silica content of 1.0 mol/kg fly ash, the densification of microstructure was more pronounced. Thus mixtures with less silica content, e.g. 1.0 mol/kg fly ash compared to 1.5 mol/kg fly ash, showed a higher compressive strength and lower water permeability at 28 days.

The permeability is related to the pore threshold diameter and the effective porosity derived from MIP results. By using these two pore structure parameters as inputs to calculate the water permeability, a linear relationship was found between the calculated and measured permeability for most of the AAFA samples.

The pore structure of AAFA pastes with a silica content  $\geq 1.0$  mol/kg fly ash is very different compared to cement pastes, mainly with respect to the formation of “capillary pores”. Some large cavities were left by dissolved fly ash particles, constituting the “capillary pores” in the matrix of AAFA. These cavities appeared as “isolated” voids, bordered by the homogeneously distributed gel. These cavities in AAFA contribute less to the water permeability than the typical “capillary pores” in cement pastes (Chapter 6). However, the rate of pore refinement of some AAFA pastes at later age is significantly slower than that of cement pastes ( $w/c=0.4$ ). Thus the decrease of permeability with time for AAFA pastes is much slower than that for cement pastes. The different evolutions of pore structure and permeability as a function of time between AAFA and cement may indicate that care should be exercised in determining the long-term performance of AAFA with the evaluating systems currently used for cement-based systems.

The shrinkage of AAFA pastes was studied in Chapter 7. The experimental results showed that the chemical shrinkage of AAFA pastes, cured at 40 °C for 7 days, was similar to that of cement paste. The processes contributing to the chemical shrinkage in AAFA pastes, however, is different from that in cement paste. The mechanism of the autogenous shrinkage of AAFA pastes is also found different from that of cement paste. It is assumed that the continuous reorganization and polymerization of the gel structure induce autogenous shrinkage of AAFA paste, instead of the self-desiccation process as it occurs in cement paste. AAFA specimens with a higher amount of sodium and silica had a higher autogenous shrinkage. Under restrained condition, the stress caused by the autogenous shrinkage did not cause the early-age cracking of samples. The relationship of autogenous shrinkage/cracking potential of AAFA pastes still needs more study.

The drying shrinkage of investigated AAFA mixtures was comparable or lower than cement pastes ( $w/c=0.4$ ) after 180 days of drying at RH = 50 %. AAFA mixtures with a higher sodium and silica content exhibited a higher drying shrinkage. The drying shrinkage of different AAFA mixtures was not proportional to their weight loss. The different weight loss/drying shrinkage relationship is attributed to the different pore

structure of these mixtures, which can be explained from the capillary pressure point of view. The finer the pore structure, the higher capillary pressure that is produced during the drying process, resulting in a higher drying shrinkage. Thus the pore structure is an important factor determining the magnitude of drying shrinkage of AAFA mixtures.





# Table of Contents

## *List of Symbols*

## *List of Abbreviations*

## **Chapter 1**

### **General Introduction**

1.1	Background of the research	1
1.2	Objective of this research	2
1.3	Scope of this research	3
1.4	Research strategy and outline	3

## **Chapter 2**

### **Literature Survey**

2.1	Introduction	5
2.2	Sustainable development and Portland cement	5
2.3	Cement blended with fly ash	6
2.4	Alkali activated fly ash (AAFA)	6
	2.4.1 General introduction of AAFA.....	6
	2.4.2 Reaction mechanism and reaction products of AAFA .....	8
	2.4.3 The microstructure model of AAFA .....	11
	2.4.4 The engineering properties and applications of AAFA .....	12
2.5	Factors affecting the properties of AAFA	13
	2.5.1 Raw materials .....	14
	2.5.2 Activator.....	15
	2.5.3 Water content .....	20
	2.5.4 Curing conditions .....	20
2.6	Permeability and shrinkage issues	22
	2.6.1 Permeability.....	22
	2.6.2 Shrinkage .....	22
2.7	Concluding remarks and motivation of the research	23

## **Chapter 3**

### **Mixture Design for Alkali Activated Fly Ash**

3.1	Introduction	25
3.2	Materials	26
	3.2.1 Characterization of fly ash .....	26
	3.2.2 Activating solutions.....	28
3.3	Experimental Methods	29
	3.3.1 Mixing and curing.....	29
	3.3.2 Workability.....	29
	3.3.3 Setting time .....	30
	3.3.4 Heat evolution.....	30
	3.3.5 Mechanical properties .....	30
3.4	Results and discussions	32
	3.4.1 Workability.....	32
	3.4.2 Setting time .....	32
	3.4.3 Heat evolution.....	33
	3.4.4 Mechanical property.....	34
3.5	Concluding remarks	37

## **Chapter 4**

### **Solid Phases of Alkali Activated Fly Ash**

4.1	Introduction	39
4.2	Materials and Experimental Methods	39
	4.2.1 Materials.....	39
	4.2.2 Sample preparation.....	40
	4.2.3 Environmental scanning electron microscopy (ESEM).....	40
	4.2.4 Attenuated total reflectance - Fourier transform infrared spectroscopy (ATR-FTIR) .....	43
	4.2.5 X-ray diffraction (XRD) .....	43
	4.2.6 Nanoindentation.....	44
	4.2.7 Assessment of the degree of reaction of AAFA by image analysis ....	45
4.3	Results and Discussion	48
	4.3.1 Morphology of fly ash particles.....	48
	4.3.2 Morphology of hardened AAFA pastes.....	49

4.3.3	<i>Un-reacted fly ash and degree of reaction of AAFA pastes</i> .....	52
4.3.4	<i>Chemical bonds of AAFA pastes</i> .....	54
4.3.5	<i>Phase development measured by XRD of AAFA pastes</i> .....	57
4.3.6	<i>Elastic properties of AAFA pastes on micro scale</i> .....	59
4.4	Concluding remarks	67

## **Chapter 5**

### ***Pore Structure of Alkali Activated Fly Ash***

5.1	Introduction	69
5.2	Introduction of experimental techniques for pore structure characterization	69
5.2.1	<i>Mercury intrusion porosimetry</i> .....	69
5.2.2	<i>Nitrogen adsorption</i> .....	71
5.2.3	<i>Environmental scanning electron microscopy (ESEM)</i> .....	71
5.2.4	<i>Discussion on ESEM, MIP and nitrogen adsorption techniques</i> .....	71
5.3	Materials and Methods	72
5.3.1	<i>Materials</i> .....	72
5.3.2	<i>Sample preparation</i> .....	72
5.3.3	<i>MIP</i> .....	72
5.3.4	<i>Nitrogen adsorption</i> .....	73
5.4	Results and discussions	74
5.4.1	<i>Pore structure formation of AAFA by MIP and ESEM observation</i> ..	74
5.4.2	<i>Nitrogen adsorption results of AAFA pastes</i> .....	83
5.4.3	<i>Gel pore threshold diameter/ elastic modulus of the gel</i> .....	86
5.4.4	<i>Comparison of the results from MIP and nitrogen adsorption</i> .....	87
5.5	Concluding remarks	88

## **Chapter 6**

### ***Permeability of Alkali Activated Fly Ash***

6.1	Introduction	91
6.2	Materials and Experimental Methods	91
6.2.1	<i>Materials</i> .....	91
6.2.2	<i>Sample preparation for water permeability tests</i> .....	92
6.2.3	<i>Water permeability testing method</i> .....	93

6.3	Results and Discussion	95
6.3.1	<i>Permeability results</i> .....	95
6.3.2	<i>Experimentally observed relationship between water permeability and pore structure parameters derived from MIP</i> .....	99
6.3.3	<i>Prediction of the water permeability based on MIP results</i> .....	100
6.4	Concluding remarks	103

## **Chapter 7**

### ***Shrinkage of Alkali Activated Fly Ash***

7.1	Introduction	105
7.2	Materials and Experimental Methods	106
7.2.1	<i>Materials</i> .....	106
7.2.2	<i>Chemical shrinkage</i> .....	106
7.2.3	<i>Sample preparation and test methods for autogenous shrinkage</i> ....	107
7.2.4	<i>Sample preparation and test methods for drying shrinkage</i> .....	108
7.2.5	<i>Ellipse ring test of AAFA pastes: cracking of sealed specimens</i> .....	109
7.2.6	<i>Internal relative humidity of AAFA pastes</i> .....	110
7.2.7	<i>Evaporable and non-evaporable water content in AAFA pastes</i> .....	111
7.3	Results and Discussion	111
7.3.1	<i>Chemical shrinkage of AAFA pastes</i> .....	111
7.3.2	<i>Autogenous shrinkage of AAFA pastes</i> .....	112
7.3.3	<i>Cracking potential of AAFA pastes due to autogenous shrinkage</i> ..	112
7.3.4	<i>Evaporable and non-evaporable water content in AAFA pastes</i> .....	115
7.3.5	<i>The internal RH of AAFA paste</i> .....	116
7.3.6	<i>Discussion on the mechanisms of chemical and autogenous shrinkage of AAFA paste</i> .....	117
7.3.7	<i>Drying shrinkage of AAFA pastes</i> .....	120
7.3.8	<i>Relationships between drying shrinkage, weight loss and pore structure</i> .....	121
7.3.9	<i>Suggestions for the use of AAFA from the shrinkage point of view</i> .	124
7.4	Concluding remarks	125

## ***Chapter 8***

### ***Retrospection, Conclusions, Recommendations for Practice and Future Research***

8.1	Retrospection	127
8.2	Conclusions	128
8.4	Future research	133

### ***References***

### ***Samenvatting***

### ***Acknowledgement***

### ***Curriculum Vitae***



# List of Symbols

---

## Roman

$D$	[m]	pore diameter
$E$	[GPa]	elastic modulus
$Q$	[m <sup>3</sup> /s]	volume of fluid passed in unit time
$R$	[J/(mol·K)]	ideal gas constant
$T$	[K]	absolute temperature
$V_w$	[m <sup>3</sup> /mol]	mol volume of water
$W$	[g]	mass of specimen
$d_c$	[m]	threshold/critical pore diameter
$k'$	[m <sup>2</sup> ]	intrinsic permeability coefficient
$k_w$	[m/s]	permeability coefficient of water
$r$	[m]	radius of pore
$\gamma$	[N/m]	surface tension
$\alpha$	[-]	degree of reaction
$\theta$	[°]	contact angle
$\sigma_{cap}$	[MPa]	tensile stress in the pore fluid





# List of Abbreviations

---

AAFA	alkali activated fly ash
AAM	alkali activated material
ATR-FTIR	attenuated total reflectance-fourier transform infrared spectroscopy
BSE	backscattered electron
C-S-H	calcium silicate hydrates
EDX	energy dispersive X-ray analysis
ESEM	environmental scanning electron microscopy
MAS-NMR	magic angle spinning-nuclear magnetic resonance
MIP	mercury intrusion porosimetry
NMR	nuclear magnetic resonance
OPC	ordinary Portland cement
RH	relative humidity
SEM	scanning electron microscopy
w/c	water to cement ratio
w/FA	water to fly ash ratio
XRD	X-ray diffraction
XRF	X-ray fluorescence



## **Chapter 1**

# **General Introduction**

---

### **1.1 Background of the research**

Alkali activated fly ash (AAFA), also named “geopolymer”, has emerged as a novel engineering material in the construction industry. This material is normally formed by the reaction between fly ash and aqueous hydroxide or alkali silicate solution. Normally elevated temperature curing (e.g. 40 °C, 60 °C or 80 °C) is needed to get a reasonable early age strength. The reaction product is a class of alkali aluminosilicate gel, with aluminium and silicon linked in a three-dimensional tetrahedral gel framework [Provis and Van Deventer, 2009]. The aluminosilicate gel is distinctly different from the calcium silicate hydrate (C-S-H) gel in ordinary Portland cement (OPC), but has also cementitious properties. In the system of AAFA, fly ash can substitute OPC by 100 %. Consequently, it avoids the high-temperature calcination step that is needed for cement clinker production, and thus reduces the CO<sub>2</sub> emission to a large extent. Duxson et al. [2007b] stated that alkali activated binders can in general deliver an 80 % or greater reduction in CO<sub>2</sub> emission compared to OPC. In addition, since fly ash is a by-product of coal-fired electricity plants, the reuse of fly ash would reduce the storage and transportation cost for the fly ash producers, which is also environmental-friendly. Alkali activated fly ash can exhibit many excellent properties, e.g. high early age strength, low creep and shrinkage, high resistance to chemical attack and high fire resistance [Bakharev, 2005b; Fernández-Jiménez et al., 2007; Fernández-Jiménez and Palomo, 2005b; Hardjito and Rangan, 2005]. Applications of this material in constructions include the manufacturing of precast products, such as railroad sleepers, precast box culverts, sewer pipes and fire resistant wall panels. In particular, the excellent resistance to chemical attack makes these products very promising for the use of aggressive environments.

Despite these environmental benefits and technological features, alkali activated fly ash mixtures showed variations in strength and other engineering properties (e.g. setting time, shrinkage, chemical and fire resistance etc.). The reason is partially related to the variable quality (e.g. chemical composition, reactivity, particle size, etc.) of the raw material (i.e. fly ash) used to produce AAFA products. In addition, different types and contents of activator, water content and curing conditions (including temperature, curing time and moisture condition) are used to produce AAFA, which consequently lead to different microstructures and engineering properties (discussed in detail in Chapter 2). A comprehensive knowledge of the alkali

activation reaction, more specifically the parameters that may affect the microstructure and the properties of AAFA, are, therefore, important to produce AAFA products with good performance. Among all the parameters, the activator is one of the most important factors affecting the microstructure and the properties of AAFA. Thus, in this study, the microstructure and engineering properties of AAFA were investigated as a function of the content of activator ( $\text{SiO}_2$  and  $\text{Na}_2\text{O}$ ).

In order to utilize AAFA as a building material, its long-term stability is very important since it determines the safety and reliability of the structures. Due to the utilization of different fly ashes, mixtures and curing procedures to produce AAFA, its long-term stability still remains unclear. Moreover, there is no site data available to prove the long-term stability of AAFA, since it has been subjected to extensive research only recently [Provis and Van Deventer, 2009].

In a way water can be estimated as a primary agent of deterioration of hardened AAFA-based concrete structures. From one point of view, it can be a carrier of aggressive ions (e.g.  $\text{Cl}^-$ ,  $\text{CO}_3^{2-}$ ,  $\text{SO}_4^{2-}$ , etc.) that initiate the degradation of the microstructure. From another point of view, it is also a cause of microstructure deterioration through its physical transformation (in case of freezing and thawing). Both processes affect the service life of AAFA structures. Therefore, the water permeability of AAFA is one of the most important properties that affect the long-term stability of a structure.

Besides permeability, shrinkage (i.e. drying shrinkage and autogenous shrinkage) of AAFA is another important engineering property that needs special attention. The shrinkage of material determines the probability of cracking under restrained condition. When the deformations caused by shrinkage are restrained, tensile stresses develop and cracks may occur if the stress exceeds the tensile strength of the material. Cracks form an open path for the infiltration/penetration of aggressive agents (e.g.  $\text{CO}_2$ ,  $\text{Cl}^-$ ), leading to damage of the structure. A clear understanding of the shrinkage mechanisms of AAFA is still missing.

The evaluation of the strength, permeability and shrinkage behavior of AAFA requires a better understanding of its microstructure. Hardened alkali activated fly ash is a porous material. Similar to other material properties, the mechanical properties, permeability and shrinkage are all a function of the microstructure of the material. Therefore, a comprehensive characterization of the microstructure, both of its pore and solid phases, is a crucial step to assess the strength, durability and shrinkage of AAFA.

## 1.2 Objective of this research

The main goal of this research is to get a better understanding of the microstructure, mechanical properties, permeability and shrinkage of alkali activated fly ash with different silica and sodium content in the activator. Based on this, the relationships between the activator content, the microstructure and the engineering properties are explored. The outcome of the research provides a theoretical basis for the activator mix proportion and property optimization of AAFA. In addition, the information

about the microstructure and water permeability will contribute to the evaluation of the long-term performance of AAFA.

### **1.3 Scope of this research**

In this study, alkali activated fly ash will be studied with the following restrictions:

- Only alkali activated fly ash paste was studied;
- Water/fly ash mass ratio was 0.35. This value is selected as low as possible, but a workable binder can still be guaranteed;
- Activator content: SiO<sub>2</sub> content varied from 0 to 1.5 mol/kg fly ash; Na<sub>2</sub>O content varied from 1.0 to 1.5 mol/kg fly ash;
- Curing in sealed condition at 40 °C;
- No admixtures were used;
- Chemical and autogenous shrinkage were measured at 40 °C;
- Drying shrinkage was measured after 7 days curing at 40 °C and then exposed at relative humidity of 50 % ± 5 % and temperature of 20 ± 3 °C;

### **1.4 Research strategy and outline**

The research mainly focuses on the following aspects:

- Characterization of the microstructure of AAFA pastes with different activator content and different curing regimes;
- Effect of activator content, i.e. Na<sub>2</sub>O and SiO<sub>2</sub> content, and curing regime on the mechanical properties, water permeability and shrinkage of AAFA pastes;
- Relationship between these properties (mechanical properties, water permeability and shrinkage) and the microstructure of AAFA pastes;

In this study, results of experimental studies of the pore structure, permeability and shrinkage of AAFA pastes are compared with those of Portland cement pastes with w/c=0.4, which have similar strength at 7 and 28 days as AAFA pastes studied here. These comparisons address the differences between AAFA and cement system on the microstructure and the macro-properties. These differences are very important for AAFA as an alternative material to cement.

The outline of the thesis is given in Figure 1.1.

In Chapter 1, the background, the objectives and the scope of the research are presented. Chapter 2 gives a literature overview of the environmental and

technological features of the alkali activated fly ash, reaction mechanisms, microstructure description and factors influencing its properties.

In Chapter 3, a local fly ash (from The Netherlands) is used to produce AAFA. Based on the results of setting time, workability, mechanical properties and heat evolution, a group of mixtures with promising engineering properties is selected for the next step investigation.

Chapters 4 and 5 give a comprehensive description on the solid phases and pore structure of investigated AAFA pastes. In Chapter 4, the reaction products of AAFA pastes are examined with respect to the spatial distribution of the reaction products, the degree of reaction, the chemical bonds and the micro-mechanical properties (elastic modulus) by environmental scanning electron microscopy (ESEM), x-ray diffraction (XRD), fourier transform infrared spectroscopy (FTIR) and nanoindentation, respectively. The strength results obtained in Chapter 3 are then correlated to the solid phase development, as also discussed in Chapter 4. In Chapter 5, the pore structure of AAFA pastes is studied by mercury intrusion porosimetry (MIP) and nitrogen adsorption. Observation of the pores by ESEM is used to assist the evaluation of the MIP results of AAFA pastes.

The water permeability of AAFA pastes is studied in Chapter 6. The relationship between permeability and pore structure is discussed and a quantitative correlation is established. In Chapter 7, the chemical shrinkage, autogenous shrinkage and drying shrinkage of AAFA pastes is explored. The shrinkage mechanism of AAFA pastes and its correlation with microstructure parameters are discussed.

Chapter 8 summarized the results and conclusions of this study. Recommendations for engineering practice and for future research are given.

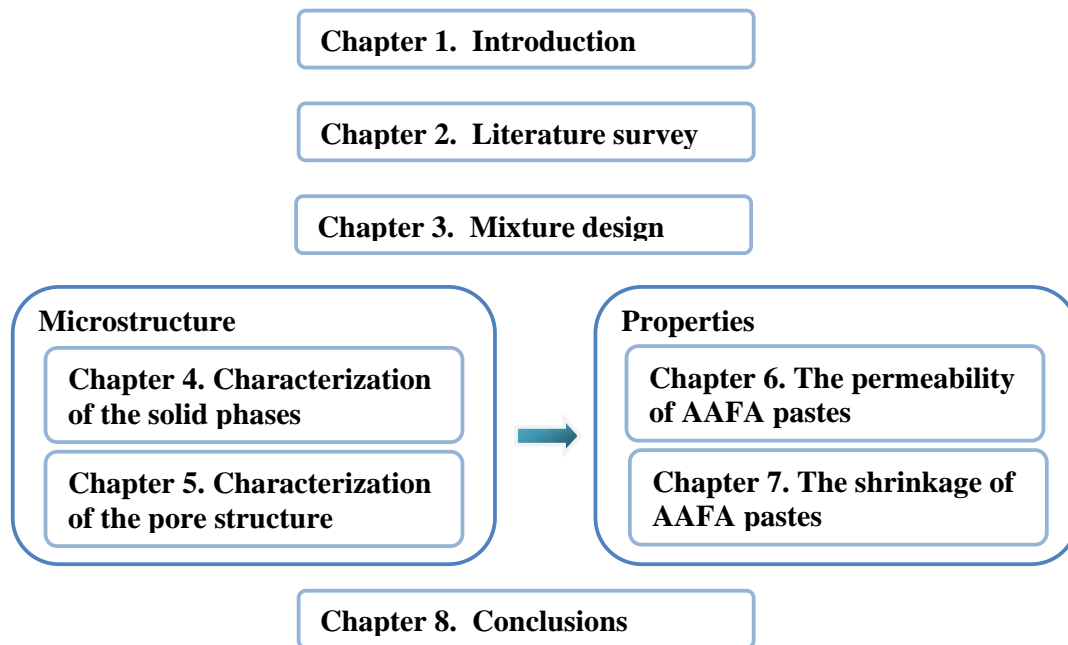


*Figure 1.1 Outline of the thesis*

## **Chapter 2**

# **Literature Survey**

---

### **2.1 Introduction**

This chapter provides a brief overview of the most important aspects of the alkali activated fly ash (AAFA) technology. First, the environmental benefit of the application of alkali activated fly ash is discussed. Second, a general introduction of AAFA of reaction mechanisms, microstructure formation, engineering properties and potential application fields is given. In the third part, the technological and engineering challenges for the broad utilization of AAFA in the construction industry are discussed. The factors that affect the engineering properties of AAFA are reviewed. Durability and shrinkage related issues of AAFA are emphasized. Finally, concluding remarks are made.

### **2.2 Sustainable development and Portland cement**

According to the Brundtland Report released by the United Nations in 1987, sustainable development is defined as “development that meets the needs of the present without compromising the ability of future generations to meet their own needs”. For the civil engineering community, the concept of sustainable development involves the use of high-performance materials produced at a reasonable cost and with the lowest possible environmental impact [Bilodeau and Malhotra, 2000].

Portland cement concrete is the most commonly used construction material worldwide, with more than 1 m<sup>3</sup> of concrete produced annually for every human being on the planet [Huntzinger and Eatmon, 2009]. Concrete is thus the second most used commodity in the world, only behind water [Aïtcin, 2000]. However, the production of cement, an essential ingredient of concrete, releases a significant amount of CO<sub>2</sub> and other greenhouse gases in the atmosphere. It has been reported that approximately one ton of CO<sub>2</sub> is liberated by the calcinations of limestone and the combustion of fuels to manufacture one ton of cement clinker [Van Oss and Padovani, 2003]. Due to the increasing construction needs, in particular from developing countries, the manufacture of cement keeps on increasing in recent years [Taylor et al., 2006]. For example, based on the United States Geological Survey (USGC) Mineral Program Cement Report (2012), the cement production in the world increased from 2.3 billion tons in 2005 to around 3.3 billion tons in 2010. China accounts for more than half of



the world's total cement capacity, with around 1.1 billion tons in 2005, 1.8 billion tons in 2010 and 2.1 billion tons in 2011. The enormous production of cement makes the cement industry one of the main sources of greenhouse gas (5-8 % of CO<sub>2</sub> emissions globally [Scrivener and Kirkpatrick, 2008]), leading to a huge impact on the environment and also on sustainable development. The construction industry has recognized these issues and looks for ways to reduce the CO<sub>2</sub> emissions.

### **2.3 Cement blended with fly ash**

One way to implement sustainable development in the cement industry is to partially substitute cement with industrial by-products, such as fly ash. The replacement of fly ash contributes to a lower CO<sub>2</sub> emission by reducing the cement content [Bilodeau and Malhotra, 2000], which is environment friendly. It has been widely reported that up to 30 % by mass of cement can be replaced by fly ash [Feldman et al., 1990; Lam et al., 2000; Mehta and Gjorv, 1982]. Nowadays, the European standard EN197 (2000) allows even a higher fly ash content, up to 55 %. Meanwhile, the reuse of fly ash (industrial waste material) would reduce the storage and transportation cost for the fly ash producers, which is also environment-friendly [Ahmaruzzaman, 2010].

Fly ash has pozzolanic characteristics. It can react with calcium hydroxide and form binding compounds, i.e. calcium silicate hydrate (C-S-H). The application of fly ash as a pozzolanic ingredient can be traced back to 1914, while the earliest noteworthy study of its use was in 1937 [Davis et al., 1937]. The pozzolanic property of fly ash greatly improves the strength development and densification of the cement matrix at later ages, resulting in a durable structure. In the meantime, the spherical shape of fly ash particles can also improve the workability of concrete mixtures while reducing water demand [Applications and Association, 1995].

### **2.4 Alkali activated fly ash (AAFA)**

#### **2.4.1 General introduction of AAFA**

In recent years, a new application of fly ash as construction material by the alkali activation technology has been widely reported [Davidovits, 1989; Duxson et al., 2007a; Palomo et al., 1999]. In this system, fly ash can substitute cement by 100 %, which would greatly reduce greenhouse gas emissions [Davidovits, 2002]. The CO<sub>2</sub> reduction is mainly due to the avoidance of the high-temperature calcinations step of limestone and fuel. Duxson et al. [2007b] reported that alkali activated binders can in general deliver an 80 % or larger reduction in CO<sub>2</sub> emission compared to ordinary Portland cement (OPC). In addition, AAFA concretes have two further environmental benefits, i.e. lower water demand (due to the spherical shape of fly ash particles) and no need for superplasticising chemical additives [Hardjito and Rangan, 2005]. As a result, alkali activated fly ash is a competitive construction material with great potential for sustainable development.

Alkali activated fly ash is also named “geopolymers”, “inorganic polymers”, “alkali-bounded-ceramics” or “soil cement”. However, in all cases alkali-activation is

essentially involved. Activation of fly ash is achieved by the addition of aqueous alkali hydroxide or alkali silicate solutions. Normally elevated temperature curing (e.g. 40 °C, 60 °C or 80 °C) is needed in the early age. The framework of the reaction product of AAFA (aluminosilicate gel) is a highly connected three-dimensional network of aluminate ( $\text{AlO}_4$ ) and silicate tetrahedral ( $\text{SiO}_4$ ), with the negative charge balanced by the alkali metal cations [Provis and Van Deventer, 2009]. According to the number of silicon atoms replaced by aluminium, the polymeric forms of -Si-O-Al- can be classified into polysialate (PS), polysialate-siloxo (PSS) and polysialate-disiloxo (PSDS), as shown in Figure 2.1a [Davidovits, 1999]. An example of the chemical structure of the aluminosilicate gel network is given in Figure 2.1b. However, it has also been stated that such descriptions (only based on integer Si/Al ratios) cannot adequately represent the full range of possible structures of AAFA binder [Provis et al., 2005]. Thus, aluminosilicate gel is used in general to describe the reaction product of AAFA.

It is important to note that the use of fly ash as the source material for alkali activation is different from its utilization as supplementary material in cement, as the major products in the process of alkali activation is an amorphous aluminosilicate material [Palomo, Grutzeck et al., 1999; Van Jaarsveld et al., 2002], while the calcium silicate hydrate is formed in fly ash blended cement. The hardened aluminosilicate gel provides most of the strength just like the role of C-S-H gel in Portland cement hydrates.

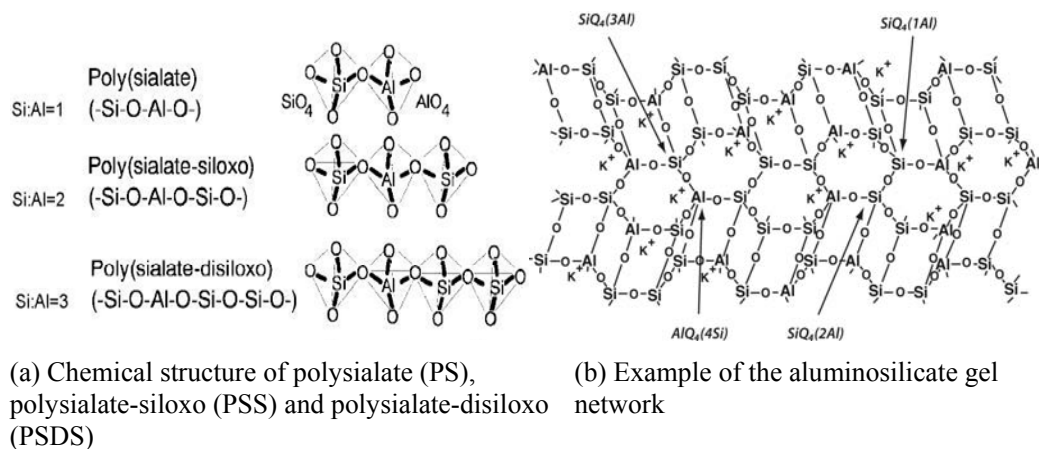


Figure 2.1 Chemical structure of aluminosilicate gel [Davidovits, 1999]

The alkali activated fly ash is one type of alkali activated materials (AAM). In general, alkali activated materials can be classified into two categories based on their components of the reaction products:

- Those based on silicon and calcium composition (e.g. blast furnace slag), with C-S-H as the main reaction products;
- Those based on silicon and aluminum composition (e.g. metakaolin and fly ash), with tetrahedral aluminosilicate gel as the main products [Palomo et al., 2004].

The research on the first category (alkali activated slag) can be traced back to the early 20th century [Kühl, 1908; Purdon, 1940]. After that, extensive research work was carried out by the team of Glukhovsky [Glukhovsky, 1959; Glukhovsky et al., 1980; Glukhovsky, 1994] and alkali activated slag was applied in construction of buildings, railway sleepers pre-cast slabs and blocks et al. in the former Soviet Union. The research on the alkali activated metakaolin and fly ash became popular mainly due to the work of Davidovits in the late 1970s, who named it “geopolymer”. Metakaolin was first used in “geopolymer” synthesis by Davidovits with the aim to develop a fire-resistant alternative to organic thermosetting polymers. Early “metakaoline based geopolymer” displayed high early compressive strength (60 MPa after one day), as well as super thermal stability up to 1000-1200 °C, where all organic resins or cement failed to perform [Davidovits, 1989; Davidovits, 1999]. Such findings indicate that it can be potentially used for ceramic, refractory lining materials, as well as building materials. The reaction products of alkali activated metakaolin and fly ash are similar, a three-dimensional aluminosilicate network (aluminosilicate gel). Compared to fly ash, metakaolin is a much purer aluminosilicate resource for alkali activation, with higher reactivity. However, as the interest of geopolymer application shifted to construction materials, fly ash appeared to be a more economic and environment friendly raw material than metakaolin, while the use of metakaolin is limited mainly because of the high water demand and low workability [Provis and Van Deventer, 2009].

#### 2.4.2 Reaction mechanism and reaction products of AAFA

Glukhovsky [1967] proposed a general model for the activation mechanism of alkali activated aluminosilicate materials. This reaction model divides the reaction process into three main steps: (a) destruction-coagulation, (b) coagulation-condensation and (c) condensation-crystallization. Recently, extensive work on alkali activated material has been carried out by two research groups of Prof. Jannie van Deventer and Prof. Angel Palomo, respectively. They have developed and expanded Glukhovsky’s theory and applied the existing knowledge of zeolite synthesis to explain the formation of products in alkali activated aluminosilicate in more detail [Provis and Van Deventer, 2009].

According to the description of Duxson et al. [2007a], initially, the contact between the solid particles and the alkaline solution causes the vitreous/amorphous component (Si-O-Al and Si-O-Si bonds) of these particles to dissolve:



The degree of silicon hydroxylation may rise to more than two or three unites, forming intermediate complexes that decompose into silicic acid  $\text{Si}(\text{OH})_4$  (silicate monomer) [Glukhovsky, 1967]. The hydroxyl groups affect the Si-O-Al bond in the same way, forming  $\text{Al}(\text{OH})_4^-$  (aluminate monomer). These monomers inter-react to form dimers, which in turn react with other monomers to form trimers, tetramers and so on:

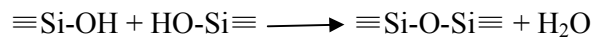


Table 2.1 shows some examples of the chemical structure of silicate species in solutions. Aluminate monomer also participates in these reactions, substituting for silicate tetrahedral, forming new Si-O-Al bonds [Glukhovskiy, 1967].

Table 2.1 Chemical structure of some silicate species in solutions

Silicate species	Monomer	Dimer	Linear trimer
Chemical structure	$\begin{array}{c} \text{OH} \\   \\ \text{HO-Si-OH} \\   \\ \text{OH} \end{array}$	$\begin{array}{c} \text{OH} \quad \text{OH} \\   \quad   \\ \text{HO-Si-O-Si-OH} \\   \quad   \\ \text{OH} \quad \text{OH} \end{array}$	$\begin{array}{c} \text{OH} \quad \text{OH} \quad \text{OH} \\   \quad   \quad   \\ \text{HO-Si-O-Si-O-Si-OH} \\   \quad   \quad   \\ \text{OH} \quad \text{OH} \quad \text{OH} \end{array}$

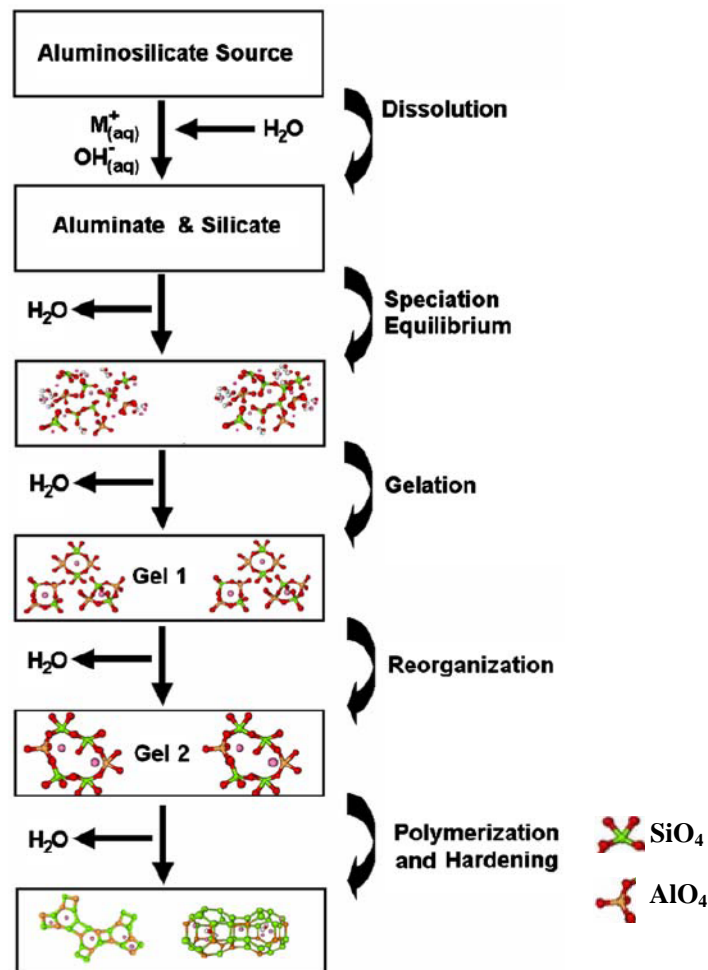


Figure 2.2 Conceptual reaction model of AAFA [Duxson, Fernández-Jiménez et al., 2007a]

When the solution saturates, aluminosilicate gel forms (gelation). It is suggested [Duxson, Fernández-Jiménez et al., 2007a] that water, normally consumed during the dissolution process, is released during the gelation process. Thus water plays the role of a reaction medium and resides in pores in the gel. The system continues to rearrange and the connectivity of the gel network increases, resulting in the presence of multiple gel stages (Gel 1 and Gel 2, see Figure 2.2). In the NaOH activated fly ash system, Fernández-Jiménez and Palomo [2005a] identified two stages of gel evolution: initially a meta-stable aluminum-rich gel (denominated Gel 1), which is formed mainly due to the higher  $\text{Al}^{3+}$  ion content in the alkaline medium in the early stages (reactive aluminum dissolves more rapidly than silicon), and a more stable silica-rich gel (Gel 2), which forms as more Si-O groups in the initial solid source dissolve, increasing the silicon concentration in the medium. The system undergoes further rearrangement and polymerization (also known as growth), when the nuclei reach a critical size and the crystals begin to grow.

The reaction product of alkali activation reaction is often described as “X-ray amorphous” [Alonso and Palomo, 2001]. However, many authors claimed that the reaction products are actually semi-crystalline or polycrystalline, particularly when a relatively high temperature is applied [Provis, Lukey et al., 2005; Van Jaarsveld and Van Deventer, 1999a]. Under certain conditions (discussed in Section 2.5), alkali activation results in the formation of zeolites, which also consist of polymeric -Si-O-Al- framework, similar to AAFA. The main difference with AAFA is that zeolites are crystalline instead of “X-ray amorphous” [Alonso and Palomo, 2001]. Provis et al. [2009] compared the systems of alkali activated fly ash/metakaolin with zeolite systems and concluded that the binder phase formed in the alkali reaction comprises agglomerates of nanocrystalline zeolites compacted by an amorphous gel phase. In other words, the reaction products include both gel and zeolitic phases. Under certain conditions (discussed in Section 2.5), the aluminosilicate gel is likely to convert to some zeolites (grey arrow as shown in Figure 2.3) [Duxson, Provis et al., 2007b]. It is, therefore, stated that the aluminosilicate gel is also considered as “zeolite precursor” [Palomo, Grutzeck et al., 1999].

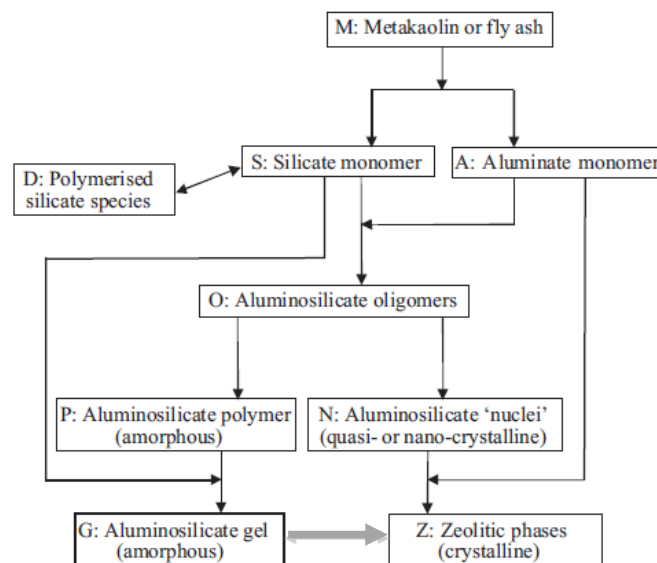


Figure 2.3 The reaction model of AAFA [Provis and van Deventer, 2007]

### 2.4.3 The microstructure model of AAFA

The microstructure development of the alkali activated fly ash is shown in Figure 2.4 [2005c]. Fernández-Jiménez et al. [2005c] discovered that the primary reaction product resulting from the alkali activation is a sodium silicate gel and forming a cementitious matrix [Fernández-Jiménez, Palomo et al., 2005c]. Figure 2.4(a) shows the scanning electron microscope (SEM) image of un-reacted fly ash. After the alkali activation by NaOH for 20 hours (at 85 °C), a few small fly ash particles, which have reacted with the alkali solution (NaOH), were observed to co-exist with some remaining unreacted spheres and even with particles partially covered with reaction products (Figure 2.4 (b)). On the other hand, for the paste activated with sodium silicate solution, they observed a very uniform and scantily porous microstructure, with only a few unreacted fly ash particles present (Figure 2.4 (c)).

Based on the SEM observations, the authors [Fernández-Jiménez, Palomo et al., 2005c] proposed a descriptive model to explain the reaction process during alkali hydroxide activation of fly ash (Figure 2.5). According to their description, the initial chemical attack starts at the surface of a partially hollow spherical fly ash particle with other smaller ashes inside (Figure 2.5 (a)). Reaction product is generated both inside and outside the particle (Figure 2.5 (b)) until the ash is completely or almost consumed (Figure 2.5 (c)). Dissolution is the main mechanism involved in this process. At the same time, as the alkali solution also reacts with the smaller ash particles inside the bigger particles, the interior of the partially hollow spherical particle becomes filled with reaction product, forming a dense matrix. As the reaction products precipitate at the outer surface of the fly ash particles, the layer of products prevents the contact of further dissolution of the fly ash particle (Figure 2.5 (e)), reducing the reaction rate. In this case the reaction is governed by a diffusion mechanism. The processes vary locally from one point in the matrix to another, mainly depending on the distribution of particle size and the local chemistry (e.g. pH, reactivity of fly ash particle). Finally, it results in a microstructure containing several phases and morphologies: unreacted particles, particles attacked by alkali solution but still maintain their spherical shape and reaction products (Figure 2.5 (d)).

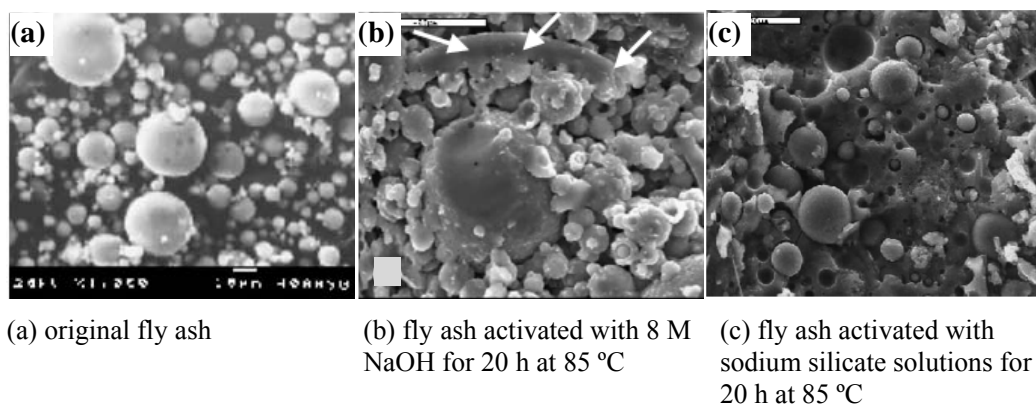


Figure 2.4 SEM pictures of fly ash and AAFA [Fernández-Jiménez, Palomo et al., 2005c]

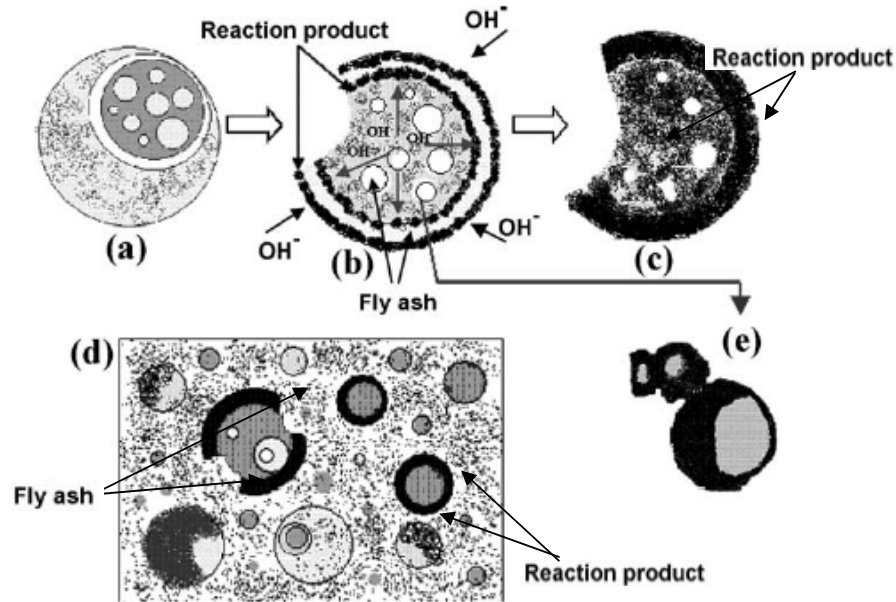


Figure 2.5 Microstructure description of the formation of alkali activated fly ash [Fernández-Jiménez, Palomo et al., 2005c]

#### 2.4.4 The engineering properties and applications of AAFA

Given a proper mix proportion and curing condition, the general engineering properties of alkali activated fly ash-based mixtures can be almost equal or even superior to Portland cement-based mixtures [Duxson, Provis et al., 2007b]. Elevated temperature curing is normally applied on AAFA synthesis in order to achieve relatively high early age strength. Fernández-Jiménez and Palomo [2005b] reported that the compressive strength for some AAFA paste samples can reach as high as 90 MPa after only 20 hours cured at 85 °C. Hardjito and Rangan [2005] obtained a mixture of AAFA concrete that can achieve more than 60 MPa in compression after only 1 day curing at 60 °C. Another advantage of heat curing at early age is the very low drying shrinkage (< 200 micro-strain) and low creep of AAFA concrete [Hardjito et al., 2004]. Moreover, AAFA samples were observed to exhibit higher resistance to chemical attack compared to Portland cement samples. Many investigations [Bakharev, 2005b; Fernández-Jiménez, Garcia-Lodeiro et al., 2007; Hardjito and Rangan, 2005] indicated that no significant differences were observed in the gel composition and microstructure of the alkali activated fly ash samples (paste/mortar/concrete) after contact to sulfate solutions. The good resistance to sulfate of AAFA is mainly due to the absence of ettringite in AAFA systems (with low-calcium content), while in Portland cement, the formation of ettringite (expansive) leads to cracking [Provis and Van Deventer, 2009]. In addition, the resistance of alkali activated fly ash to acid, such as nitric acid, sulphuric acid or hydrochloric acid, was also claimed to be far better than that of Portland cement [Allahverdi and Skvara, 2001a; Allahverdi and Skvara, 2001b; Allahverdi and Skvara, 2005; Bakharev, 2005b]. Additionally, these materials exhibit very good thermal resistance, with very

little structural damage at temperatures up to 600 °C in many instances [Fernández-Jiménez et al., 2008; Krivenko and Kovalchuk, 2002; Škvára et al., 2005].

These advantages open the way to many application fields of AAFA as an alternative to Portland cement. Nowadays, these materials have been reported in the manufacture of many precast products, such as railroad sleepers, precast box culverts, sewer pipes and fire and chemically resistant wall panels (as shown in Figure 2.6) [Cheema et al., 2009; Gourley and Johnson, 2005; Lloyd and Rangan, 2010]. Test results have shown that these AAFA products performed well and met the requirements of such products. Moreover, the excellent resistance to chemical attack makes these materials very promising for the use in aggressive environments, such as mining, manufacturing industries and sewer systems [Lloyd and Rangan, 2010]. Other applications of alkali activated fly ash include the immobilization of nuclear waste and toxic wastes [Van Jaarsveld et al., 1997; 1999b]. This is mainly due to the similar nature of aluminosilicate gel and zeolitic materials that are known to strongly bind the radioactive or toxic wastes chemically into the matrix. [Provis and Van Deventer, 2009].



Figure 2.6 Applications of alkali activated fly ash: (a) box culverts [Lloyd and Rangan, 2010]; (b) sewer pipes [Gourley and Johnson, 2005].

## 2.5 Factors affecting the properties of AAFA

Though activated fly ash has a great potential for the development of environment friendly construction materials, challenges still exist in the technological and engineering aspects for a broader utilization of this material. Since AAFA is made from ashes with variable sources, the ability to produce AAFA products with good and consistent performance is always the main focus for the industry [Duxson, Provis et al., 2007b]. A well-developed raw material characterization, tailored mix design and processing procedure (curing condition) are critical for achieving a good quality product. It, therefore, requires sufficient knowledge and understanding of the reaction of alkali activation, specifically, of the parameters that may affect the chemistry and the properties of AAFA.



### 2.5.1 Raw materials (Fly ash)

Fly ash is generated during the combustion of coal for energy production. It consists of fine particles, predominantly spherical in shape, either solid or hollow, and contains glassy (amorphous) and crystalline constituents in nature, e.g. quartz ( $\text{SiO}_2$ ) and mullite ( $3\text{Al}_2\text{O}_3 \cdot 2\text{SiO}_2$ ). Fly ashes with low calcium content (Class F according to ASTM C618) are mostly used to produce AAFA samples. Investigations on the alkali activation of high calcium ashes (Class C) are limited, possibly due to the rapid setting and low workability of the binders made by these ashes. The active portion of fly ash consists of silica and alumina.

Fly ash, considered as an industrial byproduct, reflects the scatter in the starting material. The particle size, chemical composition, as well as the reactivity varies significantly from different sources. Even different batches of ash from the same source may differ. Thus the ability to understand and control the AAFA products with consistent and repeatable properties is always the primary focus for researchers and producers. Duxson and Provis [2008] compared the ash composition and strength data obtained from various investigations, attempting to find a trend for the raw material composition that is suitable for AAFA synthesis. In this study, the mass content of  $\text{SiO}_2$ ,  $\text{Al}_2\text{O}_3$  and the total amount of alkali and alkaline earth metal oxides (e.g.  $\text{Na}_2\text{O}$ ,  $\text{K}_2\text{O}$  and  $\text{CaO}$ ) in fly ash were used to form a pseudo-ternary diagram, as shown in Figure 2.7. It is found from the figure that ashes with low alkali and alkali earth oxide content tend to produce poor reaction products (lower strength). High-strength samples are normally obtained with ashes of high alumina content (Figure 2.7).

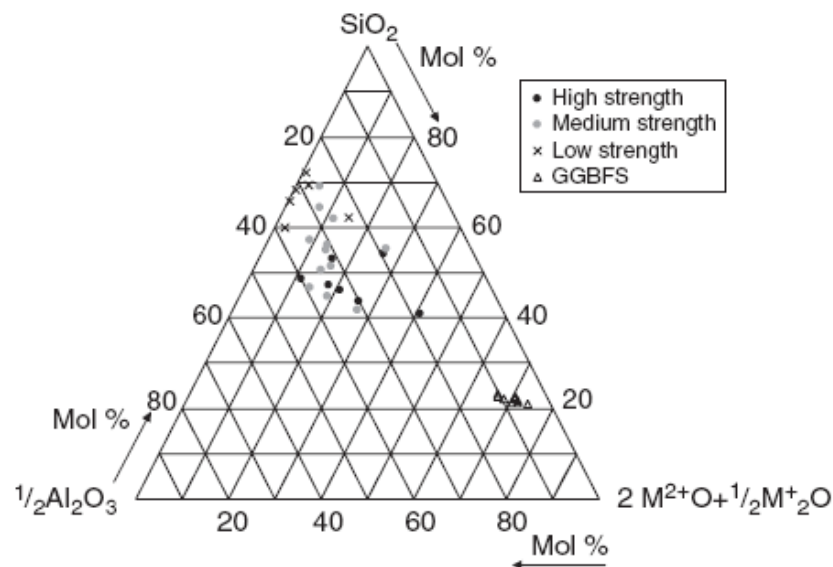


Figure 2.7 Pseudo-ternary composition diagram for fly ashes [Duxson and Provis, 2008]

Fernández-Jiménez and Palomo [2003] characterized five different fly ashes both from the physical and chemical point of view in order to determine their suitability for being alkali activated. The results revealed that the fly ash with unburned material content lower than 5 %,  $\text{Fe}_2\text{O}_3$  content lower than 10 %, high reactive silica content, high vitreous phase and a finer particle size distribution was suitable for alkali activation. According to their later study [Fernández-Jiménez et al., 2006d], they found that fly ash with higher reactive aluminum content (22.46 %) resulted in a much higher degree of reaction and compressive strength than fly ash with a lower reactive aluminum content (12.6 %). Thus, the availability of aluminum is an important factor for the properties of AAFA.

### 2.5.2 Activator

Due to the low reactivity of fly ash, strong alkali solutions are required to initiate the reaction. The commonly used alkali solutions for alkali activation are  $\text{NaOH}$ ,  $\text{Na}_2\text{SiO}_3$ ,  $\text{KOH}$  and  $\text{K}_2\text{SiO}_3$ . In some cases,  $\text{Na}_2\text{CO}_3$  and  $\text{K}_2\text{CO}_3$  are also used as activator. Fernández-Jiménez et al. [2006a] reported that the use of mixed hydroxide carbonate activating solutions showed a poorly reacted, porous product. It is claimed that the alkalinity of carbonate solution is not high enough to dissolve fly ash particles for the reaction. Thus, the carbonate activating solutions will be excluded in the following discussion.

#### *Sodium hydroxide solution (NaOH)*

Sodium hydroxide solution is usually used to mix with solid fly ash.  $\text{NaOH}$  solution is normally prepared in advance to avoid the high heat release associated with  $\text{NaOH}$  dissolution. With the help of attenuated total reflectance - fourier transform infrared spectroscopy (ATR-FTIR), Rees et al. [2007a] observed that an induction period existed when fly ash is activated by sodium hydroxide. As shown in Figure 2.8, the intensity of the “main band” that is attributed to the aluminosilicate gel network structure became stronger after 42.5 hours (arrowed in Figure 2.8) in contact with alkali solution. According to the same authors the induction period is determined by the time taken to form stable “gel nuclei”, around which the aluminosilicate gel grows. The nucleation sites were likely to be provided by the surfaces of solid particles. By seeding with high surface-area nanoparticles, the induction period disappeared [Rees et al., 2008].

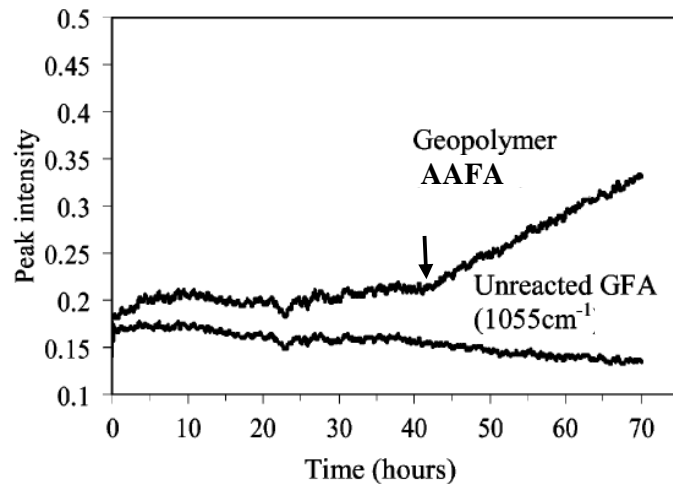


Figure 2.8 Functional group (T-O band, T=Si or Al) analysis of AAFA sample activated with 6M NaOH, derived from ATR-FTIR tests: the functional group that is attributed to the gel network became stronger after 42.5 hours [Rees, Provis et al., 2007a]

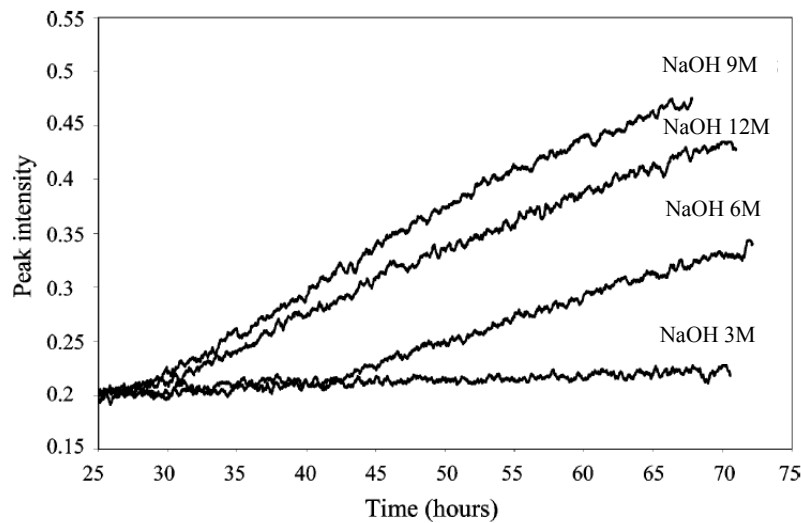


Figure 2.9 Functional group (T-O band, T=Si or Al) analysis for AAFA samples activated with different concentrations of sodium hydroxide (M: mol), derived from ATR-FTIR tests: sample with different NaOH concentrations shows different induction period [Rees, Provis et al., 2007a]

The effect of the sodium hydroxide concentration on the aluminosilicate gel growth was also examined by Rees et al. [2007a] with the help of ATR-FTIR. The results (Figure 2.9) showed that samples activated with the lowest NaOH concentration (3M, where M is mol) gave the longest induction period; the rate of gel formation increased with higher NaOH concentration, until a maximum was reached (9M), after which the rate was reduced by additional NaOH (12M). Similar findings were also reported by Alonso and Palomo [2001] when metakaolin was used as raw material for alkali

activation. By measuring the heat evolution of samples with different NaOH concentration, they observed a lower reaction rate when the sodium hydroxide concentration increased above 10 M. It is concluded that the increase of sodium hydroxide content speed up the dissolution of solid fly ash particles; however, the rate of the network formation was not always increased when more sodium hydroxide was added [Alonso and Palomo, 2001]. Thus an optimal concentration of NaOH exists for AAFA synthesis.

The use of sodium hydroxide for the alkali activation results in the formation of zeolitic structures, e.g. hydrated sodalite (also known as hydroxysodalite ( $\text{Na}_4\text{Al}_3\text{Si}_3\text{O}_{12}\text{OH}$ )), Na-chabazite (also known as herschelite ( $\text{NaAlSi}_2\text{O}_6 \cdot 3\text{H}_2\text{O}$ )) and faujasite [Fernández-Jiménez and Palomo, 2005b]. Crystalline zeolites develop more quickly at higher temperature and higher water contents. Criado et al. [2007b] observed that the amount of hydrated sodalite ( $\text{Na}_4\text{Al}_3\text{Si}_3\text{O}_{12}\text{OH}$ ) remained unchanged through all the time, while the Na-chabazite ( $\text{NaAlSi}_2\text{O}_6 \cdot 3\text{H}_2\text{O}$ ) content increased with prolonged curing age. It is still not clear whether the crystallization will lead to strength decrease. Some studies on the alkali activated metakaolin [De Silva and Sagoe-Crenstil, 2008; Provis and Van Deventer, 2009] showed a strength drop with the formation of zeolites. In the alkali activated fly ash system, Criado et al. [2007b] suggested that a higher content of zeolites in AAFA prevented the strength development, while in the accelerated ageing test (aged at 95 °C in sealed condition) of AAFA, Lloyd et al. [2009] revealed that zeolite formation was actually beneficial to the strength.

### *Sodium silicate solution*

The gel structures formed through silicate activation and hydroxide activation of fly ash are rather similar. However, compared to sodium hydroxide solution, the application of sodium silicate solution as activator is known to lead to higher strength and more homogeneous microstructure in the early age. For example, Palomo et al. [1999] found that after 24 h cured at 85 °C, fly ash activated with NaOH (8-12 M) produced a material with compressive strength around 35-40 MPa, while up to 90 MPa was obtained when sodium silicate solution was used as activator. Criado et al. [2007b] observed that the increase of silica content resulted in a higher compressive strength only after a short curing time (8 h) at 85 °C. The application of sodium silicate solution also affects the microstructure of AAFA. Fernández-Jiménez et al. [2005c] and Rees et al. [2007b] both observed that an increase of silicate concentration in the activating solution reduced the number of large interconnected pores, and increased the size and density of the gel particulates, resulting in a denser and more homogenous microstructure.

The  $\text{SiO}_2/\text{Na}_2\text{O}$  ratio is reported to significantly influence the performance of the AAFA [Criado, Fernandez-Jimenez et al., 2007b; Škvára, Jílek et al., 2005]. Table 2.2 lists detailed information of the fly ash, activator, curing condition and optimal content of activator derived from recent studies on AAFA [Bakharev, 2005a; Criado, Fernandez-Jimenez et al., 2007b; Fernández-Jiménez and Palomo, 2005b; Škvára, Jílek et al., 2005].

Table 2.2 Detail information of AAFA in previous studies

	Fly ash chemical composition		Activating solution		Curing condition	Optimal activator content
1 Bakharev [2005a]	SiO <sub>2</sub> (%)	50.0	SiO <sub>2</sub> (%) <sup>a</sup>		75°C till 28 D	Na <sub>2</sub> O content 8 %
	Al <sub>2</sub> O <sub>3</sub> (%)	28.0	Na <sub>2</sub> O(%) <sup>a</sup>	2.0~8.0		
	Reactive SiO <sub>2</sub> (%)		SiO <sub>2</sub> /Na <sub>2</sub> O	constant at 2.02		
	Reactive Al <sub>2</sub> O <sub>3</sub> (%)		water/FA	0.30		
2 Fernández-Jiménez and Palomo [2005b]	SiO <sub>2</sub> (%)	53.1	SiO <sub>2</sub> (%) <sup>a</sup>	0~9.52	85°C for 20 h	SiO <sub>2</sub> /Na <sub>2</sub> O = 0.118 and 1.23, with different sol./FA ratio
	Al <sub>2</sub> O <sub>3</sub> (%)	24.8	Na <sub>2</sub> O(%) <sup>a</sup>	5.55~14.90		
	Reactive SiO <sub>2</sub> (%)	50.4	SiO <sub>2</sub> /Na <sub>2</sub> O	0.037~1.28		
	Reactive Al <sub>2</sub> O <sub>3</sub> (%)		Sol./FA <sup>c</sup>	0.35/0.40		
3 Škvára et. al [2005]	SiO <sub>2</sub> (%)	51.9	SiO <sub>2</sub> (%) <sup>a</sup>		80°C for 12 h	SiO <sub>2</sub> /Na <sub>2</sub> O = 1.1 and Na <sub>2</sub> O content 7.5 %
	Al <sub>2</sub> O <sub>3</sub> (%)	32.8	Na <sub>2</sub> O(%) <sup>a</sup>	5.0~9.0		
	Reactive SiO <sub>2</sub> (%)		SiO <sub>2</sub> /Na <sub>2</sub> O	0.9~1.9		
	Reactive Al <sub>2</sub> O <sub>3</sub> (%)		Sol./FA	0.30		
4 Criado et. al [2007b]	SiO <sub>2</sub> (%)	53.1	SiO <sub>2</sub> (%) <sup>b</sup>	0~9.07	85°C till 180 D	SiO <sub>2</sub> /Na <sub>2</sub> O = 0.69
	Al <sub>2</sub> O <sub>3</sub> (%)	24.8	Na <sub>2</sub> O(%) <sup>b</sup>	around 8		
	Reactive SiO <sub>2</sub> (%)	50.4	SiO <sub>2</sub> /Na <sub>2</sub> O	0.19~1.17		
	Reactive Al <sub>2</sub> O <sub>3</sub> (%)		Sol./FA	0.40		

<sup>a</sup> weight ratio with respect to fly ash content.

<sup>b</sup> weight ratio with respect to activator content.

<sup>c</sup> “solution/fly ash” ratio (in weight)

As can be seen in Table 2.2, the optimal SiO<sub>2</sub>/Na<sub>2</sub>O ratio reported their studies vary significantly, mainly depending on the nature of the raw material and probably the curing conditions. It, therefore, requires an in-depth analysis of the reaction kinetics, as well as the chemical and physical structure of the reaction product to better understand the effect of SiO<sub>2</sub> and Na<sub>2</sub>O in the activator. Extensive work was performed by Criado et al. [2007a] to examine the chemical structure of aluminosilicate gel by using sodium silicate solutions with different SiO<sub>2</sub>/Na<sub>2</sub>O ratios (0, 0.19, 0.69 and 1.17, mainly different in SiO<sub>2</sub> content). The results obtained from infrared spectroscopy (FTIR) indicated that in the absence of soluble silica, the aluminum content in the resulting gel was high (Al-rich gel). The addition of a small amount of monomeric soluble silica (SiO<sub>2</sub>/Na<sub>2</sub>O = 0.19) accelerated the reaction, but the reaction product was still an Al-rich gel. When more silicate was present (SiO<sub>2</sub>/Na<sub>2</sub>O = 0.69 and 1.17), the reaction kinetics was modified, with the formation of more Si-rich gels. According to Fernández-Jiménez et al. [Fernández-Jiménez, Palomo et al., 2006d], the Si-rich gel is of higher mechanical strength than the Al-rich gel. The <sup>29</sup>Si MAS-NMR results [Criado et al., 2008] revealed that the silica speciation in the activating solutions was decisive for the kinetics and structure of the gel. Sodium silicate solutions with more monomers and dimers in the system (SiO<sub>2</sub>/Na<sub>2</sub>O = 0.19) shorten the time needed to initiate the gel-formation reaction,

while silicate solution with cyclic silicate trimers ( $\text{SiO}_2/\text{Na}_2\text{O} = 0.69$  and  $1.17$ ) gave rise to initially more stable gels that retarded the subsequent reaction of the ash. Similar results were also reported by Rees et al. [2007b]. They revealed that an Al-rich gel formed initially when the silica concentration varied from 0 to 1.2 M. Further increasing the amount of monomeric silicates led to a rapid attainment of steady gel composition without first forming an Al-rich gel. A minimum silicate monomer concentration of approximately 0.6 M is required to shift the reaction mechanism from hydroxide activation to silicate activation. Criado et al. [2008] further suggested that the addition of silica affected the intermediate stages of the reaction (chemical bonding of Si and Al) but not the end results: there seems to be a threshold value of the Si/Al ratio of the final products (at around 2), regardless of the initial conditions.

The apparent structural stability of aluminosilicate gel is known to increase with the addition of soluble silica to the activating solution [Duxson, Fernández-Jiménez et al., 2007a; Palomo, Alonso et al., 2004]. In other words, the presence of dissolved silica suppressed the formation of zeolites. It was reported by Criado et al. [2007b] that when the silica content was 5.4 % (weight ratio with respect to activating solution), the appearance of zeolites was only visible after 28 days heat curing at 85 °C; and no zeolites were observed when the silica content increased to 9.07 %. Similar results were also reported by Rees et al. [2007b] that no zeolites were detected in samples with 3.5-4.9 M  $\text{SiO}_2$  in activating solution. The addition of soluble silica to the activating solutions was regarded to substantially reduce the level of long-range structural ordering, but does not fundamentally change the reaction mechanism [Duxson, Fernández-Jiménez et al., 2007a]. Besides the silica content, the alkali content was also reported to have a significant impact on zeolites crystallization. By performing a series of accelerated aging tests with alkali activated fly ash samples (cured at 95 °C), Lloyd [Provis and Van Deventer, 2009] observed that different types of zeolites formed and their amount increased when the  $\text{Na}_2\text{O}$  content varied from 7 % to 15 % by weight.

### ***Potassium hydroxide and silicate***

Fly ash activated with potassium-based activators (KOH or  $\text{K}_2\text{SiO}_3$ ) has been much less intensively studied than Na-based activators. One of the reasons is the considerably higher price of potassium. Further, Fernández-Jiménez et al. [2006a] reported that KOH led to a lower extent of reaction of AAFA than NaOH. It indicates that  $\text{K}^+$  cations favor the association with large silicate oligomers while  $\text{Na}^+$  cations are prone to associate with monomeric silicate anions [McCormick and Bell, 1989], according to the ion size difference. Thus, Na-based activators tend to have a greater capacity to liberate silicate and aluminate monomers than the K-based activators. This will play an increasingly significant role when higher-silicate activating solutions are used [Duxson et al., 2005; Xu and van Deventer, 2003]. In addition, potassium-activated aluminosilicate binders tend to show a lower tendency to crystallization than Na binders [Fernández-Jiménez, Palomo et al., 2006a]. Provis et al. [Provis, Lukey et al., 2005] demonstrated that Na-containing aluminosilicate binders have higher dissolution rates, and thus will have more time and freedom to form highly-ordered crystalline species. K-based binders have higher polycondensation rates, and thus display less crystallinity.

### 2.5.3 Water content

It is well known that in most cases a higher water content leads to a lower strength of AAFA [Duxson, Provis et al., 2007b]. Results obtained by Hardjito and Rangan [2005] showed that the compressive strength constantly decreased with higher water content, regardless the curing temperature (Figure 2.10). Škvára et al. [2005] examined the pore structure of AAFA pastes with different water content and found that a lower water content was associated with a finer pore size distribution and denser microstructure of the pastes. Such a trend is analogous to the effect of water in Portland cement paste, although the chemical processes involved in the formation of the microstructure are entirely different: water exists in the AAFA system mainly as free water [Duxson, Fernández-Jiménez et al., 2007a; Duxson, Provis et al., 2007b], while in Portland cement paste most of the water is chemically bonded in the C-S-H gel. It has been reported that the addition of extra water in the AAFA system decrease the pH in the activator, reducing the dissolution rate of fly ash [Duxson, Provis et al., 2007b]. Based on the reported investigations, in this study the water content was kept as low as possible (with water/fly ash mass ratio at 0.35), where a workable AAFA binder can still be guaranteed.

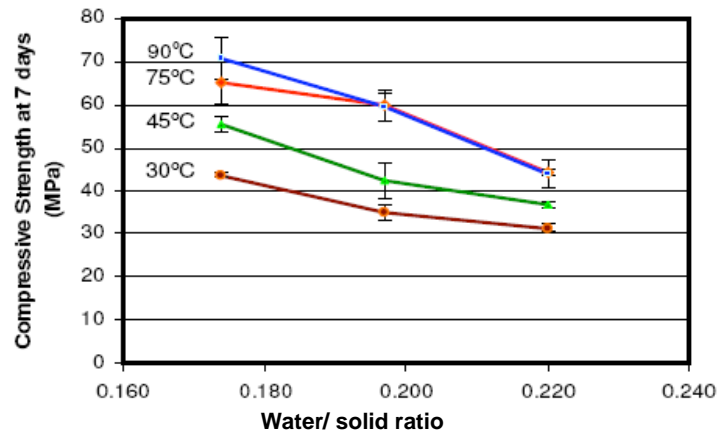


Figure 2.10 The effect of water/solid ratios on the compressive strength (7days) of AAFA concrete samples [Hardjito and Rangan, 2005]

### 2.5.4 Curing conditions

#### *Curing temperature*

While in some cases AAFA are reported to be cured successfully at environmental temperature, e.g. 23 °C [Lloyd et al., 2009c; 2009a; 2009b], elevated temperature curing is normally used for the alkali activation of fly ash get a relatively high strength at early ages. Palomo et al. [1999] demonstrated that elevated temperature is particularly important during the first 2 to 5 hours of curing when the strength increased significantly. Hardjito and Rangan [2005] compared the compressive strength of two mixes of AAFA concretes at five different curing temperatures: i.e. 30

°C, 45 °C, 60 °C , 75 °C, and 90 °C. They observed that higher curing temperature resulted in a higher compressive strength. The increase of curing temperature led to an acceleration of both the dissolution and polymerization process, thus a higher degree of reaction is achieved.

### ***Curing time***

While it is generally accepted that curing at elevated temperature is beneficial for the strength development of AAFA, results about the effect of curing time at elevated temperature are not always consistent. Hardjito and Rangan [2005] demonstrated that with longer curing time at elevated temperature (60 °C), the compressive strength of AAFA concretes increased, as shown in Figure 2.11. Similar findings were also reported by Palomo et al. [1999], who found that longer curing time under heating resulted in a higher compressive strength. On the other hand, van Jaarsveld et al. [2002] found that prolonged curing at high temperature (70-80 °C) led to a decrease of the strength. He suggested the reduction of the strength was likely due to the evaporation of pore water at elevated temperature, which led to dehydration of AAFA reaction products, and in turn caused an excessive shrinkage of the samples.

### ***Curing at sealed/unsealed condition***

Bakharev [2005a] observed a drop of strength of AAFA samples when moisture evaporation was allowed during heating. Kovalchuk et al. [2007] compared three groups of AAFA samples under different curing conditions, i.e. sealed curing, dry curing and steam curing. Results showed that sealed curing gave the highest compressive strength. Drying curing gave the lowest compressive strength. Steam curing gave an intermediate effect on strength development, somewhere between sealed curing and dry curing. Furthermore, sealed curing and steam curing prevent the AAFA samples from carbonation, while it happened when drying curing was applied, especially in the early age when most of the alkali cations did not react with fly ash [Kovalchuk, Fernandez-Jimenez et al., 2007]. It is stated that the initial carbonation reduced the pH levels in the pore solution, resulting in a lower dissolution rate of the ash and lower strength of the samples [Kovalchuk, Fernandez-Jimenez et al., 2007].

In this research, sealed curing at 40 °C is used as the curing condition in most of the experiments. Plastic bags were used to prevent water evaporation and carbonation of AAFA samples. From literature, it can be concluded that on the one hand high temperature curing is beneficial to the strength development of AAFA. On the other hand, high temperatures also cause a high possibility of moisture loss of the samples, and in turn lead to a high shrinkage.



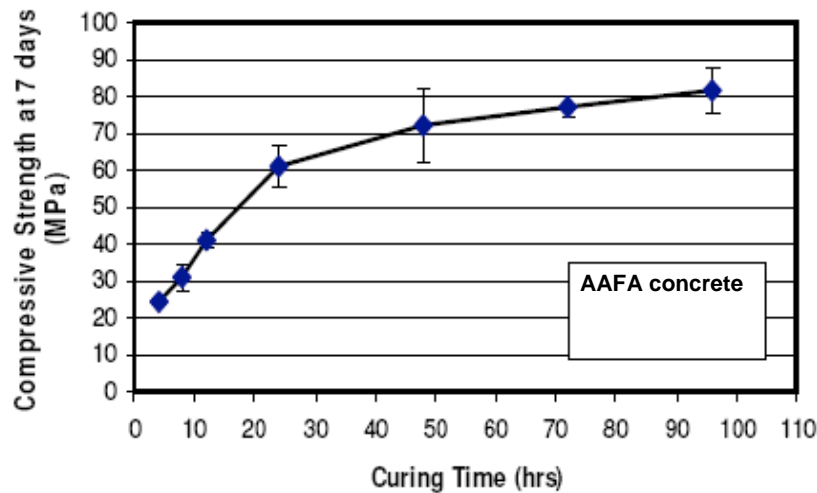


Figure 2.11 The effect of temperature (60 °C) curing time on the compressive strength (7days) of AAFA concrete samples [Hardjito and Rangan, 2005]

## 2.6 Permeability and shrinkage issues

### 2.6.1 Permeability

Although it is shown in previous studies that AAFA pastes has good durability, e.g. resistance to chemical attack, various acids, alkali and sulphate in the accelerating tests [Allahverdi and Skvara, 2001a; Allahverdi and Skvara, 2001b; Bakharev, 2005b], these results can only give indications of the expected performance, rather than definitive proof [Provis and Van Deventer, 2009]. This is mainly due to different fly ash resources utilized, as well as various recipes, mixing procedures and curing conditions used to produce AAFA (Table 2.2), leading to different microstructure and strength. For this reason, the reported results from different groups on the durability of AAFA are hard to compare. The precise evaluation and prediction of the durability of AAFA require a comprehensive understanding of the microstructure and water permeability of AAFA. Water permeability, pore structure characteristics and relevant ion transport properties are closely linked to durability issues. Water can be a carrier of aggressive ions (e.g.  $\text{Cl}^-$ ,  $\text{CO}_3^{2-}$ ,  $\text{SO}_4^{2-}$ , etc.) that can penetrate into the matrix, leading to a change of the microstructure and degradation of the material. To this end, water permeability is considered to be important for durability related issues [Nyame and Illston, 1981].

### 2.6.2 Shrinkage

Drying shrinkage of AAFA is caused by the loss of water that leads to the contraction of a material. When the deformation is restrained, cracking may happen and reduce the service life of structures. Fernández-Jiménez et al. [2006e] found that the drying shrinkage of AAFA mortars (steam curing at 85 °C for 20 h before the drying is performed) after 90 days were under 0.025 % (drying at 50 % relative humidity, at 21 °C), much lower than the shrinkage of OPC mortars of water/cement ratio 0.5 (20 h at 22 °C, 98% relative humidity before the drying tests). Wallah and Rangan [2006] compared the drying shrinkage of heat-cured (sealed at 60 °C for 24 h before drying

tests) and ambient-cured (sealed at 18-25 °C for 24 h before the drying tests) AAFA concretes (the same mixture, drying at relative humidity 40-60%, at 23 °C). The result is shown in Figure 2.12. Obviously, the drying shrinkage of AAFA is sensitive to the curing conditions. It is evident from the figure that drying shrinkage of AAFA concretes cured under ambient conditions was significantly larger than that of samples cured at elevated temperature.

As previously stated in this chapter, other reaction parameters (e.g. activator, water content) also have a significant effect on the properties of AAFA (Table 2.2). The effect of these parameters on the shrinkage, however, has hardly been investigated before. Besides drying shrinkage, studies on autogenous shrinkage of AAFA are also rare. Autogenous deformation is the self-created deformation of a paste, mortar or concrete during hardening. The autogenous deformation of a construction material is important in view of early age cracking when the material is under restrained condition. Material with high autogenous shrinkage is prone to cracking. In OPC mixtures the autogenous deformation is closely related to the chemical reaction, microstructure development and moisture conditions (internal relative humidity) of the material. The reaction mechanism and microstructure formation of AAFA, however, is completely different from OPC. It is conceivable that the autogenous shrinkage mechanism of AAFA is different from that of OPC. These uncertainties about the shrinkage of AAFA hamper the broader acceptance and application of this material in the building industry.

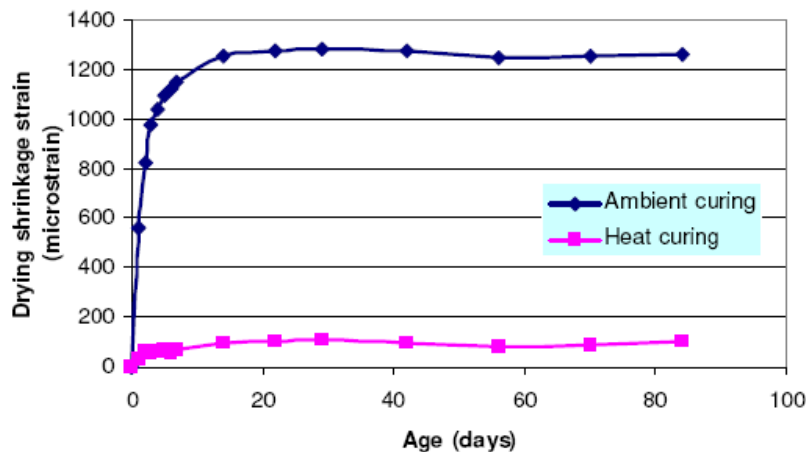


Figure 2.12 Drying shrinkage of heat-cured (sealed at 60 °C for 24 h before drying tests) and ambient-cured (sealed at 18-25 °C for 24 h before drying tests) AAFA concrete (the same mixture, drying at relative humidity 40-60%, at 23 °C) [Wallah and Rangan, 2006]

## 2.7 Concluding remarks and motivation of the research

In this chapter, a brief overview of the properties of alkali activated fly ash was given. The utilization of alkali activated fly ash as a new type of inorganic binder for the

building materials results in a lower CO<sub>2</sub> emission compared to OPC, which is good from the sustainability point of view.

Fly ash is mixed with aqueous alkali hydroxide or alkali silicate solutions to produce AAFA. The reaction product of AAFA is an alkali aluminosilicate gel, with tetrahedral aluminum and silicon atoms forming a highly cross-linked three-dimensional structure and alkali metal cations balancing the negative charge [Palomo, Grutzeck et al., 1999]. The gel structure is known to be analogous to zeolites (aluminosilicate crystalline), but mostly present as “X-ray amorphous”. The aluminosilicate gel is thus denoted as “zeolite precursor” [Palomo, Grutzeck et al., 1999]. Recent studies on the reaction mechanism revealed that several reaction steps are involved in the alkali activation, namely dissolution, speciation equilibrium, gelation, reorganization and polymerization. Because the inhomogeneous nature of fly ash, the microstructure of AAFA may also contain some unreacted or partially reacted fly ash particles embedded in the gel matrix.

Previous investigations have shown that alkali activated fly ash has many superior properties, e.g. high early mechanical strength, low creep and shrinkage, high resistance to chemical attack and good fire-resistance [Duxson, Fernández-Jiménez et al., 2007a]. These properties make the material suitable for precast products, particularly for use in aggressive environments, such as mining, manufacturing industries and sewer systems, as well as fire and chemically resistant wall panels. However, these excellent properties can only be achieved as long as a proper mix design and curing regime are applied [Duxson, Provis et al., 2007b].

The literature study has shown that the properties of AAFA products largely depend on the physicochemical nature of the raw material, type and content of the activator, water content and curing conditions (temperature, curing time and moisture condition). The permeability and shrinkage of AAFA are important engineering properties. However, these properties of AAFA are not fully understood. Better understanding and assessment of these engineering properties of AAFA require a better insight into the microstructure of AAFA. Therefore, in this thesis the development of the microstructure, the mechanical properties, permeability and shrinkage of alkali activated fly ash will be investigated experimentally. The microstructure parameters, which are dominant to these properties, are discussed and an attempt is made to quantitatively correlate the engineering properties to the microstructure.

## Chapter 3

# Mixture Design for Alkali Activated Fly Ash

---

### 3.1 Introduction

As stated in Chapter 2, fly ash is a highly variable material and its heterogeneity is on both inter-particle and intra-particle level [Provis and Van Deventer, 2009]. The expected performance of fly ash after alkali activation is largely dependent on the particle size, chemical composition and reactivity of the individual ash source, as well as on the mix proportion of activator and curing conditions. As a result, no “universal” mixture design exists for all types of fly ash. For each individual fly ash, it is necessary to characterize the material and determine the optimal mixture before other engineering properties (e.g. permeability and shrinkage) are evaluated.

This chapter presents a preliminary study on the mixture design of alkali activated fly ash (AAFA) in the laboratory. The activator content ( $\text{SiO}_2$  and  $\text{Na}_2\text{O}$ ), as the most important reaction parameter, is the main variable for the mixture design of AAFA. Other parameters, e.g. water content, curing condition and curing temperature were all kept constant in this study. The main objectives of this preliminary study include:

- To evaluate whether the fly ash used in this study is suitable for alkali activation;
- To investigate the behavior of the fresh AAFA slurry, including workability and setting time;
- To obtain a series of mix proportions for AAFA mixtures with comparable performance as cement pastes for further study in the following chapters;
- To get a first impression of the effect of activator content ( $\text{SiO}_2$  and  $\text{Na}_2\text{O}$ ) on the performance of AAFA mixtures.

In order to achieve these objectives, the chemical composition, particle size distribution and surface area of the fly ash used in the thesis are characterized first. Further, the amorphous components (including reactive silica and aluminum) in the fly ash are determined by the chemical dissolution method. All these parameters are considered important for the performance of AAFA mixtures. The current practice of ordinary Portland cement (OPC) paste producing and testing methods are applied for AAFA pastes. The workability, setting time, heat release and compressive strength are measured to evaluate the performance of AAFA pastes at early ages.

## 3.2 Materials

### 3.2.1 Characterization of fly ash

Fly ash used in this study is Class F fly ash (according to ASTM C 618), produced in The Netherlands. The chemical composition, loss on ignition, surface area and the mean particle size of the fly ash are given in Table 3.1. The chemical composition of fly ash was determined by X-ray fluorescence spectrometry (XRF). The loss on ignition of the fly ash was determined according to ASTM D 7348-08 and the surface area was measured by BET-nitrogen adsorption method. As shown in Table 3.1, the  $\text{Fe}_2\text{O}_3$  content is 4.44 % and the loss on ignition (L.I.) is 4.89 %. These values meet the recommended values of fly ash for alkali activation proposed by Fernández-Jiménez and Palomo [2003] ( $\text{Fe}_2\text{O}_3$  content  $\leq 10$  % and L.I.  $\leq 5$  %). Figure 3.1 shows the particle size distribution curve of the fly ash, measured by laser-diffraction.

Table 3.1: Chemical composition and physical properties of fly ash

Oxide	$\text{SiO}_2$	$\text{Al}_2\text{O}_3$	$\text{Fe}_2\text{O}_3$	CaO	MgO	$\text{K}_2\text{O}$	Na <sub>2</sub> O	$\text{TiO}_2$	$\text{P}_2\text{O}_5$	$\text{SO}_3$	L.I.
Weight (%)	48.36	31.36	4.44	7.14	1.35	1.64	0.72	1.24	1.90	1.18	4.89
Mean particle size ( $\mu\text{m}$ ):	21.46		Surface area ( $\text{m}^2/\text{kg}$ ):		1600		Density ( $\text{g}/\text{m}^3$ ):		2.44		

L.I. = loss on ignition

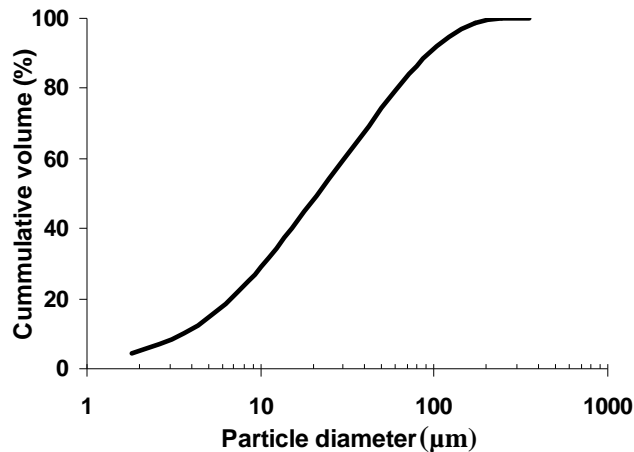


Figure 3.1 Particle size distribution of the fly ash (measured by laser-diffraction)

The crystalline phases in the fly ash were analyzed by X-ray diffraction (XRD). The XRD spectrum is shown in Figure 3.2. The result reveals that the major crystalline phases in the fly ash are quartz ( $\text{SiO}_2$ ) and mullite ( $3\text{Al}_2\text{O}_3 \cdot 2\text{SiO}_2$ ). The amorphous part in the fly ash exhibited a bump between  $17^\circ$  to  $35^\circ$   $2\theta$  (Figure 3.2). The

amorphous content in the fly ash was measured by the chemical dissolution treatment as described in EN 196, Part 2, Section 10. The principle of this method is to initially dissolve fly ash in a hydrochloric acid solution, followed by treating the solid with a boiling potassium hydroxide solution. After ignition, the residue is determined gravimetrically, and the amorphous content of fly ash is the dissolved fraction (Table 3.2). Figure 3.3 shows the XRD spectrum of the fly ash after the chemical dissolution treatment. It is obvious from Figure 3.3 that the bump representing the amorphous content in fly ash completely disappeared, and only the crystalline phases (quartz and mullite) were observed in the XRD spectrum. The residue obtained after the chemical dissolution treatment was further subject to XRF test and the result is shown in Table 3.3. From the  $\text{SiO}_2$  and  $\text{Al}_2\text{O}_3$  content in the residue (Table 3.3, measured by XRF), together with the residue fraction (31.8 wt. %), the reactive  $\text{SiO}_2$  and  $\text{Al}_2\text{O}_3$  content in the fly ash can be calculated. The results are presented in Table 3.2. The results show that the reactive  $\text{SiO}_2$  and reactive  $\text{Al}_2\text{O}_3$  content of the fly ash is 34.9 wt. % and 16.2 wt. % of fly ash content, respectively. These values are similar to the fly ashes used for the alkali activation in previous studies [Fernández-Jiménez and Palomo, 2003; Fernández-Jiménez, Palomo et al., 2006d].

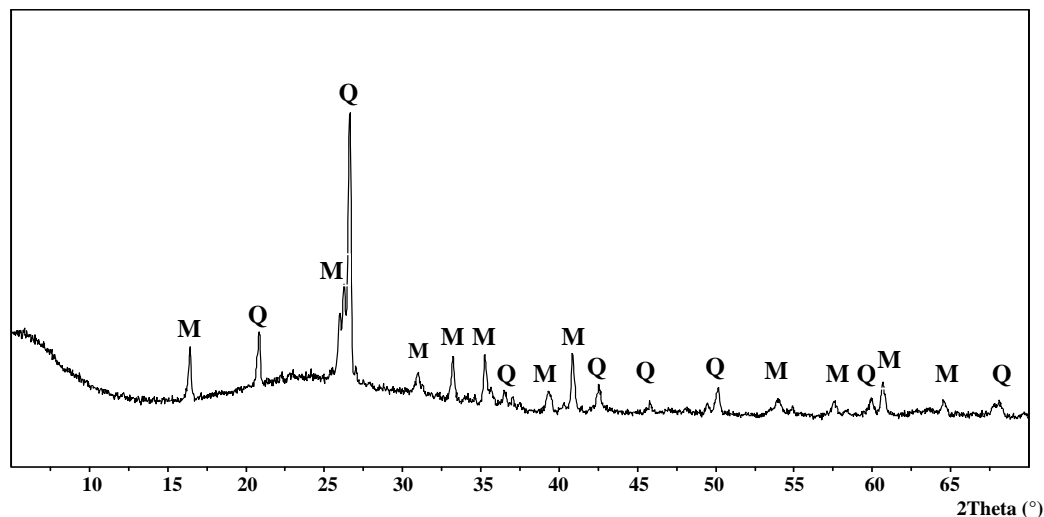


Figure 3.2 X-ray diffraction analysis of the fly ash, Q=quartz ( $\text{SiO}_2$ , PDF# 85-0457); M=mullite ( $\text{Al}_{4.8}\text{O}_{9.54}\text{Si}_{1.2}$ , PDF# 84-1205)

Table 3.2 Reactivity of fly ash determined by chemical treatment and XRF (wt. %)

I.R.	Amorphous content	$\text{SiO}_2$ (total)	Reactive $\text{SiO}_2$	$\text{Al}_2\text{O}_3$ (total)	Reactive $\text{Al}_2\text{O}_3$
31.8	69.2	48.4	34.9	31.4	16.2

I.R. = insoluble residue.

Table 3.3 Chemical composition of the insoluble residue of the fly ash by XRF (before normalization)

Oxide	SiO <sub>2</sub>	Al <sub>2</sub> O <sub>3</sub>	Fe <sub>2</sub> O <sub>3</sub>	CaO	MgO	K <sub>2</sub> O	Na <sub>2</sub> O	TiO <sub>2</sub>	P <sub>2</sub> O <sub>5</sub>	SO <sub>3</sub>
Weight (%)	42.36	51.64	2.41	0.18	0.23	0.22	0.03	2.47	0.04	--

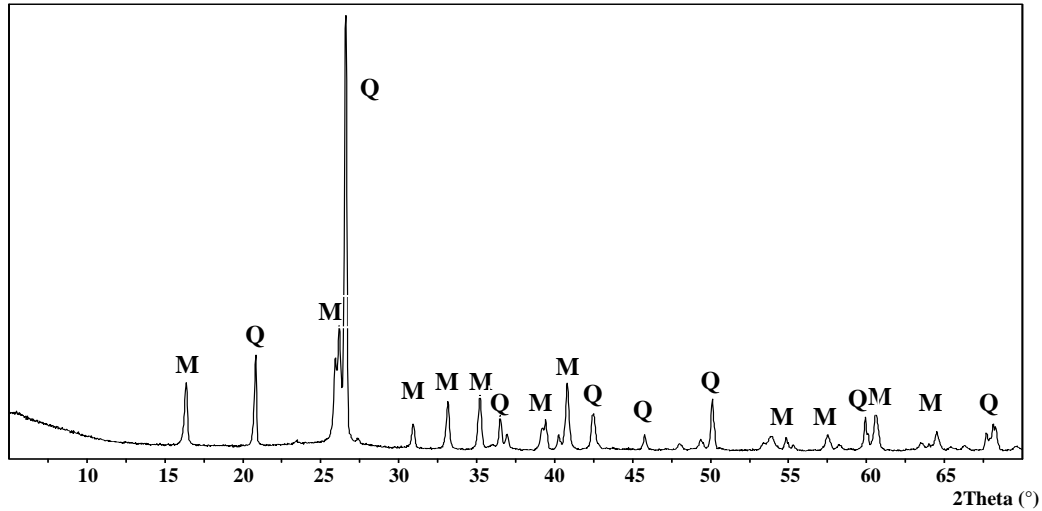


Figure 3.3 X-ray diffraction analysis of the fly ash after chemical dissolution treatment, Q=quartz (SiO<sub>2</sub>, PDF# 85-0457); M=mullite (Al<sub>4.8</sub>O<sub>9.54</sub>Si<sub>1.2</sub>, PDF# 84-1205)

### 3.2.2 Activating solutions

The activating solutions were prepared by mixing sodium hydroxide (analytical grade, >98 % purity) with distilled water and sodium silicate solution (Na<sub>2</sub>O: 8.25 wt. %, SiO<sub>2</sub>: 27.50 wt. %). The activating solutions were prepared one day before the sample preparation.

A series of activating solutions with different SiO<sub>2</sub> and Na<sub>2</sub>O contents were prepared. The SiO<sub>2</sub> content was in the range of 0-1.5 mol/kg fly ash, and Na<sub>2</sub>O content was between 1.0 and 1.5 mol/kg fly ash. The composition of the activator for each mixture is given in Table 3.4. Also mixtures, with higher SiO<sub>2</sub> (2.0 mol/kg fly ash) or lower alkali Na<sub>2</sub>O (0.5 mol/kg fly ash) were prepared. However, it was found that some solutions (SiO<sub>2</sub>=2.0 mol/kg fly ash) were not stable with precipitation (Na<sub>2</sub>SiO<sub>3</sub>·9H<sub>2</sub>O) formed. Other samples, with Na<sub>2</sub>O=0.5 mol/kg fly ash, could not set due to the low alkali content and are not studied further. The water to fly ash ratio was chosen as low as possible (as discussed in Section 2.5.3). In this study, the mass ratio of water to fly ash was kept constant at 0.35, where a workable binder can still be guaranteed.

### 3.3 Experimental Methods

#### 3.3.1 Mixing and curing

Fly ash was mixed with the activating solution in a HOBART<sup>®</sup> mixer for 4 minutes. The fresh AAFA slurry had a dark grey color (Figure 3.4). Compared to Portland cement paste, a longer vibration time was needed (2 minutes in this study) in order to remove the entrapped air. A curing temperature of 40 °C was used.

*Table 3.4 Composition in activating solutions with respect to 1 kg fly ash*

Sample (SiO <sub>2</sub> -Na <sub>2</sub> O)	SiO <sub>2</sub> (mol) (wt. %) <sup>a</sup>	Na <sub>2</sub> O(mol) (wt. %) <sup>a</sup>	H <sub>2</sub> O (g)
1.5-1.5	1.5 (9.0 %)	1.5 (9.3 %)	350
1.3-1.5	1.3 (7.8 %)	1.5 (9.3 %)	350
1.0-1.5	1.0 (6.0 %)	1.5 (9.3 %)	350
0.5-1.5	0.5 (3.0 %)	1.5 (9.3 %)	350
0-1.5	0.0	1.5 (9.3 %)	350
1.5-1.3	1.5 (9.0 %)	1.3 (8.0 %)	350
1.3-1.3	1.3 (7.8 %)	1.3 (8.0 %)	350
1.0-1.3	1.0 (6.0 %)	1.3 (8.0 %)	350
1.5-1.0	1.5 (9.0 %)	1.0 (6.2 %)	350
1.3-1.0	1.3 (7.8 %)	1.0 (6.2 %)	350
1.0-1.0	1.0 (6.0 %)	1.0 (6.2 %)	350
0.5-1.0	0.5 (3.0 %)	1.0 (6.2 %)	350
0-1.0	0.0	1.0 (6.2 %)	350

<sup>a</sup> weight percentage with respect to fly ash content.



*Figure 3.4 The fresh state of AAFA slurry*

#### 3.3.2 Workability

Workability is defined as the property of freshly mixed concrete or mortar that determines the ease with which it can be mixed, placed, consolidated, and finished to a homogenous condition (ACI committee 116R-00). In this study, the workability of AAFA pastes was measured by a mini-slump test [Li and Ding, 2003]. In this test, the



freshly mixed paste was poured into a slump cone with a top diameter of 36 mm, a bottom diameter of 60 mm and a height of 60 mm. The cone was placed in the center of a square plate of glass. After filled with paste, the cone was lifted and the paste flowed out. After one minute, the average spread of the paste, as measured along the two diagonals and two median directions, was recorded. For comparison, the spread of cement paste (CEM I 42.5) with  $w/c=0.4$  was also measured.

### 3.3.3 Setting time

The setting time of AAFA is an important parameter since it reflects the time available for transport, placing and compaction of the product. In this study, the setting time of AAFA mixture was determined by the Vicat needle method according to standard NEN-EN 196-3:2005. An automatic recording Vicat apparatus was used (Figure 3.5). According to the standard, the initial setting time was the time elapsed between “zero time” (the time when the activating solution was mixed with fly ash) to the time at which the distance between the needle and the base-plate was  $6 \pm 3$  mm. The final setting time was the elapsed time, measured from the “zero time” to that at which the needle first penetrated only 0.5 mm into the specimen.

### 3.3.4 Heat evolution

The chemical reaction in AAFA samples is exothermic [Davidovits, 1999]. Isothermal calorimetry provides continuous monitoring of the heat released by the AAFA mixture right after mixing. In this study, the rate of heat evolution of all the AAFA mixtures was measured by an isothermal conduction calorimeter (TAM-Air-314, Figure 3.6). Prior to the experiment, the calorimeter was calibrated at 40 °C and the materials (fly ash and activating solutions) were stored at 40 °C for 24 hours. In the testing procedure, fly ash powder was first mixed with the alkali solution for 1 minute, and then  $10 \pm 0.01$  g paste sample was carefully poured into a glass ampoule and transferred into the calorimeter channel. The whole procedure lasted for about 3 minutes. For this reason, the first heat peak, which occurs immediately after mixing, was not recorded. There were at least 2 replicates for each mixture. The heat flow was recorded and the cumulative heat was calculated up to 168 hours.

### 3.3.5 Mechanical properties

The flexural strength was measured by a standard three point bending test on  $40 \times 40 \times 160$  mm prisms and the compressive strength test was carried out on  $40 \times 40 \times 40$  mm cubes (NEN-EN-196-1). At least three specimens were tested for each measurement.



Figure 3.5 The setting time measurement by Vicat apparatus



Figure 3.6 Isothermal conduction calorimeter (TAM-Air-314)

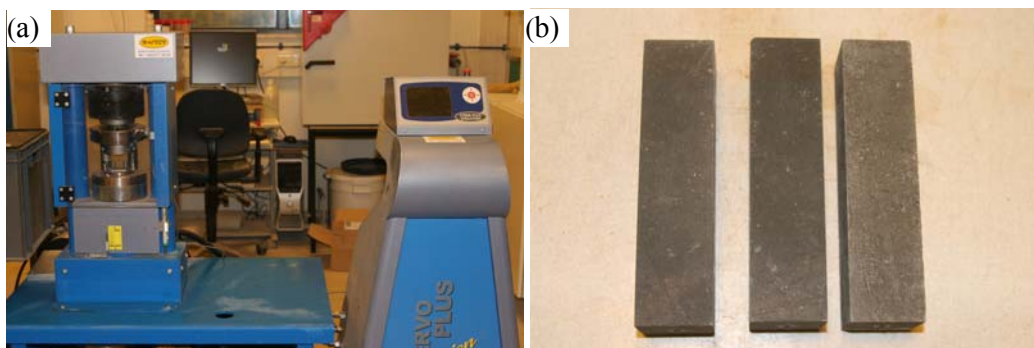


Figure 3.7 (a) The apparatus for compression and bending tests, (b) AAFA paste samples for mechanical tests

### 3.4 Results and discussions

#### 3.4.1 Workability

The results of the mini-slump spread tests are shown in Table 3.5. Mixtures with a higher mini-slump spread diameter exhibit a better flowability and workability. In general, the flowability of AAFA pastes ( $w/FA=0.35$ ) was higher than that of Portland cement paste ( $w/c=0.4$ ). It is evident from Table 3.5 that cement paste had the lowest spread diameter ( $104.25 \pm 0.8$  mm). Figure 3.8 also shows that AAFA pastes flowed more continuously than cement paste (Figure 3.8b). No bleeding was observed for all AAFA pastes, whereas some bleeding was observed for cement paste with  $w/c=0.4$ . The spread diameter of AAFA pastes was largely affected by the  $SiO_2$  content. As shown in Table 3.5, the spread diameter of specimens 1.0-1.5, containing  $SiO_2$  content of 1 mol/kg fly ash in the activator, was much higher than that of specimens 0-1.5, containing no  $SiO_2$  in the activator. For specimens 1.5-1.5, with a  $SiO_2$  content of 1.5 mol/kg fly ash, the spread diameter was similar to that of specimens 1.0-1.5 (Table 3.5). For AAFA mixtures with lower sodium content, e.g. 1 mol/kg fly ash of specimens 1.0-1.0, the mini-slump spread diameter was the highest ( $224.8 \pm 4.8$  mm).

Table 3.5 Mini-slump spread diameter of AAFA mixtures and Portland cement paste

Mixtures ( $SiO_2$ - $Na_2O$ )	0-1.5	1.0-1.5	1.5-1.5	1.0-1.0	PC ( $w/c=0.4$ )
Spread diameter (mm)	$136.3 \pm 2.7$	$214 \pm 2.3$	$215 \pm 3.5$	$224.8 \pm 4.8$	$104.25 \pm 0.8$

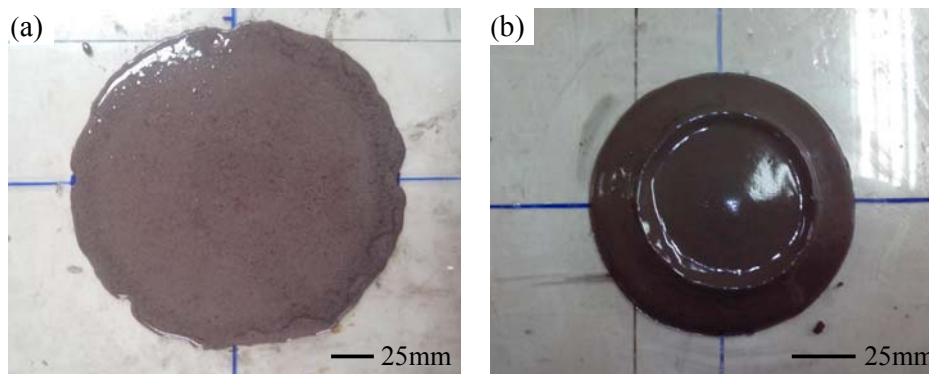


Figure 3.8 Photos of mini-slump spread test of (a) AAFA paste (1.0-1.5) and (b) Portland cement paste (without superplasticizer) ( $w/c=0.4$ )

#### 3.4.2 Setting time

The initial setting times of different AAFA pastes, cured at  $40^\circ C$ , are summarized in Figure 3.9. With different activator contents, the setting time of AAFA varied from 2 hours to more than 8 hours. The final setting time was normally 30-40 minutes after the initial setting. When the specimens were cured at room temperature, around  $20^\circ C$ , the setting time was much longer: the fresh AAFA slurry could be handled up to more

than 2 hours without any indication of setting. The obtained setting time of AAFA mixtures observed in this study was significantly longer than the values reported by Sindhunata et al. [2006], in which AAFA pastes set between 10 and 75 minutes. On the other hand, Hardjito et al. [2009] found that the initial setting time of AAFA was around 4 hours when cured at 65 °C. The scatter in setting time of AAFA largely depends on the nature of fly ash. According to previous studies, fly ash with high calcium content normally showed a fast setting after mixing [Xu and Van Deventer, 2000].

The setting time is largely affected by the  $\text{Na}_2\text{O}$  and  $\text{SiO}_2$  content, as can be observed from Figure 3.9. For example, the setting time increased from around 2.5 hours to 8.5 hours for samples with a higher  $\text{Na}_2\text{O}$  content in the activator (compare samples 1.5-1.0, 1.5-1.3 and 1.5-1.5 with increasing  $\text{Na}_2\text{O}$  content). A higher  $\text{SiO}_2$  content also led to an increase of setting time (compare samples 1.0-1.5, 1.3-1.5 and 1.5-1.5 in Figure 3.9). It seems that the addition of extra  $\text{Na}_2\text{O}$  and  $\text{SiO}_2$  in the activator resulted in an increase of the time needed for saturation of the aluminates and silicates species in the solution, resulting in a longer setting time.

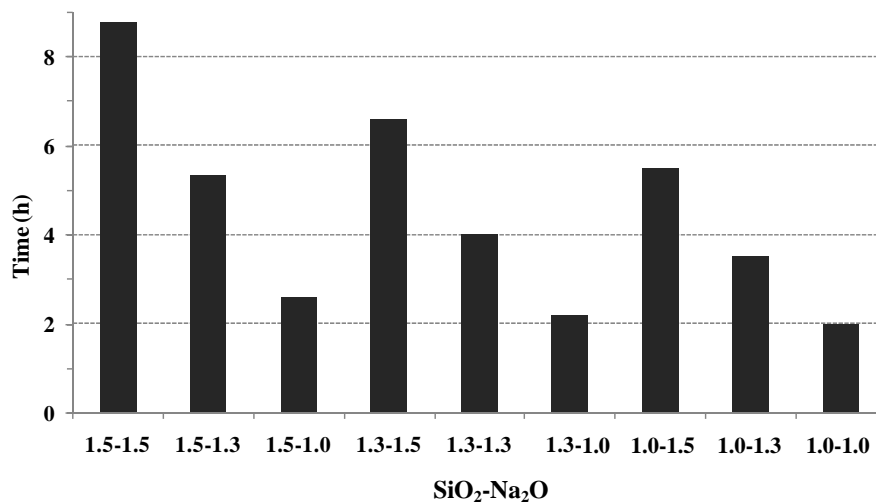


Figure 3.9 Initial setting time of AAFA mixtures with different  $\text{Na}_2\text{O}$  and  $\text{SiO}_2$  content (mole with respect to 1 kg fly ash), cured at 40 °C

### 3.4.3 Heat evolution

The cumulative heat evolution of investigated alkali activated fly ash pastes during the first 168 hours is presented in Figure 3.10 (cured at 40 °C). In general, the released heat of all investigated AAFA pastes after 7 days (168 h) was lower than 120 J/g, which is considerably lower than that of Portland cement paste (around 350 J/g after 7 days at 20 °C [Sánchez de Rojas et al., 1993]). For some AAFA samples (e.g.  $\text{SiO}_2\text{-Na}_2\text{O}=1.0\text{-}1.0$ ,  $1.3\text{-}1.0$ ,  $1.5\text{-}1.0$  etc.), the heat release was so low that it could not be detected by the machine. For this reason, the accumulation of the heat evolution stopped for these AAFA samples at a certain time.

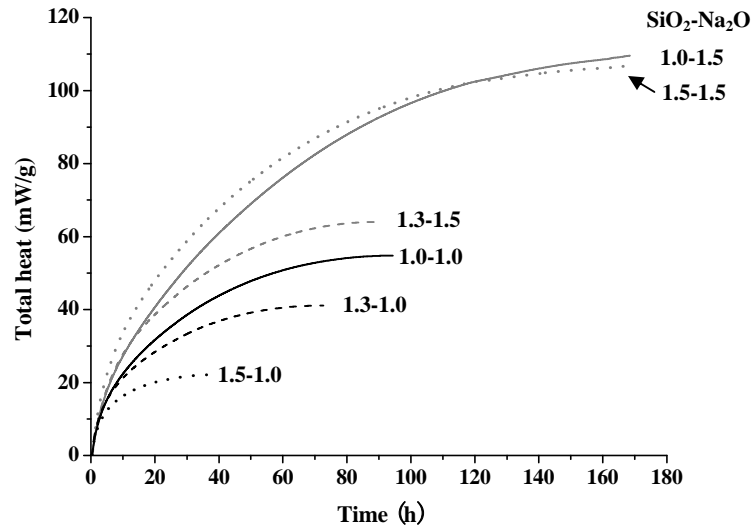


Figure 3.10 Cumulative heat evolution of alkali activated fly ash mixtures with different  $\text{Na}_2\text{O}$  and  $\text{SiO}_2$  content (mole with respect to 1 kg fly ash), cured at  $40^\circ\text{C}$

As can be seen from Figure 3.10, an increase of  $\text{SiO}_2$  content resulted in a lower heat release (mixtures  $\text{SiO}_2\text{-Na}_2\text{O}=1.0\text{-}1.0$ ,  $1.3\text{-}1.0$  and  $1.5\text{-}1.0$ ), whereas an increase of  $\text{Na}_2\text{O}$  content was associated with a higher total heat release (compare mixtures  $1.5\text{-}1.0$  and  $1.5\text{-}1.5$ , or  $1.3\text{-}1.0$  and  $1.3\text{-}1.5$ , or  $1.0\text{-}1.0$  and  $1.0\text{-}1.5$ ). It is well known that the heat release reflects the extent of the reaction. Thus, the heat evolution results indicate that the addition of more  $\text{SiO}_2$  led to a lower degree of reaction, while an increase of  $\text{Na}_2\text{O}$  content was favorable for the reaction. By using the acid attack method, Criado et.al [Criado, Fernandez-Jimenez et al., 2007b] also found a lower reaction degree of AAFA mixtures with a higher silica content in the activator. In this study, the degree of reaction of different AAFA mixtures will also be measured by the image analysis method in Chapter 4. More discussion on the effect of silica and sodium content on the reaction will be given in the following chapters.

### 3.4.4 Mechanical property

#### *Compressive strength at 7 days*

Figure 3.11 shows the compressive strength of AAFA mixtures at the curing age of 7 days (the error bars represent one standard deviation). It is found that the compressive strength increased for samples with a higher  $\text{SiO}_2$  content. For example, for specimens  $1.5\text{-}1.5$ , with the highest silica content, the compressive strength at 7 days was the highest (52 MPa), while for specimens  $0\text{-}1.5$ , with no silica, the strength (12 MPa) was the lowest (Figure 3.11). A substantial increase of the compressive strength was observed when the silica content increases from 0.5 to 1 mol/kg fly ash (Figure 3.11). With further addition of silica, the increase of compressive strength was within 10 MPa.

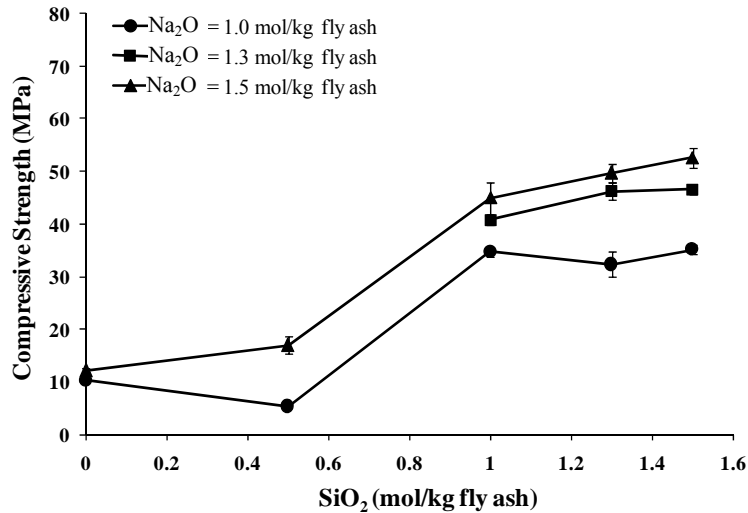


Figure 3.11 Influence of  $\text{SiO}_2$  and  $\text{Na}_2\text{O}$  content on compressive strength at 7 days,  $40^\circ\text{C}$ , water/FA ratio=0.35

Figure 3.11 also shows that the compressive strength at 7 days was higher for samples with a higher  $\text{Na}_2\text{O}$  content ( $\text{Na}_2\text{O}$  content of 1.0, 1.3 and 1.5 mol/kg fly ash). These results are in line with the findings of Bakharev [2005a], who reported that a higher compressive strength value was derived when the  $\text{Na}_2\text{O}$  content increased from 2 wt. % to 8 wt. % of fly ash. However, for an alkali content of 14.9 wt. % of fly ash, a decrease of compressive strength was found [Fernández-Jiménez and Palomo, 2005b]. In this study, the highest alkali content was 1.5 mol/kg fly ash (9.3 wt. % of fly ash), which is lower than 14.9 wt. % of fly ash used by Fernández-Jiménez and Palomo [Fernández-Jiménez and Palomo, 2005b]. Further addition of alkali (2 mol/kg fly ash) resulted in precipitation in the activating solution when also silica was present in the solution. It can be observed from Figure 3.11 that when both silica and alkali contents were equal to or more than 1.0 mol/kg fly ash, the obtained compressive strength at 7 days was higher than 30 MPa. This range of silica and alkali content is regarded as the proper compositions of the activator for alkali activation of the fly ash used in this study in view of the compressive strength.

The trend of the compressive strength of pastes made with different  $\text{Na}_2\text{O}$  content was the same as that of the heat evolution: an increase of  $\text{Na}_2\text{O}$  content led to a higher heat release (higher degree of reaction, as discussed in Section 3.4.3), and a higher compressive strength (Figure 3.11). On the other hand, samples with a higher silica content had a lower heat release at 7 days (lower extent of reaction, discussed in Section 3.4.3). The compressive strength of these samples, however, increased with an increase of silica content (Figure 3.11). It means that the effect of the silica content on the degree of reaction is not consistent with its effect on the compressive strength. It indicates that other parameters (e.g. solid phase or/and pore structure) are involved, having a more decisive impact on the compressive strength than the degree of reaction. In-depth investigations will be carried out in Chapter 4 and 5 in order to have a clearer view on the effect of silica on the microstructure of AAFA mixtures and the resulting strength.

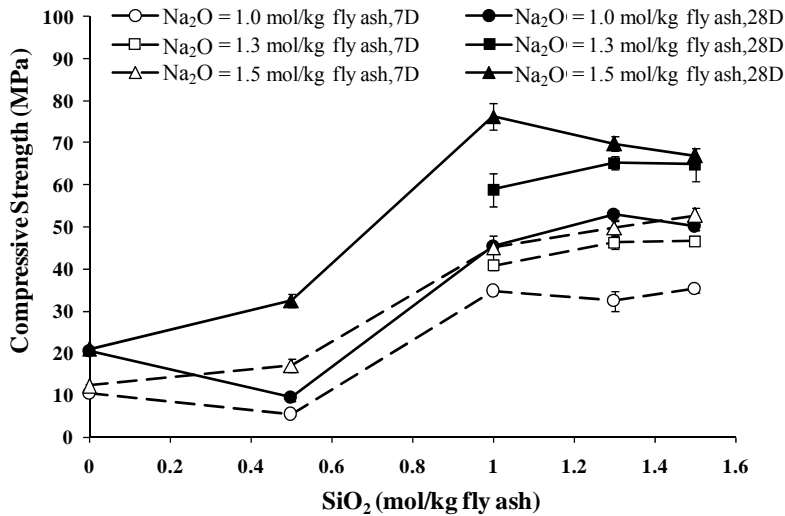


Figure 3.12 Influence of  $\text{SiO}_2$  and  $\text{Na}_2\text{O}$  content on compressive strength at 28 days (solid lines), compared to at 7 days (dashed lines), cured at  $40^\circ\text{C}$ , water/FA ratio=0.35

### Compressive strength at 28 days

After 28 days curing at  $40^\circ\text{C}$ , the compressive strength of all AAFA mixtures increased compared to that at 7 days (Figure 3.12). However, the highest compressive strength at 28 days appeared for different silica content. For example, when the  $\text{Na}_2\text{O}$  content was 1.5 mol/kg fly ash, samples 1.0-1.5 showed the highest compressive strength at 28 days (see solid line with triangle marked in Figure 3.12), instead of samples 1.5-1.5 at 7 days (see dashed line with triangle marked in Figure 3.12). More sodium content led to a higher compressive strength at 28 days. This trend is in consistent with the results at 7 days.

### Flexural strength

For the flexural strength of AAFA, a different trend was found compared to the compressive strength both at 7 days and 28 days curing ages. As shown in Figure 3.13, when the  $\text{SiO}_2$  content was in the range of 1.0 to 1.5 mol/kg of fly ash, an increase of both the  $\text{SiO}_2$  and  $\text{Na}_2\text{O}$  content led to a decrease of the flexural strength (Figure 3.13). The reason for this is still not clear. It is assumed that the reduction of flexural strength is related to the structural ordering of the reaction products of AAFA. The most plausible reason might be a reduced level of long-range structural ordering when more silica and sodium is added to the activating solution [Duxson et al., 2007].

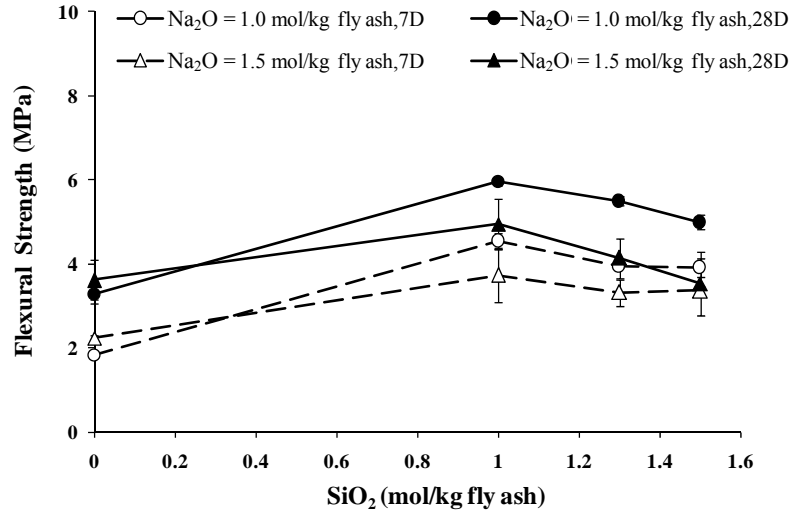


Figure 3.13 Influence of  $\text{SiO}_2$  and  $\text{Na}_2\text{O}$  content on flexural strength at 7 days (dashed lines) and 28 days (solid lines),  $40^\circ\text{C}$ , water/FA ratio=0.35

From the experimental results presented in this chapter it can be concluded that with the selected activator solutions, when both the silica and sodium content exceed 1.0 mol/kg of fly ash, the AAFA pastes showed good workability. The strength of the investigated mixtures was in the same range as Portland cement pastes with  $w/c=0.4$  ( $\geq 30$  MPa). In addition, the heat release of these AAFA pastes was much lower than that of cement paste. The setting time (between 2-8 h) ensured sufficient time available for transport, placing and compaction for the product. Thus, these AAFA mixtures were chosen for further investigations in the following chapters.

### 3.5 Concluding remarks

In this chapter, a preliminary study on the mixture design of AAFA pastes was presented. The fly ash used in the study was tested to see if this ash is suitable for alkali activation. Different mixing proportions of AAFA were evaluated in terms of workability, setting time, heat evolution and mechanical properties. The following conclusions can be drawn from the experimental results:

- The physical and chemical properties of the fly ash used in this study meet the recommended values of fly ash for alkali activation proposed in previous studies on AAFA [Fernández-Jiménez and Palomo, 2003; Fernández-Jiménez, Palomo et al., 2006d].
- The AAFA slurry with a  $\text{SiO}_2$  and  $\text{Na}_2\text{O}$  content in the activator larger than 1.0 mol/kg fly ash showed good workability and an initial setting time between 2 hours to 8 hours, depending on the  $\text{SiO}_2$  and  $\text{Na}_2\text{O}$  content.
- When both the  $\text{SiO}_2$  and  $\text{Na}_2\text{O}$  contents are higher than 1.0 mol/kg fly ash the compressive strength of AAFA mixtures after 7 days cured at  $40^\circ\text{C}$  is higher than 30 MPa. For some mixtures (e.g.  $\text{SiO}_2\text{-Na}_2\text{O}=1.5\text{-}1.5$ ), the compressive



strength even exceeded 50 MPa. These mixtures are regarded as promising mixes for further investigation.

- An increase in  $\text{Na}_2\text{O}$  content resulted in a higher heat release and a higher compressive strength. The addition of more  $\text{SiO}_2$  retarded the reaction, but still led to an increase of the compressive strength at 7 days.
- For mixtures with different silica content, the trend of the degree of reaction is not consistent with the compressive strength development. It means other parameters are involved having a more decisive impact on the strength. It, therefore, requires an in-depth investigation of its solid phases and pore structure development to better understand the mechanisms of the strength development, as will be discussed in the following chapters.

## **Chapter 4**

# **Solid Phases of Alkali Activated Fly Ash**

---

### **4.1 Introduction**

Literature has shown that the solid phases in hardened alkali activated fly ash (AAFA) mainly consist of aluminosilicate gel and un-reacted fly ash. Under certain conditions (e.g. high temperature curing), crystalline zeolites are also present. The amount and distribution of reaction products determine the engineering properties of AAFA, such as mechanical and transport properties. In order to better understand and assess the performance of AAFA, an extensive characterization of the reaction products is necessary. Therefore, in this chapter, the reaction products of AAFA are characterized with respect to their distribution, their degree of reaction, the chemical bonds, the elastic modulus and the mineral composition. Based on this information about the reaction products of AAFA, the correlation between the microstructure and mechanical properties will be discussed.

The distribution and the degree of reaction of aluminosilicate gel are examined by environment scanning electron microscopy (ESEM). Fourier transform infrared spectroscopy (FTIR) and X-ray diffraction (XRD) are applied to study the chemical bonds and the mineral composition of the reaction products of AAFA. Nanoindentation sensing technique is used to characterize the elastic modulus of the aluminosilicate gel.

### **4.2 Materials and Experimental Methods**

#### **4.2.1 Materials**

The fly ash used in this chapter was the same as in Chapter 3. The chemical and physical properties of the fly ash were given in Section 3.2.1. A group of activating solutions with different silica and sodium oxide content were prepared (Table 4.1). This group of activating solutions was selected based on the experimental results shown in Chapter 3. It includes the mixture with the highest compressive strength at 28 days age ( $\text{SiO}_2\text{-Na}_2\text{O}=1.0\text{-}1.5$ ) and the mixture with the lowest sodium content (in order to save costs), but having reasonable compressive strength ( $\text{SiO}_2\text{-Na}_2\text{O}=1.0\text{-}1.0$ ).

*Table 4.1 Mix composition of AAFA mixtures*

Sample (SiO <sub>2</sub> -Na <sub>2</sub> O)	Fly Ash (g)	SiO <sub>2</sub> (mol)	Na <sub>2</sub> O (mol)	H <sub>2</sub> O (g)
0-1.5	1000	0.0	1.5	350
0.5-1.5	1000	0.5	1.5	350
1.0-1.5	1000	1.0	1.5	350
1.5-1.5	1000	1.5	1.5	350
1.0-1.3	1000	1.0	1.3	350
1.0-1.0	1000	1.0	1.0	350

### 4.2.2 Sample preparation

The mixing procedure for AAFA paste was the same as in Chapter 3. After mixing, the pastes were poured into plastic bottles. The bottles were put on the vibrating table for 2 minutes to remove air bubbles and then sealed with a lid. Afterwards the sealed bottles were put in an oven at 40 °C until the age of testing. For the FTIR test, specimens at the age of 3 days, 7 days, 14 days and 28 days were analysed. For the other tests (ESEM, XRD and nanoindentation), the AAFA samples at 7 and 28 days curing age were tested.

### 4.2.3 Environmental scanning electron microscopy (ESEM)

#### *General introduction*

Scanning electron microscopy (SEM) is a type of electron microscope which can generate information about the sample's surface topography, composition and phase distribution [Goldstein et al., 2003]. Conventional SEM requires samples to be imaged under vacuum, while ESEM allows samples to be observed in low-pressure gaseous environment and high relative humidity. The formation of images is based on the signals produced by the interaction between the electron beam and the atoms in the sample [Goldstein, Newbury et al., 2003]. The signals produced by a SEM include secondary electrons (SE), back-scattered electrons (BSE), characteristic X-rays and Auger electrons (see Figure 4.1). Accordingly, the principal images produced in the SEM are of three types: SE images, BSE images and elemental X-ray maps. The intensity of SE depends on the local inclination of the specimen surface, and they are used for imaging of fracture surfaces and providing surface topographic data. For BSE, the intensity depends principally on the local atomic number of the specimen: elements with high atomic number backscatter electrons more strongly than elements with low atomic number, and thus appear brighter in the image. Hence, BSE is used to detect contrast between areas with different chemical composition. In this chapter, BSE was applied to study the space distribution and the amount of aluminosilicate gel.

A polished AAFA paste sample viewed with BSE is shown in Figure 4.2. As previously reported by Lloyd et al. [2009a; 2009b], the un-reacted fly ash particles with obvious shapes appear bright; the aluminosilicate gel dark grey. The pores filled with epoxy do not scatter electrons and appears uniformly black.

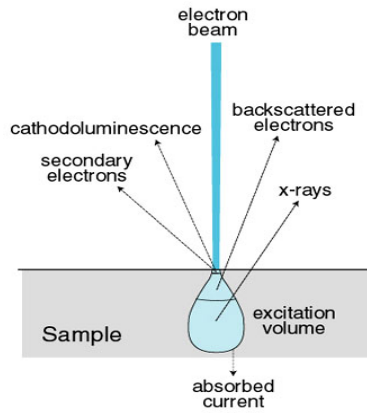


Figure 4.1 Different signals produced by a SEM derived at (<http://www4.nau.edu/microanalysis/microprobe-sem/signals.html>)

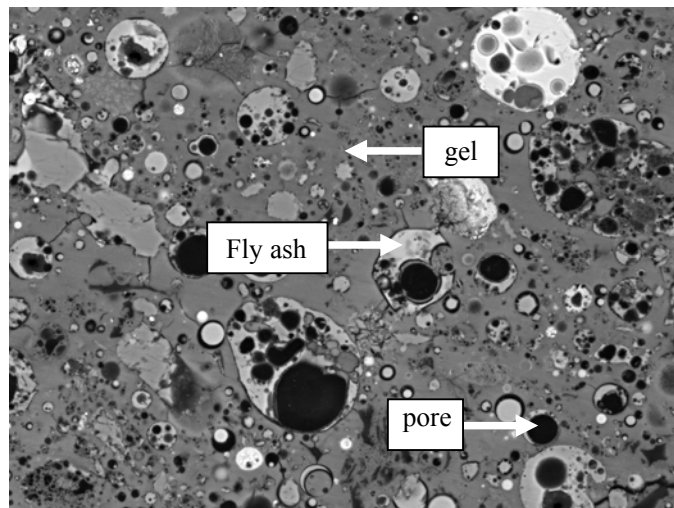


Figure 4.2 ESEM image of AAFA paste at 7 days curing ( $248 \times 188 \mu\text{m}$ )

### Sample preparation for ESEM

At each curing age, the samples for ESEM examination were first crushed (by hammer) into small pieces with dimensions of 1-2 cm<sup>3</sup> (Figure 4.3a). These pieces were then immersed in liquid nitrogen to stop the chemical reaction and placed in a vacuum freeze-dryer at -28 °C until constant weight. This quick freezing and drying process at low temperatures allows the remaining liquid solution in pores transforming into ice microcrystal and further removed by sublimation without a significant damage to the material microstructure [Ye, 2003].

The specimen preparation for ESEM observations is very important since it facilitates the examination and interpretation of microstructural features. Scanning electron microscope analysis using BSE requires a well-polished surface for optimal analysis. A proper sample preparation process for ESEM observations includes epoxy impregnation, cutting, grinding and polishing. In order to obtain a high quality image,

specimens need to be well grinded and polished. To prepare the samples, the surfaces of the specimens were first ground on the middle-speed lap wheel with different SiC papers (3 minutes for each SiC paper): p320, p500, p800, p1200 and p4000. The samples were then polished on a lap wheel with different finer grades of diamond abrasive cloth: 6, 3, 1 and 0.25  $\mu\text{m}$ . The final polishing was carried out on a low-relief polishing cloth. For the grinding and polishing procedure, ethanol was used as the lubricant. After polishing, the specimens were cleaned in an ultrasonic bath to remove the dust and diamond particles left on the surface (more details about the sample preparation procedure were previously reported in [Ye, 2003]). Figure 4.3b shows an example of the AAFA sample ready for the ESEM observation.

### *Image acquisition*

For ESEM observations, the BSE mode was used to study the pore structure of AAFA. The images were obtained by using a Philips-XL30-ESEM (Figure 4.4). The acceleration voltage was 15-20 kV (as long as a good image was obtained) and the water vapor pressure was at 1.0 Torr. The physical size of the reference region of each image is 248  $\mu\text{m}$  in length and 188  $\mu\text{m}$  in width. The magnification was 500 $\times$  and the image size was 1424  $\times$  968 pixel. Thus the resolution of the image was 0.19  $\mu\text{m}$ /pixel.

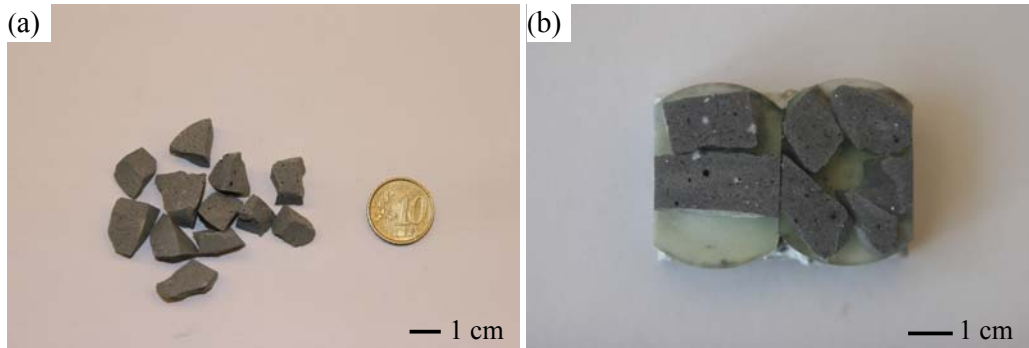


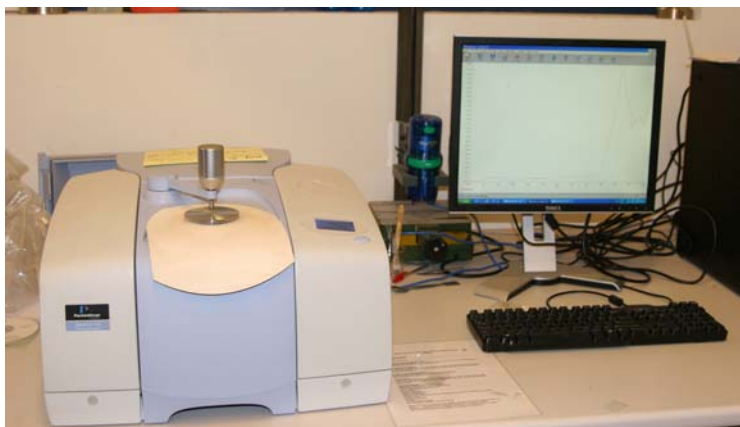
Figure 4.3 (a) Small AAFA samples; (b) AAFA samples ready for ESEM observation



Figure 4.4 Photo of the Philips-XL30-ESEM used for ESEM observation

#### 4.2.4 Attenuated total reflectance - Fourier transform infrared spectroscopy (ATR-FTIR)

FTIR is an analytical technique which allows the identification of different chemical bonds in a molecule from the absorption of infrared radiation at various wavelengths. The ATR technique enables examination of samples directly in the solid or liquid state without further preparation, such as mixing with KBr. By monitoring the change of band wavelength that is related to the aluminosilicate gel network, the compositional change of gel can be derived. In this study, the FTIR spectra of AAFA paste samples were collected using Spectrum TM 100 Optical ATR-FTIR spectrometer (in Figure 4.5). Spectra analysis was performed over the wavelength range of  $4000$  to  $400\text{ cm}^{-1}$  at a resolution of  $4\text{ cm}^{-1}$ . At each curing age, dried AAFA samples were grinded into powder, spread on the testing plate (ATR crystal) and pressed to obtain good contact. Specimens at the curing age of 3 days, 7 days, 14 days and 28 days were measured.



*Figure 4.5 Photo of the ATR-FTIR spectrometer*

#### 4.2.5 X-ray diffraction (XRD)

X-ray diffraction is a non-destructive analytical technique that allows the identification of crystalline phases in a solid material. This technique is based on observing the scattered intensity of an X-ray beam hitting a sample as a function of incident and scattered angle. XRD powder diffractograms of AAFA paste samples were collected on a Philips PW 1830 powder diffractometer (Figure 4.6). Energy source was  $\text{CoK}\alpha$  ( $1.789\text{\AA}$ ) and the tube settings were 45 kV and 30 mA. Step scans were performed from  $5\sim 70^\circ 2\theta$  at  $0.03^\circ 2\theta$  steps, and a rate of 3.0 seconds per step.

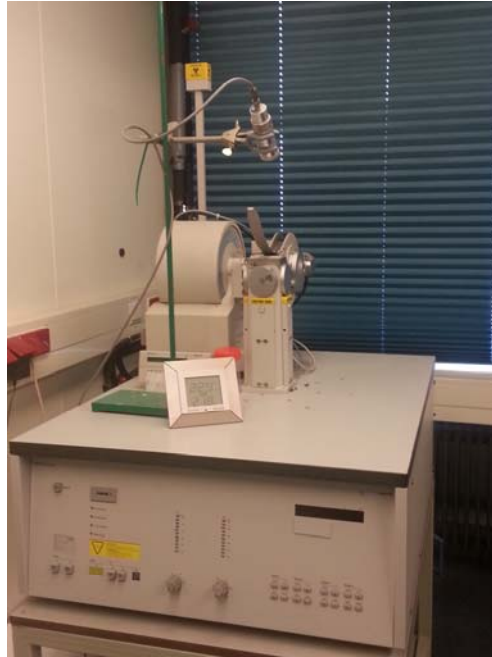


Figure 4.6 Photo of X-ray diffractometer

#### 4.2.6 Nanoindentation

Nanoindentation technique enables the characterization of intrinsic elastic properties of materials on the micrometer and submicrometer scale. In this study, nanoindentation tests were conducted using Agilent Nano Indenter G200 (Figure 4.7), equipped with a berkovich tip (with projected area  $24.5h^2$ ,  $h$  is the contact depth) to determine the elastic modulus ( $E$ ) of different phases (e.g. un-reacted fly ash particles and aluminosilicate gel). All testing was programmed in such a way that the loading was performed when the indenter came into contact with the surface of the sample until a specified maximum penetration depth ( $h$ ) was reached (1000 nm in this study). Afterwards, the load was maintained for 10 seconds followed by the unloading process. A typical load-penetration ( $P$ - $h$ ) curve is shown in Figure 4.8. The Continuous Stiffness Method (CSM Method) developed by Oliver and Pharr [1992] was used for the analysis of the results, and the average  $E$ -modulus was determined in the loading range between 200 and 800 nm depth (Poisson's ratio was assumed to be 0.18 for all measurements).

For sample preparation, the specimens were first cut into slices of around 10 mm thickness. Afterwards, the specimens were grinded and polished with SiC papers and diamond abrasive cloth, respectively, in order to obtain a very flat and smooth ("mirror-like") surface. After polishing, the specimens were cleaned in an ultrasonic bath. The measurements were performed on the top surface of the specimens. The distance between individual indents was 10  $\mu\text{m}$ . Information about the elastic modulus was obtained from a matrix of a minimum of 240 indents covering a representative area of at least  $50 \times 390 \mu\text{m}^2$  on the surface. Three representative areas were selected for each AAFA specimen in this study. All together, around 720 indents were carried out for each AAFA sample.

After the nanoindentation measurements, the tested areas were examined using ESEM in BSE mode (working distance of 10 mm, accelerating voltage at 20 kV), combined with energy dispersive X-ray analysis (EDX), for the qualitative determination of the chemical composition.

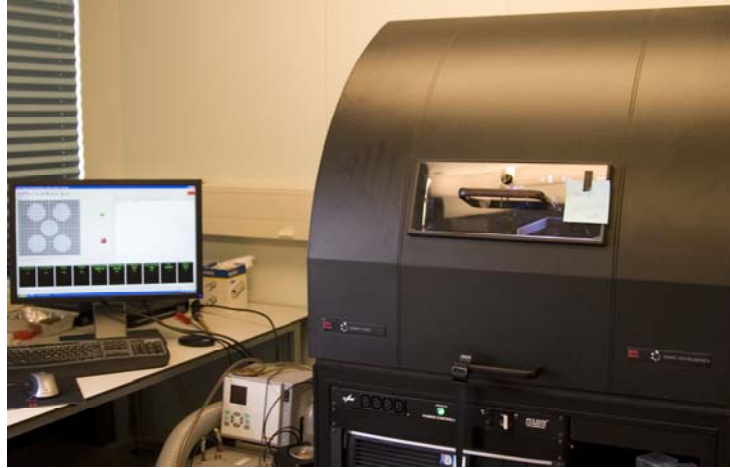


Figure 4.7 Photo of the nanoindentation machine

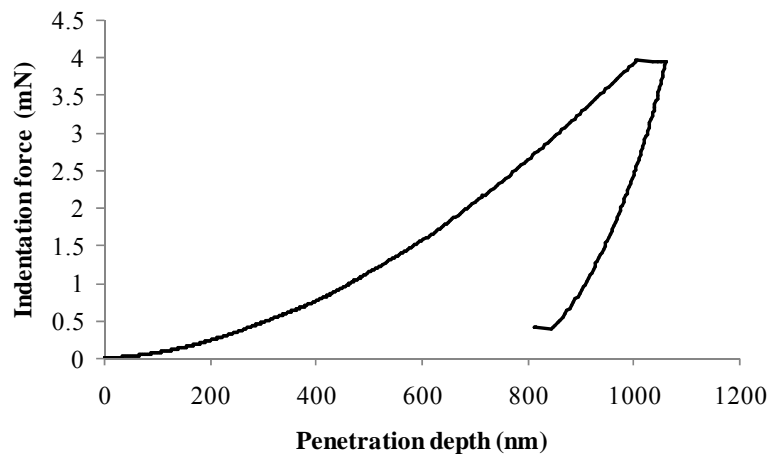


Figure 4.8 Example of load-penetration curve on AAFA samples by nanoindentation

#### 4.2.7 Assessment of the degree of reaction of AAFA by image analysis

The BSE image analysis technique was applied for quantitative characterization of the amount of reaction product (degree of reaction). The BSE image includes 256 grey level values, ranging from 0 (black) to 255 (white). It provides image contrast as a function of element composition (atomic weight) [Goldstein, Newbury et al., 2003]: material with a higher atomic number being brighter, and that with a lower atomic number is darker. Thus, according to the brightness/grey level histogram of the image,



the components of different phases can be identified. The image analysis was then based on the distribution of the grey levels of all pixels in the image [2003].

Figure 4.9 shows the BSE image and the corresponding grey level histogram of a typical AAFA paste. The un-reacted fly ash presented the highest average atomic number. Thus the peak corresponding to the right side of the grey level histogram (Figure 4.9b) represented the phase of un-reacted fly ash. The peak in the middle of the grey level histogram is the reaction product (aluminosilicate gel). The pores distinguished as black in the BSE image, corresponding to the left peak as shown in Figure 4.9b. It is stated by Ye [2003] that 95 % degree of confidence could be achieved when the number of images submitted to image analysis is 12 or more. In this study, a total number of 15 images on randomly selected locations were captured for each sample.

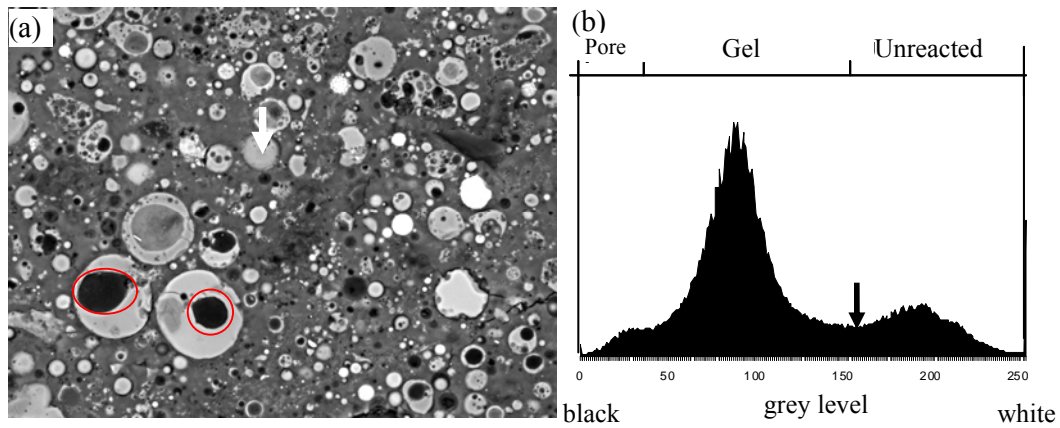


Figure 4.9 (a) Original backscattered electron (BSE) images of a typical AAFA paste sample; (b) Corresponding grey level histogram

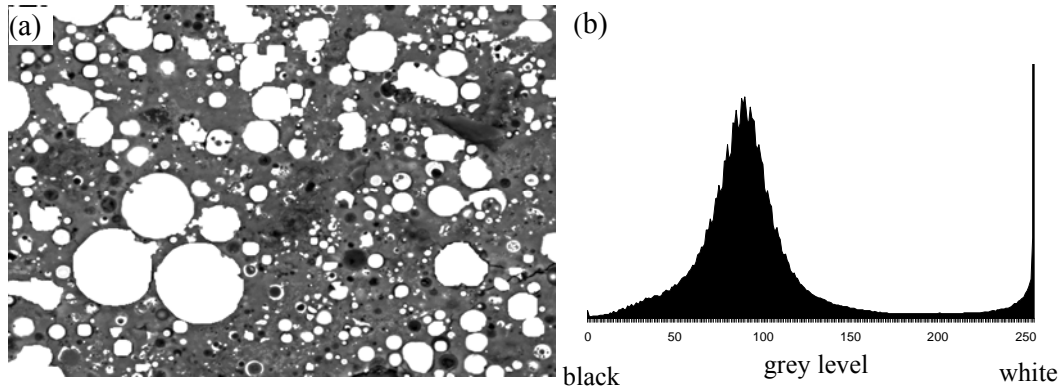


Figure 4.10 (a) Original backscattered electron (BSE) images of a typical AAFA paste sample after segmentation; (b) Corresponding grey level histogram

The degree of reaction of AAFA can be determined by measuring the area fraction of the un-reacted fly ash particles in the images. To do this, the area corresponding to the un-reacted fly ash particles needs to be separated from the image to calculate its area fraction. In the simplest situation, by choosing a proper grey level value as the threshold, the segmentation can be directly performed on the basis of the histogram. However, in the case of AAFA, the determination of the threshold value is difficult. This is mainly because the grey level of some fly ash particles is similar to the grey level of the reaction products, especially for the un-reacted fly ash particles with Si-rich part (arrowed in Figure 4.9a) and the aluminosilicate gel with high density. For this reason it is difficult to accurately determine the boundary between the un-reacted fly ash particles and the gel (arrowed in Figure 4.9b). Another phenomenon in the BSE image of AAFA paste is that there are some pores inherent to fly ash particles. These pores normally exist in hollow fly ash particles and become visible when the sample is grinded/polished for ESEM observation. Normally these pores are present in the ash particles (circled in Figure 4.9a). When the segmentation of the un-reacted fly ash is applied, this type of pores should be also included. However, it cannot be achieved by simply threshold segmentation.

In order to solve these problems, the segmentation of the un-reacted fly ash particles from the image was based mainly on the *area selection tool*. The *area selection tool* mainly has two functions. First, by choosing one object area (e.g. one fly ash particle), this tool can automatically select all the areas in the BSE image with similar grey levels. The range of the similar grey levels can be determined by setting a grey level tolerance. In this function, the grey level value of each pixel is compared to the neighbor pixel; pixels that are within the tolerance are selected. In this study, a grey level tolerance 5 was set. The second function of the area selection tool is that you can manually add or remove the areas that are needed or not wanted in the image. In this way, the area that belongs to the fly ash particles but its histogram overlapped with that of the reaction product can be selected separately. The pores inherent to the fly ash particles can also be selected. After all the fly ash particles were selected, the delete button was used to turn the selected image into white (grey level 255). In this way, the fly ash particles were separated from the image. The accuracy of the area selection can be controlled by comparing the original and segmented images. Figure 4.10 shows the BSE images after segmentation and the corresponding grey level histogram. It can be seen from the grey level histogram (Figure 4.10b) that after the segmentation, the boundary between the un-reacted fly ash particles and the reaction products becomes much clearer.

The ESEM image after the segmentation was then transformed into a binary image with the un-reacted fly ash particles as white and the rest phases as black background. The resulting image is shown in Figure 4.11, including only the un-reacted fly ash particles. By using the thresholding technique, the percentage of the un-reacted fly ash particles is obtained.

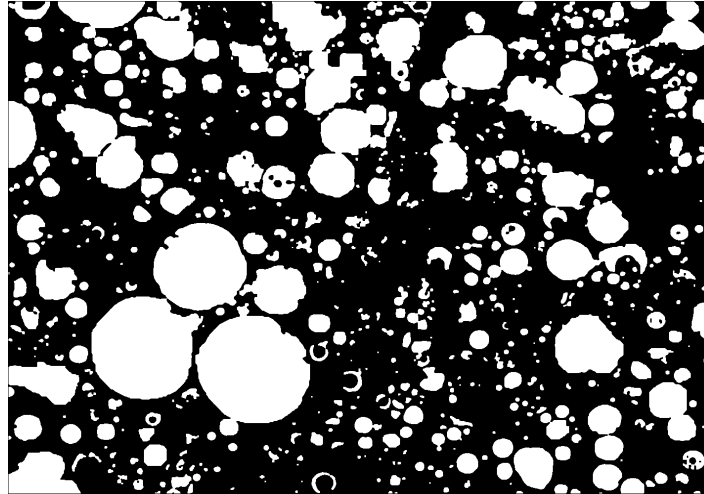


Figure 4.11 Binary image of the AAFA paste sample

The degree of the reaction of AAFA at certain time,  $\alpha(t)$ , can be calculated from the following equations:

$$\alpha(t) = (1 - U_t/U_0) \times 100 \% \quad (4.1)$$

where  $U_t$  is the volume fraction of un-reacted fly ash particles at the age  $t$  (obtained from the image analysis);  $U_0$  is the initial volume fraction of fly ash particles. The initial volume fraction of fly ash particles is calculated as the initial activating solution/fly ash volume ratio. For the mixtures  $\text{SiO}_2\text{-Na}_2\text{O}=1.0\text{-}1.0$ ,  $1.0\text{-}1.3$ ,  $1.0\text{-}1.5$  and  $1.5\text{-}1.5$  pastes, the volume of the activating solution was measured 0.360 L, 0.359 L, 0.358 L and 0.368 L (mixed with 1 kg fly ash), respectively. The measured density of the fly ash was  $2.44 \text{ g/cm}^3$ , which corresponded to a volume of 0.41 L of 1 kg fly ash. Thus the initial volume fraction of fly ash of mixtures  $\text{SiO}_2\text{-Na}_2\text{O}=1.0\text{-}1.0$ ,  $1.0\text{-}1.3$ ,  $1.0\text{-}1.5$  and  $1.5\text{-}1.5$  was calculated at 53.2 %, 53.3 %, 53.4 % and 52.7 %, respectively.

### 4.3 Results and Discussion

#### 4.3.1 Morphology of fly ash particles

Figure 4.12 shows the representative BSE image of raw fly ash particles (sample prepared by epoxy impregnation). The fly ash particles have a size range from  $1 \mu\text{m}$  to more than  $50 \mu\text{m}$ . Generally, the shape of fly ash particles was spherical (points 1 in Figure 4.12). Irregular shapes of the fly ash particles were also observed (points 2 in Figure 4.12). All the particles contained a heterogeneous distribution of chemical compositions and showed different brightness (points 1, 2 and 3 in Figure 4.12).

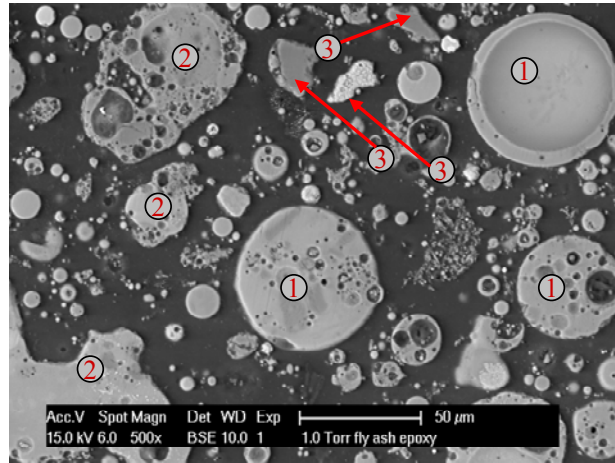


Figure 4.12 BSE image of fly ash particles

### 4.3.2 Morphology of hardened AAFA pastes

Figures 4.13 and 4.14 show the BSE images of AAFA samples with different sodium and silicate content at the ages of 7 days and 28 days, respectively. It has been previously reported that both an increase of the silicate content in the activating solution of AAFA pastes led to a denser and more homogenous microstructure with less large pores [Lloyd, Provis et al., 2009b; Rees, Provis et al., 2007b; Van Deventer et al., 2007]. This was also confirmed in this study. When the  $\text{SiO}_2$  content is zero (0-1.5) or very low (0.5 mol/kg fly ash for 0.5-1.5), the formation of the aluminosilicate gel was limited and mainly grew around the un-reacted fly ash particles, resulting in a loose and porous microstructure at both 7 days and 28 days (Figure 4.13a, b and Figure 4.14a, b). When the  $\text{SiO}_2$  content  $\geq 1.0$  mol/kg fly ash, the aluminosilicate gel was homogeneously distributed in the matrix, connecting all the un-reacted fly ash particles to form a dense matrix (Figure 4.13c-f and Figure 4.14c-f). Additionally, the homogeneous gel in the AAFA matrix occupied most of the bulk space. The typical capillary pores generally observed in cement paste, were not found in these AAFA samples. Instead, only a small number of large cavities were observed in these samples (arrows in Figure 4.13b-e). These large cavities were partially formed by the dissolved fly ash particles and partially resulted from the un-reacted fly ash particles with hollow inside (also known as cenospheres). These cavities were in the range of several microns to larger than 10  $\mu\text{m}$  in diameter, appearing as disconnected and bounded by the aluminosilicate gel in the BSE images. The pore structure of AAFA will be studied in more detail in Chapter 5.

No obvious differences were shown in the BSE images of samples with different  $\text{Na}_2\text{O}$  content at both 7 days and 28 days (samples  $\text{SiO}_2\text{-Na}_2\text{O}=1.0\text{-}1.5$ ,  $1.0\text{-}1.3$  and  $1.0\text{-}1.0$  in Figure 4.13 and 4.14). However, it does not mean that the gel phases of AAFA remained unchanged. The presence of the gel cannot be fully inferred from the BSE image mainly due to the limited resolution of the BSE images at the magnification of 500 $\times$ , which can only distinguish particles larger than 0.19  $\mu\text{m}$ . Other techniques (i.e. FTIR, XRD and nanoindentation) were also applied in this chapter to obtain more information about the gel phase in AAFA mixtures.

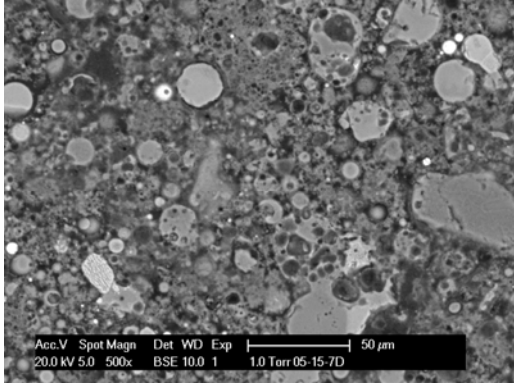
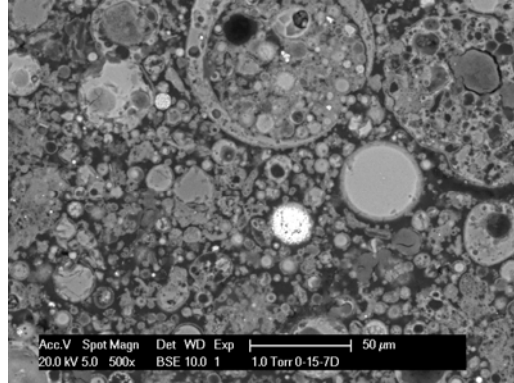
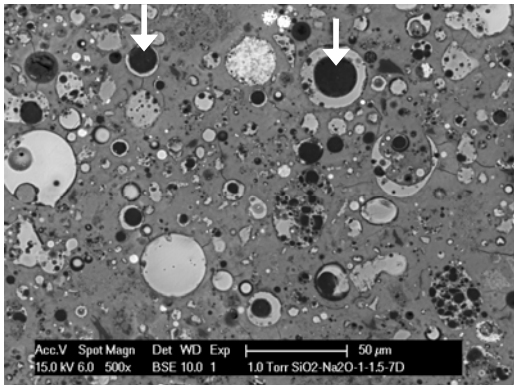
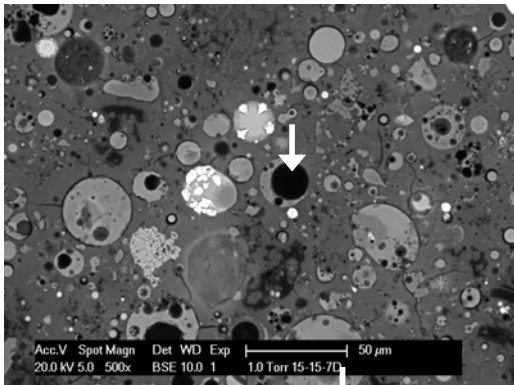
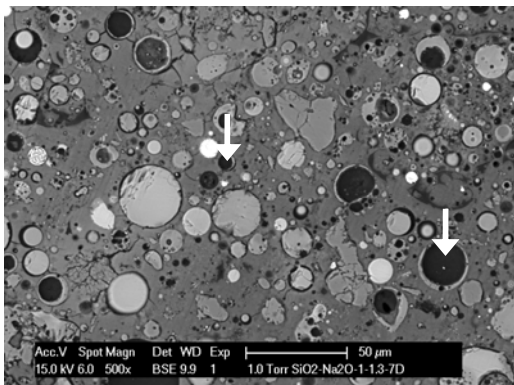
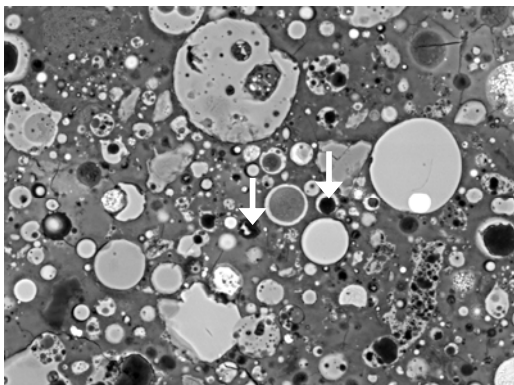
(a)  $\text{SiO}_2\text{-Na}_2\text{O}$ : 0 -1.5(b)  $\text{SiO}_2\text{-Na}_2\text{O}$ : 0.5 -1.5(c)  $\text{SiO}_2\text{-Na}_2\text{O}$ : 1.0 -1.5(d)  $\text{SiO}_2\text{-Na}_2\text{O}$ : 1.5-1.5(e)  $\text{SiO}_2\text{-Na}_2\text{O}$ : 1.0 -1.3(f)  $\text{SiO}_2\text{-Na}_2\text{O}$ : 1.0-1.0

Figure 4.13 BSE images of AAFA with different  $\text{SiO}_2$  and  $\text{Na}_2\text{O}$  content at the ages of 7 days ( $40^\circ\text{C}$ ) ( $248 \times 188 \mu\text{m}$ ); samples were named as  $\text{SiO}_2\text{-Na}_2\text{O}$  mole content with respect to 1 kg/fly ash; arrows indicate the cavities in AAFA

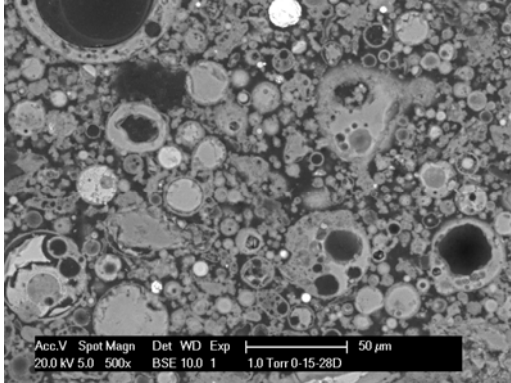
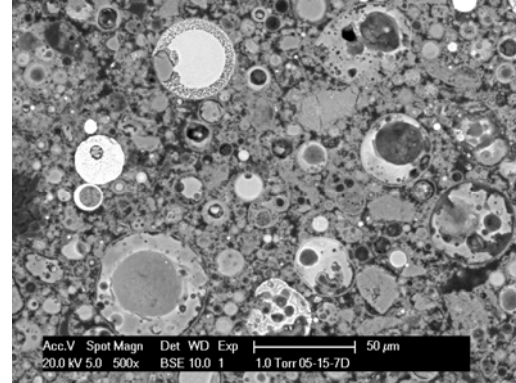
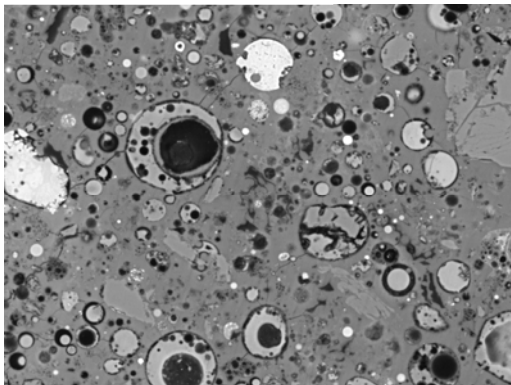
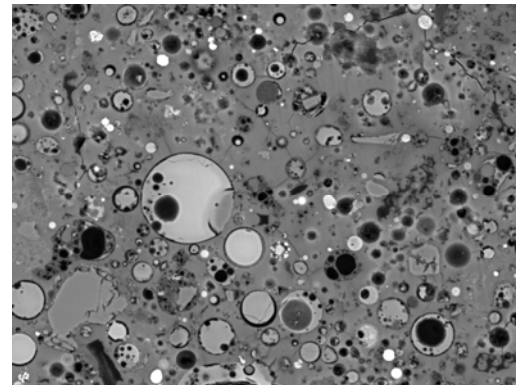
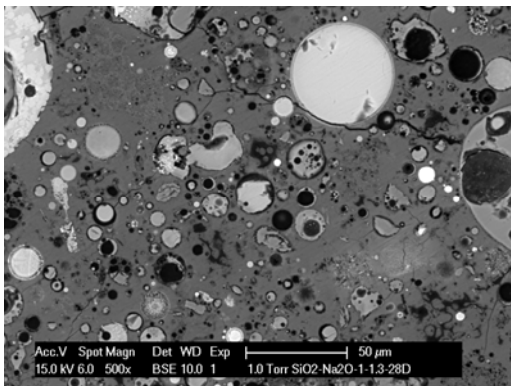
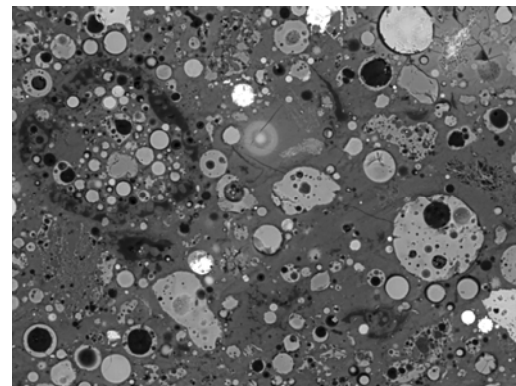
(a)  $\text{SiO}_2\text{-Na}_2\text{O}$ : 0 -1.5(b)  $\text{SiO}_2\text{-Na}_2\text{O}$ : 0.5 -1.5(c)  $\text{SiO}_2\text{-Na}_2\text{O}$ : 1.0 -1.5(d)  $\text{SiO}_2\text{-Na}_2\text{O}$ : 1.5-1.5(e)  $\text{SiO}_2\text{-Na}_2\text{O}$ : 1.0-1.3(f)  $\text{SiO}_2\text{-Na}_2\text{O}$ : 1.0-1.0

Figure 4.14 BSE images of AFAA with different  $\text{SiO}_2$  and  $\text{Na}_2\text{O}$  content at the ages of 28 days ( $40^\circ\text{C}$ ) ( $248 \times 188 \mu\text{m}$ ); samples were named as  $\text{SiO}_2\text{-Na}_2\text{O}$  mole content with respect to 1 kg/fly ash

### 4.3.3 Un-reacted fly ash and degree of reaction of AAFA pastes

Using the image analysis method introduced in Section 4.2.3, the relative volume fraction of un-reacted fly ash as a function of age is plotted in Figure 4.15 for mixtures  $\text{SiO}_2\text{-Na}_2\text{O}=1.0\text{-}1.0$ ,  $1.0\text{-}1.3$ ,  $1.0\text{-}1.5$  and  $1.5\text{-}1.5$ , respectively. For the other two mixtures ( $0\text{-}1.5$  and  $0.5\text{-}1.5$ ), because the reaction products were loose and porous, the obtained BSE images (Figure 4.13a, b and Figure 4.14a, b) were not as clear as the other mixtures. It is thus difficult to distinguish between the un-reacted fly ash particles and the reaction products in the BSE images of these two mixtures. For this reason, the image analysis for mixtures  $0\text{-}1.5$  and  $0.5\text{-}1.5$  were not performed.

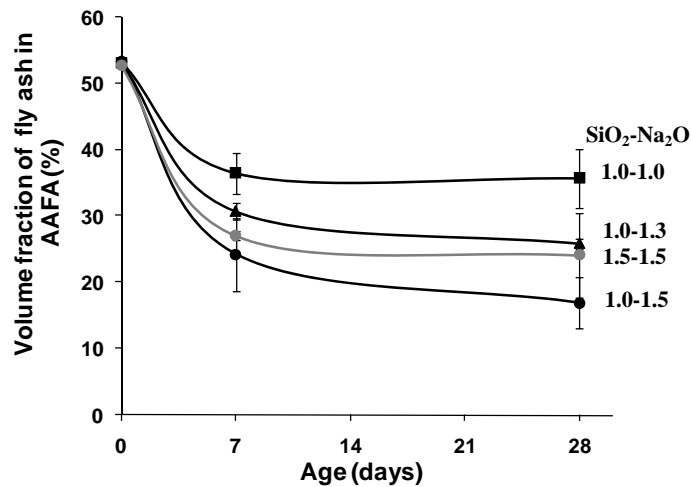


Figure 4.15 Relative volume fraction of un-reacted fly ash in AAFA mixtures at different ages, determined by BSE image analysis

Figure 4.15 shows that the relative volume fractions of un-reacted fly ash decreased with longer curing age for the investigated AAFA mixtures. The reduction of the relative volume fraction was more pronounced at 7 days than 28 days, indicating that most of the reaction happened at early ages.

According to Equation 4.1, the degree of reaction,  $\alpha(t)$ , can be calculated from the amount of the remaining un-reacted fly ash (Figure 4.15). The results are plotted in Figure 4.16. It shows that the degree of reaction of AAFA mixtures was affected by both the  $\text{SiO}_2$  and  $\text{Na}_2\text{O}$  content.

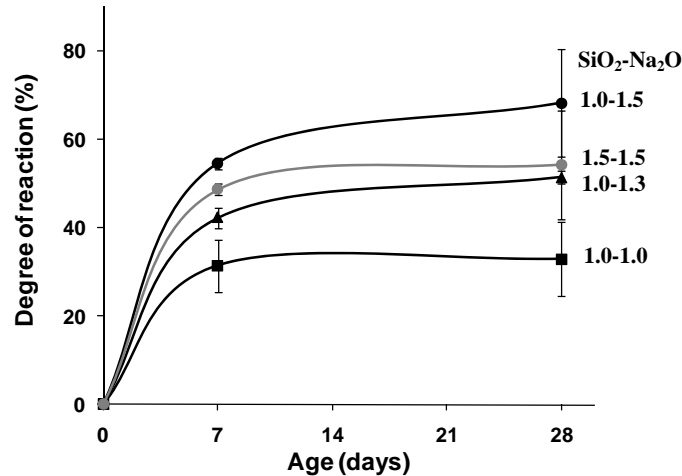


Figure 4.16 Degree of reaction of AAFA pastes with different  $\text{SiO}_2$  and  $\text{Na}_2\text{O}$  content and different ages, determined by the amount of the remaining un-reacted fly ash (Equation 4.1)

#### *The effect of sodium content*

In general, a lower  $\text{Na}_2\text{O}$  content led to a lower degree of reaction of AAFA samples. For example, for samples 1.0-1.5, with higher  $\text{Na}_2\text{O}$  content (1.5 mol/kg fly ash), the relative volume fraction of un-reacted fly ash after 7 days was 24.2 % with a standard deviation of 5.5 % (Figure 4.15), corresponding to a reaction degree of 54.6 % with a standard deviation of 10.4 % (Figure 4.16). When the  $\text{Na}_2\text{O}$  content decreased to 1.3 and 1.0 mol/kg fly ash, e.g. samples 1.0-1.3 and 1.0-1.0, the remaining fly ash volume fraction after 7 days increased to 30.7 % (with a standard deviation of 1.3 %) and 36.5 % (with a standard deviation of 3.1 %), respectively, which corresponds to the reaction degree of 42.3 % (with a standard deviation of 2.4 %) and 31.4 % (with a standard deviation of 5.9 %), respectively, much lower than that of samples 1.0-1.5. The results of degree of reaction derived from BSE image analysis at 7 days was in line with the results of heat evolution shown in Chapter 3 (Figure 3.10). As described in Chapter 2, the reaction process of alkali activation of fly ash involves five steps: namely dissolution, speciation equilibrium, gelation, reorganization and polymerization and hardening. The addition of alkali cations (expressed as  $\text{Na}_2\text{O}$  content here) into the activating solutions is considered to have two effects. First, it increases the pH in the solution. A high amount of  $\text{OH}^-$  ions helps to break the Si–O–Si and Si–O–Al bonds of the reactive fly ash into small silicon and aluminum species [Provis and Van Deventer, 2009]. These small ionic species may form a coagulated structure, resulting in a three-dimensional aluminosilicate gel. Second, the alkali cations balance the electric charge in the three-dimensional tetrahedral Si and Al structure [Criado, Fernandez-Jimenez et al., 2007b], being incorporated into the gel. With a higher alkali content, more fly ash particles dissolve in the medium, ready for the next steps of reactions (gelation and polymerization), leading to a higher degree of reaction.



### *The effect of silica content*

The silica content in the activating solutions affects the reaction in a different way. Samples with higher silica content had lower degree of reaction, e.g. Figure 4.16 shows that samples  $\text{SiO}_2\text{-Na}_2\text{O}=1.5\text{-}1.5$ , with higher silica content, showed lower degree of reaction than samples  $\text{SiO}_2\text{-Na}_2\text{O}=1.0\text{-}1.5$  both at 7 days and 28 days. According to Kinrade and Swaddle [1988a; 1988b], an increase of silica concentration led to a higher degree of silicate ion polymerization in the alkali solutions. For a higher amount of silica, the fraction of monomer and dimer form of silicate species decreased, while the fraction of trimer units grew. The monomeric and dimeric silicates can directly react with the aluminate anions, forming an initial aluminosilicate gel in fairly short time, while silicate trimers reacted relatively slowly with the aluminate anions that was dissolved from the fly ash [Rees, Provis et al., 2007a]. The phases formed with high silica addition were fairly stable [Criado, Fernandez-Jimenez et al., 2008]. This hampered the subsequent reaction and further dissolution of fly ash particles, leading to a lower degree of reaction.

### **4.3.4 Chemical bonds of AAFA pastes**

The chemical bonds of fly ash before and after the alkali activation can be monitored by the ATR-FTIR technique. This technique allows the identification of different chemical bonds in a molecule from the absorption of infrared radiation at various wavelengths. Typical FTIR spectra of the AAFA samples (mixtures  $\text{SiO}_2\text{-Na}_2\text{O}=1.0\text{-}1.5$ ) as well as the original fly ash are shown in Figure 4.17. It is observed that the spectrum of original fly ash is featureless, with predominantly broad peaks due to the glassy nature and heterogeneity of the ash. The bands generated by many phases (both crystalline and vitreous phases) overlapped in the area between  $1200$  and  $800\text{ cm}^{-1}$ , generating a wide, intense band (T-O band, T = Si or Al) as shown in Figure 4.17.

The position of the main T-O asymmetric stretching band has been used in many studies to indicate the relative changes of the gel structure (Si/Al ratio) of AAFA samples [Criado, Fernandez-Jimenez et al., 2007a; Rees, Provis et al., 2007a; Rees, Provis et al., 2007b]. The position of the T-O asymmetric stretching band is normally defined as the point of maximum absorbance in the region of  $1200\text{-}800\text{ cm}^{-1}$  [Rees, Provis et al., 2007a] and referred to as the “main band” in the spectra of fly ash and AAFA. It has been reported that the lower the wavenumber of the main T-O vibration band (main band) moves, the higher the substitution of tetrahedral Al in the network is (lower Si/Al ratio) [Criado, Fernandez-Jimenez et al., 2007a]. In Figure 4.17, it can be observed that the main band attributed to Si-O and Al-O asymmetric vibration in the FTIR spectra of fly ash was centered at  $1031\text{ cm}^{-1}$ . After the alkali activation, the main band became narrower and moved towards a lower wavenumber ( $957\text{ cm}^{-1}$ ). The movement was related to the formation of aluminosilicate gel network [Rees, Provis et al., 2007b]. This main band shifts back to a slightly higher wavenumber over time (spectra of 7 and 28 days in Figure 4.17), indicating that more Si was incorporated into the gel network, forming a Si-rich gel (higher Si/Al ratio) [Rees, Provis et al., 2007a]. The results were in line with the findings of other authors [Fernández-Jiménez and Palomo, 2005a], that during the alkali activation of fly ash an Al-rich gel was formed, followed by the formation of a Si-rich gel. Another important feature is the presence of a small peak in the region  $630\text{-}760\text{ cm}^{-1}$  (arrowed in Figure 4.17). This region generally corresponds to the aluminosilicate ring and cage structures [Criado, Fernandez-Jimenez et al., 2007b; Flanigen et al., 1971], and the peaks indicate the

presence of crystalline phases. These peaks became clear at 28 days. Further examination of the types of crystalline phases will be dealt with in more detail later when discussing the XRD results.

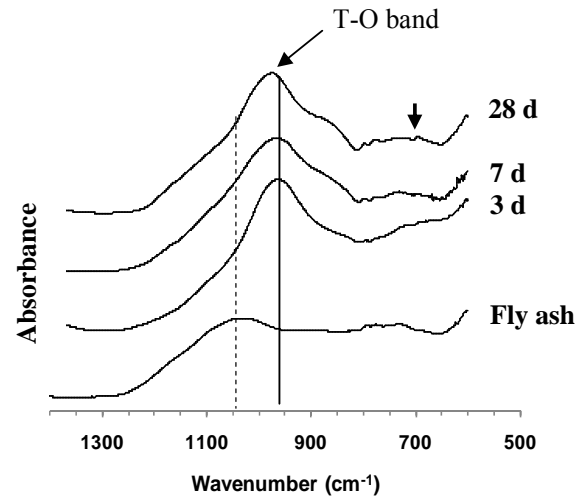


Figure 4.17 Typical FTIR spectra of AAFA pastes ( $\text{SiO}_2\text{-Na}_2\text{O} = 1.0\text{-}1.5$ ) at different ages

The effect of  $\text{SiO}_2$  and  $\text{Na}_2\text{O}$  content on the position of the main band (T-O, T = Si or Al) in aluminosilicate gel structure over 90 days are presented in Figures 4.18 and 4.19, respectively.

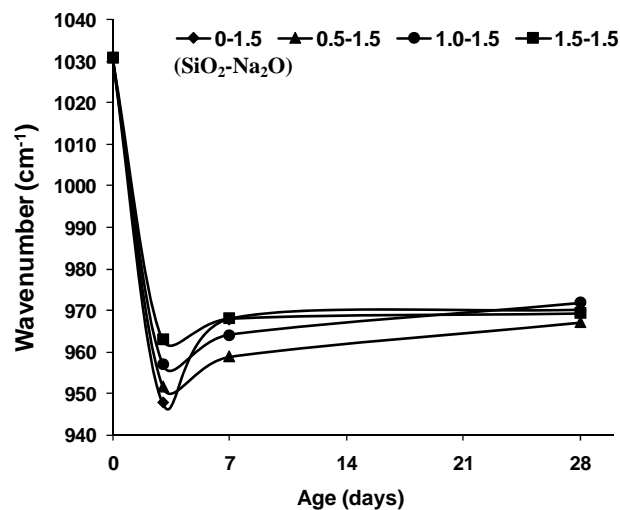


Figure 4.18 Change of the wavenumber of the T-O band for AAFA pastes with different  $\text{SiO}_2$  content at different age

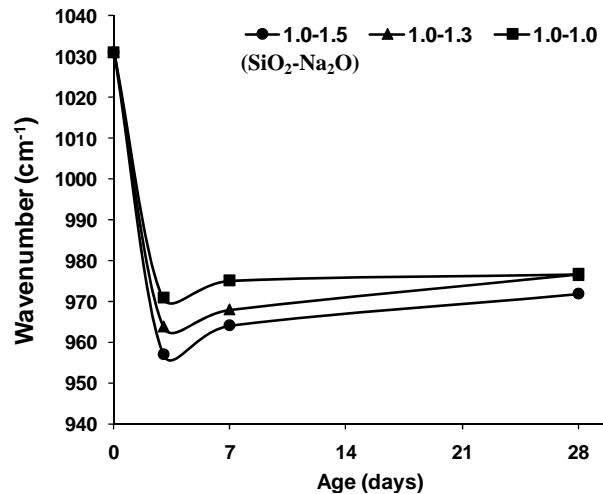


Figure 4.19 Change of the wavenumber of the T-O band for AAFA pastes with different Na<sub>2</sub>O content at different age

#### *The effect of silica content*

From Figure 4.18, it can be observed that samples with no silica (SiO<sub>2</sub>-Na<sub>2</sub>O=0-1.5) show the highest shift of the main band (T-O, T = Si or Al) at 3 days (from 1031 cm<sup>-1</sup> to 947 cm<sup>-1</sup>), while the shift of the main band was less intense with an increase of silica content in the activator, e.g. SiO<sub>2</sub>-Na<sub>2</sub>O=0.5-1.5 (from 1031 cm<sup>-1</sup> to 951 cm<sup>-1</sup>), 1.0-1.5 (from 1031 cm<sup>-1</sup> to 957 cm<sup>-1</sup>) and SiO<sub>2</sub>-Na<sub>2</sub>O=1.5-1.5 (from 1031 cm<sup>-1</sup> to 963 cm<sup>-1</sup>). This trend indicates that the addition of silica in the activator influenced the chemical structure of the resulting gel: specimens with higher silica content produced an aluminosilicate gel with higher Si/Al ratio at early ages (3 days). This is, on the one hand, because the added silica was incorporated into the aluminosilicate gel in the early age, which in turn increased the silica content in the reaction products (gel with higher Si/Al ratio). On the other hand, the addition of more silica led to a higher polymerization of the silicate species in the activator (forming trimers, rings, etc.), which retarded further dissolution of fly ash. Thus less Al was substituted in the reaction, observed as a less intense shift of the T-O band. After 7 days, the main band moved back to a higher wavenumber for all AAFA mixtures (Figure 4.18), indicating that the resulting gel was transferred from an Al-rich gel to Si-rich gel. After 28 days, the main band for all the investigated mixtures had a similar wavenumber (Figure 4.18), which indicates a similar Si/Al ratio of the resulting gel. The findings were in good agreement with the nuclear magnetic resonance (NMR) results reported by Criado et al. [2008], who found that the addition of silica affected the intermediate stages of the reaction product but not the end results.

#### *The effect of sodium content*

Figure 4.19 shows that the shift of the T-O band was less intense for specimens with higher Na<sub>2</sub>O content. For samples SiO<sub>2</sub>-Na<sub>2</sub>O=1.0-1.0, 1.0-1.3 and 1.0-1.5 the wavenumber of the main band at 3 days was lower for the higher the sodium content (971 cm<sup>-1</sup>, 964 cm<sup>-1</sup> and 957 cm<sup>-1</sup>, respectively). At 7 days, the main band shifted back to a higher wavenumber for all AAFA mixtures, but still specimens with higher Na<sub>2</sub>O content showed a lower wavenumber of the main band (Figure 4.19). This trend

persisted till the age of 28 days. This indicates that the resulting gel had a lower Si/Al ratio for AAFA samples with higher sodium content. It is known that the dissolution process of fly ash was accelerated by the addition of more sodium in the AAFA system, in which the reactive Al dissolved more rapidly than the Si [Fernández-Jiménez and Palomo, 2005a]. A higher sodium content led to a higher Al<sup>3+</sup> ion content in the medium at early age, resulting in a higher Al substitution in gel formation. As the reaction proceeded, the dissolution of Si continued. The silica was gradually incorporated into the gel, increasing the Si/Al ratio of the reaction products. This resulted in the main band moving back to a higher wavenumber after 7 days.

#### 4.3.5 Phase development measured by XRD of AAFA pastes

Figure 4.20 and Figure 4.21 show that the reaction products of AAFA pastes were predominantly amorphous compounds, regardless the SiO<sub>2</sub> and Na<sub>2</sub>O content. Quartz and mullite are the main crystalline phases that were left in the un-reacted fly ash. The vitreous phase in original fly ash exhibited a bump with its peak in the range of 20°-35° 2θ. After the reaction, the peak of the bump shifted to a higher degree in the range of 27° to 32° 2θ (Figure 4.20 and Figure 4.21).

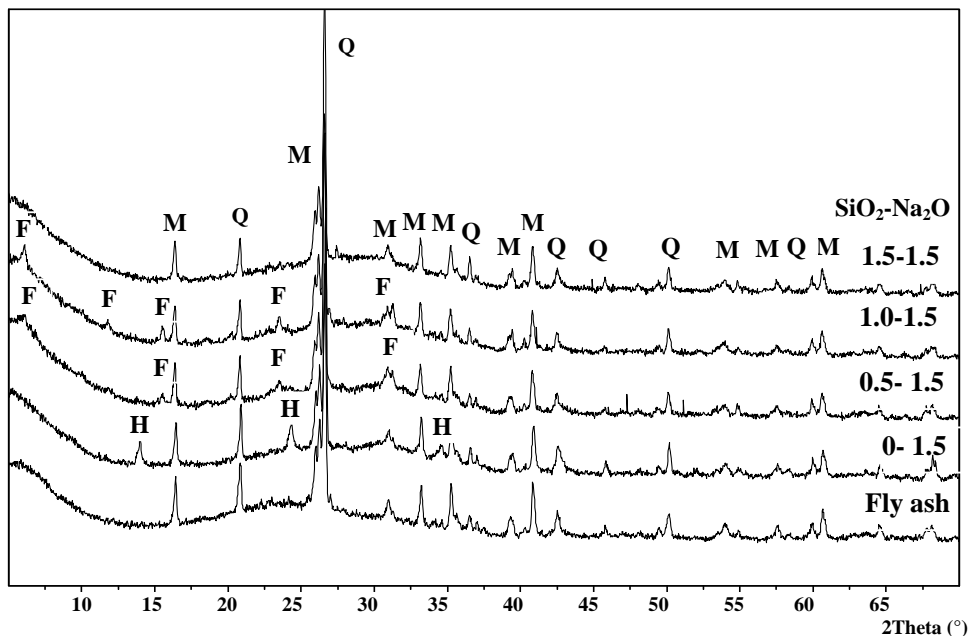


Figure 4.20 XRD of alkali activated fly ash with various SiO<sub>2</sub> content at 28 days 40°C; Q=quartz (SiO<sub>2</sub>, PDF# 85-0457); M=mullite (Al<sub>4.8</sub>O<sub>9.54</sub>Si<sub>1.2</sub>, PDF# 84-1205); H=hydroxysodalite (Na<sub>4</sub>Al<sub>3</sub>Si<sub>3</sub>O<sub>12</sub>(OH), PDF# 11-0401); F=faujasite (Na<sub>1.84</sub>Al<sub>2</sub>Si<sub>4</sub>O<sub>11.92</sub>·7H<sub>2</sub>O, PDF# 38-0238)

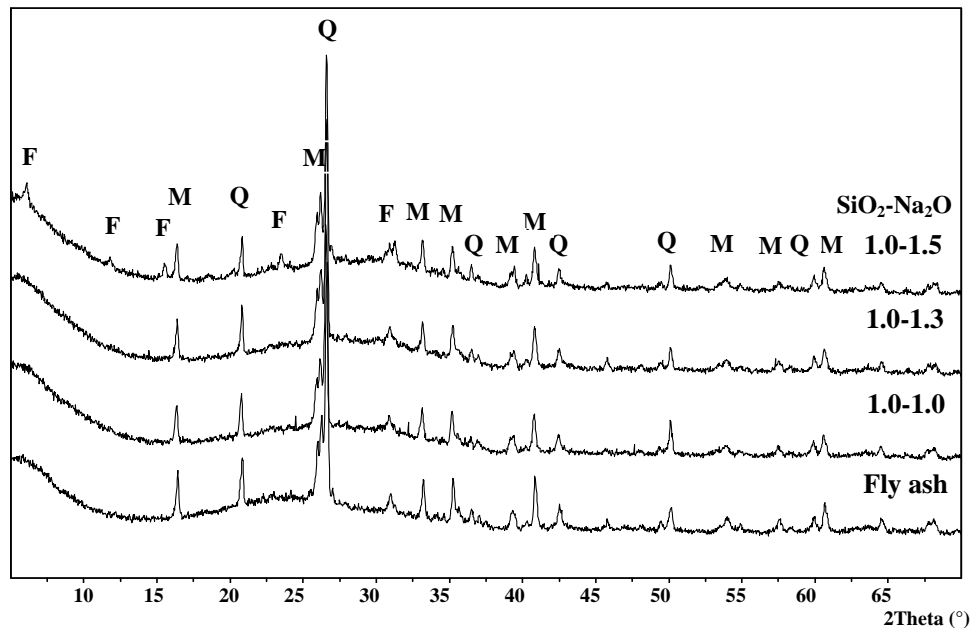


Figure 4.21 XRD of alkali activated fly ash with various Na<sub>2</sub>O at 28 days 40°C; Q=quartz (SiO<sub>2</sub>, PDF# 85-0457); M=mullite (Al<sub>4,8</sub>O<sub>9,54</sub>Si<sub>1,2</sub>, PDF# 84-1205); F=faujasite (Na<sub>1,84</sub>Al<sub>2</sub>Si<sub>4</sub>O<sub>11,92</sub>·7H<sub>2</sub>O, PDF# 38-0238)

#### *The effect of silica content*

Different types of zeolites (defined in section 2.4.2 in Chapter 2) are observed in Figure 4.20 for the AAFA samples when the silica content varied from zero to 1.0 mol/kg fly ash: hydroxysodalite (Na<sub>4</sub>Al<sub>3</sub>Si<sub>3</sub>O<sub>12</sub>(OH)) for samples 0-1.5 and faujasite-Na (Na<sub>1,84</sub>Al<sub>2</sub>Si<sub>4</sub>O<sub>11,92</sub>·7H<sub>2</sub>O) for samples 0.5-1.5 and 1.0-1.5. No new crystalline phases were detected when the silica content is 1.5 mol/kg fly ash (samples 1.5-1.5). These results are in line with the findings of other authors [Criado, Fernandez-Jimenez et al., 2007b; Fernández-Jiménez and Palomo, 2005b]. Because the AAFA samples with increasing silica content has a higher degree of silica polymerization, it then requires more energy for transforming the aluminosilicate gel into a well organized crystalline phase [Criado, Fernandez-Jimenez et al., 2007b].

#### *The effect of sodium content*

The sodium oxide content also had a significant effect on the mineralogy of AAFA samples. As shown in Figure 4.21, when the Na<sub>2</sub>O content was 1.0 and 1.3 mol/kg fly ash, no zeolite was detected for AAFA samples at 28 days (pattern 1.0-1.0 and 1.0-1.3). When the Na<sub>2</sub>O content is 1.5 mol/kg fly ash, faujasite-Na was observed at 28 days (pattern 1.0-1.5). A similar result was also reported by Lloyd [Provis and Van Deventer] in the aging of AAFA (cured at 95 °C in sealed condition).

One important reason to study the mineralogy of AAFA is to evaluate its long term stability [Provis and Van Deventer, 2009]. In previous studies about alkali activated metakaolin [De Silva and Sagoe-Crenstil, 2008; Provis and Van Deventer, 2009],

which has similar composition of raw material and reaction products as alkali activated fly ash (as discussed in Chapter 2), the strength decreased with the formation of zeolites. In the case of alkali activated fly ash, similar findings were also reported [Criado, Fernandez-Jimenez et al., 2007b], indicating that a higher content of zeolites in AAFA hampered the mechanical strength development. In the aging test of AAFA conducted by Lloyd et. al [Provis and Van Deventer, 2009], however, the strength did not decrease with the formation of zeolites (cured at 95 °C in sealed condition). In this study, it was found that samples 1.0-1.5, which had zeolites formed, exhibited the highest compressive strength at 28 days. This is in line with the findings by Lloyd et. al. However, it is also note that the formation of zeolites in samples 1.0-1.5 was limited. The small amount of zeolites may have little influence to the strength of the samples. Thus no decline of strength was observed. For the other two mixtures, i.e. samples 0-1.5 and 0.5-1.5, which also had zeolites formed but showed lower mechanical strength, the lower strength was mainly attributed to the limited amount of gel formed during the reaction and the porous microstructure of the matrix (Figure 4.13a, b and Figure 4.14a, b), rather than the formation of zeolites.

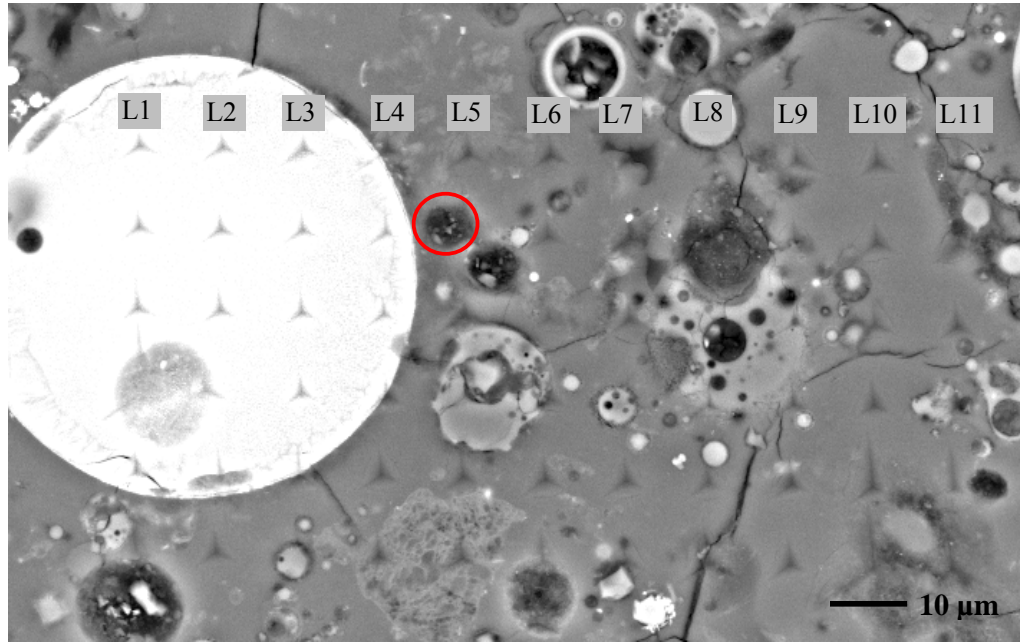
#### 4.3.6 Elastic properties of AAFA pastes on micro scale

##### *Nanoindentation combined with ESEM and EDX*

The elastic modulus of AAFA on the micrometer scale can be characterized by the nanoindentation technique. By combining the nanoindentation results, BSE image and EDX analysis, the elastic modulus value of each nano indent can be correlated to the phase where the nano indent was made. Figure 4.22 shows a typical BSE image of AAFA specimen ( $\text{SiO}_2\text{-Na}_2\text{O}=1.5\text{-}1.5$  at 7 days) after the nanoindentation test and corresponding values of the elastic modulus (Table in Figure 4.22). Figure 4.23 displays the element distribution in the corresponding area, determined by EDX mapping. Areas with high concentration of a certain element are brighter in the mapping image.

From Figure 4.23 it can be inferred that the concentrations of elements varied significantly for different un-reacted fly ash particles. For example, in Figure 4.23a, the fly ash particle marked as 1 was rich in Al (high intensity in Figure 4.23c), particle marked as 2 was rich in Si (high intensity in Figure 4.23b), particle 3 was rich in Fe (high intensity in Figure 4.23e) and particle 4 was rich in Ca (high intensity in Figure 4.23f). By locating the indents on these particles in Figure 4.22, different elastic modulus values (values with grey background) were found corresponding to the fly ash particles with different element components: e.g. For Fe-rich fly ash particle, the elastic modulus was measured between 71.0-106.0 GPa; for Al-rich fly ash particle, the measured elastic modulus was between 38.5-65.4 GPa. Si-rich fly ash particle presented the highest modulus (82.9 GPa) in AAFA matrix.

For the aluminosilicate gel matrix the EDX mapping shows that the gel mainly contained Na, Si and Al (Figure 4.23b, c and d), and these elements were homogeneously distributed in the gel matrix. The corresponding measured modulus of the aluminosilicate gel was in the range of 10.8-17.9 GPa (bold values in Figure 4.22), lower than that of the un-reacted fly ash particles. For the pores in the matrix (red circle in Figure 4.22), the measured modulus was the lowest: 1.0 GPa. The non-zero modulus of pores may be caused by the contact of indenter with some solid material when the penetration depth increased from 0 to 1000 nm.



L1	L2	L3	L4	L5	L6	L7	L8	L9	L10	L11
****	101.5	84.9	23.2	<b>12.8</b>	<b>13.7</b>	<b>16.2</b>	****	<b>14.5</b>	<b>14.5</b>	7.0
100.1	102.1	97.9	88.9	1.0	<b>13.0</b>	<b>19.8</b>	11.8	<b>13.9</b>	<b>13.9</b>	<b>11.7</b>
106.0	102.7	101.5	91.8	<b>13.7</b>	<b>10.9</b>	<b>11.4</b>	33.3	59.9	<b>12.9</b>	<b>15.2</b>
137.7	92.6	99.3	34.0	82.9	21.1	38.5	65.4	8.8	<b>15.3</b>	11.3
86.3	71.0	42.6	<b>13.0</b>	<b>14.1</b>	<b>14.6</b>	<b>12.9</b>	<b>10.9</b>	<b>16.1</b>	****	24.6
18.6	<b>13.0</b>	28.6	<b>17.2</b>	24.8	23.6	<b>14.7</b>	<b>17.9</b>	<b>16.2</b>	54.3	25.7

Figure 4.22 BSE image of the area of indents and the corresponding value of the elastic modulus (GPa) on mixture 1.5-1.5 ( $\text{SiO}_2\text{-Na}_2\text{O}$ ) at 7 days

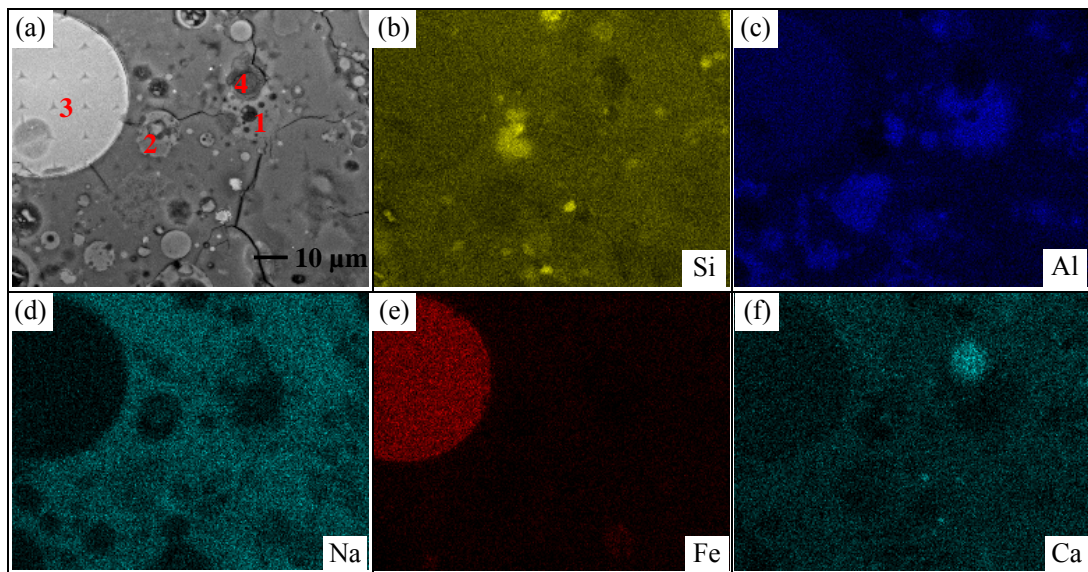
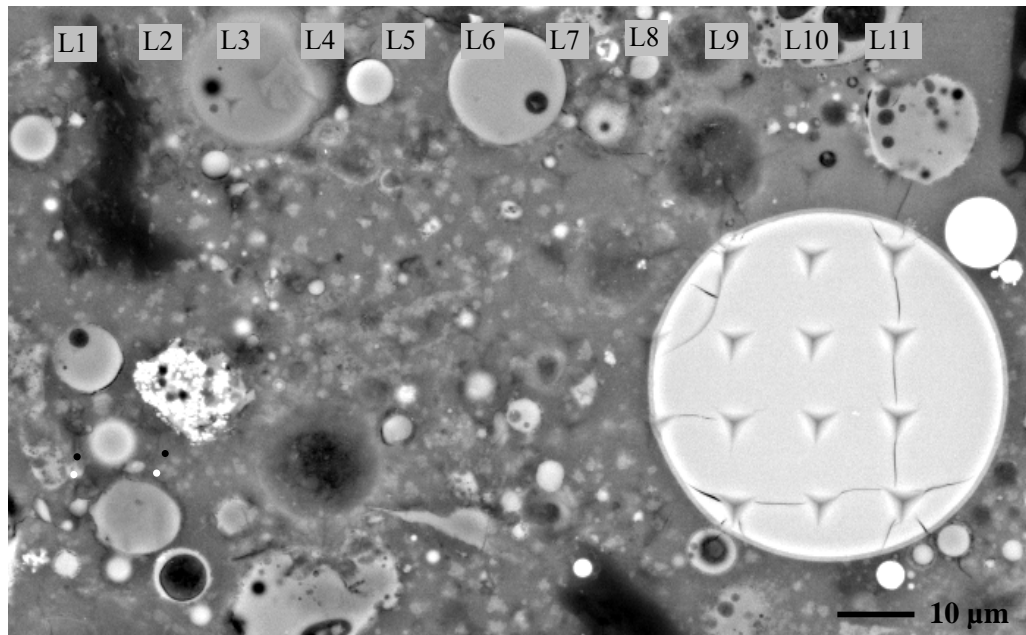


Figure 4.23 Element distribution maps of the area of indents on mixture 1.5-1.5 ( $\text{SiO}_2\text{-Na}_2\text{O}$ ) at 7 days. 1 Al-rich, 2 Si-rich, 3 Fe-rich, 4 Ca-rich fly ash particles. The higher the concentration of each element, the brighter the color in the image.

Figure 4.24 shows the BSE image and corresponding elastic modulus value of each indent (Table in Figure 4.24) of specimen  $\text{SiO}_2\text{-Na}_2\text{O}=1.0\text{-}1.0$  at the age of 7 days. Figure 4.25 displays the elementary mapping of the corresponding area. Similar to the findings in specimen  $\text{SiO}_2\text{-Na}_2\text{O}=1.5\text{-}1.5$ , the elastic modulus of the un-reacted fly ash in specimen 1.0-1.0 had the highest value (from 29.4 GPa to 91.6 GPa in Figure 4.24). However, the measured elastic modulus of the gel of specimen  $\text{SiO}_2\text{-Na}_2\text{O}=1.0\text{-}1.0$  (4.0-11.3 GPa, bold values in Figure 4.24) was much lower than that of specimen  $\text{SiO}_2\text{-Na}_2\text{O}=1.5\text{-}1.5$  (10.9-17.9 GPa). From the EDX mapping of the gel phase of specimens  $\text{SiO}_2\text{-Na}_2\text{O}=1.0\text{-}1.0$ , shown in Figure 4.25, little difference of element distribution can be found compared to specimens  $\text{SiO}_2\text{-Na}_2\text{O}=1.5\text{-}1.5$ .

The findings derived from the comparison of BSE image, EDX mapping and nanoindentation results of representative areas of AAFA pastes provide evidence for further identification of each phase (pore, gel phase or un-reacted fly ash) in the large number of data of elastic modulus derived from nanoindentation tests, as will be discussed in the next section.





L1	L2	L3	L4	L5	L6	L7	L8	L9	L10	L11
<b>8.3</b>	<b>11.3</b>	66.1	68.7	<b>9.4</b>	30.7	21.1	14.8	****	17.0	53.9
<b>8.1</b>	<b>5.9</b>	<b>5.6</b>	<b>5.2</b>	16.8	<b>5.1</b>	<b>5.6</b>	<b>8.2</b>	2.6	17.5	42.4
<b>6.5</b>	11.7	<b>4.0</b>	<b>6.9</b>	<b>5.5</b>	<b>5.4</b>	<b>7.4</b>	<b>8.9</b>	75.7	84.0	83.3
29.4	13.4	<b>4.7</b>	<b>7.8</b>	<b>9.3</b>	<b>6.9</b>	<b>5.4</b>	<b>7.7</b>	86.1	88.7	90.1
<b>5.3</b>	<b>5.0</b>	14.2	11.0	22.1	<b>4.9</b>	<b>5.4</b>	19.1	85.3	91.2	90.7
<b>5.2</b>	20.0	50.7	***	39.8	17.8	10.2	<b>6.8</b>	76.4	89.8	82.4

Figure 4.24 BSE image of the area of indents and the corresponding value of the elastic modulus (GPa) on mixture 1.0-1.0 ( $\text{SiO}_2\text{-Na}_2\text{O}$ ) at 7 days

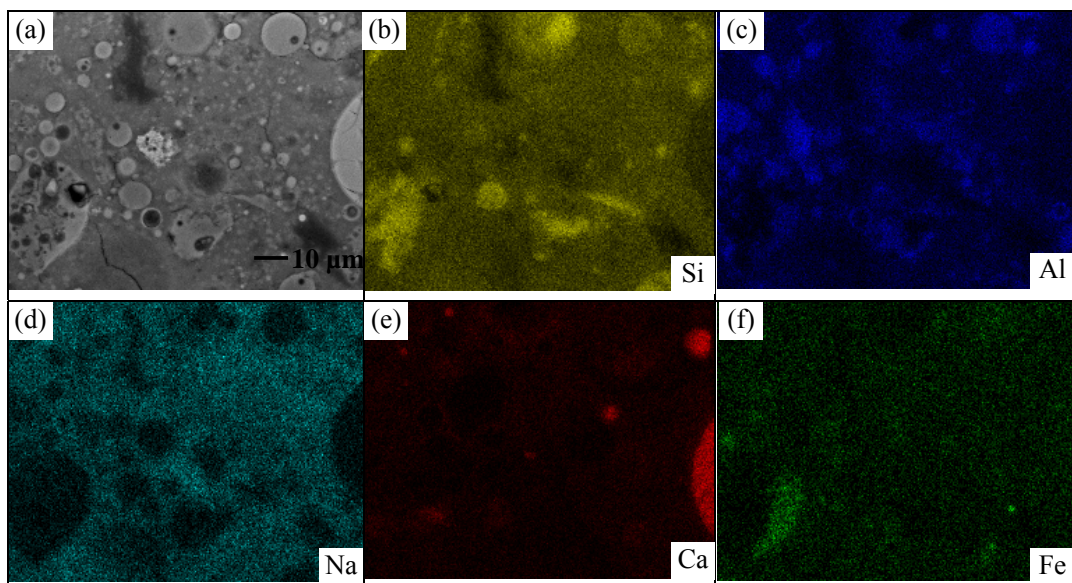


Figure 4.25 Element distribution maps of the area of indents on mixture 1.0-1.0 ( $\text{SiO}_2\text{-Na}_2\text{O}$ ) at 7 days. The higher the concentration of each element, the brighter the color in the image.

### Mapping of elastic modulus

The representative elastic modulus maps of mixtures  $\text{SiO}_2\text{-Na}_2\text{O}=1.5\text{-}1.5$ ,  $1.0\text{-}1.5$  and  $1.0\text{-}1.0$  at the age of 7 days and 28 days are given in Figure 4.26. From these maps, the effect of the activator content ( $\text{SiO}_2$  and  $\text{Na}_2\text{O}$  content) and curing age on the elastic modulus of AAFA mixtures can be directly seen. For all the AAFA mixtures, the overall modulus increased with longer curing age, evidenced by the modulus of the main phase (gel phase) in the matrix increasing to higher value with time (Figure 4.26). An increase of both silica and sodium content led to a higher elastic modulus of the specimen at 7 days. For example, in mixture  $\text{SiO}_2\text{-Na}_2\text{O}=1.0\text{-}1.0$ , with  $\text{Na}_2\text{O}$  content of 1 mol/kg fly ash, a larger area exhibited an elastic modulus between 0-10 GPa (Figure 4.26e), while in mixture  $\text{SiO}_2\text{-Na}_2\text{O}=1.0\text{-}1.5$ , with higher  $\text{Na}_2\text{O}$  content (1.5 mol/kg fly ash), a larger area corresponding to an elastic modulus between 10-20 GPa (Figure 4.26c). In mixture  $\text{SiO}_2\text{-Na}_2\text{O}=1.5\text{-}1.5$ , with both  $\text{SiO}_2$  and  $\text{Na}_2\text{O}$  contents of 1.5 mol/kg fly ash, most of the area exhibited an elastic modulus between 10-20 GPa (Figure 4.26a). The results indicate that mixture  $\text{SiO}_2\text{-Na}_2\text{O}=1.5\text{-}1.5$  had the densest matrix, followed by  $\text{SiO}_2\text{-Na}_2\text{O}=1.0\text{-}1.5$  and  $1.0\text{-}1.0$  at the age of 7 days. After 28 days, the elastic modulus of mixture  $\text{SiO}_2\text{-Na}_2\text{O}=1.0\text{-}1.0$  was still the lowest (larger area between 10-20 GPa in Figure 4.26f), while mixture  $\text{SiO}_2\text{-Na}_2\text{O}=1.0\text{-}1.5$  developed similar elastic modulus as mixture  $\text{SiO}_2\text{-Na}_2\text{O}=1.5\text{-}1.5$  (larger area between 20-30 GPa in Figure 4.26b and d).

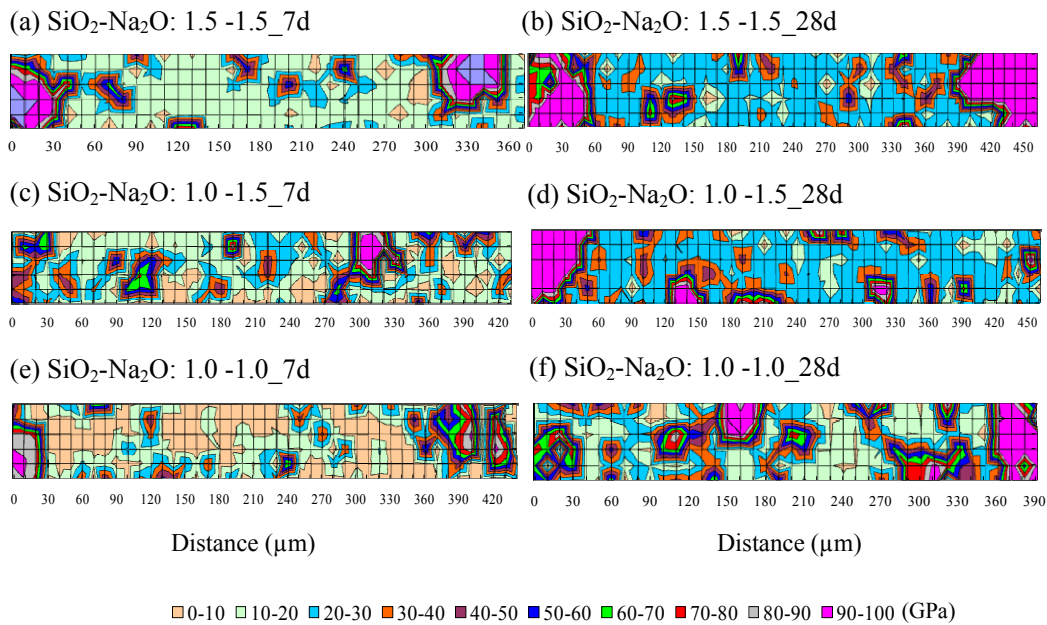


Figure 4.26 Maps of elastic modulus derived from nanoindentation tests of AAFA pastes ( $\text{SiO}_2\text{-Na}_2\text{O}$ ) at 7 days and 28 days

### Frequency histogram of the elastic modulus

The frequency histogram of the elastic modulus data obtained from each test region of AAFA pastes is shown in Figure 4.27.

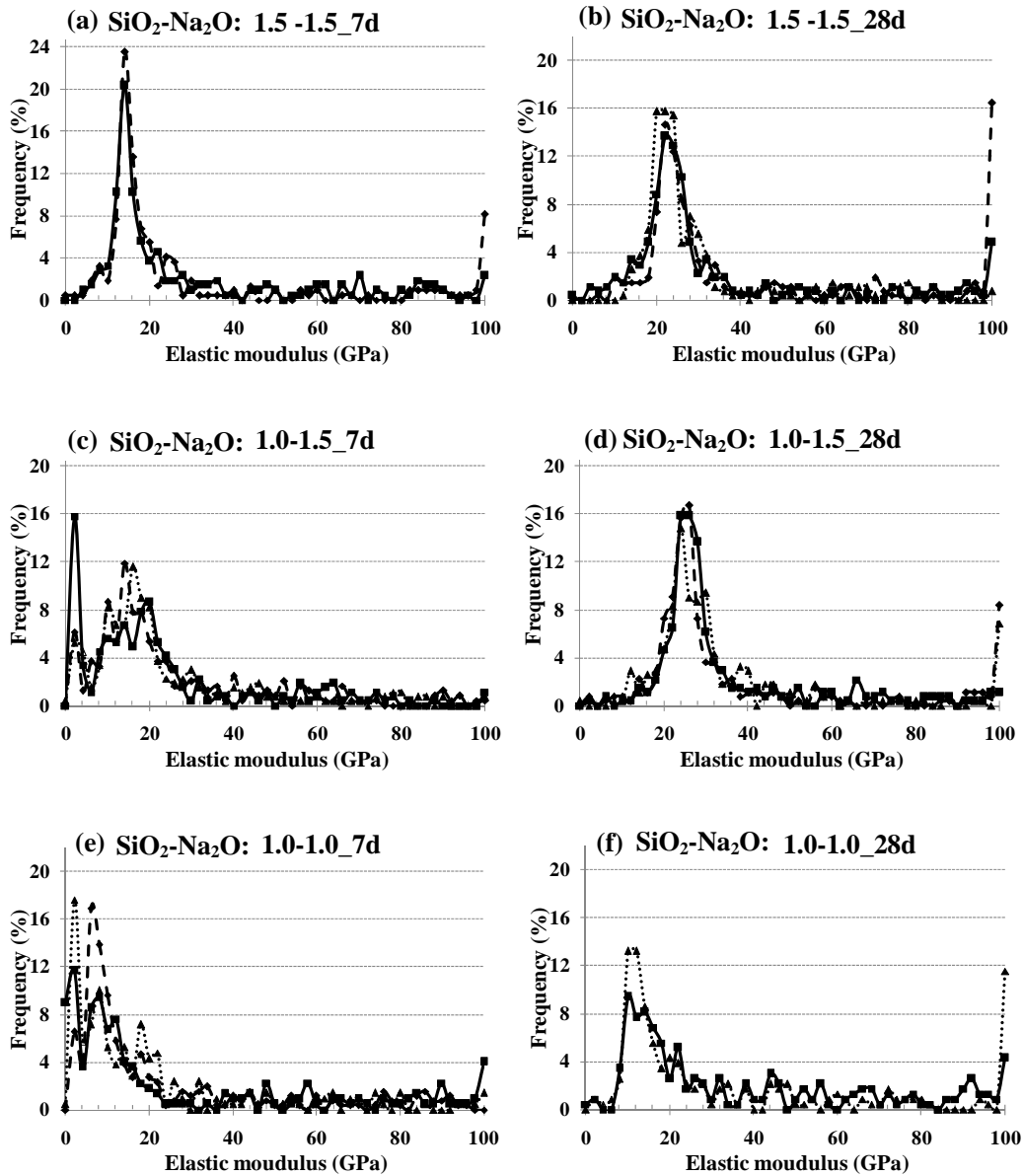


Figure 4.27 Frequency histogram of elastic modulus in two or three regions of different AAFA pastes ( $\text{SiO}_2\text{-Na}_2\text{O}$ ) at 7 days and 28 days, derived from nanoindentation tests

For each AAFA mixture, two or three representative regions were selected for the nanoindentation test. These regions were chosen in order to cover as many indents as possible that came from the gel phase. Thus, the highest peak in the frequency histogram was supposed to correspond to the gel phase. This was confirmed by checking the results of mixture  $\text{SiO}_2\text{-Na}_2\text{O}=1.5\text{-}1.5$  and  $1.0\text{-}1.0$  at 7 days as discussed in the previous section (Figure 4.22 and Figure 4.24): the elastic modulus of the gel phase was between 10.8-17.9 GPa and 4.0-11.3 GPa for mixture  $\text{SiO}_2\text{-Na}_2\text{O}=1.5\text{-}1.5$  and  $1.0\text{-}1.0$  at 7 days, respectively, which was in good agreement with the dominant peak presented in the frequency histogram (10-20 GPa and 4-12 GPa, respectively in Figure 4.27). For some specimens ( $\text{SiO}_2\text{-Na}_2\text{O}=1.0\text{-}1.0$  and  $1.0\text{-}1.5$  at 7 days), two peaks are shown in the frequency histogram (Figure 4.27e and c). The peak between 0-2 GPa is believed to be related to the pores in the test area, indicating a relatively porous matrix of the specimens.

The frequency histograms of the same mixture, but at different tested regions, were similar, with the dominant peak at almost the same value of the elastic modulus (see different lines in one figure in Figure 4.27). It indicates that the gel formed in each AAFA mixture was quite homogenous on the scale of micrometers. This is possibly due to the relative low temperature applied for the heat curing (40 °C), which gave enough time for ion transition and polymerization of species during the alkali activation reaction, resulting in a homogenous gel.

#### ***Elastic modulus/ strength***

The overall frequency histogram of the elastic modulus for each AAFA mixture is plotted in Figure 4.28. The relatively large number of data (around 720 indents) collected from each mixture ensured that the test results are reliable and representative. As can be seen from Figure 4.28, the elastic modulus of the gel phase of AAFA varies with the curing age and  $\text{SiO}_2$  and  $\text{Na}_2\text{O}$  content. The elastic modulus of the gel increased with longer curing age for all AAFA mixtures. In addition, the elastic modulus of the gel phase increased with a higher amount of both  $\text{SiO}_2$  and  $\text{Na}_2\text{O}$  at 7 days: e.g. the peak corresponding to the gel phase of mixture  $1.0\text{-}1.0$  was between 6-8 GPa (Figure 4.28c) compared to around 14 GPa of mixture  $1.5\text{-}1.5$  (Figure 4.28a). At the age of 28 days, the elastic modulus of the gel phase of  $1.0\text{-}1.0$  was still the lowest (between 10-12 GPa in Figure 4.28c), while mixture  $1.0\text{-}1.5$  exhibited higher elastic modulus of the gel phase (between 24-26 GPa in Figure 4.28b) than mixture  $1.5\text{-}1.5$  (between 22-24 GPa in Figure 4.28a).

The trend of the elastic modulus was consistent with the results derived from the compressive strength. Figure 4.29 shows that for all the AAFA mixtures, a higher elastic modulus of the gel phase was found for samples with higher compressive strength. It is important to notice that the elastic modulus measured by nanoindentation shows a local mechanical property at the nano/micro scale, whereas the compressive strength reflects the overall mechanical property of a material. The frequency histogram of the elastic modulus, as shown in Figure 4.28, however, gives the overall trend of the mechanical property of the aluminosilicate gel. Obviously there is a good correlation between the elastic modulus of the gel phase and the compressive strength of AAFA pastes, regardless of mixtures and curing age.

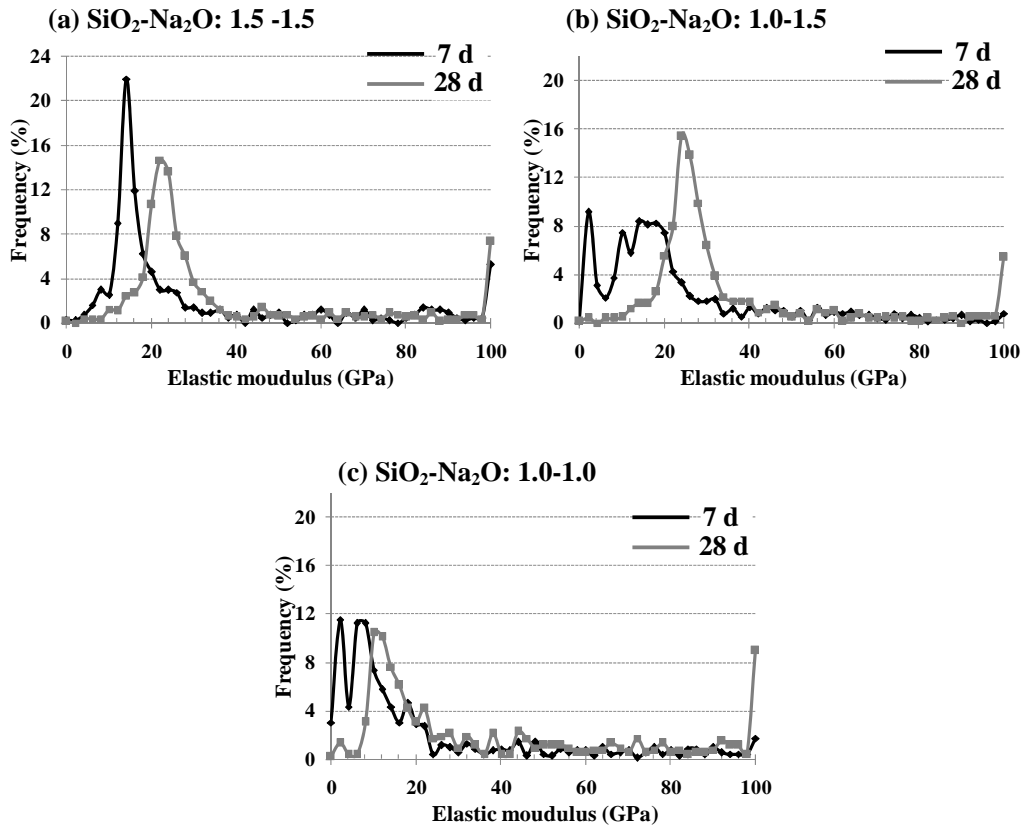


Figure 4.28 Overall frequency histogram of elastic modulus derived from experimental indentation data of AAFA paste

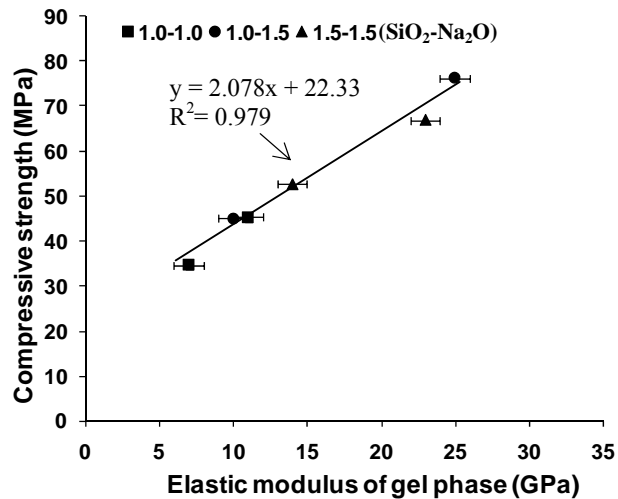


Figure 4.29 Elastic modulus of aluminosilicate gel (measured by nanoindentation) vs. compressive strength (measured by compression-testing machine) of different AAFA pastes ( $\text{SiO}_2\text{-Na}_2\text{O}$ ) at 7 and 28 days

### *Discussion on the factors affecting the elastic modulus of aluminosilicate gel*

It is known that the aluminosilicate gel undergoes a series of reorganization and polymerization processes during the alkali activation reaction, transforming from a Al-rich gel to a Si-rich gel [Fernández-Jiménez, Palomo et al., 2006d]. This phenomenon was also evidenced from the FTIR results as discussed in this study (Section 4.3.4). The formation of Si-enriched aluminosilicate gel improves the mechanical strength more significantly than the Al-rich gel of the AAFA samples [Fernández-Jiménez, Palomo et al., 2006d]. In this study, the results obtained from the FTIR and nanoindentation of each AAFA mixture at different ages also showed that the elastic modulus of the gel phase increased as the gel transformed to a Si-rich gel with longer curing age (higher Si/Al ratio of the gel). This is in line with the previously reported results in literature [Fernández-Jiménez, Palomo et al., 2006d]. However, this is not the case if we compare the FTIR and nanoindentation results of AAFA mixtures with different sodium content. As shown in Figure 4.19, samples 1.0-1.0 showed the highest wavenumber of the main T-O band at 7 days, followed by samples 1.0-1.3 and samples 1.0-1.5. This indicates that the Si/Al ratio of the gel for samples 1.0-1.0 was the highest, and that of samples 1.0-1.5 the lowest. The nanoindentation results (Figure 4.28), however, showed that mixture 1.0-1.5 had a higher elastic modulus of the gel phase than mixture 1.0-1.0 at the age of 7 days (Figure 4.28c), which is not consistent with the results of Si/Al ratio of the gel phase. It means that the elastic modulus of the gel phase of AAFA samples is not entirely determined by the Si/Al ratio of the gel. Other factors may also contribute to the elastic modulus of the gel phase of AAFA. The pore structure of the gel phase is an important one. A finer pore structure means a denser microstructure, thus a higher elastic modulus of the gel. It has been known for a long time that porosity is a major factor governing elastic modulus of elasticity of porous materials [Feldman, 1972]. Several empirical formulae connecting the elastic modulus and porosity have been proposed [Sereda, 1972]. According to these formulae, the elastic modulus decreases with increasing porosity. In this study, it is assumed that the gel phase of mixture 1.0-1.0 was of coarser pore structure than that of mixture 1.0-1.5. Though the gel phase of the AAFA mixture 1.0-1.0 had a higher Si/Al ratio than the AAFA mixture 1.0-1.5, the elastic modulus was still lower due to the coarser pore structure. This assumption was further confirmed by examining the pore structure of different AAFA mixtures later in Chapter 5.

#### **4.4 Concluding remarks**

In this chapter, the reaction product of AAFA pastes with different SiO<sub>2</sub> and Na<sub>2</sub>O content was determined experimentally in terms of the space distribution, the degree of reaction, the chemical bond, the mineral composition and the elastic modulus. Based on the experimental results, the following conclusions can be drawn:

- There are two conflicting effects of the addition of silica in AAFA samples. On the one hand, the presence of a high silica content (1.5 mol/kg fly ash) in the activator retards further dissolution of fly ash particles, resulting in a lower degree of reaction. On the other hand, the added silica improves the microstructure of AAFA samples to a more homogeneous and denser matrix. FTIR results indicate that the gel of AAFA mixture with a higher silica content

(e.g. samples  $\text{SiO}_2\text{-Na}_2\text{O}=1.5\text{-}1.5$ ) had a higher Si/Al ratio, indicating the added silica becoming incorporated in the gel. Due to these two conflicting effects, AAFA mixtures with a higher silica content (e.g. 1.5 mol/kg fly ash compared to 1.0 mol/kg fly ash) had a higher elastic modulus of the gel phase at early age. At later age, however, for AAFA mixtures with lower silica content, i.e. 1 mol/kg fly ash of samples  $\text{SiO}_2\text{-Na}_2\text{O}=1.0\text{-}1.5$ , the elastic modulus of the gel phase was higher than that of samples  $\text{SiO}_2\text{-Na}_2\text{O}=1.5\text{-}1.5$ .

- The addition of sodium was essential to alkali activation reaction of AAFA pastes. An increase of  $\text{Na}_2\text{O}$  content in the activator led to a higher degree of reaction of AAFA. The resulting gel had a lower Si/Al ratio and a higher elastic modulus when the  $\text{Na}_2\text{O}$  content increased.
- Different types of zeolites were detected for samples with different silica and sodium content. An increase of silica content suppressed the formation of zeolites, while a high  $\text{Na}_2\text{O}$  content (1.5 mol/kg fly ash) resulted in the formation of zeolites. In this study, the transition of the gel phase to zeolites did not lead to strength loss in AAFA.
- The chemical structure of the gel (Si/Al ratio) and the gel pore structure are both important factors influencing the elastic modulus of the gel phase of AAFA. A good correlation was found between the elastic modulus of the gel phase and the compressive strength of AAFA pastes, regardless of mixtures and curing age.

## **Chapter 5**

# **Pore Structure of Alkali Activated Fly Ash**

---

### **5.1 Introduction**

Besides the solid phases discussed in Chapter 4, the pore structure is another important characteristic that is relevant for the physical and mechanical properties, as well as for the long-term performance of AAFA. Hardened AAFA is a porous material. The total pore volume, as well as the way in which the pores of different size are distributed in the solid, determines the extent and the rate of penetration of aggressive ions (e.g.  $\text{Cl}^-$ ,  $\text{CO}_3^{2-}$ ,  $\text{SO}_4^{2-}$ , etc.) into the material. In addition, the autogenous and drying shrinkage of AAFA is also related to the pore structure of the matrix (will be discussed in detail in Chapter 7). Thus the understanding of the pore structure is very important for the evaluation and further prediction of the permeability and shrinkage of AAFA.

The main objective of this chapter is to investigate the pore structure of AAFA pastes. Two experimental techniques, which are commonly used in cement-based materials, including mercury intrusion porosimetry (MIP) and nitrogen adsorption, are applied to study the pore structure of AAFA pastes. Environmental scanning electron microscopy (ESEM) is used to enable a more detailed evaluation of the MIP results. The obtained results were compared with those of cement pastes ( $w/c=0.4$ ). The effect of sodium and silica content and curing conditions on the pore structure of AAFA will be discussed.

### **5.2 Introduction of experimental techniques for pore structure characterization**

#### **5.2.1 Mercury intrusion porosimetry**

Mercury intrusion porosimetry (MIP) is a useful technique for characterizing the pore structure of various porous materials. It is a fast way to obtain information about the pores. Additionally, MIP is the only available technique that covers a broad range of pore sizes, from several nanometers to hundreds micrometers, by applying different pressures [Aligizaki, 2005].

The principle of the MIP technique is to progressively record the volume of mercury that intrudes into a porous sample under controlled pressures. An extrusion procedure



may follow after reaching the highest intrusion pressure. By using Equation 5.1 [Washburn, 1921], the pressures can be related to the corresponding diameter of pores and plotted versus cumulative mercury volume (known as pore size distribution curve).

$$D = \frac{-4\gamma\cos\theta}{P} \quad (5.1)$$

where  $D$  is the pore diameter,  $\gamma$  is the surface tension of mercury,  $\theta$  is the contact angle between mercury and pore surface of the sample and  $P$  is the applied pressure. By applying Equation 5.1, mercury intrusion data can be related to a pore size distribution curve and a pore size distribution differential curve as shown in Figure 5.1. From these two curves, several pore structure parameters can be derived:

1. The total porosity: The total porosity is calculated from the total volume of mercury intruded at the maximum experimental pressure divided by the bulk volume of the sample.
2. The ink-bottle porosity: During intrusion the continuous pores, including the “ink-bottle” pores [Diamond, 1971], can be detected from the intrusion curve. After intrusion, the mercury in the continuous pores is extruded from the specimen; however, the mercury in the “ink-bottle” pores will remain inside. The volume of mercury that remains inside during the extrusion is called “ink-bottle” porosity.
3. The effective porosity: The total porosity minus the ink-bottle porosity is defined as the “effective porosity” in this study.
4. The threshold (critical) pore diameter: Corresponding to the peaks in the pore size distribution differential curve. These peaks represent the pore diameters corresponding to the higher rate of mercury intrusion per change in pressure, known as the “critical” or “threshold” pore diameter [Katz and Thompson, 1986].

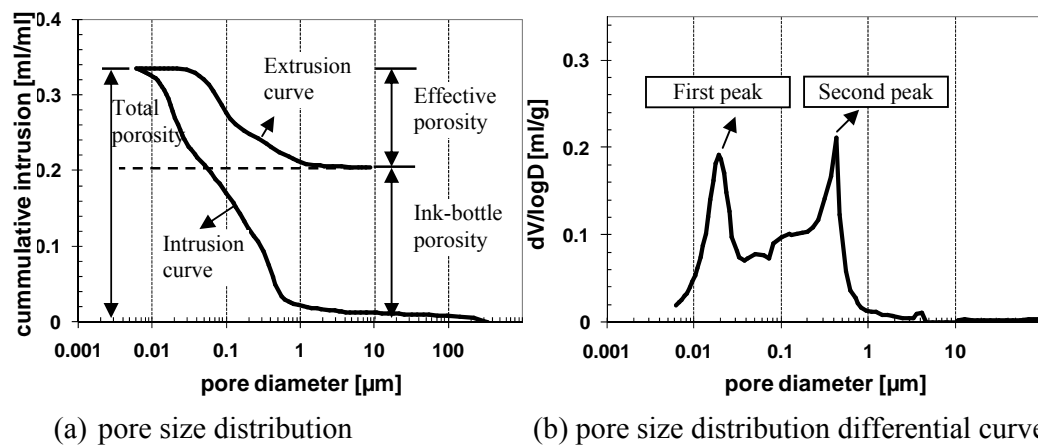


Figure 5.1 Schematic illustrations of the total porosity, ink-bottle porosity, effective porosity and threshold pore diameter (the diameter corresponding the first and the second peak in (b)) of AAFA derived from MIP results

### 5.2.2 Nitrogen adsorption

Nitrogen adsorption has been employed since a long time to characterize the pore structure of porous materials. This technique is able to distinguish pore sizes in the range of 0.3 to 300 nm [Gerhardt, 1988]. When a clean solid surface is exposed to a gas, the gas molecules impinge upon the solid and may reside on its surface for a finite time; this phenomenon is called adsorption [Aligizaki, 2005]. The adsorption process is accompanied by an increase in the mass of the samples and a decrease in the pressure of gas. Based on the amount of gas adsorbed and the corresponding relative gas pressure recorded during the experiment, an isothermal adsorption curve is obtained. The Kelvin equation is used to relate the size of the pores to the relative pressure of nitrogen,  $p/p_0$ , at which capillary condensation takes place inside the pores:

$$\ln \frac{p}{p_0} = -\frac{2\gamma V_L \cos\theta}{rRT} \quad (5.2)$$

where  $p$  ( $\text{N/m}^2$ ) is the equilibrium vapor pressure of a liquid in a pore with radius  $r$  (m),  $p_0$  is the equilibrium reference pressure of the same liquid on a plane surface ( $\text{N/m}^2$ ).  $\gamma$  is the surface tension of the liquid ( $\text{N/m}$ ),  $V_L$  is the volume of the liquid ( $\text{m}^3/\text{mol}$ ),  $\theta$  is the contact angle between the liquid and the pore wall (usually assumed to be 0),  $R$  is the gas constant = 8.314 J/(K mol),  $T$  is the temperature (K). The total pore volume is calculated from the gas adsorbed at saturated vapor pressure (capillary condensation happens). The Barrett-Joyner-Halenda (BJH) model [Barrett et al., 1951] is employed to derive the pore size distribution curve from nitrogen adsorption results in this study. In this model, it is assumed that the radius of the pore is equal to the sum of the Kelvin radius and the thickness of the adsorbed film on the pore walls. The pore surface area is calculated according to the Brunauer-Emmett-Teller (BET) method [Brunauer et al., 1938].

### 5.2.3 Environmental scanning electron microscopy (ESEM)

The general introduction of ESEM technique was presented in Section 4.2.3 in Chapter 4.

### 5.2.4 Discussion on ESEM, MIP and nitrogen adsorption techniques

The three techniques introduced above (i.e. MIP, nitrogen adsorption and ESEM) are all capable to characterize the pore structure of porous materials. Each technique has its advantages and limitations.

ESEM allows the characterization of pore geometry to be analyzed from a real image of the material. However, the minimum size of pores that can be distinguished by ESEM is limited (normally  $> 100$  nm) and mainly depends on the magnification and resolution of the image. In addition, ESEM images only provide a two-dimensional image of a sample. Thus the connectivity of pores cannot be obtained directly from ESEM images.

Nitrogen adsorption is able to detect the small pores in materials (from 2 to 100 nm in this study). Within this range, the analysis of pores in the nano-scale is possible. However, nitrogen adsorption has access only to open pores and the cylindrical pore model is assumed for the interpretation of the measurements [Aligizaki, 2005], a

condition that is never fulfilled for cement-based materials and AAFA studied here. Furthermore, the small range of pore sizes determined by nitrogen adsorption (from 2 to 100 nm in this study) cannot provide all the information of pores that is needed for AAFA studied here.

MIP is an efficient method to obtain information of porous materials. Compared to the other two techniques (ESEM and nitrogen adsorption), MIP is able to determine nearly the whole range of pore sizes that is needed to characterize a material like cement paste and AAFA (from 6 nm to 350  $\mu\text{m}$  in this study). However, like in nitrogen adsorption, the pore model (cylindrical pores) that is used to interpret the MIP results does not agree with the real pore shape of the measured material [Aligizaki, 2005]. Furthermore, usually, constant values of the surface tension and contact angle are used for mercury. In reality, however, the contact angle may differ for samples with different mixture proportion or different age, which leads to different surfaces. In addition, the presence of “ink-bottle pores” [Diamond, 1971] will lead to an overestimation of the volume of fine pores and an underestimation of the volume of wide pores. In some cases, the high pressure employed during the intrusion process may lead to damage of pores and to inaccurate results.

Based on the above discussions, it is difficult to characterize the full image of pore structure by using only one single technique. Combinations of these techniques as well as a careful interpretation of the experimental data are needed.

### **5.3 Materials and Methods**

#### **5.3.1 Materials**

The fly ash and activating solutions used for preparing the specimens are the same as in Chapter 4, as shown in Table 4.1.

#### **5.3.2 Sample preparation**

The sample mixing and curing process, as well as the drying procedure (nitrogen freeze drying) of AAFA paste for MIP and nitrogen adsorption measurements were the same as for ESEM observations, as discussed in Sections 4.2.2 and 4.2.3 in Chapter 4. The samples at 7 and 28 days at 40 °C were used for MIP and nitrogen adsorption tests. In addition, the pore structure of samples cured in another condition, i.e. 7 days at 40 °C and then at 20 °C for 3 and 6 months, was also examined by MIP technique. The obtained results from all the MIP tests will be further used in Chapter 6 to correlate them with the permeability results.

#### **5.3.3 MIP**

The porosity and pore size distribution of AAFA pastes were examined by Micromeritics Poresizer 9500 (Figure 5.2). The measurements were conducted in two stages: the first stage is the low pressure: from 0 to 0.0036 MPa; the second stage is the high pressure, running from 0.0036 to 210 MPa and followed by an extrusion running from 210 to 0.14 MPa. The surface tension used here is 0.485 N/m, and the contact angle is 132° based on previous study [Ellison et al., 1967]. With the

Washburn equation (Equation 5.1), the pore size ranging from 0.006  $\mu\text{m}$  to 350  $\mu\text{m}$  can be detected.

### 5.3.4 Nitrogen adsorption

For nitrogen adsorption tests dried samples, as shown in Figure 4.3a, were further crushed by hammer into very small pieces (about 1  $\text{mm}^3$ ). Nitrogen adsorption tests were conducted by using Gemini VII 2390 (Figure 5.3). Total pore volume available for nitrogen and pore size distribution were calculated by the BJH method [Barrett, Joyner et al., 1951]. The relative pressure range from 0.05-0.98 was recorded. Pores in the range of 2-100 nm were measured.



*Figure 5.2 Photo of Micromeritics Poresizer 9500 (MIP)*



*Figure 5.3 Photo of Gemini VII 2390 (nitrogen adsorption)*

## 5.4 Results and discussions

### 5.4.1 Pore structure formation of AAFA by MIP and ESEM observation

#### *Comparison of the pore structure of AAFA and Portland cement*

The comparison of the pore structure of AAFA pastes and Portland cement pastes addresses the differences in these two systems. The different pore size distributions, as well as the different rates of pore structure development are known to strongly affect the engineering properties [Powers, 1958; Young et al., 2002]. Knowing the differences in microstructure between AAFA and cement systems will be helpful for a better understanding of the differences in macro-properties (e.g. water permeability and shrinkage; will be discussed in Chapters 6 and 7).

Figure 5.3 shows typical pore size distribution and differential pore size distribution curves of cement pastes ( $w/c=0.4$ ) at different age (Ye, [2003]). Generally, there are two peaks in the differential curves for cement paste, corresponding to two pore systems: the capillary pores and the gel pores (Figure 5.3b). The capillary pores refer to the space not filled by the un-hydrated grains and the gel, and range from  $0.01 \mu\text{m}$  to perhaps  $10 \mu\text{m}$  [Young, Mindess et al., 2002]. The gel pores are formed within the C-S-H gel, and their pore size diameter ranges from  $0.5 \text{ nm}$  to  $0.01 \mu\text{m}$  [Young, Mindess et al., 2002]. In the MIP test, however, the peak indicating the gel pores is found in the range of  $0.02 \mu\text{m}$  to  $0.05 \mu\text{m}$ , somewhat bigger than the gel pores in cement pastes defined by Young et al. ( $< 0.01 \mu\text{m}$ ) [Young, Mindess et al., 2002].

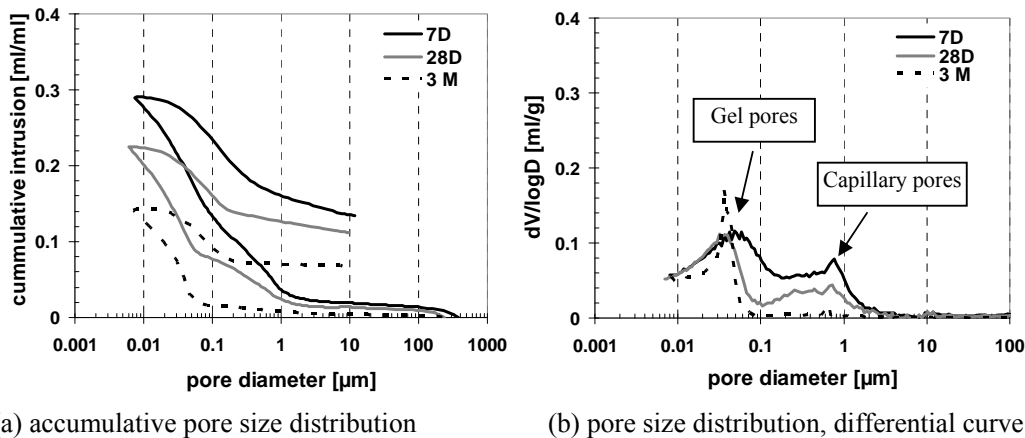
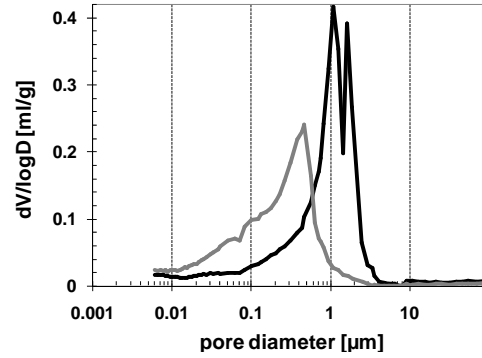
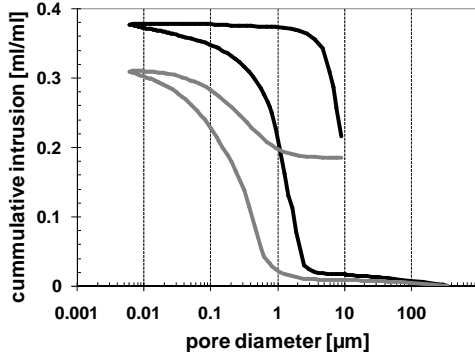
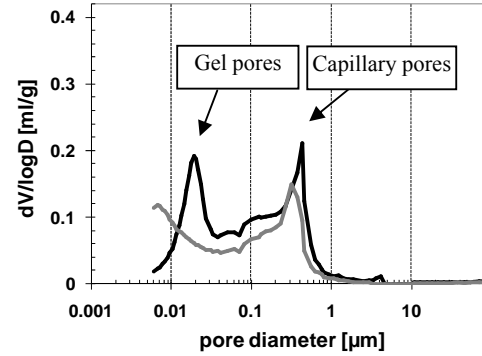
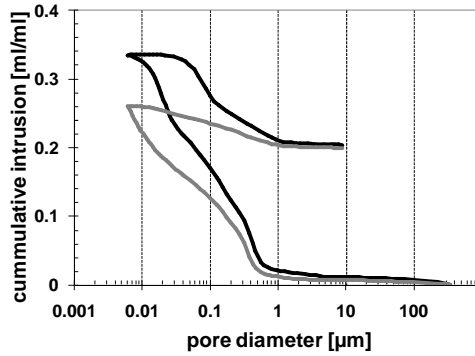
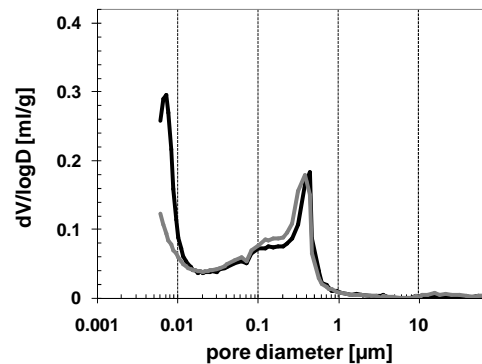
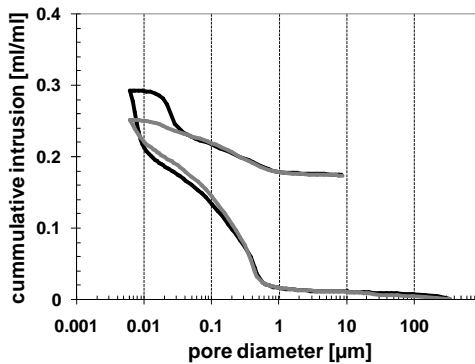
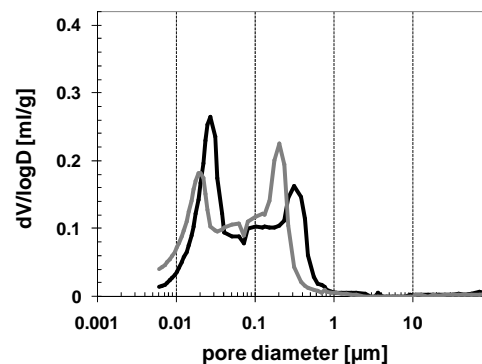
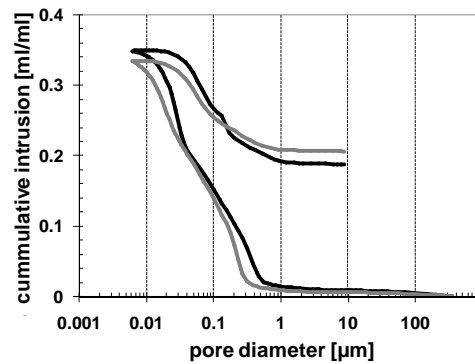


Figure 5.3 Pore size distribution of cement paste  $w/c=0.4$  at different age by Ye [2003], measured by MIP

Figure 5.4 depicts the results from MIP tests for AAFA pastes. Similar to the results of cement pastes, the differential curves of AAFA generally present two peaks, corresponding to two pore systems: the first peak (e.g. left in Figure 5.4b), reflecting pore sizes with diameter in the range of several nm to  $0.04 \mu\text{m}$ , represents the gel pores; the second peak (e.g. right in Figure 5.4b) covering pore size ranges of  $0.1\text{-}1 \mu\text{m}$  (or larger, e.g. Figure 5.4a), represent the “capillary pores”.

(a)  $\text{SiO}_2\text{-Na}_2\text{O}$ : 0.5-1.5(b)  $\text{SiO}_2\text{-Na}_2\text{O}$ : 1.0-1.5(c)  $\text{SiO}_2\text{-Na}_2\text{O}$ : 1.5-1.5(d)  $\text{SiO}_2\text{-Na}_2\text{O}$ : 1.0-1.3

— 7 days

— 28 days

Figure 5.4 Pore size distribution of AFA pastes with different  $\text{SiO}_2$  and  $\text{Na}_2\text{O}$  content at 7 and 28 days (40 °C), measured by MIP (to be continued)

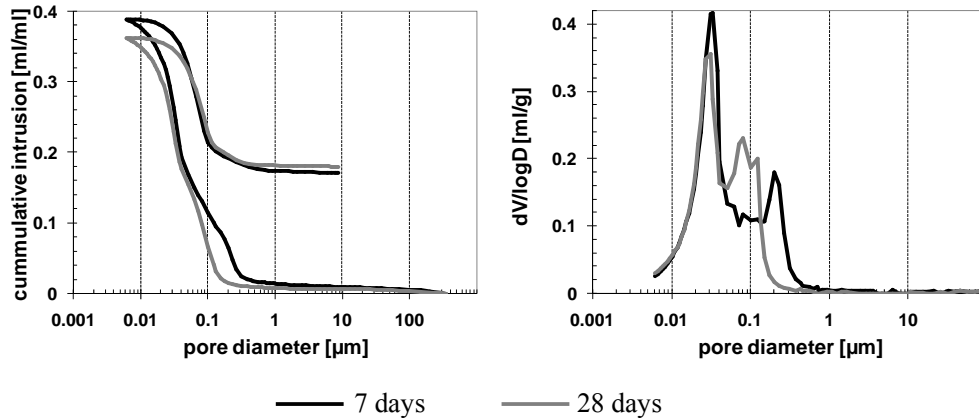
(e)  $\text{SiO}_2\text{-Na}_2\text{O}$ : 1.0-1.0

Figure 5.4 (continued) Pore size distribution of AAFA pastes with different  $\text{SiO}_2$  and  $\text{Na}_2\text{O}$  content at 7 and 28 days (40 °C), measured by MIP

The morphology of a typical AAFA paste ( $\text{SiO}_2\text{-Na}_2\text{O}=1.0\text{-}1.5$ ) and cement paste with  $w/c=0.4$  are compared in Figure 5.5. As discussed in Section 4.3.2, when the silica content in the activator exceeds 1.0 mol/kg fly ash, the homogeneous gel occupies most of the space of the AAFA matrix. A small number of cavities were observed in the AAFA matrix (arrows in Figure 5.5b). These cavities were partially formed by the dissolved fly ash particles and partially from ash particles originally with a hollow core. In addition, these cavities were in a similar pore size range as typical capillary pores in cement paste (several microns to larger than 10  $\mu\text{m}$  in diameter (Figure 5.5b)). The distribution of these “capillary pores” in AAFA pastes, however, is different from those in cement paste (arrows in Figure 5.5a). In cement paste C-S-H gel normally grows around the surface of un-hydrated cement particles, leaving the space outside the growing shell of reaction product as capillary pores. In AAFA, however, the cavities appeared as disconnected and surrounded by the aluminosilicate gel. The existence of these cavities in AAFA matrix was also reported by Lloyd et al. using Wood’s metal intrusion together with SEM images [Lloyd, Provis et al., 2009c]. Their tests revealed that these large cavities were connected to the exterior of the samples even at later curing age when the gel became denser.

By comparing the pore size distribution derived from the MIP results (Figure 5.4) with the pore diameters shown in BSE image (Figure 5.5b), the peak corresponding to the “capillary pores” (cavities) of AAFA pastes, obtained from MIP tests, is about 1 order of magnitude smaller than the pore diameters obtained from BSE images. It indicates a great “ink-bottle” effect happened during the MIP measurements of AAFA pastes. It is conceivable that these large cavities were connected by pores of 0.1-1.0  $\mu\text{m}$ . In the MIP tests mercury can only access large cavities through these smaller pores (0.1-1.0  $\mu\text{m}$ ), which in turn causes a significant “ink-bottle” effect. Therefore, these large cavities show a peak in the range of 0.1-1.0  $\mu\text{m}$  in the differential curves in Figure 5.4. Experimental studies by Lloyd et. al [2009c] indicated that cracks were formed as a result of the intrusion process during the tests. Thus the cracks, in the range of 0.1-1  $\mu\text{m}$ , may form paths that connect these large cavities to the exterior of AAFA samples during the execution of MIP tests.

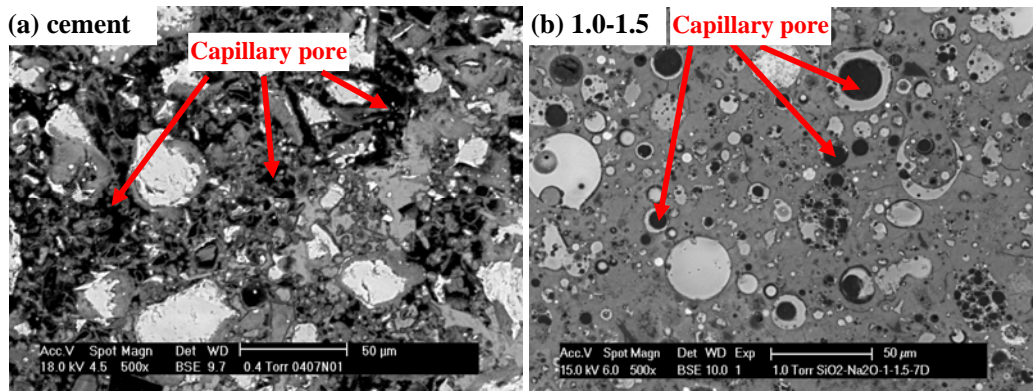


Figure 5.5 ESEM micrograph of cement paste with  $w/c=0.4$  (left) (Ye [2003]) and AAFA paste with  $SiO_2-Na_2O$  of 1.0-1.5 (right) at the age of 7 days

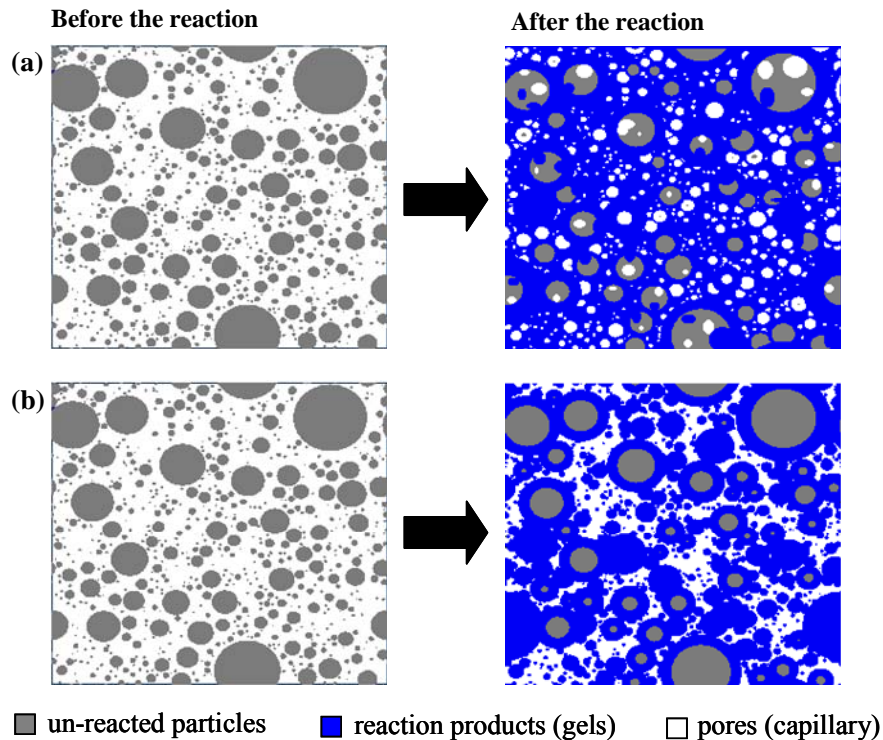


Figure 5.6 Formation of the microstructure (simplified)

(a) AAFA with high silica content in activator ( $\geq 1$  mol/kg fly ash);

(b) AAFA with no or low silica content (0.5 mol/kg fly ash) in activator. This formation of microstructure is similar to that of cement paste.

Based on the above discussion, the microstructure formation of AAFA with different silica content in the activator can be described by two simplified mechanisms, as schematically presented in Figure 5.6. On the one hand, when the added silica content is higher than 1 mol/kg fly ash, AAFA samples showed a homogenous microstructure



with reaction products evenly distributed in the matrix. Some large cavities were formed and were surrounded by the aluminosilicate gel (Figure 5.6a). MIP results showed that these large cavities were accessible through pores between 0.1 and 1.0  $\mu\text{m}$ . On the other hand, for specimens with no or very low soluble silica content, i.e. 0.5 mol/kg fly ash for mixtures  $\text{SiO}_2\text{-Na}_2\text{O}=0.5\text{-}1.5$ , the formation of the gel phase was limited and only grew around the un-reacted fly ash particles (Figure 5.6b). This resulted in the formation of a capillary pore system similar to that of cement paste [Lloyd, Provis et al., 2009b; Rees, Provis et al., 2008].

Figure 5.7 shows the total porosity, measured by MIP, of different AAFA pastes (cured at 40 °C) and Portland cement pastes (w/c=0.4, cured at 20 °C) at 7 days and 28 days. Specimens with the highest sodium and silica content, i.e. mixtures  $\text{SiO}_2\text{-Na}_2\text{O}=1.5\text{-}1.5$ , exhibited similar total porosity at 7 days (29.27 %) as cement pastes with w/c=0.4 (29.62 %). For the other AAFA mixtures, the total porosity measured by MIP was higher than that of cement pastes (w/c=0.4) at both 7 days and 28 days. Particularly for the AAFA mixtures with lower silica and sodium content, e.g. mixtures  $\text{SiO}_2\text{-Na}_2\text{O}=1.0\text{-}1.3$ , 1.0-1.0 and 0.5-1.5, the porosity was much higher than that of cement pastes (w/c=0.4), particularly at later age (Figure 5.7).

The rate at which the pore refinement develops is slower for the AAFA samples cured at 20 °C (see Figure 5.8), compared to that of cement pastes with w/c=0.4 (Figure 5.3). For example, the volume of capillary pores of cement pastes continuously decreased until the pores were totally blocked by the reaction products. As observed from MIP results (Figure 5.3b), the peak corresponding to the capillary pores of cement pastes became smaller and shifted to a lower pore diameter with time until it vanished after 3 months. In contrast to this, the peak corresponding to the “capillary pores” of AAFA mixtures still exists even after 6 months of curing (Figure 5.8).

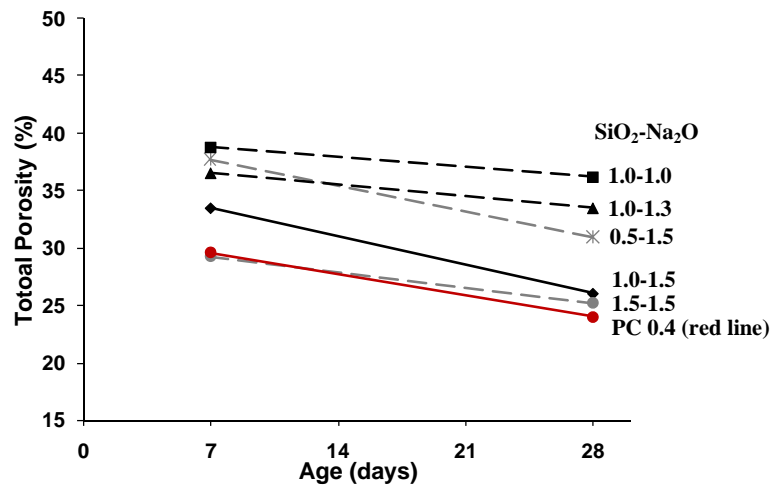
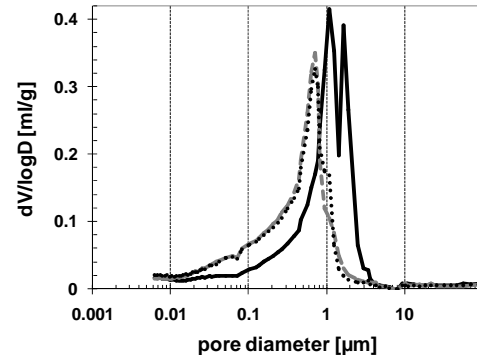
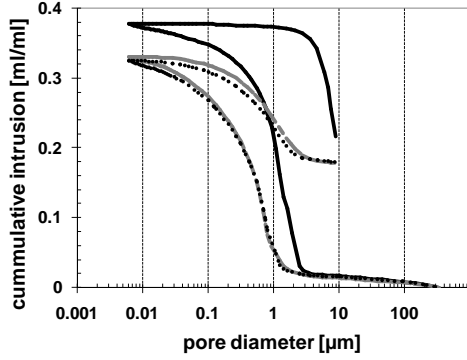
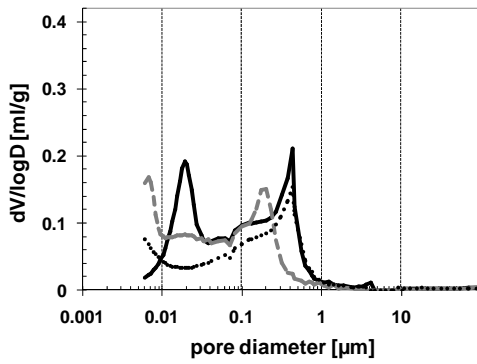
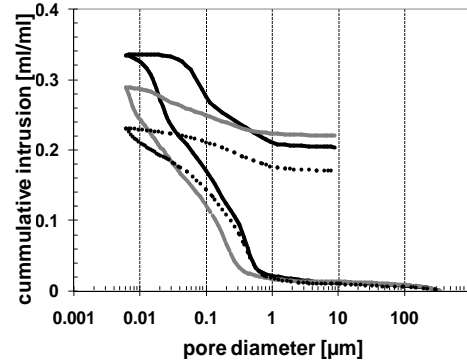
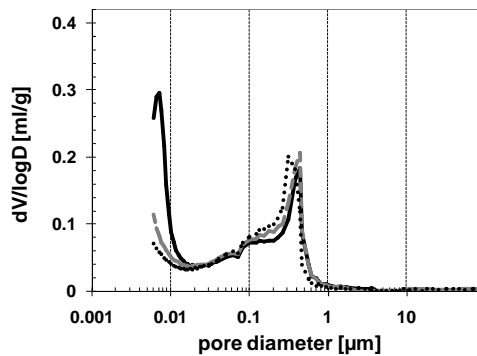
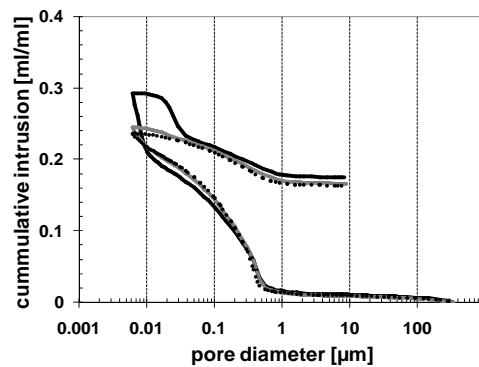
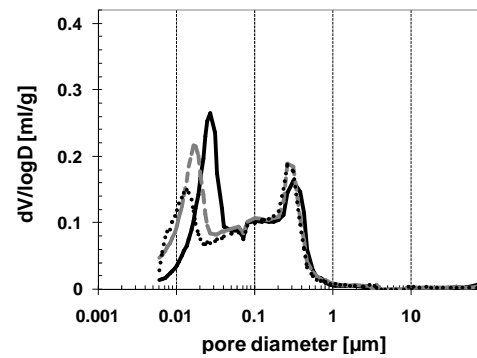
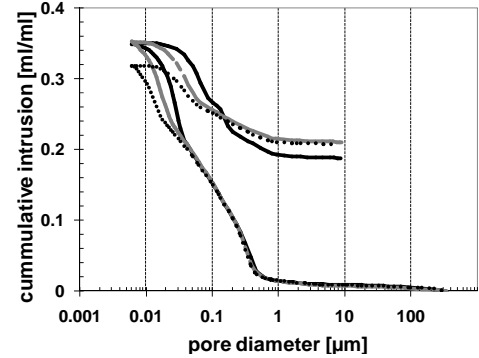


Figure 5.7 Total porosity (measured by MIP) of different AAFA pastes and Portland cement paste (w/c=0.4) as a function of the curing ages

(a)  $\text{SiO}_2\text{-Na}_2\text{O: 0.5-1.5}$ (b)  $\text{SiO}_2\text{-Na}_2\text{O: 1.0-1.5}$ (c)  $\text{SiO}_2\text{-Na}_2\text{O: 1.5-1.5}$ (d)  $\text{SiO}_2\text{-Na}_2\text{O: 1.0-1.3}$ 

— 7 days    — 3 months    ..... 6 months

Figure 5.8 Pore size distribution of different AAFA pastes with time at 20 °C (7 days cured at 40 °C in advance), measured by MIP (to be continued)

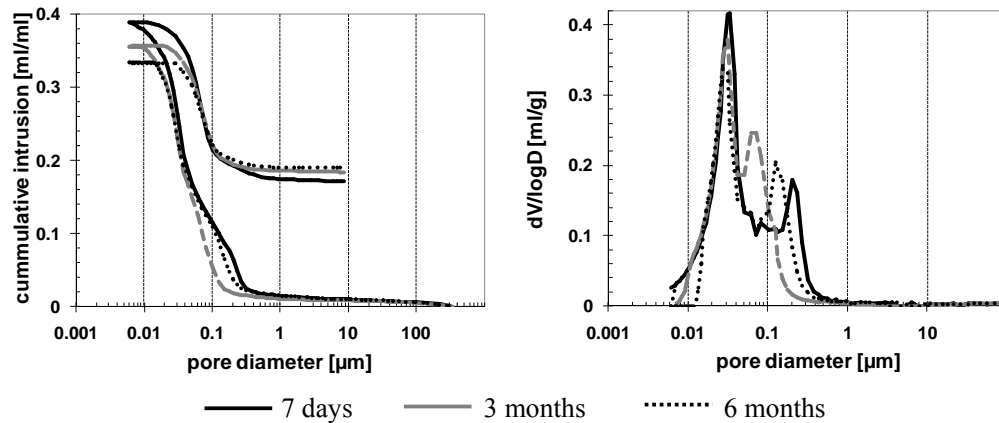
(e)  $\text{SiO}_2\text{-Na}_2\text{O}$ : 1.0-1.0

Figure 5.8 (continued) Pore size distribution of different AAFA pastes with time at 20 °C (7 days cured at 40 °C in advance), measured by MIP

### Factors influencing the pore structure of AAFA pastes

#### The silica content in the activator

The porosity and gel pore threshold diameter, derived from MIP tests, of AAFA mixtures with different silica content at 7 and 28 days, are summarized in Figure 5.9 ( $\text{Na}_2\text{O}$  content was constant at 1.5 mol/kg fly ash). For all the mixtures, the total porosity decreased in the period of 7 days to 28 days. Mixtures with a higher silica content had a lower total porosity at 7 days (Figure 5.9a). For mixtures with a silica content of 1.0 mol/kg fly ash (mixtures 1.0-1.5), the total porosity decreased the most from 7 days to 28 days. The same trend was observed for the gel pore threshold diameter of samples with different silica content (Figure 5.9b). For example, the gel pore threshold diameter at 7 days of mixtures with a silica content of 1.0 mol/kg fly ash (mixtures 1.0-1.5) was much higher than that of mixtures with a silica content of 1.5 mol/kg fly ash (mixtures 1.5-1.5). After 28 days, mixture  $\text{SiO}_2\text{-Na}_2\text{O}=1.0\text{-}1.5$  showed a similar gel pore threshold diameter as mixture 1.5-1.5 (Figure 5.9b). For mixtures with silica content of 0.5 mol/kg fly ash (mixtures 0.5-1.5), the gel pores did not show a peak in the differential pore size distribution curve (Figure 5.4a), corresponding to a porous microstructure (Figure 4.13b). Thus the capillary pore threshold diameter is used for comparison in Figure 5.9b for mixtures 0.5-1.5.

As discussed in Chapter 4, the presence of silica in the activator has two effects. On the one hand, a high silica content, i.e. 1.5 mol/kg fly ash, led to a lower degree of reaction of the AAFA (Figure 4.16). On the other hand, the silica became incorporated in the gel, leading to a dense microstructure. Thus the pore structure is finer for samples with a higher silica content. In this chapter, the MIP results at 7 days were consistent with these ESEM observations. Mixtures with a higher silica content, i.e. 1.5 mol/kg fly ash of mixtures 1.5-1.5, had a lower total porosity and a finer pore size distribution than mixtures 1.0-1.5 (a silica content of 1.0 mol/kg fly ash) at 7 days (Figure 5.9). This finer pore structure of mixtures  $\text{SiO}_2\text{-Na}_2\text{O}=1.5\text{-}1.5$  correlates to a higher compressive strength at 7 days than that of mixtures 1.0-1.5 (Figure 3.12), while the degree of reaction of mixtures 1.5-1.5 is lower. At 28 days, however,

mixtures  $\text{SiO}_2\text{-Na}_2\text{O}=1.0\text{-}1.5$  had a higher degree of pore refinement than mixtures  $\text{SiO}_2\text{-Na}_2\text{O}=1.5\text{-}1.5$ . Thus the compressive strength of mixtures  $\text{SiO}_2\text{-Na}_2\text{O}=1.0\text{-}1.5$  was higher than that of mixtures  $\text{SiO}_2\text{-Na}_2\text{O}=1.5\text{-}1.5$  at 28 days (Figure 3.12).

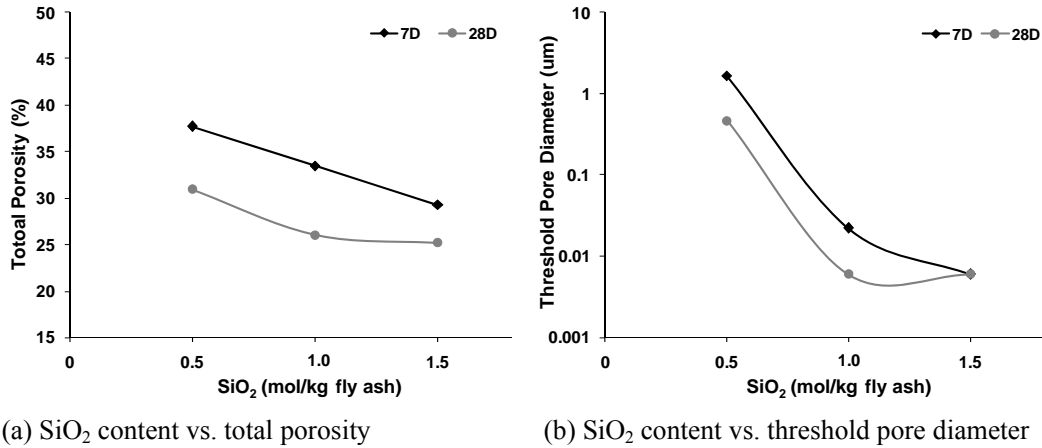


Figure 5.9 Pore structure parameters of AAFA pastes with different  $\text{SiO}_2$  content ( $\text{Na}_2\text{O}$  content was constant at 1.5 mol/kg fly ash) at 7 and 28 days, measured by MIP

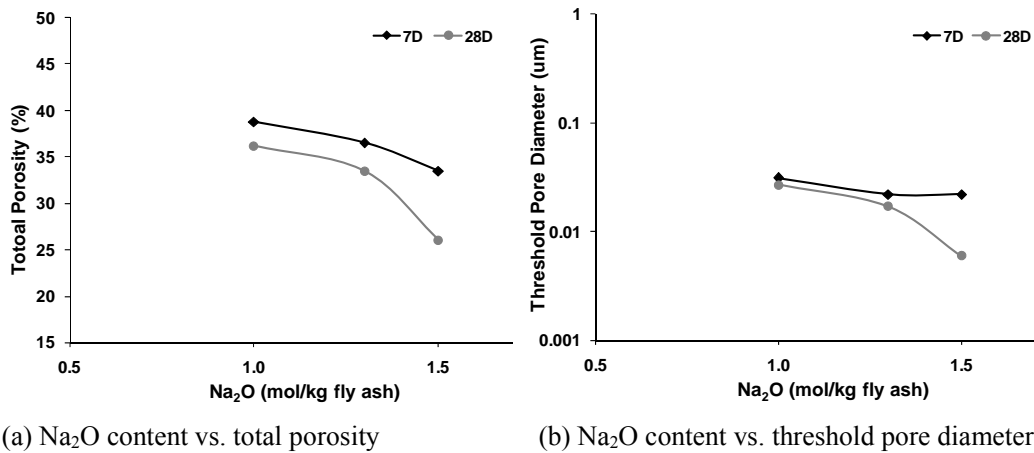


Figure 5.10 Pore structure parameters of AAFA pastes with different  $\text{Na}_2\text{O}$  content ( $\text{SiO}_2$  content was constant at 1.0 mol/kg fly ash) at 7 and 28 days, measured by MIP

#### The sodium content in the activator

The effect of the sodium content on the porosity and gel pore threshold diameter, derived from MIP tests, at 7 and 28 days are summarized in Figure 5.10. The  $\text{SiO}_2$  content in the figure was constant at 1.0 mol/kg fly ash. The addition of more sodium led to a lower total porosity at 7 days, and this effect was more pronounced at 28 day (Figure 5.10a). For mixtures with the highest sodium content, 1.5 mol/kg fly ash of mixtures 1.0-1.5, the decrease of the total porosity from 7 days to 28 days was the most pronounced. The same trend was found for the gel pore threshold diameter for AAFA samples with different sodium content, as shown in Figure 5.10b. The lower

porosity and smaller threshold pore diameter confirm that the alkali content is beneficial for the reaction of AAFA samples (higher degree of reaction in Figure 4.16). More aluminosilicate gel is produced, and the pore structure became finer for mixtures with a higher sodium content, resulting in a higher compressive strength. In addition, the denser gel pore structure of mixtures with a higher sodium content, i.e. 1.5 mol/kg fly ash in Figure 5.10 of mixtures  $\text{SiO}_2\text{-Na}_2\text{O}=1.0\text{-}1.5$ , may also explain the higher elastic modulus of the gel phase measured in the nanoindentation tests (mixtures 1.0-1.5 in Figure 4.28b).

#### *The effective porosity of AAFA mixtures*

Not only the total porosity and threshold pore diameter, but also the effective porosity can be derived from the MIP results. The effective porosity is important for the transport properties of a porous material. Figure 5.11 shows the effect of the silica and sodium content on the effective porosity, respectively. Similar to the total porosity, also the effective porosity of AAFA mixtures decreased with elapse of time (Figure 5.11). AAFA mixtures with a higher sodium content had a lower effective porosity (Figure 5.11b). Similar effects were also observed when a higher amount of silica was present in the activating solution at 7 days (Figure 5.10a). However, at the age of 28 days, the mixture with a silica content of 1.0 mol/kg fly ash (mixtures 1.0-1.5) showed the lowest effective porosity, indicating the lowest pore connectivity.

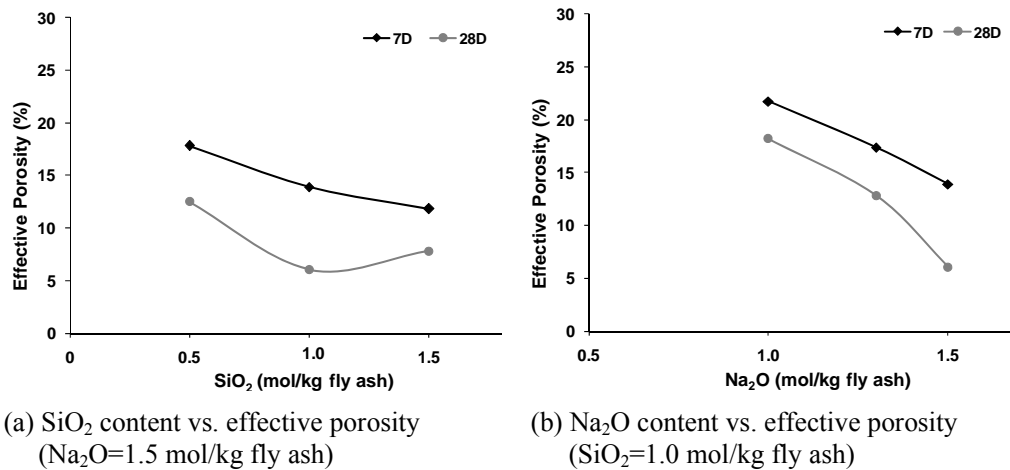
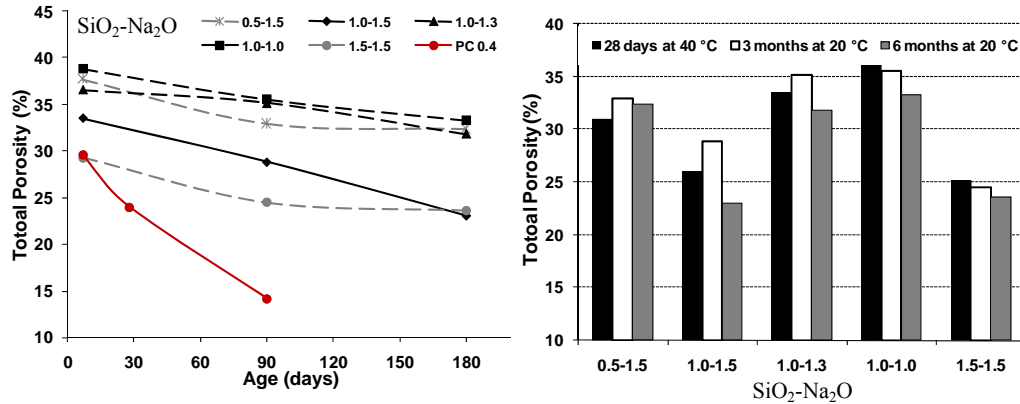


Figure 5.11 Effective porosity of AAFA pastes with different  $\text{SiO}_2$  and  $\text{Na}_2\text{O}$  content at 7 and 28 days, measured by MIP

#### *The curing temperature*

The total porosity (derived from MIP tests) of AAFA samples cured at different temperatures is presented in Figure 5.12. Figure 5.12a shows that the total porosity decreased with time for AAFA samples cured at 20 °C. Compared to cement pastes, however, the decrease of porosity with elapse of time is much slower at 20 °C. In addition, the total porosity of samples cured at higher temperature (40 °C) at 28 days was still lower than that of samples cured at 20 °C for 3 months. This indicates that

the alkali activation reaction was hampered when samples were cured at low temperature (20 °C). After 6 months curing at 20 °C, most of the AAFA samples showed a lower total porosity than those cured at 40 °C for 28 days (Figure 5.12).



(a) Total porosity of AAFA cured at 20 °C (b) Total porosity of AAFA cured at 40 and 20 °C

Figure 5.12 Total porosity of AAFA pastes cured at different temperatures (40 °C and 20 °C (7 days cured at 40 °C in advance)), measured by MIP

#### 5.4.2 Nitrogen adsorption results of AAFA pastes

Figure 5.13 shows the pore size distribution of different AAFA samples derived from nitrogen adsorption tests. The pores between 2 nm and 100 nm can be detected by nitrogen adsorption, which technique gives more detailed information of the gel pores in AAFA samples. Figure 5.13 shows that the volume of pores increased with increasing age of the AAFA samples. This result is expected, since the volume measured in the pore size range from 2 nm to 100 nm is primarily related to the gel phase. The quantity of aluminosilicate gel increased with age, causing an increase of the volume of gel pores in the system.

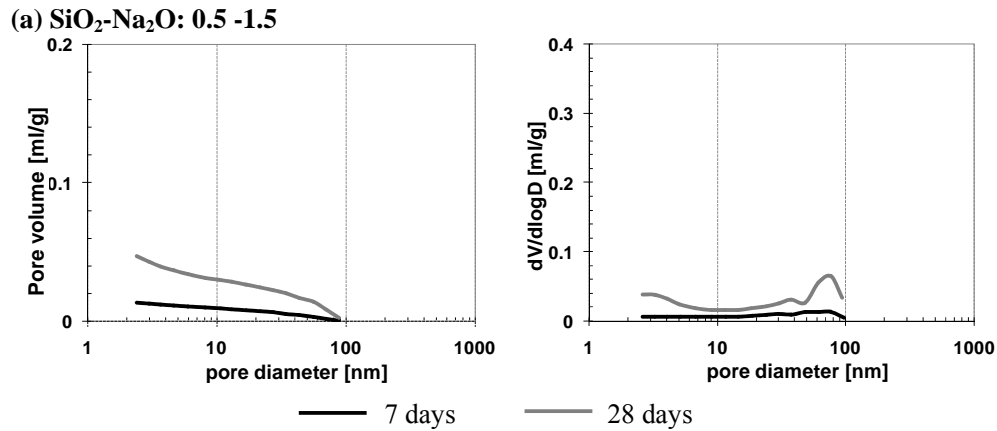
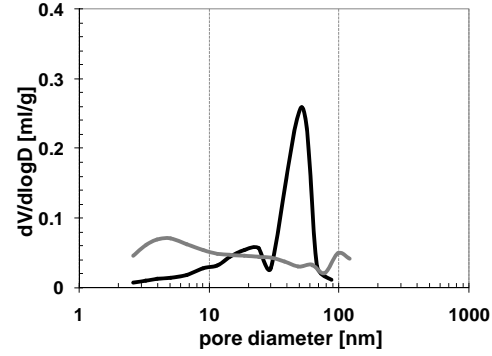
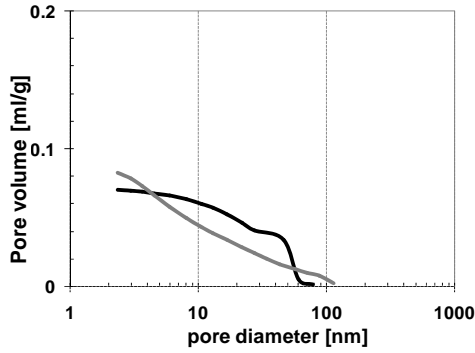
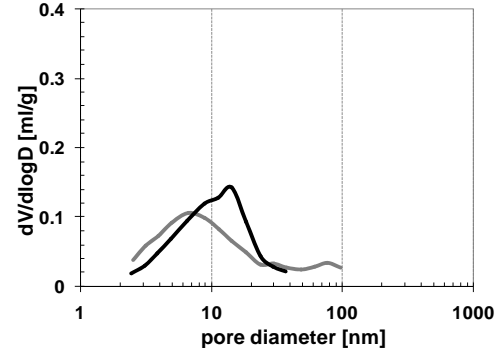
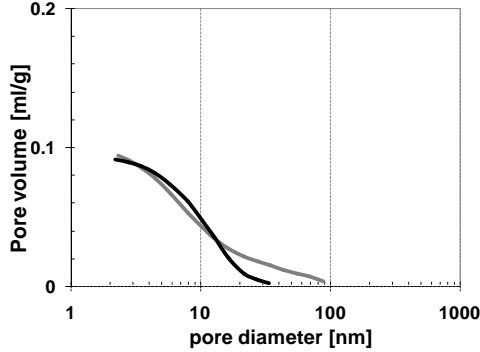
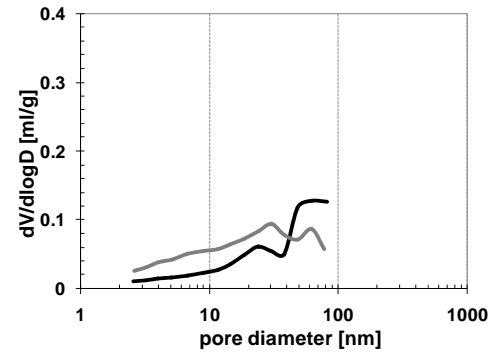
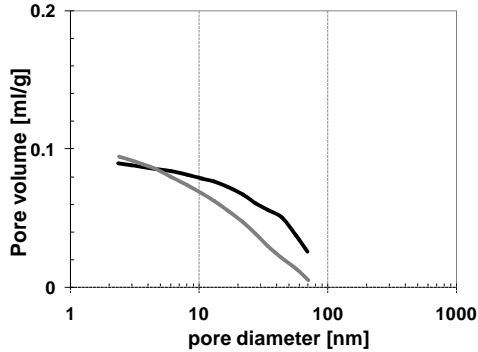
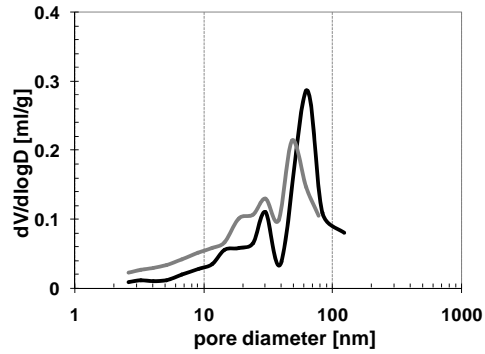
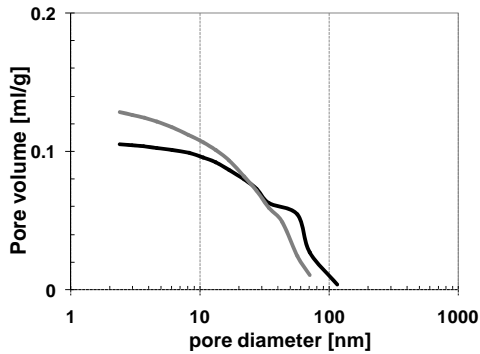


Figure 5.13 Pore size distribution of AAFA pastes (SiO<sub>2</sub>-Na<sub>2</sub>O) at the curing ages of 7 and 28 days respectively (40 °C), measured by nitrogen adsorption (to be continued)

(b)  $\text{SiO}_2\text{-Na}_2\text{O}: 1.0\text{-}1.5$ (c)  $\text{SiO}_2\text{-Na}_2\text{O}: 1.5\text{-}1.5$ (d)  $\text{SiO}_2\text{-Na}_2\text{O}: 1.0\text{-}1.3$ (e)  $\text{SiO}_2\text{-Na}_2\text{O}: 1.0\text{-}1.0$ 

— 7 days

— 28 days

Figure 5.13 (continued) Pore size distribution of AAFA pastes ( $\text{SiO}_2\text{-Na}_2\text{O}$ ) at the ages of 7 and 28 days respectively (40 °C), measured by nitrogen adsorption

The differential pore size distribution curves in Figure 5.13 generally show two peaks. The pore diameter at these peaks varied with the silica and sodium content, as well as with the curing age. For example, in specimens with lower silica content (0.5 mol/kg fly ash of mixtures 0.5-1.5), no peaks were found in the differential curve at 7 days (black line in Figure 5.13a), indicating that the amount of the reaction products was limited. At 28 days, three peaks were detected for specimens 0.5-1.5 (grey line in Figure 5.13a) at around 3 nm, 40 nm and 77 nm, respectively. It is not clear whether these peaks reflect the nano/micro-structure of the aluminosilicate gel, since these peaks appeared at different pore diameter with different mixtures and different curing age (Figure 5.13). A more detailed examination of the aluminosilicate gel at the nano/micro level is needed to better understand the gel structure.

Mixtures with a higher silica content showed a distinct peak at 7 days: e.g. at around 50 nm for mixtures 1.0-1.5 (Figure 5.13b) and 15 nm for mixtures 1.5-1.5 (Figure 5.13c). This peak shifted to a smaller pore diameter at later age. Furthermore, for mixtures 1.0-1.5, with less silica content, the peak shift with age, from 23.98 nm to 5.07 nm in Figure 5.13b, was more pronounced than that of mixtures 1.5-1.5, from 14.29 to 6.65 nm in Figure 5.13c. After 28 days, for mixtures with a silica content of 1.0 mol/kg fly ash (mixtures 1.0-1.5), the peak indicating the gel pores showed a lower pore diameter (5.07 nm) than that of mixtures with a silica content of 1.5 mol/kg fly ash (mixtures 1.5-1.5 (6.65 nm)). It indicates that mixtures 1.0-1.5, with less silica content, had a denser gel pore structure than mixtures 1.5-1.5 at 28 days.

Specimens with different sodium content exhibited similar differential curves at the age of 7 days. From Figure 5.13b, d and e (three black lines), mixtures 1.0-1.5, 1.0-1.3 and 1.0-1.0 ( $\text{Na}_2\text{O}$  content decreasing from 1.5 to 1.0 mol/kg fly ash) showed one peak between 50-60 nm, and the other peak between 20-30 nm. After 28 days, for mixtures with the highest sodium content, i.e. mixtures 1.0-1.5, the peak indicating the gel pores shifted to the lowest pore diameter (5.07 nm) compared to that of mixtures with less sodium content, i.e. mixture 1.0-1.3 and 1.0-1.0. It indicates that the pores were finer for mixtures containing more sodium. This trend is in line with the findings from the MIP results.

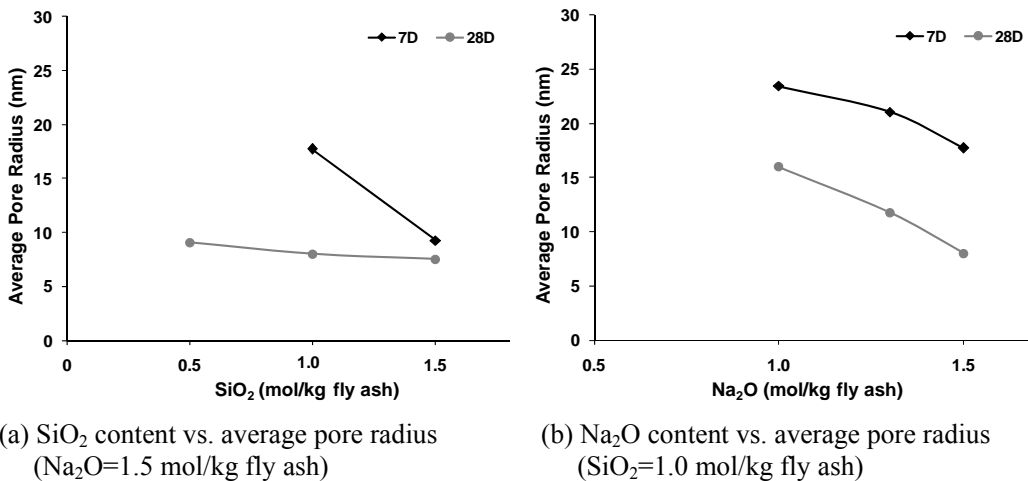


Figure 5.14 Average pore radii ( $r_a$ ) of AFA pastes with different  $\text{SiO}_2$  and  $\text{Na}_2\text{O}$  content at 7 and 28 days, measured by nitrogen adsorption



The average pore radii derived from nitrogen adsorption results of AAFA samples with different silica and sodium content at 7 and 28 days are summarized in Figure 5.14. The average pore radius ( $r_a$ ) was defined as the ratio between the total pore volume and the pore surface area, and reflects the fineness of the pore structure [Aligizaki, 2005]. Figure 5.14a shows that mixtures with a higher silica content had a lower average pore radius at 7 days. From 7 days to 28 days, the decrease of the average pore radius was more significant for the mixture with a silica content of 1.0 mol/kg fly ash than that for the mixture with a silica content of 1.5 mol/kg fly ash.

Figure 5.14b shows that the average pore radius was lower for mixtures with a higher sodium content both at 7 days and 28 days. It indicates the formation of a denser gel structure with increasing sodium content.

### 5.4.3 Gel pore threshold diameter/ elastic modulus of the gel

In Section 4.3.5 in Chapter 4, it is proposed that the elastic modulus of aluminosilicate gel is not only affected by the chemical structure of the gel phase (Si/Al ratio), but also by the pore structure of the gel phase. This assumption is confirmed in this section. Figure 5.15 shows the relationship between the gel pore threshold diameter, obtained from nitrogen adsorption, and the elastic modulus of the gel phase, obtained from nanoindentation, of AAFA samples at 7 and 28 days. The figure shows that samples with smaller gel pore threshold diameter had a higher elastic modulus of the gel phase, regardless the curing age and mix composition. A lower gel pore threshold diameter indicates a denser gel phase of AAFA, resulting in a higher elastic modulus of the gel phase.

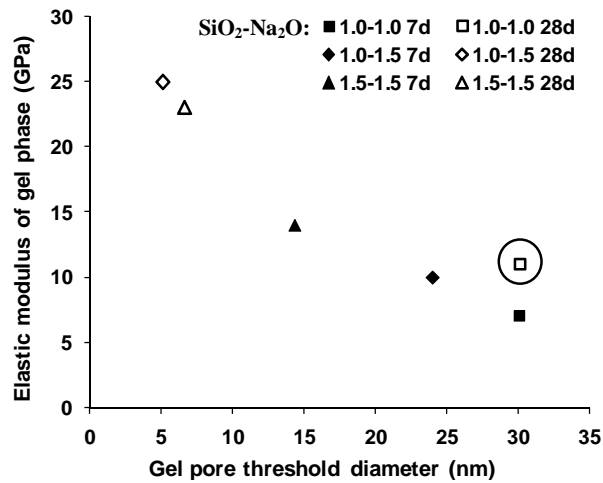


Figure 5.15 Gel pore threshold diameter vs. elastic modulus of aluminosilicate gel (determined by nanoindentation) of AAFA pastes at 7 and 28 days

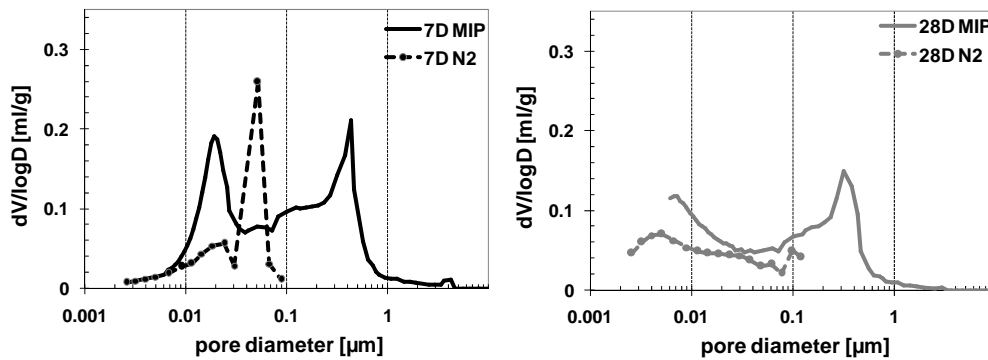
Samples SiO<sub>2</sub>-Na<sub>2</sub>O=1.0-1.0 at 28 days (square point circled in Figure 5.15) deviate from the rest of the AAFA samples. Samples 1.0-1.0 showed similar gel pore threshold diameter at 7 days and 28 days, while the elastic modulus at 28 days was higher. The little change of gel pore threshold diameter of mixtures 1.0-1.0 at 7 days and 28 days may be due to the lower reaction that happened in this period (Figure

4.16). Other parameters, e.g. the average pore radius (Figure 5.14), which also reflect the fineness of pore structure, may be a better indicator for the evolution of the elastic modulus of mixtures 1.0-1.0 than the threshold diameter.

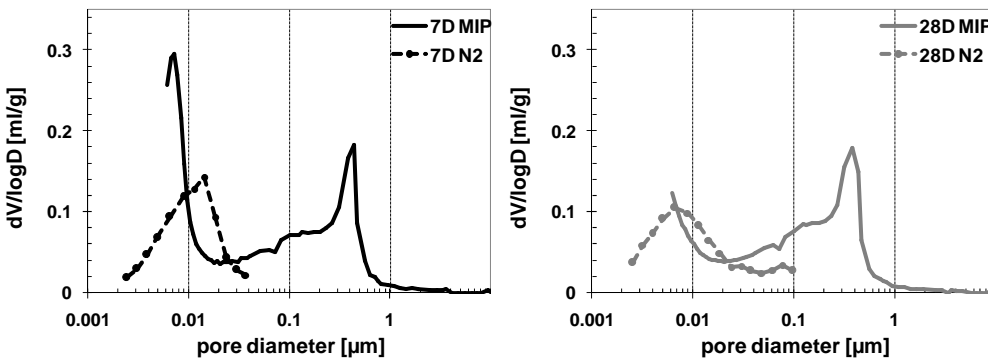
#### 5.4.4 Comparison of the results from MIP and nitrogen adsorption

Both the MIP tests and nitrogen adsorption tests provide information about the pore volume and pore size distribution of AAFA samples. Figure 5.16 compares the differential curves of the pore size distribution derived from MIP and nitrogen adsorption tests for AAFA samples at 7 days and 28 days.

(a)  $\text{SiO}_2\text{-Na}_2\text{O}$ : 1.0-1.5



(b)  $\text{SiO}_2\text{-Na}_2\text{O}$ : 1.5 -1.5



(c)  $\text{SiO}_2\text{-Na}_2\text{O}$ : 1.0-1.3

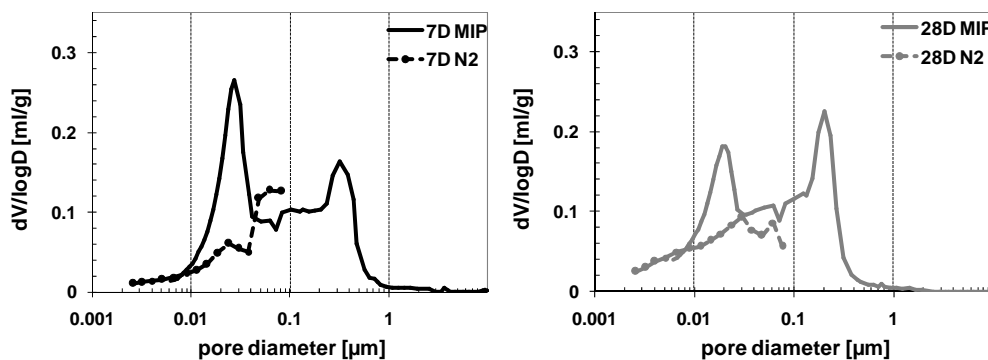


Figure 5.16 Comparison of the pore size distribution curves derived from MIP and nitrogen adsorption tests for all investigated AAFA pastes (to be continued)

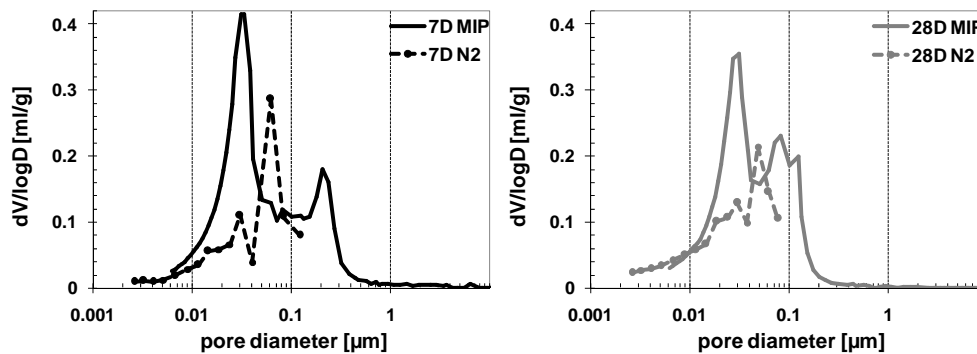
(d)  $\text{SiO}_2\text{-Na}_2\text{O: 1.0-1.0}$ 

Figure 5.16 (continued) Comparison of the pore size distribution curves derived from MIP and nitrogen adsorption tests for all investigated AAFA pastes

One clear difference is that nitrogen adsorption measurements generally reveal two peaks in the gel pore range of AAFA samples (dashed lines in Figure 5.16), while in MIP tests only one peak appears indicating the gel pores (solid lines in Figure 5.16). In addition, these peaks appear at different pore diameters and with different intensities (Figure 5.16). Such comparison between MIP and nitrogen adsorption results has been also reported for cement-based materials [Zeng et al., 2012]. These differences may be due to the different mediums (mercury compared to nitrogen) and different principles (liquid intrusion compared to gas adsorption) that are used in the MIP and nitrogen adsorption measurements. Another reason may come from the high pressure used during the MIP measurements, which may have caused damage to the pore structure, especially at smaller pore diameters when higher pressures are applied. This may lead to the appearance of only one peak indicating the gel pores in the MIP results.

Despite the differences between MIP and nitrogen adsorption results for different AAFA samples, these two methods give the same trends: samples with a higher silica content had a finer pore structure at early age (Figure 5.16b, 7 days), whereas samples with a higher sodium content developed a finer pore structure more pronounced at later age (Figure 5.16a, 28 days).

## 5.5 Concluding remarks

In this chapter, the pore structure of AAFA samples with different  $\text{SiO}_2$  and  $\text{Na}_2\text{O}$  content and different curing temperature were investigated by MIP and ESEM analyses and nitrogen adsorption methods. The experimental results were compared with those of cement pastes ( $w/c=0.4$ ). The main conclusions of this chapter can be summarized as follows:

- The MIP and ESEM results revealed that the pore structures of AAFA samples were very different from those of cement pastes when the silica content of AAFA exceeds 1 mol/kg fly ash. The aluminosilicate gel was uniformly distributed in the AAFA matrix. Large capillary pores, which can

generally be observed in cement pastes, were not found. Instead, some large cavities were detected and appeared to be surrounded by the gel. For AAFA samples with no or low silica content in the activator, however, the pore formation was similar to that of cement pastes with  $w/c=0.4$ .

- The degree of pore refinement of AAFA was slower than that of cement pastes with  $w/c=0.4$  in the period of 7 days and 3 month. This leads to a relative porous microstructure of AAFA pastes compared to that of cement pastes ( $w/c=0.4$ ) at later curing age. In addition, the different pore size distribution of capillary pores in AAFA pastes is expected to result in different permeability and shrinkage compared to that of cement pastes. This will be further studied in Chapter 6 and Chapter 7, respectively.
- The MIP and nitrogen adsorption results showed that the pore size distribution of samples with a silica content of 1.5 mol/kg fly ash (mixtures 1.5-1.5) was finer than that of mixtures with a silica content of 1.0 mol/kg fly ash (mixtures 1.0-1.5) at the age of 7 days. At 28 days, mixtures 1.0-1.5 had a finer pore structure than mixtures 1.5-1.5. This is attributed to a higher degree of reaction of mixtures 1.0-1.5 than that of mixtures 1.5-1.5.
- A higher sodium content led to a finer pore structure at 7 days, and this effect was more pronounced at 28 days.
- Extending the curing time at elevated temperature (40 °C) from 7 days to 28 days was beneficial for a finer pore structure of AAFA pastes.
- AAFA samples with a denser gel pore structure, i.e. a lower gel pore threshold diameter, showed a higher elastic modulus of the gel phase.



## Chapter 6

# Permeability of Alkali Activated Fly Ash

---

### 6.1 Introduction

The water permeability of alkali activated fly ash (AAFA) pastes is important for durability related issues. Water can act as a carrier of aggressive agents ( $\text{Cl}^-$ ,  $\text{SO}_4^{2-}$  and  $\text{CO}_2$  etc.) that can penetrate into the concrete, leading to degradation of the microstructure. Water and ion transport are related to the pore structure of the material, particularly to the volume, size distribution, connectivity and the shape of the pores [Hughes, 1985]. In Chapter 5, the pore structure of AAFA pastes was extensively investigated. In this chapter, the pore structure characteristics will be used for determining the permeability of AAFA pastes.

The water permeability was measured for pastes made with different activator content ( $\text{SiO}_2$  and  $\text{Na}_2\text{O}$ ) and for different curing ages. Darcy's law was utilized to calculate the water permeability from steady state flow measurements. The mix compositions of the samples are the same as those used for the MIP measurements (in Chapter 5). The crucial parameters of the pore structure of AAFA pastes were evaluated by correlating the MIP and water permeability results.

### 6.2 Materials and Experimental Methods

#### 6.2.1 Materials

The fly ash and activating solutions applied in this chapter are the same as mentioned in Chapter 5. The detailed mix composition of AAFA mixtures is given in Table 6.1.

*Table 6.1 Mix composition of AAFA pastes mixtures*

Sample ( $\text{SiO}_2$ - $\text{Na}_2\text{O}$ )	Fly Ash (g)	$\text{SiO}_2$ (mol)	$\text{Na}_2\text{O}$ (mol)	$\text{H}_2\text{O}$ (g)
0.5-1.5	1000	0.5	1.5	350
1.0-1.5	1000	1.0	1.5	350
1.5-1.5	1000	1.5	1.5	350
1.0-1.3	1000	1.0	1.3	350
1.0-1.0	1000	1.0	1.0	350

### 6.2.2 Sample preparation for water permeability tests

The mixing procedure for AAFA paste was the same as in Chapter 3. After mixing, the samples, in the form of slurry, were cast in Room Temperature Vulcanized (RTV) silica rubber rings (Figure 6.1). The AAFA samples were cast in a round shape with diameter of 95 mm and thickness of around 10 mm (Figure 6.2). After casting, these samples were tightly sealed in order to prevent moisture loss. At each curing age, three samples were taken out from the sealed mould and immersed in water, followed by vacuum saturation for around 17 hours.

Two different curing conditions were applied prior to testing:

*Curing condition I:* After casting the specimens were sealed and cured in an oven at 40 °C for 7 days and 28 days.

*Curing condition II:* After the specimens were cured in an oven at 40 °C for 7 days, curing continued at 20 °C until 3 or 6 months (in sealed condition).

The purpose of applying these two curing conditions was twofold:

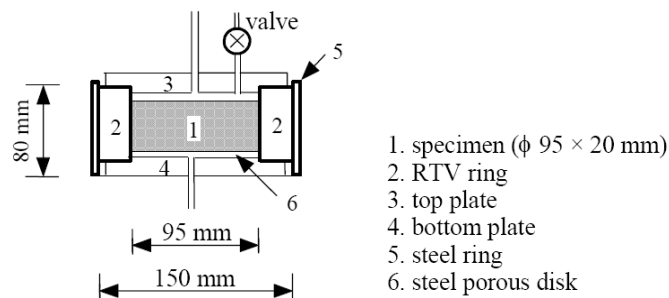


Figure 6.1 Specimen cell for water permeability test [Ye, 2003]

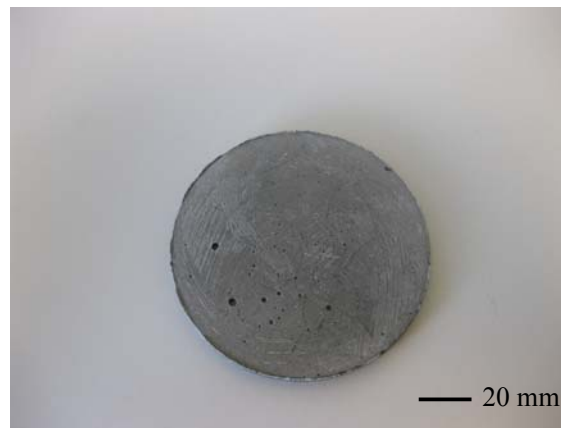


Figure 6.2 Photo of AAFA sample for water permeability test

- 1) To generate more water permeability data for AAFA pastes that can serve as a basis for a more detailed analysis of the correlation between permeability and pore structure parameters;
- 2) The curing condition II is similar to the industrial production process of AAFA samples. The long-term permeability results of AAFA obtained for this curing condition, i.e. 3 and 6 months, are important for durability related issues (e.g. Cl<sup>-</sup> penetration, carbonation).

### 6.2.3 Water permeability testing method

Up to now, there is no universally accepted standard test method for water permeability of cement-based materials [Hooton, 1988], neither there is one for AAFA. In principle, there are two techniques that can be used to measure the water permeability of porous materials. The first method is the *indirect test method*. In this method, the penetration of water into partially dried specimens under a hydrostatic pressure gradient is used. For example, the water penetration test EN 12390-8:2009 and the Figg test are indirect test method. Another method is the *direct test method*, which monitors a steady flow through saturated samples under a hydrostatic pressure gradient. In this study, the direct method was used.

The schematic illustration of the test set-up is shown in Figure 6.3. A commercial air/water converter was used to convert air pressure (0.7 MPa in this study) to water pressure. The compressed air enabled water to penetrate into the specimens fast enough to avoid a possible pore structure change caused by ongoing reaction. The air pressure should not be so high that it may cause damage to the pore structure of the tested material. De-aired water (boiled for 30 seconds) was used for the water permeability test. During the test, water was applied from the bottom of three specimens (cell 1-3) by the air/water converter (Figure 6.3). Water penetrated the specimens and accumulated in the graduated tube that was connected on the top of each cell. The total volume of the graduated tube was 50 ml with an accuracy of 0.1 ml. By monitoring the volume change in each graduated tube during a certain time interval, the water permeability of AAFA specimens can be calculated. The photograph of the whole testing system is presented in Figure 6.4.

The water permeability was calculated according to Darcy's law:

$$Q = \frac{k' \rho g A}{\mu L} \Delta h \quad (6.1)$$

where  $Q$  = the volume of fluid passed in unit time (m<sup>3</sup>/s),

$k'$  = the intrinsic permeability (m<sup>2</sup>),

$\rho$  = density of the fluid (kg/m<sup>3</sup>),

$g$  = the acceleration of gravity (9.81 m/s<sup>2</sup>),

$A$  = the cross-sectional area of the sample (m<sup>2</sup>),

$\mu$  = the dynamic viscosity of the fluid (Ns/m<sup>2</sup>),

$L$  = the thickness of the sample (m),

$\Delta h$  = the drop in hydraulic head over the thickness of the sample (m).



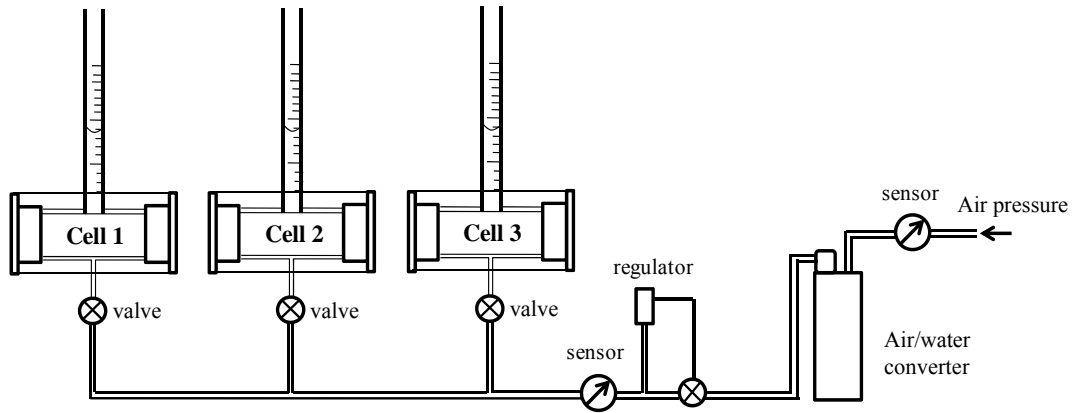


Figure 6.3 Schematic illustration of the experiment set-up for permeability test

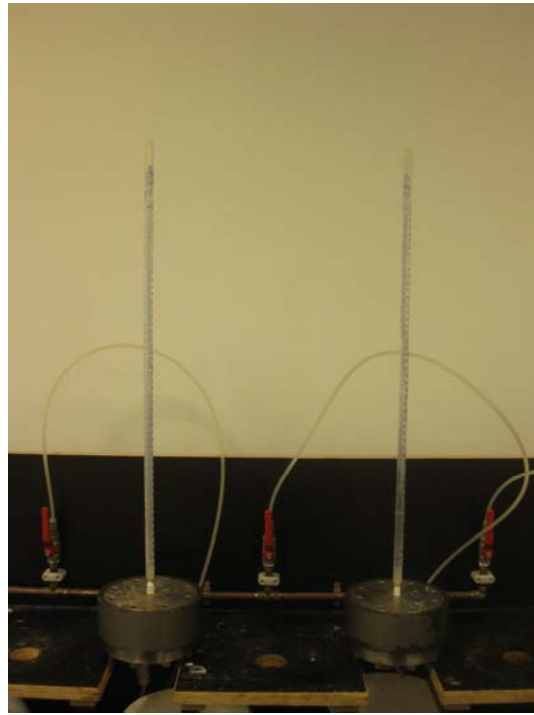


Figure 6.4 Photo of permeability test set up

$k'$  ( $\text{m}^2$ ) can be transformed to water permeability coefficient  $k_w$  (m/s) using the following equation:

$$k_w = \frac{k' \rho g}{\mu} \quad (6.2)$$

For water at 20°C, the term  $\rho g/\mu$  equals  $9.79 \times 10^6 \text{ m}^{-1} \text{ s}^{-1}$  ( $\approx 10^7$ ). When a steady-state flow  $Q$  is reached, the coefficient of permeability of the paste can be determined directly by combining Equation 6.1 and Equation 6.2:

$$k_w = \frac{LQ}{A\Delta h} \quad (6.3)$$

When “permeability” is mentioned in this study, it refers to the water permeability coefficient  $k_w$  (m/s).

### *Calculation of water permeability*

In this experiment, the diameter of the specimen was 0.095 m. Thus the water exposed area  $A$  was 0.007088 m<sup>2</sup>.  $L$  is thickness of the sample taken as the average of 10 measurements. The outlet pressure was atmospheric pressure (top of the cell), taken as 0.1013 MPa, which is equal to a water column of 10.34 m, noted as  $h_1$ . The inlet pressure is 0.7 MPa. The equivalent water column  $h_2$  can be calculated as:

$$h_2 = \frac{0.7}{0.1013} \times 10.34 = 71.43 \text{ (m)} \quad (6.4)$$

Then the hydraulic head  $\Delta h$  can be calculated as:

$$\Delta h = h_2 - h_1 = 71.43 - 10.34 = 61.09 \text{ (m)}$$

The flow rate  $Q$  for each reading during a certain time interval can be calculated as follows:

$$Q = \frac{\Delta V}{\Delta t} \quad (6.5)$$

where  $\Delta V$  (m<sup>3</sup>) is the incremental volume of water read from the graduated tube after a steady-state flow is reached,  $\Delta t$  (s) is the time interval during which the volume was collected. The steady-state flow is determined by plotting the total volume of collected water versus elapsed time. When the resulting curve is linear over the last 10 or more readings (with a time interval between 1-3 hours of each reading), the steady-state flow is assumed to have been reached. The time required to reach a steady-state flow varied from several minutes to several hours, depending on the mixture and the curing age of the specimens. The flow rate  $Q$  was taken as the average volumetric flow rate over the last ten readings.

## **6.3 Results and Discussion**

### **6.3.1 Permeability results**

#### *Scatter of permeability results*

Figure 6.5 shows the water permeability of AAFA pastes with different SiO<sub>2</sub> and Na<sub>2</sub>O content and of Portland cement with w/c=0.4 [Wang et al., 2010; Ye, 2003]. Figure 6.6 shows the water permeability of AAFA samples cured at different temperatures. The standard deviation of permeability is indicated with vertical bars. The coefficient of variation was between 1 % and 30 %. Such deviation of permeability values of AAFA pastes was much lower than that of cement pastes, of

which the deviation smaller than 200 % had already been considered as a good result [Banthia and Mindess, 1989]. This is partially attributed to the fact that pastes made of AAFA are more homogenous than cement pastes, since no bleeding occurred in AAFA pastes. Another possible reason is that the permeability of cement-based materials is largely affected by the ongoing hydration during the test period (normally one week), whereas in AAFA pastes the reaction at environmental temperature (e.g. 20 °C) is considerably slower. Thus the development of the pore structure is slower (as shown in Chapter 5).

#### *The effect of silica content*

Figure 6.5a shows that mixtures with a higher silica content had a significantly lower permeability at 7 days. Water permeability is related to the microstructure of AAFA pastes. It was found in Section 5.4.1 that an increase of silica content led to finer pore structure at 7 days (see Figure 5.9 and 5.11a). This, in turn, results in a lower permeability at 7 days.

At the age of 28 days, the permeability of mixtures with a silica content of 1.0 mol/kg fly ash (mixtures 1.0-1.5) was the lowest ( $3.60 \times 10^{-13}$  m/s). At 28 days, mixtures with a silica content of 1.0 mol/kg fly ash (mixtures 1.0-1.5) had a higher degree of pore refinement (Figure 5.9) and a smaller effective porosity (Figure 5.11a) than mixtures with a silica content of 1.5 mol/kg fly ash (mixtures 1.5-1.5). Thus mixtures 1.0-1.5 showed a lower permeability than mixtures 1.5-1.5 at 28 days.

#### *The effect of alkali content*

Figure 6.5b shows that the permeability slightly decreased for mixtures with a higher sodium content at 7 days, and this effect was more pronounced at 28 days. This is related to further reactions of the AAFA specimens with increasing sodium content (Figure 4.16 in Chapter 4). With more reaction product (aluminosilicate gel), a denser matrix was formed with a finer pore structure (see Figure 5.10 and Figure 5.11b). This results in a lower water permeability.

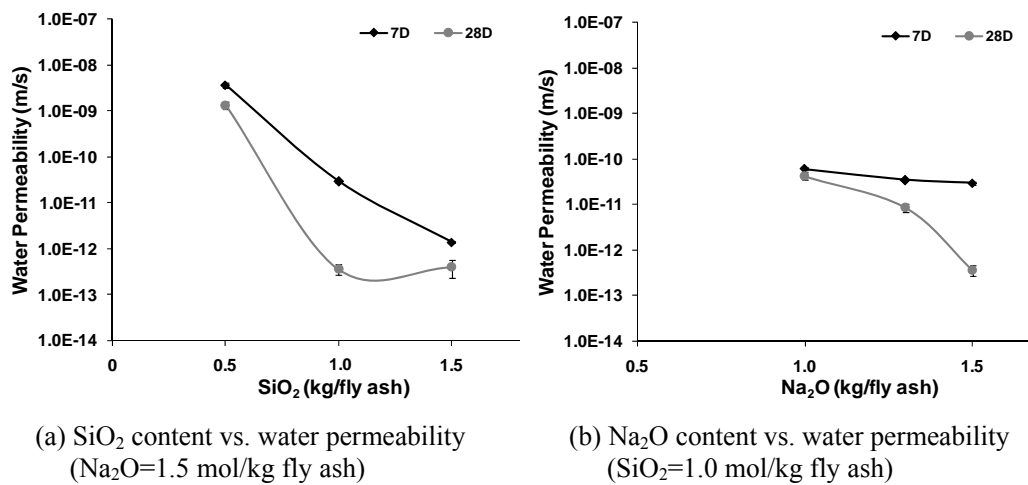
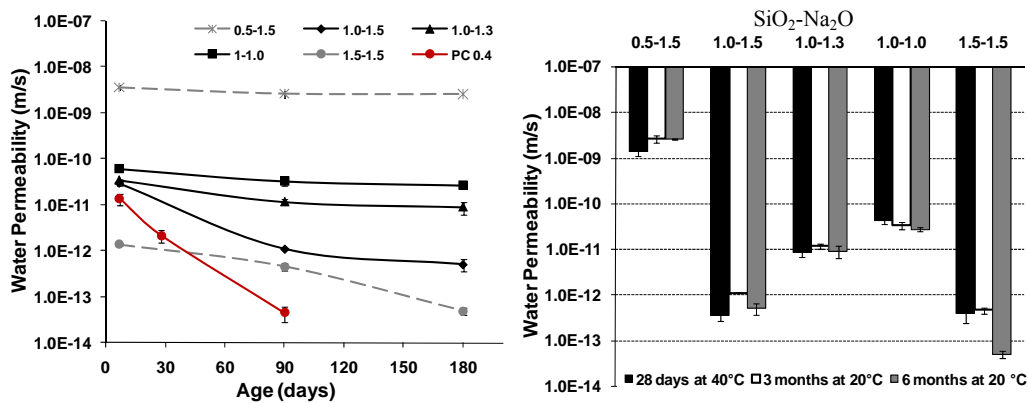


Figure 6.5 Water permeability of AAFA pastes with different SiO<sub>2</sub> and Na<sub>2</sub>O content (cured at 40 °C) at 7 and 28 days

### The effect of curing temperature

The water permeability of AAFA pastes cured at different temperatures is shown in Figure 6.6. Figure 6.6a shows that the water permeability decreased with time for the AAFA specimens cured at 20 °C. Compared to mixtures cured at a higher temperature, 40 °C, however, The water permeability of samples cured at 40 °C for 28 days was still lower than that of specimens cured at 20 °C for 3 or 6 months (Figure 6.6b). These results are consistent with the pore structure measurements (MIP) of samples cured at different temperatures (Figure 5.12). The refinement of the pore structure was less intense for samples cured at room temperature (20 °C) than for those cured at elevated temperature (40 °C). Thus samples cured at 20 °C for 3 months exhibited a higher water permeability than samples cured at 40 °C for 28 days.



(a) Water permeability of AAFA cured at 20 °C (b) Water permeability of AAFA cured at 20 and 40 °C

Figure 6.6 Comparison of water permeability of AAFA pastes cured at different curing temperatures (for specimens cured for 3 and 6 months at 20 °C, 7 days curing at 40 °C in advance was applied)

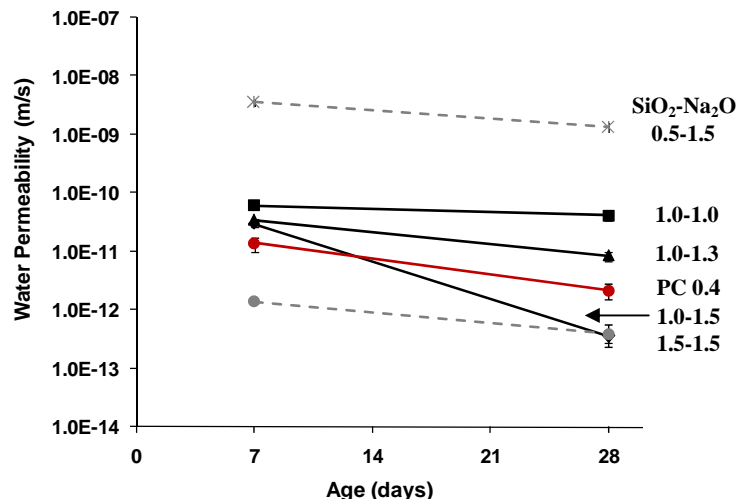


Figure 6.7 Comparison of the water permeability between AAFA pastes, cured at 40 °C, and cement pastes with w/c=0.4 [Wang, Ye et al., 2010; Ye, 2003]

*Comparison with cement paste*

Figures 6.6a and 6.7 compare the water permeability between AAFA pastes and cement pastes ( $w/c=0.4$ ) obtained from [Wang, Ye et al., 2010; Ye, 2003]. Both figures show that the water permeability of AAFA mixtures with low silica or sodium content ( $< 1.5$  mol/kg fly ash) (i.e. 0.5-1.5, 1.0-1.3 and 1.0-1.0) is much higher than that of cement pastes ( $w/c=0.4$ ), especially at later age. The permeability of mixtures with silica and sodium content of 1.5 mol/kg fly ash (mixtures 1.5-1.5) is lower than that of cement pastes ( $w/c=0.4$ ) at 7 days and 28 days cured at 40 °C. For samples 1.0-1.5, the water permeability was lower than that of cement pastes ( $w/c=0.4$ ) at the age of 28 days (Figure 6.7). The water permeability of all the AAFA samples cured at 20 °C for 3 month, however, is lower than that of cement pastes ( $w/c=0.4$ ) (Figure 6.6a). This is related to the less intense pore structure refinement of AAFA samples cured at 20 °C. The slower rate of pore refinement and permeability development of AAFA mixtures are important issues be taken into account when it comes to predictions of the long-term performance of these AAFA mixtures.

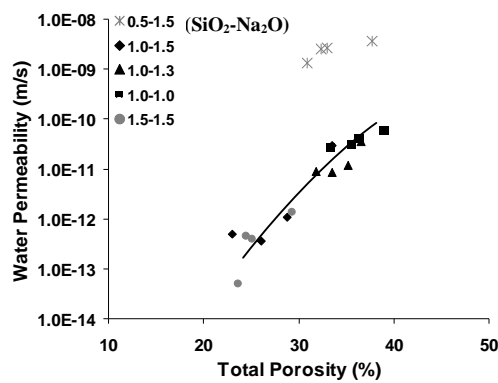
It is generally assumed that samples with higher porosity are more permeable. However, for some AAFA pastes and cement pastes, this seems not to be always the case. Table 6.2 shows the total porosity (measured by MIP) and water permeability of some AAFA samples and cement paste samples ( $w/c=0.4$ ) at 7 and 28 days. It is found that for some AAFA samples, although the total porosity was higher than that of cement pastes ( $w/c=0.4$ ), the water permeability was much lower. It indicates that the pore structure of AAFA pastes is very different from that of cement pastes. This suggests a different pore shape and pore connectivity. As discussed in Chapter 5, the main difference of pore structure between AAFA pastes with silica content  $\geq 1$  mol/kg fly ash and cement pastes is the distribution of the “capillary pores”. The capillary pores in cement paste, left by the remaining free water, were initially connected at early age. The pores became gradually filled with reaction products and became disconnected at later age. In the case of AAFA pastes (with silica content  $\geq 1$  mol/kg), however, the “capillary pores” were the cavities left by dissolved fly ash particles and appeared as voids surrounded by the gel. From MIP measurements it could be inferred that these large cavities were accessible through pores between 0.1 and 1  $\mu\text{m}$ . The different pore structures between AAFA and cement pastes indicate a different connectivity of pores. It is assumed that these large cavities in AAFA pastes contributed less to the water permeability than the contribution of typical capillary pores in cement pastes, especially at early age (7 days). This might have been the reason why the water permeability of AAFA pastes is lower than that of cement pastes while the total porosity is higher.

*Table 6.2 Total porosity and permeability of AAFA pastes and Portland cement (PC) pastes ( $w/c=0.4$ )*

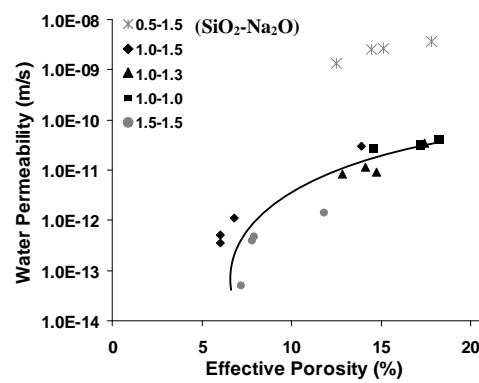
Sample	1.5-1.5, 7 days	PC $w/c=0.4$ , 7 days	1.5-1.5, 28 days	1.0-1.5, 28 days	PC $w/c=0.4$ , 28 days
Total Porosity (%)	29.27	29.06	26.02	25.17	22.52
$k(\text{m/s}) \times 10^{-12}$	1.38	13.90	0.40	0.36	2.19

### 6.3.2 Experimentally observed relationship between water permeability and pore structure parameters derived from MIP

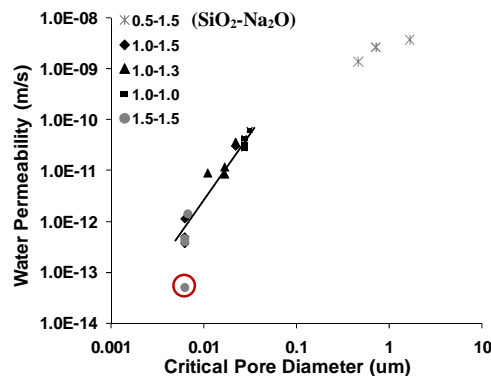
It is known that the pore size distribution, the pore connectivity, the shape and also the volume of the pore space are important parameters that influence the water permeability of porous materials. In Figure 6.8, the measured permeability is plotted against the total porosity, the effective porosity and the critical (threshold) pore diameter, respectively, derived from MIP tests. The figure shows a relationship between the water permeability and the total porosity (Figure 6.8a), the effective porosity (Figure 6.8b) and the critical pore diameter (Figure 6.8c) of AAFA samples, respectively, regardless of the activator content, curing age and curing temperature.



(a) Total porosity vs. water permeability



(b) Effective porosity vs. water permeability



(c) Critical pore diameter vs. water permeability

Figure 6.8 Correlations between pore structure parameters deduced from MIP results and the water permeability of AAFA pastes, in (c), critical pore diameter data with red circles are affected by the measuring limit of MIP tests, thus they are not used in curve fitting

A strong correlation is found between the gel pore threshold diameter and water permeability of most the AAFA mixtures, while such correlation is not found between the capillary pore threshold diameter and water permeability (Table 6.3). Thus the critical (threshold) pore diameters, as shown in Figure 6.8c, are the gel pore threshold diameters, instead of the capillary pore threshold diameter. This may be related to the special distribution of “capillary pores” in AAFA as discussed in Chapter 5.

*Table 6.3 Capillary pore and gel pore threshold diameter and permeability of different AAFA pastes at 7 and 28 days*

AAFA pastes (SiO <sub>2</sub> -Na <sub>2</sub> O)	Age (days)	k(m/s)×10 <sup>-12</sup>	Gel pore threshold diameter (μm)	Capillary pore threshold diameter (μm)
1.5-1.5	7	1.38	0.006	0.437
1.0-1.5	7	29.40	0.022	0.380
1.0-1.3	7	34.90	0.022	0.315
1.0-1.0	7	60.70	0.031	0.203
1.5-1.5	28	0.40	0.006	0.381
1.0-1.5	28	0.36	0.006	0.315
1.0-1.3	28	8.52	0.017	0.203
1.0-1.0	28	42.00	0.027	0.082

From all investigated cases, the microstructure of specimens 0.5-1.5, with a low silica content, differs significantly from all other AAFA specimens: the water permeability was the highest, while the total porosity and the effective porosity were similar to that of the other AAFA pastes (Figure 6.8a, b). Further, the highest water permeability of specimens 0.5-1.5 correlates well with the largest critical pore diameter (Figure 6.8c). This indicates that the critical pore diameter dominates the permeability of specimens 0.5-1.5.

For specimens 1.5-1.5, i.e. the mixture with a high silica content, different values of permeability were found to correspond to the same critical pore diameter (circled point in Figure 6.8c). This is caused by the measuring limit of the MIP equipment used in this study. The gel pore threshold diameter for specimens 1.5-1.5 at later ages (e.g. 6 months cured at 20 °C) was even smaller than the measuring limit of the MIP equipment. If a higher pressure can be provided by the MIP equipment (> 210 MPa), a lower threshold pore diameter is expected to be obtained, corresponding to the lower water permeability of specimens 1.5-1.5 at later ages. The MIP results for specimens 1.5-1.5 at the age of 6 months were not used for permeability prediction in the next section.

### 6.3.3 Prediction of the water permeability based on MIP results

In Figure 6.8, same trends were shown regarding the relationship between the total porosity, the effective porosity, the critical pore diameter (measured by MIP) and the water permeability of AAFA. The remaining question is whether it is possible to predict the water permeability of AAFA based on MIP data. In fact, many attempts have been made for the prediction of water permeability of *cement-based materials* by using the data obtained from MIP and electrical conductivity measurements [Bentz

and Garboczi, 1991; Christensen et al., 1996; El-Dieb and Hooton, 1994]. A critical review of the water transport theories and their applicability to cement-based materials has been reported by Garboczi [Garboczi, 1990]. It was concluded that the intrinsic permeability coefficient,  $k'$  ( $\text{m}^2$ ), can be expressed as a function of pore structure parameters as follows:

$$k' = d_c^2 \eta \varphi \quad (6.6)$$

where  $d_c$  is a length scale that characterizes the pore diameter that dominates fluid transport;  $\eta$  is the porosity or pore volume fraction;  $\varphi$  is a dimensionless parameter ( $< 1$ ), that takes into account the tortuosity and connectivity of the pore network.

In this study, an attempt was made to make use of microstructure parameters derived from the MIP tests (Table 6.4) as input to calculate permeability. According the Katz-Thompson theory [Katz and Thompson, 1986; Katz and Thompson, 1987],  $d_c$  can be obtained from the MIP measurements, equal to the critical pore diameter. The physical meaning of a critical pore diameter is that pores whose diameter is greater than this diameter can form no connected path throughout the sample [Cui and Cahyadi, 2001]. In this study, the gel pore threshold diameter was assigned to parameter  $d_c$ . The term  $\eta \cdot \varphi$  stands for the effective porosity,  $\eta_{eff}$ , which can also be determined from MIP measurements. It means the permeability is related to the critical pore diameter that dominates fluid transport, i.e.  $d_c$ , and the porosity that eliminates the effect of ink-bottles, i.e. effective porosity ( $\eta_{eff}$ ).

*Table 6.4 Measured permeability, porosity, threshold radius and effective porosity of AAFA pastes (derived from MIP tests)*

AAFA pastes (SiO <sub>2</sub> -Na <sub>2</sub> O)	Age (days)	k (m/s)×10 <sup>-12</sup>	Threshold radius $d_c$ (μm),	Effective porosity $\eta_{eff}$ (%),
0.5-1.5	7	3600	1.651	17.80
	28	1350	0.466	12.51
	90	2620	0.712	15.15
	180	2560	0.712	14.46
1.0-1.5	7	29.4	0.022	13.50
	28	0.36	0.006	6.05
	90	1.09	0.006	6.84
	180	0.503	0.006	6.03
1.0-1.3	7	34.9	0.022	17.41
	28	8.52	0.017	12.86
	90	11.7	0.017	14.14
	180	8.95	0.011	14.72
1.0-1.0	7	60.7	0.031	21.73
	28	42.0	0.027	18.21
	90	32.9	0.027	17.17
	180	26.8	0.027	14.49
1.5-1.5	7	1.38	0.006	11.83
	28	0.40	0.006	7.81
	90	0.46	0.006	7.91
	180	0.049	0.006	7.23



Table 6.4 lists the pore parameters (derived from MIP tests) and measured water permeability of different AAFA pastes at 7, 28, 90 and 180 days. By using these data as input (Table 6.4), the calculated permeability (using equation 6.6) versus the measured permeability of AAFA pastes is plotted in Figure 6.9. A linear relationship was found between the calculated and measured permeability for most of the AAFA specimens, regardless their age and curing condition. The gradient between the measured permeability and the calculated permeability is 0.031 (Figure 6.9). This means that the calculated permeability (equation 6.6) is about 100 times bigger than the measured permeability.

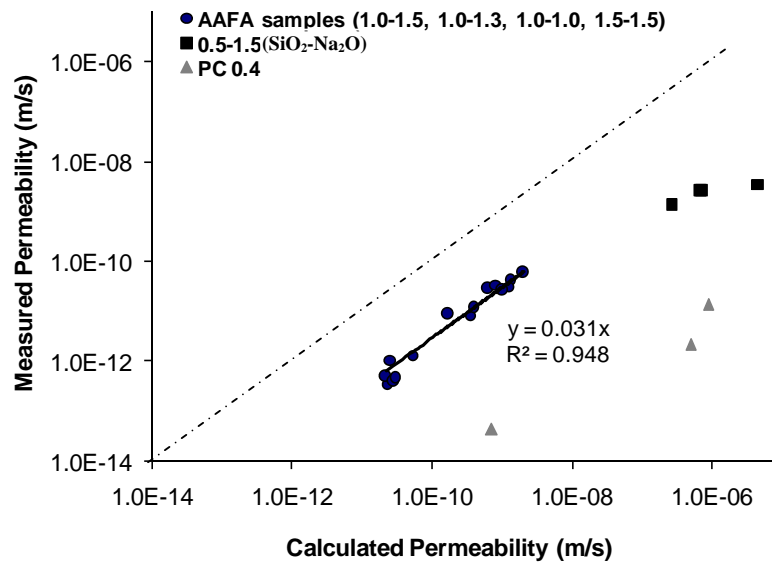


Figure 6.9 Correlation between the calculated and measured water permeability of AAFA pastes and cement pastes ( $w/c=0.4$ )

The correlation between calculated permeability and measured permeability of specimens  $\text{SiO}_2\text{-Na}_2\text{O}=0.5\text{-}1.5$  and cement pastes ( $w/c=0.4$ ) is found to be different from those of the other AAFA samples (see Figure 6.9). This is attributed to the different pore structure of these samples compared to the other AAFA samples. As we know in cement paste, both the capillary pores and gel pores contribute to the water permeability [Cui and Cahyadi, 2001]. Normally two processes are involved in the permeability of cement paste. When the matrix is very porous, water mainly flows through the capillary pores. The contribution of the gel pores can be ignored. As the reaction continues, the capillary pores of cement paste became gradually disconnected by the reaction products. The contribution of the capillary and gel pores should then both be taken into account. For AAFA pastes with the silica content  $\geq 1$  mol/kg, the large pores (cavities) are disconnected and only accessible through small pores. From Table 6.3 it can be inferred that for all the AAFA mixtures the water permeability was lower for mixtures with a smaller gel pore threshold diameter. It indicates that the gel pore system was the main factor affecting the water permeability of AAFA pastes. It

is assumed that the densification of the gel increases the tortuosity of pores, resulting in a decrease of the pore connectivity in AAFA pastes and a lower water permeability.

#### 6.4 Concluding remarks

In this chapter, the water permeability of alkali activated fly ash pastes with different activator content ( $\text{SiO}_2$  and  $\text{Na}_2\text{O}$ ) and different curing temperatures was measured at different curing ages. The main conclusions from the experimental studies can be summarized as follows:

- The effect of the silica and sodium content on the water permeability is consistent with its effect on the pore structure. At 7 days, mixtures with a silica content of 1.5 mol/kg fly ash (mixtures 1.5-1.5) had a finer pore structure than mixtures with a silica content of 1.0 mol/kg fly ash (mixtures 1.0-1.5). Thus the water permeability of mixtures 1.5-1.5 was lower than that of mixtures 1.0-1.5 at 7 days.

At 28 days, mixtures with a silica content of 1.0 mol/kg fly ash (mixtures 1.0-1.5) had a higher degree of pore refinement and a lower effective porosity than mixtures with a silica content of 1.5 mol/kg fly ash (mixtures 1.5-1.5). Thus mixtures 1.0-1.5 had a lower water permeability than mixtures 1.5-1.5 at 28 days.

- A higher sodium content resulted in a finer pore structure and a lower water permeability of AAFA pastes. The degree of pore refinement was more pronounced at later age for mixtures with a higher sodium content. Consequently the decrease of the water permeability in the period of 7 days and 28 days was the most pronounced for mixtures with the highest sodium content, i.e. 1.5 mol/kg fly ash of mixtures 1.0-1.5.
- For most of the AAFA pastes, the rate of pore refinement at later age, e.g. 28 days, 3 and 6 months, is significantly slower than that of cement pastes with  $w/c = 0.4$ . Thus the decrease of permeability with time for AAFA pastes is much slower than that for cement pastes ( $w/c = 0.4$ ). The slower rate of pore refinement of AAFA mixtures is important when it comes to predictions of the long-term performance of these mixtures.
- The permeability is related to the pore threshold diameter and the effective porosity (derived from MIP results). By using these two pore structure parameters as inputs to calculate the water permeability, a linear relationship was found between the calculated and measured permeability for most of the AAFA samples.



## Chapter 7

# Shrinkage of Alkali Activated Fly Ash

---

### 7.1 Introduction

In concrete technology cement hydration and drying are the two main processes that lead to shrinkage. Shrinkage induced by the hydration of cement includes chemical shrinkage and autogenous shrinkage. Chemical shrinkage is known as the volume reduction associated with the chemical reaction between cement and water [Powers, 1935]. Autogenous shrinkage is defined as the bulk deformation of a sealed cured system not subjected to external forces and no moisture transfer [Jensen and Hansen, 2001]. Before setting, when cement paste is fluid, the chemical shrinkage may be totally converted into external volume change [Lura and Jensen, 2007]. The chemical shrinkage is equal to the autogenous shrinkage at this stage. As long as a solid skeleton is formed, the volume change caused by chemical shrinkage is resisted by the newly-formed structure. This will lead to the formation of water-air menisci and internal relative humidity (RH) drops [Jensen and Hansen, 2001]. Thus, after setting, autogenous shrinkage of cement is governed by the self-desiccation process, and its magnitude is much smaller than that of chemical shrinkage.

Drying shrinkage is caused by the loss of water to the environment. It happens when the external humidity is lower than the humidity inside the material. Autogenous shrinkage is caused by the water consumption inside the hardening sample (self-desiccation [Jensen and Hansen, 2001]). For evaluating both autogenous and drying shrinkage, we have to know the state of water in the material.

A clear understanding of the shrinkage of alkali activated fly ash (AAFA) pastes is a prerequisite for the control of shrinkage-induced cracking in concrete structures. Shrinkage of AAFA systems is not studied as extensively as that of cement-based material. The shrinkage mechanisms are still not fully understood. In this chapter, the mechanisms that induce shrinkage of AAFA pastes, as well as the relevant shrinkage parameters, will be discussed and compared to that of cement pastes.

Measurement results of chemical shrinkage, autogenous shrinkage and drying shrinkage of AAFA pastes are presented in this chapter. The internal relative humidity (RH) and the non-evaporable water content in AAFA pastes are measured. With these two parameters, the state of moisture in the material is defined. They are important to understand the mechanisms of shrinkage in AAFA. Ellipse ring tests are performed to

assess the proneness to cracking of AAFA pastes under restrained condition. The test results are compared to those of cement pastes ( $w/c=0.4$ ).

## 7.2 Materials and Experimental Methods

### 7.2.1 Materials

The fly ash used in this chapter is the same as in previous chapters. Three AAFA mixtures were selected, shown in Table 7.1. They include the mixture with the highest compressive strength at 7 days ( $\text{SiO}_2\text{-Na}_2\text{O}=1.5\text{-}1.5$ ), the mixture having the highest degree of reaction and compressive strength at 28 days ( $\text{SiO}_2\text{-Na}_2\text{O}=1.0\text{-}1.5$ ) and the mixture with the lowest sodium content (saving cost), but still having a reasonable compressive strength ( $\text{SiO}_2\text{-Na}_2\text{O}=1.0\text{-}1.0$ ). For these three mixtures, the effect of silica and sodium content on the shrinkage of AAFA pastes was studied.

*Table 7.1 Mix composition of AAFA mixtures*

Sample ( $\text{SiO}_2\text{-Na}_2\text{O}$ )	Fly Ash (g)	$\text{SiO}_2$ (mol)	$\text{Na}_2\text{O}$ (mol)	$\text{H}_2\text{O}$ (g)
1.0-1.5	1000	1.0	1.5	350
1.5-1.5	1000	1.5	1.5	350
1.0-1.0	1000	1.0	1.0	350

### 7.2.2 Chemical shrinkage

The chemical shrinkage of AAFA pastes was measured according to ASTM Standard C 1608-07 (Procedure A) [2007], except that the temperature of the water bath was kept at 40 °C, instead of 20 °C (elevated temperature is needed for the alkali activation of fly ash). In this method, 100 g fly ash was mixed with the alkali solution in a container using a small blender. After mixing, about 7 g freshly mixed AAFA paste was placed in the bottom of a small glass vial (Figure 7.1), with a diameter of 25 mm and a height of about 50 mm. The surface of the paste was covered with a thin layer (about 0.7 ml) of distilled water. Afterwards, the remaining space of the vial was filled with paraffin oil and closed with a rubber stopper encasing a graduated tube (Figure 7.1) with a total volume of 1 ml and an accuracy of 0.01 ml. The vial was then immersed in a temperature controlled water bath at 40 °C. A control sample using only paraffin oil was used as a reference and to eliminate the effect of temperatures. The first measurement was performed after 30 min immersion of the samples in the water bath when the read of the control sample remained constant. Measurements were performed for 7 days. The chemical shrinkage per gram of initial solid (including fly ash, added  $\text{Na}_2\text{O}$  and  $\text{SiO}_2$ ) was determined by normalizing the change in volume to the mass of solid in the sample. For each mixture, three samples were tested.

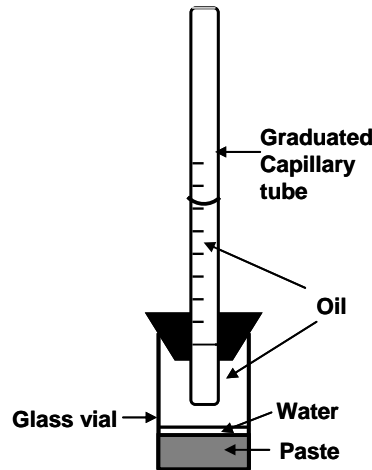


Figure 7.1 Glass vial with graduated tube for measurements of chemical shrinkage

### 7.2.3 Sample preparation and test methods for autogenous shrinkage

Two commonly used methods were used to measure the autogenous shrinkage of AAFA pastes: corrugated tube method and ASTM C 157 method. These two methods start to measure the autogenous shrinkage of materials from different age of the samples: the corrugated tube method measures the shrinkage of specimens from the moment of final setting, while the linear measurement records the deformation of specimens after demolding of the samples normally 24 h after casting.

#### *Corrugated tube measurement*

In this method, autogenous shrinkage of AAFA is measured according to ASTM C 1698–09 [2009]. The test device consists of a corrugated mould with two end plugs, a dilatometer bench, a length measuring gauge, and a reference bar (Figure 7.2 [2009]). The corrugated mould can transform volumetric deformations into linear deformations when the paste is in a fluid state [Lura and Jensen, 2007]. The corrugated mould effectively prevents moisture loss and minimizes restraint to volume change during hardening. For sample preparation, the freshly mixed AAFA paste was cast into a corrugated mould with a length-to-diameter ratio of approximately 420:29 mm on a vibrating table. The mould was then sealed with plugs and stored at a constant temperature of 40 °C in an oven. The first measurement was carried out by using the length measuring gauge (with a measuring accuracy of about 6  $\mu\text{m}/\text{m}$ ) at the final setting time (determined by Vicat needle test). The length change was recorded during a period of 28 days. Three samples were measured for each mixture.



Figure 7.2 The apparatus for corrugated tube measurement for autogenous shrinkage [ASTM 1698-09, 2009]

#### *ASTM C 157 method*

In this method, the length measurement is performed according to ASTM C157. The freshly mixed AAFA pastes were cast in moulds with the dimension of 40×40×160 mm and sealed cured in an oven at 40 °C for 24 h. After that, the specimens were removed from the moulds, wrapped with an inner layer of plastic foil and an outer layer of aluminum foil, and sealed with tape to avoid moisture loss. The sealed specimens were then stored at a constant temperature of 40 °C. Measurements of the length change of specimens were performed over a period of 28 days by using a comparator (accuracy of 0.001 mm). The average length change of at least two specimens was calculated for each mixture.

#### **7.2.4 Sample preparation and test methods for drying shrinkage**

The test method for the drying shrinkage of AAFA pastes was similar to that of the ASTM C 157 method of autogenous shrinkage mentioned above, except that specimens for drying shrinkage test were not sealed, but exposed to an environment with RH 50 % ± 5 %. The specimens were cast in 40 × 40 × 160 mm moulds and sealed cured (with plastic film) at 40 °C in an oven for 7 days. After elevated temperature curing at 40 °C, the specimens were removed from the oven and cooled down to room temperature of 20 ± 3 °C. Afterwards, the specimens were exposed in a room with a constant temperature of 20 ± 3 °C and a relative humidity of 50 % ± 5 % (Figure 7.3a). The length and mass changes of AAFA specimens were monitored by using a comparator with a measuring accuracy of 0.001 mm (Figure 7.3b) and a balance with an accuracy of 0.01 g. For comparison, the drying shrinkage of cement paste with w/c=0.4 was also measured. The measurements started after sealed curing at 20 °C for 7 days. At least two samples were measured in parallel for each mixture.

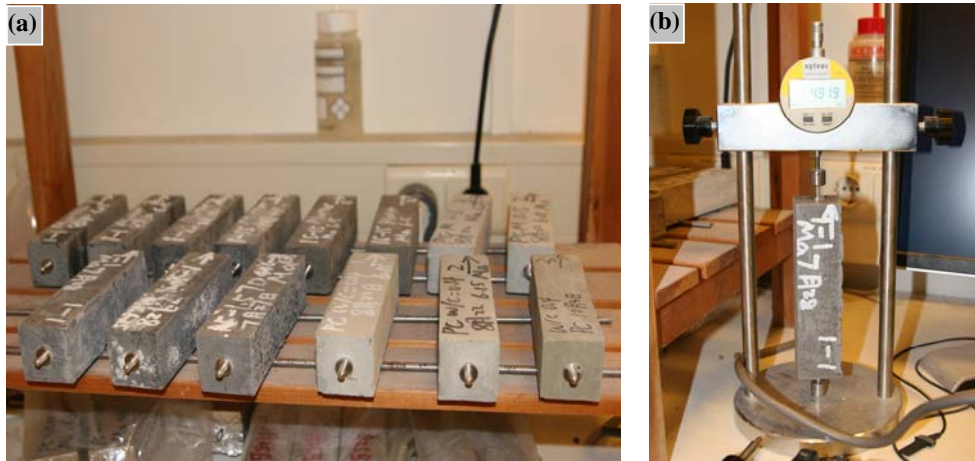


Figure 7.3 Photos for the drying shrinkage tests of AAFA samples

### 7.2.5 Ellipse ring test of AAFA pastes: cracking of sealed specimens

The ellipse ring test is a simple and fast way to assess the material's proneness to early-age cracking under restrained condition. The apparatus used in the ellipse ring test is shown in Figure 7.4 (with pastes filled). The test sample (AAFA pastes in this study) was cast in an annular space (40 mm wide) around a steel ellipse ring with long axis of 560 mm and short axis of 200 mm. The height of the ellipse ring was 80 mm. Compared to a circular shape, an elliptical shape can generate a high stress concentration [He and Li, 2005]. When the sample shrinks (induced by autogenous shrinkage in this study), the steel ring limits this movement resulting in the development of tensile stress. If the tensile stress exceeds the tensile strength of the tested sample, cracking will occur. In an ellipse ring test, although the stress state in the samples at the location of the crack is not exactly known, the ellipse ring test provides an indication of the cracking tendency of mixtures by monitoring the appearance of cracks. (The ellipse ring tests were performed in South China University of Technology, Guangzhou, China)

AAFA mixtures with  $\text{SiO}_2\text{-Na}_2\text{O}=1.0\text{-}1.5$ ,  $1.5\text{-}1.5$  and  $1.0\text{-}1.0$  (with respect to 1 kg fly ash) were prepared for the ellipse ring test. After casting, the ellipse ring test specimens were sealed with plastic film and cured in an oven at  $40\text{ }^\circ\text{C}$ , the samples were checked regularly by visual observation to see if cracks formed at the surface of AAFA samples during the first 7 days of curing.





*The dimensions of ellipse sample:*

Outer ellipse long axis (mm)	Outer ellipse short axis (mm)	Inner ellipse long axis (mm)	Inner ellipse short axis (mm)	Height (mm)
600	240	560	200	80

*Figure 7.4 Ellipse ring test setup [He and Li, 2005]*

### 7.2.6 Internal relative humidity of AAFA pastes

The internal RH development of AAFA pastes was measured by Rotronic HygroLab C1 (Figure 7.5a) equipped with two HC2-AW RH station probes with an accuracy  $\pm 1\%$  RH (Figure 7.5b). The RH probes were placed in a temperature controlled room at  $40 \pm 1^\circ\text{C}$ . Before the measurements, the RH probes were calibrated using saturated salt solutions with known constant RH in the range of 65-95 %. After calibration, the freshly mixed AAFA pastes were cast in two plastic sample containers and then put into the measuring chambers. The RH in the samples and the temperature were recorded every 1 minute for about 3 days.



(a) Rotronic HygroLab C1

(b) HC2-AW RH station probes

*Figure 7.5 The apparatus for internal RH measurement*

### 7.2.7 Evaporable and non-evaporable water content in AAFA pastes

Both the evaporable and non-evaporable water in AAFA pastes were measured. The categorization of water in AAFA pastes in evaporable and non-evaporable is similar to that used for cement-based materials by Powers and Brownyard [1946]. The content of non-evaporable water was normally used as an indicator of the degree of hydration of cement-based materials. In those materials, the evaporable water is determined by measuring the weight loss per gram of the sample after heating it at 105 °C to constant weight. The non-evaporable water content is determined by measuring the weight loss per gram of the sample between 105 °C and 950 °C. The evaporable ( $W_e$ ) and non-evaporable ( $W_{ne}$ ) water content are calculated according to the following equation:

$$W_e = \frac{W_0 - W_1}{W_0} \quad (7.1)$$

$$W_{ne} = \frac{W_1}{W_2} (1 - L) - 1 \quad (7.2)$$

Where  $W_0$  = mass of original specimen used (g),

$W_1$  = mass of specimen after heating at 105 °C (g),

$W_2$  = the mass of specimen after heating at 950 °C (g),

$L$  = loss on ignition of a sample of the original dry powder (g/g of original sample).

The evaporable and non-evaporable water content of AAFA pastes were measured at the age of 1, 3, 7, 14, 28, 56 and 90 days (sealed cured at 40 °C). The average of three samples was calculated in parallel for each mixture.

## 7.3 Results and Discussion

### 7.3.1 Chemical shrinkage of AAFA pastes

Figure 7.6 shows the chemical shrinkage of the three investigated AAFA mixtures as a function of curing age. In general, the chemical shrinkage of all three AAFA mixtures after 7 days was between 0.04-0.05 ml/g of initial solid (including fly ash, Na<sub>2</sub>O and SiO<sub>2</sub>).

The chemical shrinkage happens because the reaction products occupy less volume than the initial reactant. It is generally accepted that the extent of chemical shrinkage is proportional to the degree of reaction that happens in the material [Criado, Fernandez-Jimenez et al., 2007b; Parrott et al., 1990]. Figure 7.6 shows that the specimens with the lowest SiO<sub>2</sub> and Na<sub>2</sub>O content (SiO<sub>2</sub>-Na<sub>2</sub>O=1.0-1.0) exhibited the lowest chemical shrinkage after 7 days, indicating that these mixtures had the lowest degree of reaction. Mixtures SiO<sub>2</sub>-Na<sub>2</sub>O=1.5-1.5 and 1.0-1.5 showed similar chemical shrinkage after 7 days (Figure 7.6), while mixtures 1.5-1.5 had a lower degree of reaction than mixtures 1.0-1.5 (Chapter 4). The reason is still not clear. Mixtures 1.5-

1.5 had a higher amount of silica than mixtures 1.0-1.5 (0.5 mol/kg fly ash more). It is possible that the extra silica reacts with the aluminum species dissolved from the fly ash particles, which also contributes to the contraction of the material. Thus, mixture 1.5-1.5 showed similar chemical shrinkage as mixture 1.0-1.5, although the degree of reaction of mixture 1.5-1.5 was lower.

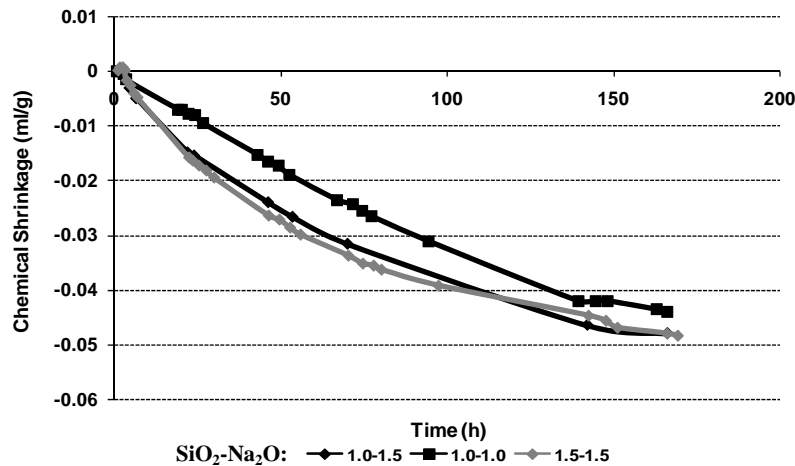


Figure 7.6 The chemical shrinkage of AAFA pastes with different  $\text{SiO}_2$  and  $\text{Na}_2\text{O}$  content at 40 °C

### 7.3.2 Autogenous shrinkage of AAFA pastes

Figures 7.7 and 7.8 show the autogenous shrinkage of AAFA pastes measured with the corrugated tube method and ASTM C157 testing method, respectively. From both figures, it is clear that most of the autogenous deformation of AAFA mixtures happened in the first 1-3 days. Only little autogenous shrinkage happened beyond 3 days. Specimens with the highest sodium and silica content (specimens  $\text{SiO}_2\text{-Na}_2\text{O}=1.5\text{-}1.5$ ) exhibited the highest autogenous strain, followed by specimens  $\text{SiO}_2\text{-Na}_2\text{O}=1.0\text{-}1.5$  and  $1.0\text{-}1.0$ .

### 7.3.3 Cracking potential of AAFA pastes due to autogenous shrinkage

In an aggregate-paste mixture, i.e. concrete, the magnitude of autogenous shrinkage of AAFA pastes is important for the internal tensile stress built up in the matrix. If a large autogenous strain is developed under restrained condition, there is a (high) probability of cracking. It is noticed that in Figure 7.7 the autogenous strain was very high for the three AAFA pastes. Although the shrinkage was very large, it did not cause an early age cracking of paste samples in the ellipse ring tests. As shown from the ellipse ring tests performed on these three AAFA pastes (Figure 7.9), no cracks were observed at the surface of the AAFA mixtures after sealed curing at 40 °C for 7 days. Specimens were demolded to see clearly if cracking has happened at the surface

of the samples but no cracks were found (Figure 7.9). It indicates that the stress caused by the autogenous strain is lower than the tensile strength of the samples.

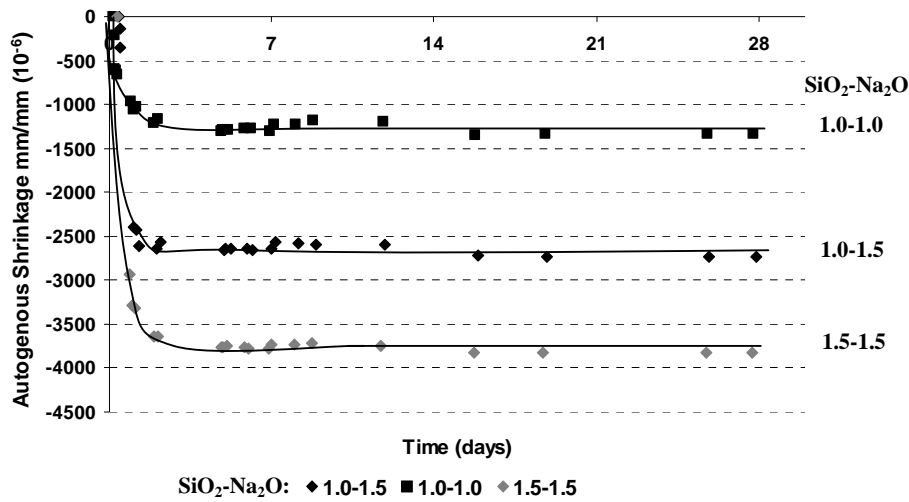


Figure 7.7 Autogenous shrinkage of AAFA pastes with different  $\text{SiO}_2$  and  $\text{Na}_2\text{O}$  content, 40 °C (corrugated tube method, measurement started after the time of final setting)

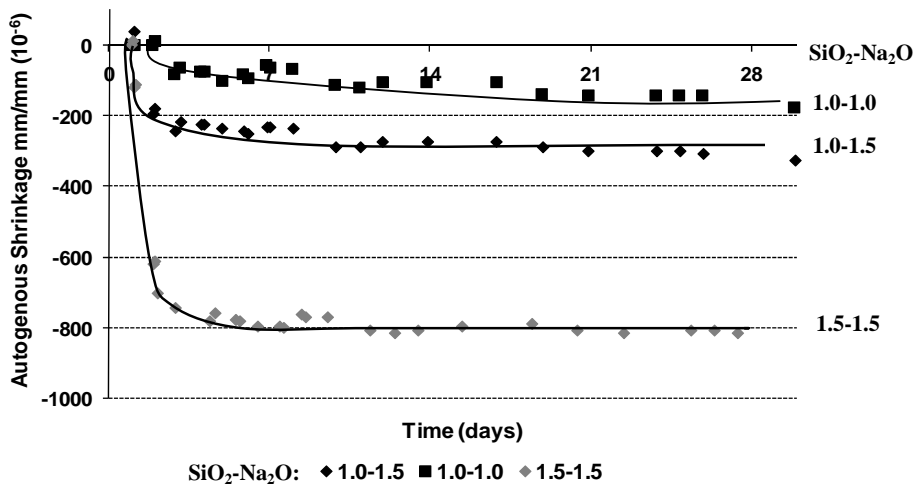


Figure 7.8 Autogenous shrinkage of AAFA pastes with different  $\text{SiO}_2$  and  $\text{Na}_2\text{O}$  content, 40 °C (ASTM C157 method, measurement started after 24 hour of casting)



Figure 7.9 Ellipse ring test for AAFA pastes after sealed cured at 40 °C for 7 days (demolded): cracking was not observed on the surface of all AAFA pastes.

The autogenous strain measured by the corrugated tube method was much higher than that measured by the ASTM C 157 method. For instance, the autogenous shrinkage of specimens 1.5-1.5 at 28 days was 800  $\mu\text{m}/\text{m}$  by using ASTM C 157 method (Figure 7.8), while around 3800  $\mu\text{m}/\text{m}$  was measured by using corrugated tube method (Figure 7.7). This is because in the corrugated tube method the measurement of autogenous shrinkage starts from the final setting time of the pastes, which is earlier than in the ASTM C 157 method, which starts the measurement 24 hours after casting. Thus the ASTM C 157 method is missing an important part of the shrinkage behavior of samples in the first 24 hours. This led to a significant underestimation of the autogenous shrinkage of AAFA pastes. The autogenous shrinkage after 24 hours onwards, measured by the corrugated tube method, however, corresponds very well with the results obtained from the ASTM C 157 tests (Figure 7.10).

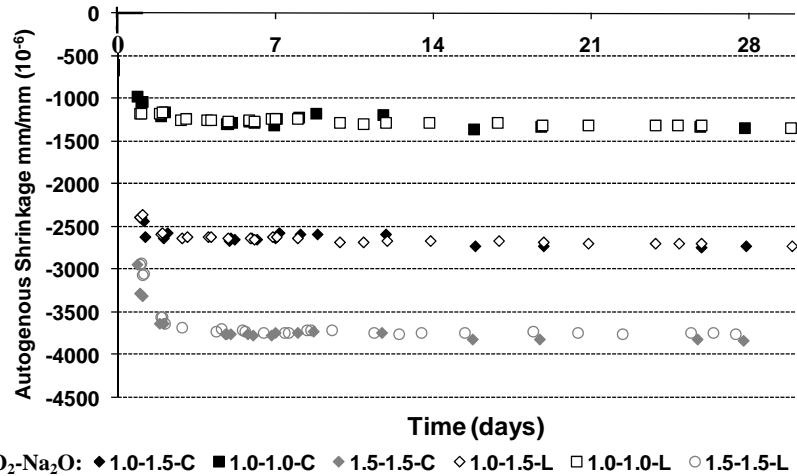


Figure 7.10 Comparison of autogenous shrinkage measured by corrugated tube method (C) and ASTM C 157 method (L) of AAFA pastes

### 7.3.4 Evaporable and non-evaporable water content in AAFA pastes

The evaporable and non-evaporable water contents (per gram of original solid) of AAFA pastes are displayed in Figure 7.11 as a function of curing age. It is found that the content of non-evaporable water in all investigated AAFA pastes was very low. Most of the water in the matrix was present as free water. For example, after 90 days of curing, the non-evaporable water content for all three AAFA mixtures was less than 5 % of the original solid by weight (Figure 7.11b). This value is much lower than that in cement paste, where the non-evaporable water content after 90 days of curing from 12% to 16% was reported [Powers and Brownyard, 1946], depending on the degree of hydration. It indicates the different state of water in these two systems.

The different state of water in these two systems (i.e. cement paste and AAFA paste) can be explained if we look to the different chemical reactions that happen in these two materials. In cement paste, water reacts with cement particles, producing C-S-H gel. Part of the water in cement paste is chemically bonded in the C-S-H gel and the calcium hydroxide (CH) [Powers and Brownyard, 1946]. In the system of AAFA paste, the reaction product is a highly connected aluminosilicate (AlO<sub>4</sub>) and silicate (SiO<sub>4</sub>) tetrahedral network, with the negative charge balanced by the alkali metal cations [Provis and Van Deventer, 2009]. Most of the water is not chemically incorporated (or weakly bounded) in the aluminosilicate gel. More than 75 % of the water, i.e. 15 % by the weight of the original solid in Figure 7.11a, was still free water even after 90 days of curing.

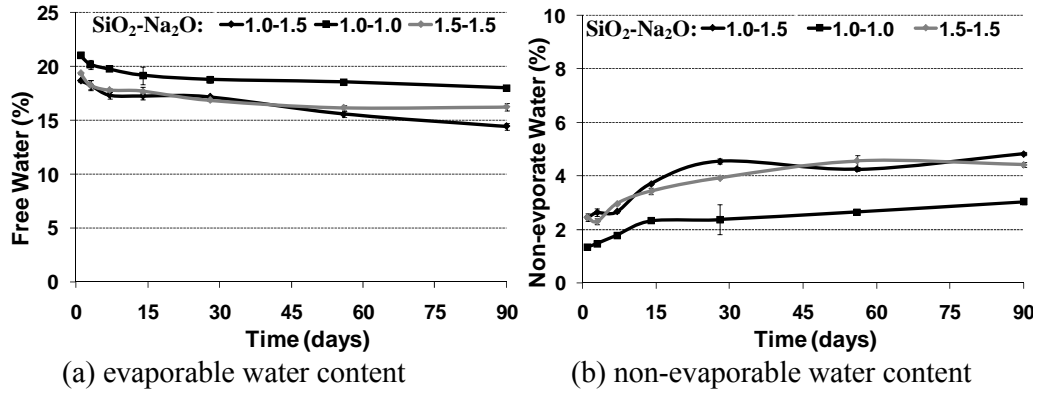


Figure 7.11 Evaporable and non-evaporable water content of AAFA pastes (weight percent with respect to original solid);

### 7.3.5 The internal RH of AAFA paste

The measured internal RH of a typical AAFA paste SiO<sub>2</sub>-Na<sub>2</sub>O=1.5-1.5 at curing temperature of 40 °C is shown in Figure 7.12. The internal RH was measured on two samples. Figure 7.12 shows a fast increase of the RH in the first 1-2 hours from roughly 80 % to about 90 %. After that, the RH gradually increased with time. After about 40 hours, a high internal RH (> 98 %) was reached.

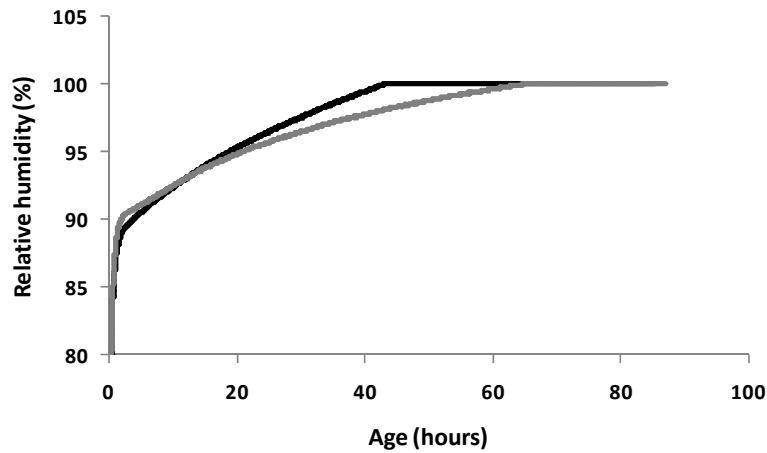


Figure 7.12 Measured internal RH with curing time for two samples of AAFA pastes 1.5-1.5 (curing temperature 40 °C)

The increase of the measured RH in the first 40 hours may be caused by two processes:

- 1) The moisture equilibration process between the RH sensor and the specimens.
- 2) The decrease of salts content ( $\text{Na}^+$  and  $\text{Si}^{4+}$ ) in the activating solution with progress of the reaction. In the beginning, the activating solution contains a certain amount of silica and sodium. Due to these salts, the initial RH is lower than 100 % (86 % calculated according to Raoult's law [Jensen and Hansen, 2001]). During the alkali activation, the alkali and silica ions react with the fly ash particles and will become incorporated in the reaction products. The concentration of these ions in the pore fluid decreases, which in turn leads to an increase of internal RH with time (Figure 7.12).

### 7.3.6 Discussion on the mechanisms of chemical and autogenous shrinkage of AAFA paste

#### *Discussion on the mechanisms of chemical shrinkage*

Like in Portland cement, the chemical shrinkage in AAFA pastes happens because the reaction products occupy less volume than the initial reactant. As stated in Chapter 2, the reaction of AAFA consists of the following steps: dissolution of fly ash, speciation equilibrium, gelation (condensation), reorganization and polymerization of reaction products. The presence of  $\text{OH}^-$  ions (provided by NaOH) initiates the rupture of the Si-O-Si, Al-O-Al and Al-O-Si bonds in original fly ash particles, producing silicon and aluminum species (e.g.  $\text{Si}(\text{OH})_4$  and  $\text{Al}(\text{OH})_4^-$ ). The formation of more silicon and aluminum species enhances the contact among these species, forming a coagulated structure, where the hydroxyl groups (e.g.  $\text{Si}(\text{OH})_4$  and  $\text{Al}(\text{OH})_4^-$ ) become connected to produce new Si-O-Si and Si-O-Al bonds, plus the by-products of water [Brinker and Scherer, 1990]. This type of reaction can continue to build larger and larger molecules, forming a continuous inorganic polymer network [Provis and van Deventer, 2007].

The reaction process of AAFA described above is analogous to the sol gel process [Brinker and Scherer, 1990], where a solution of fine colloidal particles (the sol) link together into a continuous solid phase (the gel). It has been reported that the morphology of the gel depends strongly on the degree of reversibility of the condensation reaction [Scherer, 1999; Thomas and Jennings, 2006]. If the condensation reaction is irreversible, a space-filling gel will form, resulting in a continuous gel network [Scherer, 1999; Thomas and Jennings, 2006]. If the condensation reaction is reversible, the monomers restructure and reorganize themselves into a more stable and dense state. Thus dense particles are formed occupying only a small fraction of the original sol volume [Scherer, 1999; Thomas and Jennings, 2006].

For AAFA, the reaction seems intermediate between the reversible and irreversible cases. The BSE image of AAFA pastes revealed that the aluminosilicate gel has a lower density than the original fly ash (lower brightness) (Figures 4.13 and 4.14). This indicates that the volume of the aluminosilicate gel is larger than that of the original



fly ash. Thus the aluminosilicate gel is a space-filling gel. However, this gel also undergoes reorganization and polymerization with elapse of time, transforming into a denser gel. The reorganization process of the gel is evidenced by the formation of two stages of gel (Al-rich gel and Si-rich gel) mentioned in Section 4.3.4, as well as the formation of crystalline phases (zeolite) (Section 4.3.5).

As mentioned, the chemical shrinkage of AAFA pastes happens because the reaction products occupy less volume than the initial reactant. The aluminosilicate gel has a larger volume than the original fly ash. It is assumed that the following processes will contribute to the decrease of volume of AAFA, measured as chemical shrinkage:

- 1) The sodium and silica in the activating solution became chemically bonded in the aluminosilicate gel;
- 2) Part of the water in AAFA, e.g. about 2-3 % by the weight of the original solid at 7 days (Figure 7.11b), became chemically bonded in the aluminosilicate gel;
- 3) As fly ash dissolved in the activating solution, pores in hollow fly ash particles were exposed to the activating solution. Part of the free water enters into these pores, resulting in a decrease of the whole volume.

The schematic illustration of the volume change of AAFA in the initial stage is given in Figure 7.13.

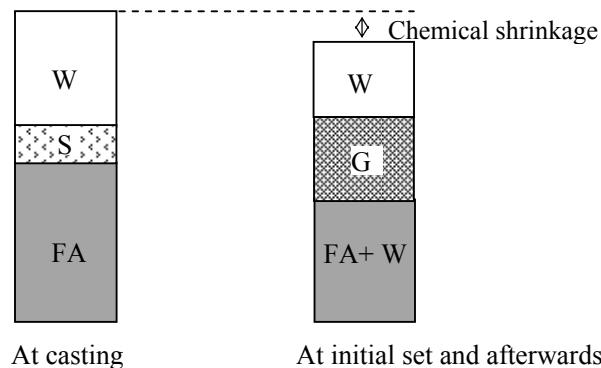


Figure 7.13 A schematic illustration of the chemical shrinkage of AAFA, FA = fly ash, S= sodium silicate, W = water, G = aluminosilicate gel. After the reaction, part of the water became chemically bonded in the gel, and part of the water entered into the pores of hollow fly ash particles.

#### *Discussion on the mechanisms of autogenous shrinkage*

##### *Cement pastes*

In cement pastes with low w/c ratio ( $w/c < 0.4$ ), the autogenous shrinkage happens (after setting) because of self-desiccation of the hydrating mixtures. When a solid structure is formed (setting), the stiffness of the material increases, and the chemical shrinkage is restrained by this skeleton. This gives rise to the formation of water-air

menisci and internal relative humidity (RH) drops (Kelvin's law). The formation of menisci goes along with capillary pressure in the pore fluid (Laplace's law), leading to the autogenous shrinkage of the material.

#### *AAFA pastes*

For AAFA pastes the correlation between internal RH and autogenous shrinkage appears to be different from that of cement pastes. Figure 7.12 indicates that the internal RH in AAFA remains at a high value ( $> 98\%$ ). This is much different from that in cement paste, where the internal RH decreases with ongoing hydration. It seems that the autogenous shrinkage of AAFA is not caused by a selfdesiccation process as it happens in cement paste. The continuous reorganization and polymerization of the aluminosilicate gel structure are more likely to cause the autogenous shrinkage of AAFA.

#### *Autogenous shrinkage of AAFA pastes and pore structure*

It is found that AAFA samples with a finer pore structure had a higher autogenous shrinkage. In Figures 7.14 and 7.15 the pore structure obtained from both the MIP and nitrogen adsorption tests of three 7 days old AAFA pastes are presented. Mixtures  $\text{SiO}_2\text{-Na}_2\text{O}=1.5\text{-}1.5$  exhibited the finest pore structure. This mixture also showed the highest autogenous shrinkage (Figure 7.7 and 7.8). For mixtures  $\text{SiO}_2\text{-Na}_2\text{O}=1.0\text{-}1.5$  and  $1.0\text{-}1.0$ , a lower autogenous shrinkage was found (Figure 7.7 and 7.8) for the mixtures with a coarser pore structure (Figure 7.14 and 7.15). This finding indicates that there might be a relationship between the autogenous shrinkage and the pore structure of AAFA systems. The finer pore structure of AAFA may be attributed to a higher degree of polymerization of the gel structure at early age, resulting in a denser matrix with smaller volume. This will then be observed as autogenous shrinkage. It indicates that the autogenous shrinkage of AAFA may be the same as its chemical shrinkage.

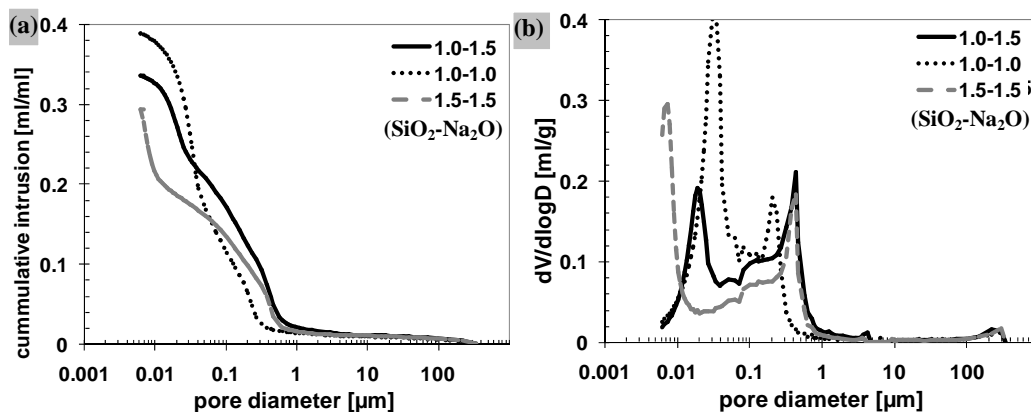


Figure 7.14 Pore size distribution of 7 days old AAFA pastes derived from MIP

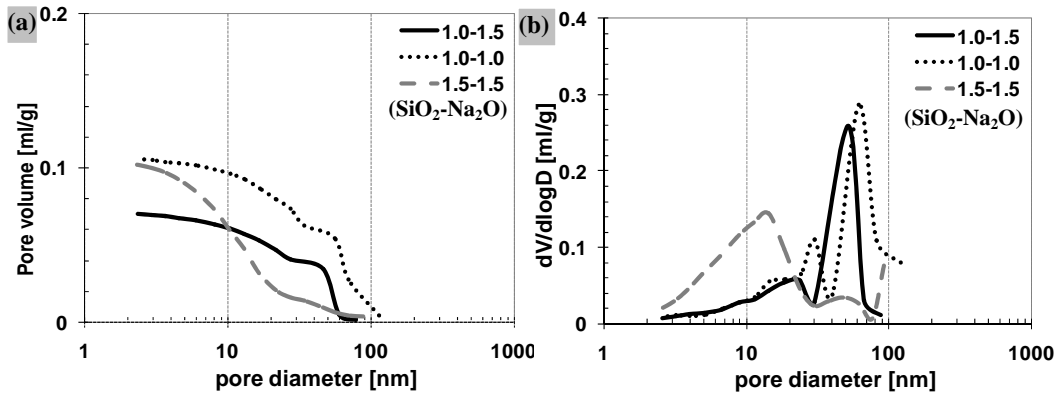


Figure 7.15 Pore size distribution of 7 days old AAFA pastes from  $N_2$  adsorption

### 7.3.7 Drying shrinkage of AAFA pastes

The drying shrinkage of three investigated AAFA mixtures, from 7 days to 180 days, is shown in Figure 7.16. For comparison, the drying shrinkage of cement paste ( $w/c=0.4$ ) is also given. Before starting the measurements, cement pastes were sealed cured at  $20\text{ }^\circ\text{C}$  for 7 days; and AAFA pastes were sealed cured at  $40\text{ }^\circ\text{C}$  for 7 days. This age (7 days) was chosen because after this age the autogenous shrinkage of all the AAFA mixtures was very small (Figure 7.7 and 7.8). Thus the shrinkage measured after 7 days is mainly caused by the drying shrinkage.

Figure 7.16 shows that the drying shrinkage of AAFA pastes is strongly affected by the silica and sodium content. Specimens with a higher sodium and silica content exhibited a larger drying shrinkage.

The drying shrinkage of AAFA measured in this study was higher compared to the test results reported in previous studies [Fernández-Jiménez et al., 2006b; Hardjito et al., 2004]. Their specimens, however, were cured at a higher temperature ( $60\text{ }^\circ\text{C}$  or  $80\text{ }^\circ\text{C}$ ) before starting the drying tests. This is expected to result in a much denser matrix and hence an increase of the rigidity of the network, leading to a higher resistance to drying shrinkage.

Compared to cement pastes ( $w/c=0.4$ ), AAFA pastes had a lower or similar drying shrinkage at 180 days. For example, specimens  $\text{SiO}_2\text{-Na}_2\text{O}=1.0\text{-}1.0$  and  $1.0\text{-}1.5$  exhibited a lower drying shrinkage (about 800 and 2100  $\mu\text{m}/\text{m}$ , respectively) than cement paste ( $w/c=0.4$ ) (around 2500  $\mu\text{m}/\text{m}$ ) after 180 days of drying (Figure 7.16). For specimens  $\text{SiO}_2\text{-Na}_2\text{O}=1.5\text{-}1.5$ , though the rate of drying shrinkage was different from that of cement pastes, a similar drying shrinkage was reached at 180 days (Figure 7.16).

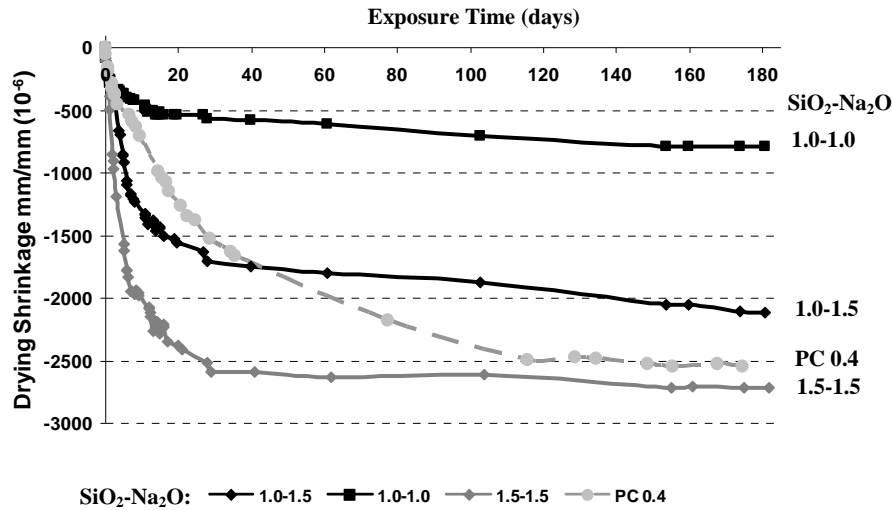


Figure 7.16 Drying shrinkage of AAFA pastes and cement paste with  $w/c=0.4$ . Prisms  $40 \times 40 \times 160$  mm, ambient  $RH=50\%$ . Measurement begun after 7 days sealed curing at  $40^\circ\text{C}$  for AAFA pastes and  $20^\circ\text{C}$  for cement pasts.

After AAFA specimens were exposed to the air for drying tests (after 7 days curing at  $40^\circ\text{C}$ ), some white substances were observed on the surface of specimens with high sodium content (i.e. mixtures  $\text{SiO}_2\text{-Na}_2\text{O}=1.0\text{-}1.5$  and  $1.5\text{-}1.5$ ) (see Figure 7.3a). This is caused by the efflorescence effect, where the un-reacted sodium migrates out of the sample and reacts with  $\text{CO}_2$  in the air, resulting in the formation of white compounds on the surface. When these mixtures were sealed cured at  $40^\circ\text{C}$  for longer age (e.g. 28 days), which accelerated the reaction and resulted in a denser microstructure, this phenomenon was not found.

### 7.3.8 Relationships between drying shrinkage, weight loss and pore structure

Drying shrinkage is caused by the evaporation of free water from the pores of the hardened material. Experimental results shown in Figure 7.11a reveal that most of the water in AAFA pastes is free water. The free water in AAFA pastes is distributed both in the cavities left by the dissolved fly ash particles and in the aluminosilicate gel pores [Lloyd, Provis et al., 2009c]. When water is removed from the AAFA pastes by evaporation (drying process), a meniscus is formed, which generates tensile stresses in the capillary water. In turn, these tensile stresses are balanced by compressive stresses acting on the solid of materials, leading to the contraction of the paste.

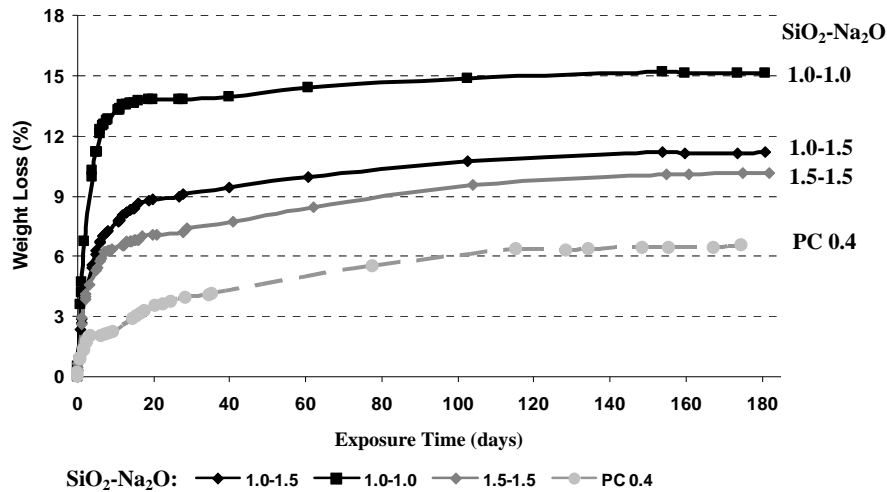


Figure 7.17 Mass change of AAFA pastes and cement paste with  $w/c=0.4$ , prism  $40 \times 40 \times 160$  mm, ambient  $RH=50\%$  (weight loss in percent of the total specimen weight)

Figure 7.17 shows the weight loss with time of both AAFA and cement pastes during the drying process, expressed as the weight percent of the total specimen. It is found that cement pastes ( $w/c=0.4$ ) had a much lower weight loss than the AAFA mixtures. This indicates that more free water has left AAFA mixtures. In addition, it is noticed that specimens  $\text{SiO}_2\text{-Na}_2\text{O}=1.5\text{-}1.5$ , with the highest drying shrinkage (around  $2700 \mu\text{m/m}$  after 180 days in Figure 7.16), showed the lowest weight loss during drying (about 10 % by weight in Figure 7.17). Specimens  $\text{SiO}_2\text{-Na}_2\text{O}=1.0\text{-}1.0$ , having the smallest drying shrinkage (about  $800 \mu\text{m/m}$  at 180 days in Figure 7.16), however, showed the highest weight loss (about 15 % by weight in Figure 7.17). This weight loss/drying shrinkage relationship of different AAFA mixtures is very different from that in cement pastes, where the magnitude of drying shrinkage is normally proportional to the weight loss of samples [Hansen, 1987].

If the drying shrinkage of AAFA pastes is plotted against the weight loss, as shown in Figure 7.18, we see that for specimens  $\text{SiO}_2\text{-Na}_2\text{O}=1.0\text{-}1.0$  most of the water was lost without causing large drying shrinkage in the initial stage of drying. The slope of the weight loss-drying strain curve of  $\text{SiO}_2\text{-Na}_2\text{O}=1.0\text{-}1.0$  increased when the weight loss exceeds 12 % by weight (Figure 7.18). For the other two mixtures (i.e.  $\text{SiO}_2\text{-Na}_2\text{O}=1.0\text{-}1.5$  and  $1.5\text{-}1.5$ ), the change of drying shrinkage with weight loss is more intense. It indicates that although the drying shrinkage is caused by the loss of water from the samples, the magnitude of drying shrinkage is also affected by the microstructure of samples.

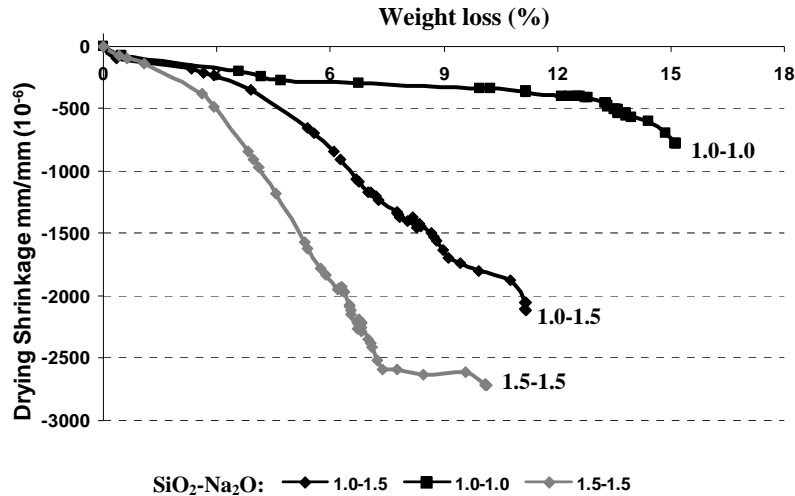


Figure 7.18 Weight loss as a function of drying shrinkage of AAFA pastes, prism  $40 \times 40 \times 160$  mm, ambient  $RH=50\%$

In fact, it is well known that the pore structure strongly affects the drying shrinkage of cement-based materials. According to Kelvin equation, drying to equilibrium at a given  $RH$  empties all pores larger than a given pore size ( $r$ ):

$$r = -\frac{2\gamma \cdot V_w \cdot \cos \theta}{\ln RH \cdot RT} \quad (7.3)$$

where  $\gamma$  is the surface tension of the pore fluid,  $0.073$  N/m for pure water,  $V_w$  is the molar volume of water,  $18.0 \times 10^{-6}$  m<sup>3</sup>/mol,  $\theta$  the contact angle between water and solids,  $r$  (m) the radius of the meniscus,  $R$  the ideal gas constant,  $8.314$  J/(mol·K), and  $T$  (K) the absolute temperature, in this study  $293.15$ K.

This equation (Kelvin equation) is also applicable to AAFA pastes. According to Thomas and Jennings [2006], the shrinkage stress (compressive stress acting on the solid of materials) induced by the capillary pressure depends on both the size of the smallest pores emptied and the volume fractions of these pores. If perfect wetting of the water-solid surface is assumed, the contact angle  $\theta$  is zero and thus  $\cos \theta = 1$ . With this assumption, when the drying of samples at  $RH = 50\%$  reaches equilibrium, the radius of the smallest pore emptied during the drying process can be calculated according to Equation 7.3:

$$r = -\frac{2\gamma \cdot V_w}{\ln RH \cdot RT} = -\frac{2 \cdot 0.073 \cdot 18.0 \cdot 10^{-6}}{\ln 0.5 \cdot 8.314 \cdot 293.15} = 1.55(\text{nm})$$

This corresponds to a pore diameter of  $3.1$  nm. It means that pores with diameter larger than  $3.1$  nm are emptied by the drying process at  $RH 50\%$ . The tensile stress ( $\sigma_{\text{cap}}$ ) in the pore fluid can be calculated by the Laplace equation, for circular cylindrical pores:

$$\sigma_{\text{cap}} = -\frac{2\gamma}{r} \quad (7.4)$$

According to the Laplace equation (equation 7.4), pores with smaller pore diameter cause a much higher tensile stress than larger pores. When the internal RH of AAFA decreased from initial saturated state (100 %) to 50 % during the drying process, the total drying shrinkage is the sum of strain produced from pores smaller than about 100 nm (corresponding to a RH of 99 %) to pores smaller than 3.1 nm. Samples with a larger volume fraction of smaller pores would have a higher compressive stress acting on the solid skeleton of materials, thus a higher shrinkage strain.

The volume fractions of pores can be derived from the MIP results. In order to compare the volume fraction of smaller pores in different AAFA mixtures, in this study, the volume fraction of pores smaller than 25 nm was used as a reference. The MIP results (Figure 7.14) revealed that mixtures  $\text{SiO}_2\text{-Na}_2\text{O}=1.5\text{-}1.5$  contained the largest volume fraction of pores smaller than 25 nm (i.e. 38.4 %), followed by mixtures  $\text{SiO}_2\text{-Na}_2\text{O}=1.0\text{-}1.5$  (22.59 %) and  $1.0\text{-}1.0$  (21.03 %). Thus, mixtures  $\text{SiO}_2\text{-Na}_2\text{O}=1.5\text{-}1.5$  are expected to cause the largest stress in the solid, corresponding to the largest magnitude of drying shrinkage. Samples  $\text{SiO}_2\text{-Na}_2\text{O}=1.0\text{-}1.0$ , with the smallest volume fraction of pores smaller than 25 nm, cause the lowest stress, corresponding to lowest drying shrinkage (Figure 7.16). These results are consistent with findings on alkali activated slag [Collins and Sanjayan, 2000; Melo Neto et al., 2008], in which the pore size refinement was also suggested to contribute to the increased capillary tension in the alkali activated slag system, resulting in a high drying shrinkage.

### 7.3.9 Suggestions for the use of AAFA from the shrinkage point of view

In this chapter, three AAFA mixtures ( $\text{SiO}_2\text{-Na}_2\text{O}=1.0\text{-}1.5$ ,  $1.5\text{-}1.5$  and  $1.0\text{-}1.0$ ) were selected to study the chemical, autogenous and drying shrinkage behavior. Results showed that the autogenous shrinkage of AAFA pastes mainly happened in the first 1-3 days (40 °C). These large strains did not result in early age cracking of AAFA pastes. The shrinkage caused by the drying may give rise to cracking. It is found that most of the water in AAFA is free water. During drying, the free water will leave the AAFA matrix, leading to contraction of the material. AAFA specimens with a coarse pore structure (e.g.  $\text{SiO}_2\text{-Na}_2\text{O}=1.0\text{-}1.0$  and  $1.0\text{-}1.5$ ) exhibited a low drying shrinkage, but a high water loss. Specimens  $\text{SiO}_2\text{-Na}_2\text{O}=1.5\text{-}1.5$ , having a finer pore structure, showed a higher drying shrinkage, but a low water loss. In order to obtain AAFA specimens with low drying shrinkage, a higher curing temperature (e.g. 60 or 80 °C) is recommended at early age, where specimens can gain higher strength in a short time, which increases the resistance to drying shrinkage.

Mixtures  $\text{SiO}_2\text{-Na}_2\text{O}=1.5\text{-}1.5$  exhibited the highest compressive strength (52 MPa, Chapter 3) and the lowest water permeability ( $1.38 \times 10^{-12}$  m/s, Chapter 6) at the age of 7 days. This mixture, however, had a large drying shrinkage, i.e. around 2700  $\mu\text{m}/\text{m}$  for paste samples. For concretes, the drying shrinkage is expected to be much lower than the paste samples. But there is a high risk of internal or external cracking. Thus, mixture  $1.5\text{-}1.5$  is not recommended for the application where a low shrinkage is required. The other two AAFA mixtures ( $\text{SiO}_2\text{-Na}_2\text{O}=1.0\text{-}1.5$  and  $1.0\text{-}1.0$ ), with mechanical properties similar to those of cement pastes ( $w/c=0.4$ ), showed much

smaller drying shrinkage than cement pastes. They are, therefore, recommended for further research.

#### 7.4 Concluding remarks

In this chapter, the chemical shrinkage, autogenous shrinkage and drying shrinkage of AAFA pastes with different activator content were measured. The shrinkage mechanisms of AAFA pastes and their main influencing factors were investigated and discussed. Based on the experimental results, the main conclusions of this chapter can be summarized as follows:

- The chemical shrinkage of three investigated AAFA pastes, cured at 40 °C for 7 days, was between 0.04-0.05 ml per gram of original solid (fly ash together with added  $\text{SiO}_2$  and  $\text{Na}_2\text{O}$ ). The processes contributing to the chemical shrinkage in AAFA pastes is different from that in cement paste.
- The autogenous shrinkage of AAFA pastes, cured at 40 °C, mainly happened in the first 1-3 days. Specimens with a higher amount of sodium and silica had a higher autogenous shrinkage. Under restrained condition, the stress caused by the autogenous shrinkage did not cause the early-age cracking of samples. Experimental results revealed a different mechanism of autogenous shrinkage in AAFA pastes compared to that in cement paste. It is assumed that the continuous reorganization and polymerization of the gel structure induce the autogenous shrinkage of AAFA paste, instead of the self-desiccation process as it occurs in cement paste. AAFA specimens with a finer pore size distribution exhibited a larger autogenous strain, which may be related to a higher degree of reorganization of the gel structure.
- Compared to cement pastes ( $w/c=0.4$ ), AAFA mixtures  $\text{SiO}_2\text{-Na}_2\text{O}=1.0\text{-}1.5$  and  $1.0\text{-}1.0$  had a lower drying strain after 180 days of drying at  $\text{RH} = 50\%$ . For mixtures  $1.5\text{-}1.5$ , a similar drying shrinkage is found to that of cement pastes ( $w/c=0.4$ ).
- AAFA mixtures with a higher sodium and silica content exhibited a higher drying shrinkage. The drying shrinkage of different AAFA mixtures was not proportional to their weight loss. The different weight loss/drying shrinkage relationship is attributed to the different pore structure of these mixtures, which can be explained from the capillary pressure point of view. The capillary pressure depends on the pore size distribution of AAFA. It thus suggests that the pore structure is an important factor determining the magnitude of shrinkage of AAFA mixtures.





## **Chapter 8**

# **Retrospection, Conclusions, Recommendations for Practice and Future Research**

---

### **8.1 Retrospection**

In the introduction of this thesis the environmental and technological benefits of alkali activated fly ash (AAFA) were mentioned. These advantages make AAFA a promising sustainable material for the construction industry. As a potential construction material, the ability to produce AAFA with good and consistent performance is crucial. However, because of the utilizations of different fly ashes, mixtures and curing procedures, variations in performance are almost unavoidable. Even if a good mixture of AAFA is obtained with satisfying early age properties, the long-term stability of this material cannot be fully guaranteed due to the lack of long-term performance data of this relatively new material. A reasonable and accurate evaluation of the long-term performance of AAFA requires a better understanding of the microstructure, which is a prerequisite for producing reliable and durable products.

This study aims at a better understanding of the microstructure and engineering properties (including mechanical properties, permeability and shrinkage) of AAFA with different activator content, i.e.  $\text{SiO}_2$  and  $\text{Na}_2\text{O}$ . With the information about the microstructure (Chapters 4 and 5), we could better understand how different activator content influences the engineering properties of AAFA. The evaluation of the mix proportion of the activator is not only based on the early age properties of AAFA, e.g. setting time, workability, heat release, mechanical properties (Chapter 3), but also takes into account the durability related issues, such as permeability (Chapter 6) and shrinkage (Chapter 7). The measurements results of AAFA were compared with those of Portland cement. These comparisons and further discussions reveal how the differences in microstructure affect the macro-properties of these two systems. In addition, the different performance of AAFA and Portland cement should be carefully evaluated when AAFA is used as an alternative to Portland cement.

This study started from the very beginning of AAFA production. A series of activating solutions with different  $\text{SiO}_2$  and  $\text{Na}_2\text{O}$  content were prepared to produce AAFA. Before synthesis the chemical composition, particle size distribution, chemical reactivity of the raw material, i.e. fly ash, was evaluated to see if it is suitable for alkali activation. The performance of AAFA mixtures was evaluated with

respect to the workability, setting time, heat release and mechanical strength. Based on the experimental results, a group of AAFA mixtures with 7 and 28 days strength similar or superior to those of cement pastes ( $w/c=0.4$ ) were chosen for further study.

In Chapter 4 and Chapter 5 of this thesis, the microstructure of AAFA pastes was experimentally studied with respect to the solid phases and the pore structure. The effect of the  $\text{SiO}_2$  and  $\text{Na}_2\text{O}$  content on the degree of reaction, the chemical structure and the micro-mechanical properties of the reaction products of AAFA were investigated. The pore structure of AAFA pastes was extensively studied by the MIP and nitrogen adsorption. With the information about the microstructure, the relationship between the microstructure and the engineering properties (including mechanical strength, permeability and shrinkage) were discussed. The dominant microstructure parameters that determine the compressive strength of AAFA pastes were explored in this study (Chapter 4). In addition, the permeability of AAFA, one of the most important factors in view of long-term performance, is linked to the pore structure parameters derived from MIP tests (Chapter 6).

The shrinkage (including chemical shrinkage, autogenous shrinkage and drying shrinkage) of AAFA pastes was studied as well (Chapter 7). The state of moisture in AAFA pastes was studied by measuring the internal relative humidity (RH) and the non-evaporable water content in AAFA. Ellipse ring tests were performed to assess the potential of cracking due to autogenous shrinkage of AAFA pastes under restrained condition. Based on the experimental results, the mechanisms of chemical and autogenous shrinkage of AAFA were discussed. The main influencing factors were studied.

## 8.2 Conclusions

The general conclusions are shown in Table 8.1 and summarized as follows:

- *Microstructure of AAFA pastes with different silica content and its relations to mechanical strength*

The effect of the silica content on the microstructure of AAFA pastes is twofold: On the one hand, the addition of a higher amount of silica (e.g. 1.5 mol/kg fly ash compared to 1.0 mol/kg fly ash) hampered the dissolution of fly ash particles, leading to a lower degree of reaction (both at 7 and 28 days). On the other hand, the added silica was incorporated in the gel, which resulted in a more homogeneous and denser matrix of AAFA pastes, and a high elastic modulus of the gel phase. Due to these two conflicting effects, AAFA mixture with a silica content of 1.5 mol/kg fly ash (mixtures  $\text{SiO}_2\text{-Na}_2\text{O}=1.5\text{-}1.5$ ) had a denser microstructure at 7 days than mixtures with silica content of 0.5 and 1.0 mol/kg fly ash (mixtures 0.5-1.5 and 1.0-1.5). A denser microstructure corresponds to a higher elastic modulus of the gel phase and a higher compressive strength. At 28 days, for AAFA mixtures with a silica content of 1.0 mol/kg fly ash (mixtures  $\text{SiO}_2\text{-Na}_2\text{O}=1.0\text{-}1.5$ ), the densification of microstructure was more pronounced than the other two mixtures with a silica content of 0.5 and 1.5 mol/kg fly ash. Thus, mixtures 1.0-1.5 showed the highest elastic modulus of the gel phase and compressive strength at 28 days.

Table 8.1 Summary of the effect of SiO<sub>2</sub> and Na<sub>2</sub>O content on the relevant properties of investigated AAFA pastes

Properties	Age (day)	SiO <sub>2</sub> content in activator (mol/kg fly ash) <sup>a</sup>			Age (day)	Na <sub>2</sub> O content in activator (mol/kg fly ash) <sup>b</sup>		
		0.5	1.0	1.5		1.0	1.3	1.5
<b>Compressive Strength</b>	7 28	→ Highest			7, 28	→ Increasing		
<b>Micro-elastic modulus of aluminosilicate gel</b>	7 28	→ Highest			7, 28	→ Increasing		
<b>Degree of reaction</b>	7, 28	→ Decreasing			7, 28	→ Increasing		
<b>Pore structure</b>	7 28	→ Finest			7, 28	→ Refining		
<b>Permeability</b>	7 28	→ Lowest			7, 28	→ Decreasing		
<b>Autogenous shrinkage (in the first 7 days)</b>		→ Increasing				→ Increasing		
<b>Drying shrinkage (from 7-180 days)</b>		→ Increasing				→ Increasing		

<sup>a</sup> with constant Na<sub>2</sub>O content in activator (1.5 mol/kg fly ash);

<sup>b</sup> with constant Si<sub>2</sub>O content in activator (1 mol/kg fly ash);

- *Microstructure of AAFA pastes with different sodium content and its relations to mechanical strength*

The addition of a higher amount of sodium in the activator, e.g. 1.5 mol/kg fly ash (mixtures  $\text{SiO}_2\text{-Na}_2\text{O}=1.0\text{-}1.5$ ) compared to 1.0 and 1.3 mol/kg fly ash (mixtures  $\text{SiO}_2\text{-Na}_2\text{O}=1.0\text{-}1.0$  and  $1.0\text{-}1.3$ ), enhanced the dissolution of fly ash particles, leading to a higher degree of reaction and a denser microstructure both at 7 and 28 days. AAFA mixtures with a denser microstructure had a higher elastic modulus of the gel phase and a higher mechanical strength.

- *Permeability of AAFA pastes with different silica and sodium content and its correlation to the pore structure*

The permeability of mixtures with a higher silica content is lower at 7 days, e.g. mixtures  $\text{SiO}_2\text{-Na}_2\text{O}=1.5\text{-}1.5$  compared to mixtures  $0.5\text{-}1.5$  and  $1.0\text{-}1.5$ . At 28 days, mixtures with a silica content of 1.0 mol/kg fly ash (mixtures  $1.0\text{-}1.5$ ) had the lowest water permeability. Mixtures with a higher sodium content had a lower water permeability both at 7 days and 28 days, e.g. mixtures  $\text{SiO}_2\text{-Na}_2\text{O}=1.0\text{-}1.5$  compared to mixtures  $1.0\text{-}1.0$  and  $1.0\text{-}1.3$ . The lower water permeability is attributed to a finer pore structure of AAFA pastes. The permeability can be related to the pore threshold diameter and the effective porosity derived from MIP results. By using these two pore structure parameters as input to calculate the water permeability, a linear relationship (equation 6.6) was found between the calculated and measured permeability for most of the AAFA samples.

- *Comparison of the pore structure and permeability of AAFA pastes and cement pastes*

The pore structure of AAFA pastes with a silica content  $\geq 1$  mol/kg fly ash, differed from that of cement pastes, mainly with respect to the formation of “capillary pores”. Some large cavities were left by dissolved fly ash particles, constituting the “capillary pores” in the matrix of AAFA. These cavities appeared as “isolated” voids, bordered by the homogeneously distributed gel. Due to this different distribution of pores, these cavities in AAFA contribute less to the water permeability than the typical “capillary pores” in cement pastes. However, the rate of pore refinement of some AAFA pastes at later age is significantly slower than that of cement pastes ( $w/c=0.4$ ). Thus the decrease of permeability with time for AAFA pastes is much slower than that for cement pastes. The different evolutions of pore structure and permeability as a function of time between AAFA and cement may indicate that care should be exercised with determining the long-term performance of AAFA with the evaluation methods currently used for cement-based systems.

- *Autogenous shrinkage of AAFA pastes with different silica and sodium content and its relations to pore structure*

The autogenous shrinkage of AAFA pastes mainly happened in the first 1-3 days of curing at elevated temperature (40 °C). Though a significant large autogenous shrinkage was measured in the first 24 hours, this did not result in an early age cracking of AAFA samples in the ellipse ring tests.

Water is not a reactant in the reaction of AAFA, but mainly acts as a medium. Thus the internal RH in AAFA pastes did not decrease with ongoing reaction, but stayed at very a high value (98 %). It is assumed that the autogenous shrinkage of AAFA pastes is caused by the continuous reorganization and polymerization of the aluminosilicate gel structure, instead of the self-desiccation process known to happen in cement pastes. AAFA mixtures with a higher content of silica and sodium content had a finer pore size distribution and a higher autogenous shrinkage. This may be related to the higher degree of reorganization and polymerization of the gel phase.

- *Drying shrinkage of AAFA pastes with different silica and sodium content and its relations to pore structure*

The drying shrinkage over a period from 7 days to 28 days of investigated AAFA pastes was lower or similar to that of cement pastes ( $w/c=0.4$ ). AAFA mixtures with a higher content of silica and sodium content exhibited a higher drying shrinkage. The pore structure of AAFA mixtures is an important factor determining the magnitude of drying shrinkage. The finer the pore structure, the higher capillary pressure that is produced during the drying process, resulting in a higher drying shrinkage.

### 8.3 Recommendations for practice

Based on the experimental results, some practical recommendations about AAFA synthesis are given below:

- *The addition of silica in the activator*

An optimal silica content exists for the mix design of AAFA. In this study, a silica content of 1.0 mol/kg fly ash is found as the optimal silica content (curing at 40 °C). Although mixtures with a high soluble silica content (e.g. 1.5 mol/kg fly ash in this study) showed a refined microstructure, high compressive strength and low permeability at early age (e.g. mixtures  $\text{SiO}_2\text{-Na}_2\text{O}=1.5\text{-}1.5$  in this study), the high content of silica hampered the dissolution of fly ash particles, leading to lower values of the mechanical properties at later ages compared to mixtures with a lower silica content (e.g. mixtures  $\text{SiO}_2\text{-Na}_2\text{O}=1.0\text{-}1.5$ ). In addition, these samples exhibited a high autogenous shrinkage, giving rise to a high probability of cracking under restrained conditions. Although the ellipse ring test results showed that the high autogenous shrinkage of the mixtures investigated in this study did not result in early age cracking, there is a potential risk. Moreover, the drying shrinkage of mixtures with high silica content is also high, which indicates a high probability to cracking during drying.

By evaluating the mix proportion of activator both from the early age and long-term properties, the optimal silica content obtained in this study is 1.0 mol/kg fly ash (6 % by weight of fly ash). This value is similar to the silica content used in studies presented in literature. For example, Fernández-Jiménez et.al used the activator with  $\text{SiO}_2$  content of 4.17 % by weight of fly

ash (0.7 mol/kg fly ash) to produce mortars and concretes made of AAFA (curing at 85 °C for 20 hours) [Fernández-Jiménez, Palomo et al., 2006e]. The silica content of 7 % by weight of fly ash (1.2 mol/kg fly ash) was used by Provis et. al [Provis and Van Deventer, 2009] in the aging tests of AAFA samples. It appears that there is a range of silica content (from about 4 % to 7 % by weight of fly ash) that is suitable for the mix design of AAFA mixtures. But it seems applicable to the fly ash with similar properties (chemical composition, reactivity, loss on ignition, particle size distribution). For fly ash with very different properties, e.g. high Ca or Fe content, low reactive Si and Al content, however, it is necessary to investigate the mix proportion of silica to obtain the optimal activator content.

- *The addition of sodium in activator*

In general, a high sodium content is favorable for the AAFA. A high sodium content in the activator results in a high degree of reaction and a denser microstructure of AAFA (e.g. mixtures 1.0-1.5 in this study). This leads to a higher compressive strength and a lower permeability. However, when a higher sodium content is used, special attention has to be paid to the efflorescence effect of samples, where the un-reacted sodium migrates out of the sample and reacts with CO<sub>2</sub> in the air, resulting in the formation of white compounds (Na<sub>2</sub>CO<sub>3</sub>) on the surface. To avoid the efflorescence effect, it is recommended to cure samples under sealed or high RH conditions. In addition, extending the curing time at elevated temperature, or using a higher curing temperature (e.g. 60 or 80 °C instead of 40 °C) are also recommended. These processes accelerate the alkali activation reaction, and then more sodium is chemically bound in the gel.

- *The addition of water in activator*

A low water content of AAFA is recommended. For paste samples, the w/FA mass ratio is recommended to keep lower than 0.35, as used in this study. For concretes made of AAFA, however, it may be difficult to keep below 0.35. It is still recommended to keep w/b ratio for concretes as low as possible. Since most of the water in AAFA is free water, under drying condition this water will leave the samples, causing capillary forces and drying shrinkage. This will increase the probability of cracking of samples. The use of a high curing temperature at early age results in a lower drying shrinkage of AAFA.

- *Mixture optimization for specific properties*

By adjusting the mix proportion, AAFA mixtures can exhibit different properties. For example, in this study mixture SiO<sub>2</sub>-Na<sub>2</sub>O=1.0-1.0 exhibits relatively high permeability, relatively high mechanical properties (≥ 30 MPa at 7 days) and very low drying shrinkage. These properties may indicate the potential application of AAFA in permeable pavements. When AAFA mixtures with lower permeability and higher mechanical strength (e.g. around 45 MPa at 7 days) are desired, these can be achieved by increasing the sodium content in the activator (e.g. mixtures SiO<sub>2</sub>-Na<sub>2</sub>O=1.0-1.5). However, special attention needs to be paid to the efflorescence effect of samples when a high sodium content is added as stated above. Another way to produce mixtures

with finer pore structure is to partially replace fly ash with blast furnace slag [Lloyd, Provis et al., 2009c]. The alkali activated fly ash-blast furnace slag blended systems have currently been used in the industry. However, the reaction products of fly ash-slag systems are not purely aluminosilicate gel, but also contain C-S-H gel with high degree of Al-substituent. It means that the microstructure and the evaluation of the long-term performance of this system are different from those of AAFA system and the cement system. This is, however, beyond the scope of this study.

#### 8.4 Future research

Perhaps the most relevant future work is to see the long-term performance of AAFA (e.g. Cl<sup>-</sup> diffusion, CO<sub>2</sub> ingress and frost attack). In fact, the information about the microstructure presented in this thesis is considered essential for evaluating the long-term performance. If a quantitative link can be made between the microstructure and durability related issues, predictions of the durability and service life of AAFA can be performed. Such predictions and evaluations have been performed on cement-based materials lately by Zhang [2013].

Besides these, there are some other aspects for future research of AAFA:

- A closer examination of the pore structure of AAFA samples. Due to the limitations of experimental techniques applied in this study (MIP and nitrogen adsorption), efforts are still needed in order to obtain a more realistic pore structure, which can provide the information about the three dimensional pore structure regarding the connectivity and tortuosity of pores in AAFA.
- The effect of the variations of the chemical composition, the particle size distribution and the reactivity of fly ash on the microstructure and engineering properties of AAFA. In this study, only one type of fly ash was studied. A comparison of results obtained from different fly ash resources is badly needed for a broader application of AAFA in real structures.
- The microstructure and engineering properties of AAFA mortar and concrete samples, because mortar and concrete are the final products applied in structures. Additionally, the possibility of the alkali aggregate reaction, that may happen in AAFA systems, is very important for the assessment of the long-term stability of AAFA.
- The modeling of the chemical reaction and microstructure of AAFA. To achieve this, it is important to know how the aluminosilicate gel forms and reorganize, especially with the presence of silica in the activating solutions. It will establish a quantitative correlation between the processing (reaction parameters) and macro-properties of AAFA.





# References

- 1698-09, A.C. (2009). Standard Test Method for Autogenous Strain of Cement Paste and Mortar, ASTM International.
- Ahmaruzzaman, M. (2010). "A review on the utilization of fly ash." Progress in Energy and Combustion Science **36**(3): 327-363.
- Aitcin, P.C. (2000). "Cements of yesterday and today: Concrete of tomorrow." Cement and Concrete Research **30**(9): 1349-1359.
- Aligizaki, K. (2005). Pore structure of cement-based materials: testing interpretation and requirements, Taylor & Francis.
- Allahverdi, A. and Skvara, F. (2001a). "Nitric acid attack on hardened paste of geopolymeric cements. Part 1." Ceramics **45**(3): 81-88.
- Allahverdi, A. and Skvara, F. (2001b). "Nitric acid attack on hardened paste of geopolymeric cements. Part 2." Ceramics **45**(4): 143-149.
- Allahverdi, A. and Skvara, F. (2005). "Sulfuric acid attack on hardened paste of geopolymer cements-Part 1. Mechanism of corrosion at relatively high concentrations." CERAMICS SILIKATY **49**(4): 225.
- Alonso, S. and Palomo, A. (2001). "Alkaline activation of metakaolin and calcium hydroxide mixtures: influence of temperature, activator concentration and solids ratio." Materials Letters **47**(1): 55-62.
- Applications, U.S.F.H.A.O.o.T. and Association, A.C.A. (1995). Fly Ash Facts for Highway Engineers, Federal Highway Administration, Office of Technology Applications.
- Bakharev, T. (2005a). "Geopolymeric materials prepared using Class F fly ash and elevated temperature curing." Cement and Concrete Research **35**(6): 1224-1232.
- Bakharev, T. (2005b). "Resistance of geopolymer materials to acid attack." Cement and Concrete Research **35**(4): 658-670.
- Banthia, N. and Mindess, S. (1989). "Water permeability of cement paste." Cement and Concrete Research **19**(5): 727-736.
- Barrett, E.P., Joyner, L.G., et al. (1951). "The determination of pore volume and area distributions in porous substances. I. Computations from nitrogen isotherms." Journal of the American Chemical society **73**(1): 373-380.
- Bentz, D.P. and Garboczi, E.J. (1991). "Percolation of phases in a three-dimensional cement paste microstructural model." Cement and Concrete Research **21**(2-3): 325-344.
- Bilodeau, A. and Malhotra, V.M. (2000). "High-volume fly ash system: concrete solution for sustainable development." Aci Materials Journal **97**(1).
- Brinker, C.J. and Scherer, G.W. (1990). Sol-gel science: the physics and chemistry of sol-gel processing, Academic Press.
- Brunauer, S., Emmett, P.H., et al. (1938). "Adsorption of gases in multimolecular layers." Journal of the American Chemical society **60**(2): 309-319.
- C-1608-07, A. (2007). Standard Test Method for Chemical Shrinkage of Hydraulic Cement Paste. ASTM International.

- Cheema, D., Lloyd, N., et al. (2009). Durability of geopolymer concrete box culverts-A green alternative. Proceedings of the 34th Conference on Our World in Concrete and Structures.
- Christensen, B.J., Mason, T.O., et al. (1996). "Comparison of measured and calculated permeabilities for hardened cement pastes." Cement and Concrete Research **26**(9): 1325-1334.
- Collins, F. and Sanjayan, J. (2000). "Effect of pore size distribution on drying shrinking of alkali-activated slag concrete." Cement and Concrete Research **30**(9): 1401-1406.
- Criado, M., Fernandez-Jimenez, A., et al. (2007a). "Alkali activation of fly ash: Effect of the SiO<sub>2</sub>/Na<sub>2</sub>O ratio Part I: FTIR study." Microporous and Mesoporous Materials **106**(1-3): 180-191.
- Criado, M., Fernandez-Jimenez, A., et al. (2007b). "An XRD study of the effect of the SiO<sub>2</sub>/Na<sub>2</sub>O ratio on the alkali activation of fly ash." Cement and Concrete Research **37**(5): 671-679.
- Criado, M., Fernandez-Jimenez, A., et al. (2008). "Effect of the SiO<sub>2</sub>/Na<sub>2</sub>O ratio on the alkali activation of fly ash. Part II: Si-29 MAS-NMR Survey." Microporous and Mesoporous Materials **109**(1-3): 525-534.
- Cui, L. and Cahyadi, J.H. (2001). "Permeability and pore structure of OPC paste." Cement and Concrete Research **31**(2): 277-282.
- Davidovits, J. (1989). "Geopolymers and geopolymeric materials." Journal of Thermal Analysis and Calorimetry **35**(2): 429-441.
- Davidovits, J. (1999). "Chemistry of geopolymeric systems, terminology." Geopolymere **99**: 9-39.
- Davidovits, J. (2002). 30 years of successes and failures in geopolymer applications. Market trends and potential breakthroughs. Keynote Conference on Geopolymer Conference.
- Davis, R.E., Carlson, R.W., et al. (1937). Properties of cements and concretes containing fly ash. ACI Journal Proceedings, ACI.
- De Silva, P. and Sagoe-Crenstil, K. (2008). "Medium-term phase stability of Na<sub>2</sub>O-Al<sub>2</sub>O<sub>3</sub>-SiO<sub>2</sub>-H<sub>2</sub>O geopolymer systems." Cement and Concrete Research **38**(6): 870-876.
- Diamond, S. (1971). "A critical comparison of mercury porosimetry and capillary condensation pore size distributions of portland cement pastes." Cement and Concrete Research **1**(5): 531-545.
- Duxson, P., Provis, J.L., et al. (2005). "Understanding the relationship between geopolymer composition, microstructure and mechanical properties." Colloids and Surfaces a-Physicochemical and Engineering Aspects **269**(1-3): 47-58.
- Duxson, P., Fernández-Jiménez, A., et al. (2007a). "Geopolymer technology: the current state of the art." Journal of Materials Science **42**(9): 2917-2933.
- Duxson, P., Provis, J.L., et al. (2007b). "The role of inorganic polymer technology in the development of 'green concrete'." Cement and Concrete Research **37**(12): 1590-1597.
- Duxson, P. and Provis, J.L. (2008). "Designing Precursors for Geopolymer Cements." Journal of the American Ceramic Society **91**(12): 3864-3869.
- El-Dieb, A. and Hooton, R. (1994). "Evaluation of the Katz-Thompson model for estimating the water permeability of cement-based materials from mercury intrusion porosimetry data." Cement and Concrete Research **24**(3): 443-455.
- Ellison, A.H., Klemm, R., et al. (1967). "Contact angles of mercury on various surfaces and the effect of temperature." Journal of Chemical and Engineering Data **12**(4): 607-609.

- Feldman, R., Carette, G., et al. (1990). "Studies on mechanics of development of physical and mechanical properties of high-volume fly ash-cement pastes." Cement and concrete composites **12**(4): 245-251.
- Feldman, R.F. (1972). "Factors affecting Young's modulus—porosity relation of hydrated Portland cement compacts." Cement and Concrete Research **2**(4): 375-386.
- Fernández-Jiménez, A. and Palomo, A. (2003). "Characterisation of fly ashes. Potential reactivity as alkaline cements." Fuel **82**(18): 2259-2265.
- Fernández-Jiménez, A. and Palomo, A. (2005a). "Mid-infrared spectroscopic studies of alkali-activated fly ash structure." Microporous and Mesoporous Materials **86**(1-3): 207-214.
- Fernández-Jiménez, A. and Palomo, A. (2005b). "Composition and microstructure of alkali activated fly ash binder: Effect of the activator." Cement and Concrete Research **35**(10): 1984-1992.
- Fernández-Jiménez, A., Palomo, A., et al. (2005c). "Microstructure development of alkali-activated fly ash cement: a descriptive model." Cement and Concrete Research **35**(6): 1204-1209.
- Fernández-Jiménez, A., Palomo, A., et al. (2006a). "Alkali activated fly ash binders. A comparative study between sodium and potassium activators." Materiales De Construccion **56**(281): 51-65.
- Fernández-Jiménez, A., de la Torre, A.G., et al. (2006b). "Quantitative determination of phases in the alkaline activation of fly ash. Part II: Degree of reaction." Fuel **85**(14-15): 1960-1969.
- Fernández-Jiménez, A., Palomo, A., et al. (2006d). "The role played by the reactive alumina content in the alkaline activation of fly ashes." Microporous and Mesoporous Materials **91**(1-3): 111-119.
- Fernández-Jiménez, A., Garcia-Lodeiro, I., et al. (2007). "Durability of alkali-activated fly ash cementitious materials." Journal of Materials Science **42**(9): 3055-3065.
- Fernández-Jiménez, A., Palomo, A., et al. (2008). "New Cementitious Materials Based on Alkali-Activated Fly Ash: Performance at High Temperatures." Journal of the American Ceramic Society **91**(10): 3308-3314.
- Fernández-Jiménez, A.M., Palomo, A., et al. (2006e). "Engineering properties of alkali-activated fly ash concrete." Aci Materials Journal **103**(2): 106-112.
- Flanigen, E.M., Khatami, H., et al. (1971). "Infrared structural studies of zeolite frameworks." Adv. Chem. Ser **101**: 201-229.
- Garboczi, E.J. (1990). "Permeability, diffusivity, and microstructural parameters: a critical review." Cement and Concrete Research **20**(4): 591-601.
- Gerhardt, R. (1988). As Review Of Conventional And Non-Conventional Pore Characterization Techniques, Cambridge Univ Press.
- Glukhovskiy, V. (1959). "Soil silicates." Gostroiizdat Publish. Kiev, USSR.
- Glukhovskiy, V. (1967). "Soil silicate articles and constructions." Budivel'nik Publish., Kiev, USSR.
- Glukhovskiy, V., Rostovskaja, G., et al. (1980). High strength slag-alkaline cements.
- Glukhovskiy, V.D. (1994). Ancient, modern and future concretes, Kiev, Ukraine.
- Goldstein, J., Newbury, D.E., et al. (2003). Scanning electron microscopy and X-ray microanalysis, Springer.
- Gourley, J. and Johnson, G. (2005). Developments in geopolymer precast concrete.

- Hansen, W. (1987). "Drying shrinkage mechanisms in Portland cement paste." Journal of the American Ceramic Society **70**(5): 323-328.
- Hardjito, D., Wallah, S.E., et al. (2004). "On the development of fly ash-based geopolymer concrete." ACI Materials Journal-American Concrete Institute **101**(6): 467-472.
- Hardjito, D., Wallah, S.E., et al. (2004). "On the development of fly ash-based geopolymer concrete." Aci Materials Journal **101**(6): 467-472.
- Hardjito, D. and Rangan, B.V. (2005). "Development and properties of low-calcium fly ash-based geopolymer concrete." Research report GC 1.
- Hardjito, D., Cheak, C.C., et al. (2009). "Strength and setting times of low calcium fly ash-based geopolymer mortar." Modern Applied Science **2**(4): P3.
- He, Z. and Li, Z. (2005). "Influence of alkali on restrained shrinkage behavior of cement-based materials." Cement and Concrete Research **35**(3): 457-463.
- Hooton, R.D. (1988). What Is Needed In A Permeability Test For Evaluation Of Concrete Quality, Cambridge Univ Press.
- Hughes, D. (1985). "Pore structure and permeability of hardened cement paste." Magazine of Concrete Research **37**(133): 227-233.
- Huntzinger, D.N. and Eatmon, T.D. (2009). "A life-cycle assessment of Portland cement manufacturing: comparing the traditional process with alternative technologies." Journal of Cleaner Production **17**(7): 668-675.
- Jensen, O.M. and Hansen, P.F. (2001). "Autogenous deformation and RH-change in perspective." Cement and Concrete Research **31**(12): 1859-1865.
- Kühl, H. (1908). Slag cement and process of making the same. Office U.S.P. USA. U.S. Patent 900939.
- Katz, A. and Thompson, A. (1986). "Quantitative prediction of permeability in porous rock." Physical review. B, Condensed matter **34**(11): 8179-8181.
- Katz, A. and Thompson, A. (1987). "Prediction of rock electrical conductivity from mercury injection measurements." Journal of Geophysical Research **92**(B1): 599-607.
- Kinrade, S.D. and Swaddle, T.W. (1988a). "Silicon-29 NMR studies of aqueous silicate solutions. 1. Chemical shifts and equilibria." Inorganic Chemistry **27**(23): 4253-4259.
- Kinrade, S.D. and Swaddle, T.W. (1988b). "Silicon-29 NMR studies of aqueous silicate solutions. 2. Transverse silicon-29 relaxation and the kinetics and mechanism of silicate polymerization." Inorganic Chemistry **27**(23): 4259-4264.
- Kovalchuk, G., Fernandez-Jimenez, A., et al. (2007). "Alkali-activated fly ash: Effect of thermal curing conditions on mechanical and microstructural development - Part II." Fuel **86**(3): 315-322.
- Krivenko, P. and Kovalchuk, G.Y. (2002). Heat-resistant fly ash based geocements.
- Lam, L., Wong, Y., et al. (2000). "Degree of hydration and gel/space ratio of high-volume fly ash/cement systems." Cement and Concrete Research **30**(5): 747-756.
- Li, Z. and Ding, Z. (2003). "Property improvement of Portland cement by incorporating with metakaolin and slag." Cement and Concrete Research **33**(4): 579-584.
- Lloyd, N. and Rangan, B. (2010). Geopolymer Concrete with Fly Ash. Second international conference on sustainable construction materials and technologies.
- Lloyd, R.R., Provis, J.L., et al. (2009a). "Microscopy and microanalysis of inorganic polymer cements. 1: remnant fly ash particles." Journal of Materials Science **44**(2): 608-619.

- Lloyd, R.R., Provis, J.L., et al. (2009b). "Microscopy and microanalysis of inorganic polymer cements. 2: the gel binder." Journal of Materials Science **44**(2): 620-631.
- Lloyd, R.R., Provis, J.L., et al. (2009c). "Spatial distribution of pores in fly ash-based inorganic polymer gels visualised by Wood's metal intrusion." Microporous and Mesoporous Materials **126**(1-2): 32-39.
- Lura, P. and Jensen, O.M. (2007). "Measuring techniques for autogenous strain of cement paste." Materials and Structures **40**(4): 431-440.
- McCormick, A. and Bell, A. (1989). "The solution chemistry of zeolite precursors." Catalysis Reviews—Science and Engineering **31**(1-2): 97-127.
- Mehta, P. and Gjørv, O.E. (1982). "Properties of Portland cement concrete containing fly ash and condensed silica-fume." Cement and Concrete Research **12**(5): 587-595.
- Melo Neto, A.A., Cincotto, M.A., et al. (2008). "Drying and autogenous shrinkage of pastes and mortars with activated slag cement." Cement and Concrete Research **38**(4): 565-574.
- Nyame, B. and Illston, J. (1981). "Relationships between permeability and pore structure of hardened cement paste." Magazine of Concrete Research **33**(116): 139-146.
- Oliver, W.C. and Pharr, G.M. (1992). "Improved technique for determining hardness and elastic modulus using load and displacement sensing indentation experiments." Journal of materials research **7**(6): 1564-1583.
- Palomo, A., Grutzeck, M., et al. (1999). "Alkali-activated fly ashes: a cement for the future." Cement and Concrete Research **29**(8): 1323-1329.
- Palomo, A., Alonso, S., et al. (2004). "Alkaline activation of fly ashes: NMR study of the reaction products." Journal of the American Ceramic Society **87**(6): 1141-1145.
- Parrott, L.J., Geiker, M., et al. (1990). "Monitoring Portland cement hydration: Comparison of methods." Cement and Concrete Research **20**(6): 919-926.
- Powers, T. (1935). "Absorption of water by portland cement paste during the hardening process." Industrial & Engineering Chemistry **27**(7): 790-794.
- Powers, T. and Brownyard, T. (1946). "Studies of the physical properties of hardened Portland cement pastes." J American Concrete Institute Proc **43**: 492-498.
- Powers, T.C. (1958). "Structure and physical properties of hardened Portland cement paste." Journal of the American Ceramic Society **41**(1): 1-6.
- Provis, J.L., Lukey, G.C., et al. (2005). "Do geopolymers actually contain nanocrystalline zeolites? A reexamination of existing results." Chemistry of Materials **17**(12): 3075-3085.
- Provis, J.L. and van Deventer, J.S.J. (2007). "Geopolymerisation kinetics. 2. Reaction kinetic modelling." Chemical Engineering Science **62**(9): 2318-2329.
- Provis, J.L. and Van Deventer, J. (2009). Geopolymers: Structure, processing, properties and industrial applications, Woodhead Publ. Limited.
- Purdon, A.O. (1940). "The action of alkalis on blast-furnace slag." Journal of the Society of Chemical Industry **59**: 191-202.
- Rees, C.A., Provis, J.L., et al. (2007a). "In situ ATR-FTIR study of the early stages of fly ash geopolymer gel formation." Langmuir **23**(17): 9076-9082.
- Rees, C.A., Provis, J.L., et al. (2007b). "Attenuated total reflectance Fourier transform infrared analysis of fly ash geopolymer gel aging." Langmuir **23**(15): 8170-8179.

- Rees, C.A., Provis, J.L., et al. (2008). "The mechanism of geopolymer gel formation investigated through seeded nucleation." Colloids and Surfaces a-Physicochemical and Engineering Aspects **318**(1-3): 97-105.
- Sánchez de Rojas, M.I., Luxan, M.P., et al. (1993). "The influence of different additions on portland cement hydration heat." Cement and Concrete Research **23**(1): 46-54.
- Scherer, G.W. (1999). "Structure and properties of gels." Cement and Concrete Research **29**(8): 1149-1157.
- Scrivener, K.L. and Kirkpatrick, R.J. (2008). "Innovation in use and research on cementitious material." Cement and Concrete Research **38**(2): 128-136.
- Sereda, P.J. (1972). "Significance of microhardness of porous inorganic materials." Cement and Concrete Research **2**(6): 717-729.
- Sindhunata, Van Deventer, J., et al. (2006). "Effect of curing temperature and silicate concentration on fly-ash-based geopolymerization." Industrial & Engineering Chemistry Research **45**(10): 3559-3568.
- Škvára, F., Jilek, T., et al. (2005). "Geopolymer materials based on fly ash." Ceramics–Silikáty **49**(3): 195-204.
- Taylor, M., Tam, C., et al. (2006). "Energy efficiency and CO<sub>2</sub> emissions from the global cement industry." International Energy Agency.
- Thomas, J.J. and Jennings, H.M. (2006). "A colloidal interpretation of chemical aging of the CSH gel and its effects on the properties of cement paste." Cement and Concrete Research **36**(1): 30-38.
- Van Deventer, J., Provis, J., et al. (2007). "Reaction mechanisms in the geopolymeric conversion of inorganic waste to useful products." Journal of hazardous materials **139**(3): 506-513.
- Van Jaarsveld, J., Van Deventer, J., et al. (1997). "The potential use of geopolymeric materials to immobilise toxic metals: Part I. Theory and applications." Minerals Engineering **10**(7): 659-669.
- Van Jaarsveld, J. and Van Deventer, J. (1999a). "The effect of metal contaminants on the formation and properties of waste-based geopolymers." Cement and Concrete Research **29**(8): 1189-1200.
- Van Jaarsveld, J., Van Deventer, J., et al. (1999b). "The potential use of geopolymeric materials to immobilise toxic metals: Part II. Material and leaching characteristics." Minerals Engineering **12**(1): 75-91.
- Van Jaarsveld, J., Van Deventer, J., et al. (2002). "The effect of composition and temperature on the properties of fly ash-and kaolinite-based geopolymers." Chemical Engineering Journal **89**(1-3): 63-73.
- Van Oss, H.G. and Padovani, A.C. (2003). "Cement manufacture and the environment, Part II: Environmental challenges and opportunities." Journal of Industrial Ecology **7**(1): 93-126.
- Wallah, S. and Rangan, B.V. (2006). "Low-calcium fly ash-based geopolymer concrete: Long-term properties." Perth, Curtin University of Technology **107**.
- Wang, Y., Ye, G., et al. (2010). Study on Micronized Sands as Cement Replacement. Second International Conference on Sustainable Construction Materials and Technologies. Ancona, Italy **2**: 991-1000.
- Washburn, E.W. (1921). "The dynamics of capillary flow." Physical review **17**(3): 273.

- Xu, H. and Van Deventer, J. (2000). "The geopolymerisation of aluminosilicate minerals." International Journal of Mineral Processing **59**(3): 247-266.
- Xu, H. and van Deventer, J.S.J. (2003). "The effect of alkali metals on the formation of geopolymeric gels from alkali-feldspars." Colloids and Surfaces A: Physicochemical and Engineering Aspects **216**(1-3): 27-44.
- Ye, G. (2003). The microstructure and permeability of cementitious materials. PhD thesis, Delft University of Technology.
- Young, J.F., Mindess, S., et al. (2002). Concrete, Prentice.
- Zeng, Q., Li, K., et al. (2012). "Pore structure characterization of cement pastes blended with high-volume fly-ash." Cement and Concrete Research **42**(1): 194-204.
- Zhang, M. (2013). Multiscale Lattice Boltzmann-Finite Element Modelling of Transport Properties in Cement-based Materials. PhD thesis, Delft University of Technology.





# Samenvatting

---

Alkali geactiveerd vliegas (AAFA), ook “geopolymeer” genoemd, heeft zich ontpopt als een vernieuwend bouw materiaal in de constructie industrie. Dit materiaal wordt normaliter gevormd door de reactie tussen vliegas en opgeloste hydroxide of alkalisilicaatoplossing. Het reactieproduct is een alkalialuminosilicaatgel, welke verschilt van de calciumsilicaathydraat (C-S-H) gel gevormd in portlandcement, maar die ook cementachtige eigenschappen heeft. Met het juiste mengselontwerp, kan AAFA vergelijkbare of superieure technische eigenschappen vertonen aan portlandcement. Bovendien toont dit materiaal veel potentie voor duurzame ontwikkeling, gezien de productie een aanzienlijke lagere CO<sub>2</sub>-uitstoot geeft dan de productie van portlandcement. Ondanks deze milieutechnische en technologische eigenschappen van AAFA, bestaan nog steeds uitdagingen voor de evaluatie van de lange-termijn stabiliteit van dit materiaal, gerelateerd aan de mengselverhouding van de hoeveelheid activator en de ontwikkeling van de onderliggende microstructuur.

Deze studie beoogt een beter begrip van de microstructuur en technische eigenschappen (waaronder mechanische eigenschappen, permeabiliteit en krimp) van AAFA met verschillende hoeveelheid activator, zijnde SiO<sub>2</sub> en Na<sub>2</sub>O. De evaluatie van de mengselverhouding van de activator is niet alleen gebaseerd op de eigenschappen van AAFA op jonge leeftijd, zoals zettingstijd, verwerkbaarheid, warmteafgifte, mechanische eigenschappen (hoofdstuk 3), maar houdt ook rekening met de duurzaamheid gerelateerde onderwerpen, zoals permeabiliteit (hoofdstuk 6) en krimp (hoofdstuk 7). De meetresultaten van AAFA werden vergeleken met die van portlandcement, bijvoorbeeld de resultaten van poriestructuur, permeabiliteit, watergehalte en krimp. Deze vergelijkingen en verdere discussies laten zien hoe de verschillen in microstructuur de macro eigenschappen van deze twee systemen beïnvloeden. Bovendien dienen de verschillende prestaties van AAFA en portlandcement zorgvuldig te worden geëvalueerd wanneer AAFA toegepast wordt als alternatief voor portlandcement.

In hoofdstuk 3 werd een reeks van activatieoplossingen bereid met verschillende SiO<sub>2</sub> en Na<sub>2</sub>O gehalten om AAFA te produceren. Voor de synthese werden de chemische samenstelling, deeltjesgrootteverdeling, chemische reactiviteit van de grondstof, zijnde vliegas, beoordeeld om te zien of het geschikt is voor alkali activatie. De prestaties van AAFA mengsels werden beoordeeld met betrekking tot de verwerkbaarheid, zettingstijd, warmteafgifte en mechanische sterkte. Op basis van experimentele resultaten werd een groep van AAFA mengsels gekozen voor verdere studie met een sterkte vergelijkbaar of superieur aan dat van cementpasta's (wcf=0,4).

Het effect van SiO<sub>2</sub> en Na<sub>2</sub>O op de microstructuur van AAFA pasta's werd experimenteel bestudeerd in hoofdstuk 4 en hoofdstuk 5. De experimentele resultaten toonden aan dat een grotere hoeveelheid natrium (tussen 1,0 mol/kg vliegas en 1,5 mol/kg vliegas) de desintegratie van vliegas verbeterde, wat leidt tot een hogere reactiegraad en een dichtere microstructuur, zowel op 7 als 28 dagen. Dus toonden

AAFA mengsels met een hoger natriumgehalte een hogere mechanische sterkte en een lagere waterdoorlatendheid (hoofdstuk 6), zowel op 7 dagen als 28 dagen.

Het effect van het silicagehalte op AAFA is tweeledig: Enerzijds vertraagt de hogere gehalte aan silica (bijvoorbeeld 1,5 mol/kg vliegas tegenover 1,0 mol/kg vliegas) de desintegratie van vliegas, leidend tot een lagere reactiegraad op zowel 7 als 28 dagen. Anderzijds werd het toegevoegde silica opgenomen in de gel, resulterend in een meer homogene en dichtere matrix van AAFA pasta's, en een hoge elasticiteitsmodulus van de gel-fase. Vanwege deze tegenstrijdige effecten vertoonde een AAFA mengsel met hoger silicagehalte (bijvoorbeeld 1,5 mol/kg vliegas tegenover 1,0 mol/kg vliegas) een dichtere microstructuur, hogere druksterkte en lagere waterdoorlatendheid na 7 dagen. Echter, na 28 dagen was de verdichting van de microstructuur meer uitgesproken voor AAFA mengsels met een lager silicagehalte, zoals een silicagehalte van 1,0 mol/kg vliegas. Dus toonden mengsels met een lager silicagehalte, zoals 1,0 mol/kg vliegas in vergelijking met 1,5 mol/kg vliegas, een hogere druksterkte en lagere waterdoorlatendheid na 28 dagen.

De permeabiliteit is gerelateerd aan de drempel poriediameter en de effectieve porositeit afgeleid van MIP resultaten. Door deze twee parameters voor poriestructuur te gebruiken als input voor het berekenen van waterdoorlatendheid, werd een lineair verband gevonden tussen de berekende en gemeten permeabiliteit voor de meeste AAFA monsters.

De poriestructuur van AAFA pasta's met een silicagehalte  $\geq 1,0$  mol/kg vliegas verschilt zeer ten opzichte van cementpasta's, voornamelijk in relatie tot de vorming van "capillaire poriën". Sommige grote holtes werden achtergelaten door opgeloste vliegas deeltjes, die "capillaire poriën" vormen in de AAFA matrix. Deze holtes verschenen als "geïsoleerde" leegtes, begrensd door de homogeen verdeelde gel. Deze holtes in AAFA dragen minder bij aan de waterdoorlatendheid dan de typische "capillaire poriën" in cementpasta's (hoofdstuk 6). Echter, de mate van porieverfijning van enkele AAFA pasta's is beduidend langzamer dan dat van cementpasta's ( $w_{cf}=0,4$ ). Dus is de afname van permeabiliteit in de tijd voor AAFA pasta's veel langzamer dan dat voor cementpasta's. De verschillen in ontwikkeling van poriestructuur en permeabiliteit als functie van tijd tussen AAFA en cement kan erop wijzen dat zorg moet worden betracht bij het bepalen van lange termijn prestaties van AAFA met de evaluatiesystemen momenteel gebruikt voor cement gebaseerde systemen.

De krimp van AAFA pasta's werd bestudeerd in hoofdstuk 7. De experimentele resultaten lieten zien dat de chemische krimp van AAFA pasta's, nabehandeld bij 40 °C voor 7 dagen, vergelijkbaar was met dat van cementpasta. De processen die bijdragen aan chemische krimp in AAFA pasta zijn echter anders dan in cementpasta. Het mechanisme van autogene krimp van AAFA pasta is ook anders gevonden dan dat van cementpasta. Aangenomen wordt dat de continue reorganisatie en polymerisatie van de gelstructuur autogene krimp van AAFA pasta veroorzaken, in plaats van het zelf-uitdrogingsproces zoals het optreedt in cementpasta. AAFA monsters met een grotere hoeveelheid natrium en silica hadden een hogere autogene krimp. Onder belettende omstandigheden, heeft de spanning veroorzaakt door autogene krimp niet geleid tot de scheurvorming op jonge leeftijd. De relatie tussen autogene krimp en potentie tot scheurvorming van AAFA pasta's heeft nog meer onderzoek nodig.

De uitdrogingskrimp van onderzochte AAFA mengsels was vergelijkbaar of lager dan dat van cementpasta's ( $w_{cf}=0,4$ ) na 180 dagen van drogen bij  $RV = 50 \%$ . AAFA mengsels met een hoger natrium of silica gehalte vertoonden een hogere uitdrogingskrimp. De uitdrogingskrimp van de verschillende AAFA mengsels was niet evenredig aan hun massaverlies. Het verschil in verhouding massaverlies/uitdrogingskrimp wordt toegeschreven aan het verschil in poriestructuur van deze mengsels, welke kan worden verklaard uit het oogpunt van capillaire druk. Hoe fijner de poriestructuur, des te hoger de capillaire druk die wordt geproduceerd gedurende het uitdrogingsproces, resulterend in een hogere uitdrogingskrimp. Dus de poriestructuur is een belangrijke factor bepalend voor de grootte van uitdrogingskrimp van AAFA mengsels.



# Acknowledgements

---

The research work reported in this thesis was sponsored by China Scholarship Council (CSC) and Delft University of Technology (TU Delft). This research was carried out in Microlab, Section of Materials and Environment at the Faculty of Civil Engineering and Geosciences, TU Delft. CSC and TU Delft are gratefully acknowledged.

Five years' live and study in Delft has been the most important and unforgettable experience in my life. Every step and progress that I have made in these years could not be achieved without the help and support of many wonderful people around me. Therefore, I would like to express my greatest gratitude to all of them.

First I would like to acknowledge my promotor Prof.dr.ir. Klaas van Breugel, who gave me the opportunity to work and study at the Section of Materials and Environment in TU Delft. I deeply respect his knowledge, experience, insights and enthusiasm in research. I will always value his selfless guidance and support in helping me to improve my Ph.D. thesis during the last five months, which I will benefit for my whole lifetime.

Special thanks I want to give to my copromotor Dr. Guang Ye for his excellent supervision both in research and life. I am very grateful for his trust and confidence in my research. His optimistic and energetic attitude to work and life always give me energy, and lead me to see the bright side of life. Many thanks for our valuable discussions, your continuous guidance, support, patience and friendship throughout my whole Ph.D. study!

The committee members are very appreciated for their greatest insights and comments, which are very helpful for improving the quality of my thesis. In particular, I would like to thank Prof. John Provis and Dr. Siska Valcke for their inspiring comments on the draft thesis.

I would like to thank Mr. Cees Timmers and Ms. Franca Post, from the Center for International Cooperation and Appropriate Technology (CICAT) of TU Delft, for their support in helping me to come and stay in Delft.

I would like to thank Prof.dr. Lura Pietro at EMPA for his kindness help and valuable discussions on the shrinkage related issues. Thank Erik Schlangen at Microlab for helping me with the nanoindentation experiments. Thank Dessi Koleva at Microlab for helping me improve my written English.

My thanks to the helpful technicians: Gerrit Nagtegaal, Arjan Thijssen and Jon van den Berg, for giving me their practical experience and brilliant solutions for my laboratory problems.

I would like to thank all my friends and my current and former colleagues in TU Delft for their friendship, support and discussions these years. Special thanks to all of my Chinese colleagues in Microlab, i.e. Zhiwei Qian, Haoliang Huang, Hao Huang, Bei Wu, Hua Dong, Yun Zhang, Yong Zhang, Jiayi Chen, Zhuqing Yu, Xiaowei Ouyang, Chunping Gu, Tianshi Lu, for our memorable lunch, interesting discussions and valuable friendships. I would also like to thank my former Chinese colleagues, Jian Zhou, Qi Zhang, Quantao Liu, Mingzhong Zhang, Ying Wang, Tuan Nguyen, who helped me a lot for experiments and results analysis. Thank Renee Mors for helping me translate the summary into Dutch and Ms. Nynke Verhulst, Melanie Holtzapffel and Ingrid van Wingerden for their help in various kinds of documents. Special thanks to Jinghuan He and Yao Wang, who came to TU Delft together with me and became very good friends. Thanks for their lasting friendship and sharing every ups and down during my study and life in Delft.

Last, but surely not least, I want to thank my family for their endless love and support. Thanks for my parents who always are there for me and believe in me. My deepest love goes to my husband, Jie Hu, for his unconditional support, patience, encouragement and love all these years. Only with his accompany, my life abroad became the most precious time ever.

Yuwei Ma

Delft, September 2013

# List of Publications

---

Ma Y., Hu J., Ye G. (2013). "The pore structure and permeability of alkali activated fly ash." Fuel **104**: 771-780.

Ma Y., Hu J., Ye G. (2012). "The effect of activating solution on the mechanical strength, reaction rate, mineralogy and microstructure of alkali activated fly ash." Journal of Materials Science **47**(11): 4568-4578.

Ma Y., Ye G. (2012). The engineering properties of alkali activated fly ash mortar. 8<sup>th</sup> international conference: concrete in the low carbon era, Dundee, UK.

Ma Y., Ye G. (2012). Quantification of the degree of reaction of alkali activated fly ash by image analysis. International congress on durability of concrete, Trondheim, Norway.

Ma Y., Ye G. (2012). Prediction the water permeability of alkali activated fly ash based on MIP results. The 2<sup>nd</sup> international conference on microstructure related durability of cementitious composites (microdurability), April, Amsterdam, the Netherlands.

Ma Y., Ye G. (2011). The effect of Na<sub>2</sub>O on the pore structure and water permeability of alkali activated fly ash. Proceeding of the 13<sup>th</sup> international congress on the chemistry of cement, Madrid, Spain.

Ma Y., Ye G., van Breugel, K. (2012). Effect of Alkaline Activating Solutions on Fly ash-based Geopolymers. The Seventh International Symposium on Cement & Concrete and the 11th International Conference on Advance in Concrete Technology and Sustainable Development, Jinan, P. R. China

Hu, J., Koleva, D.A., Ma, Y., Schlangen, E., Petrov, P., Van Breugel, K. (2012). "The influence of admixed micelles on the microstructural properties and global performance of cement-based materials." Cement and Concrete Research **42**(8): 1122-1133.

Hu J., Zhu H., Ma Y., Yi T., Mao X., Lin A., Gan F. (2011). "Corrosion protection of stainless steel by separate polypyrrole electrode in acid solutions." Materials and Corrosion - Werkstoffe und Korrosion **62**(1): 68-73.



Hu J., Ma Y., Zhang L., Gan F., Ho. Y.S. (2010). "A historical review and bibliometric analysis of research on lead in drinking water field from 1991 to 2007." Science of the Total Environment **408**: 1738-1744.

# Curriculum Vitae

---

Name: Yuwei Ma  
Date of birth: 09<sup>th</sup> June, 1984  
Place of birth: Wuhan, Hubei Province, China  
E-mail: [yuwei.ma@hotmail.com](mailto:yuwei.ma@hotmail.com)



Oct. 2008 – Oct. 2013      Ph.D. Candidate, Microlab, Section of Materials and Environment, Faculty of Civil Engineering and Geosciences, Delft University of Technology, the Netherlands

Sept. 2006 – Jun. 2008      Master of Science (MSc.), Environmental Engineering, Wuhan University, Wuhan, Hubei, China

Sept. 2002 – Jun. 2006      Bsc. Degree, Environmental Engineering, Wuhan University, Wuhan, Hubei, China



  
**TU Delft**

Delft University of Technology

